Colloidal Self-Assembly Driven by Deformability & Near-Critical Phenomena

Universiteit Utrecht

Cover: scanning electron microscopy image of deformable, snowman-like colloids that self-assembled into a monolayer microcapsule (front), optical microscopy image of snowman-like particles that self-assembled into a micelle-like structure (back top) that falls apart upon decreasing the temperature (back middle), and colloidal particles that detach from an interface upon decreasing the temperature (back bottom). The images are false coloured and manipulated. For the microcapsule, particles with either six (blue) or five neighbours (red) are indicated.

Printed by: Uitgeverij BOXPress || Proefschriftmaken.nl

ISBN: 978-94-6295-467-0

Colloidal Self-Assembly Driven by Deformability & Near-Critical Phenomena

Colloïdale zelfassemblage gedreven door vervormbaarheid & nabij-kritische fenomenen

(met een samenvatting in het Nederlands)

Proefschrift

ter verkrijging van de graad van doctor aan de Universiteit Utrecht op gezag van de rector magnificus, prof. dr. G. J. van der Zwaan, ingevolge het besluit van het college voor promoties in het openbaar te verdedigen op woensdag 29 juni 2016 des middags te 2.30 uur

door

Chrisje Henrikus Jozef Evers

geboren op 2 april 1987 te Vierlingsbeek

Promotor: Prof. dr. W. K. Kegel

This work is part of the research programme TOP-GO with project number 700.10.355, which is financed by the Netherlands Organisation for Scientific Research (NWO).

Contents

1

Introduction

1.1. Self-Assembly

Order often spontaneously emerges out of disorder. Stars organize in galaxies; cattle graze in herds; proteins assemble into virus microcapsules; soap molecules gather in micelles; water molecules form snow flakes; and protons and neutrons arrange in atomic nuclei. In all these processes, pre-existing components spontaneously form patterns or structures without human intervention, which is a broad definition of self-assembly [1]. The last four examples are in a global or local energy minimum, while stars and cattle require input of energy to order. Furthermore, self-assembled virus microcapsules and most micelles are finite-sized, i.e. they have a well-defined size in at least one dimension. The hepatitis B core protein, for example, self-assembles into microcapsules with a diameter of either 25 or 30 nm [2, 3], while snowflakes, for instance, have a very broad size distribution [4]. In this thesis, we will focus on understanding self-assembled systems in an energy minimum and with a finite size, such as viruses and micelles.

To understand the formation of viruses, one needs to grasp the physics governing self-assembly. Furthermore, this knowledge could subsequently be exploited to produce new materials that order themselves. Eventually, computer chips, solar cells and drug delivery capsules might spontaneously be assembled from programmed building blocks. Identifying the minimal requirements for self-assembly of for example proteins is, however, extremely challenging. First of all, proteins are very complex as they are highly anisotropic, and their interactions contain contributions of van der Waals, electrostatic, steric and hydrophobic interactions and hydrogen bonding. Furthermore, due to their small size, dynamics of proteins cannot be directly visualized, and their interactions have to be deduced from indirect

measurements like scattering. Hence, simple model particles are required, such as colloids.

1.2. Colloids

Colloidal particles have a typical size between 1 nm and 1 µm, making them excellent model particles to study self-assembly. We illustrate this by examining five properties of polystyrene particles in water with a size of about 500 nm, that are used throughout this thesis. First, these particles have a similar size as the wavelength of light and a significantly larger refractive index than water [5, p867, 6, p12-178]. Consequently, they can be directly visualized over time using optical microscopy which is non-destructive and non-invasive. Furthermore, optical microscopy requires little sample preparation and interpretation and particles can be studied without addition of a dye. Secondly, in water, the diffusion constant of spheres with a diameter of 500 nm is about $4 \times 10^5\,\mathrm{nm}^2/\mathrm{s}$, and the typical time for a particle to diffuse over a distance equal to its diameter is thus about 0.3 s [6, p6-231, 7, p371]. Hence, particles are slow enough to be followed over time, but are sufficiently fast to explore many configurations in an experimental time frame. Thirdly, the gravitational length of polystyrene particles with a diameter of 500 nm in water is about 70 µm, i.e. gravity plays a minor role as long as the height of the particles does not exceed 140 times their diameter (Eq. 5.4). As a result, particles spontaneously translate in three dimensions, but can also be concentrated using sedimentation. Fourthly, by copolymerization with other monomers, functional groups can be incorporated, and the interactions between the particles can be tuned [7, p276, 8, 9, 10, 11]. Finally, polystyrene particles can be created with different shapes, ranging from spheres and ellipsoids, to snowman-like particles and exotic polyhedra [12, 13, 14, 15, 16].

By varying the interactions and shapes of particles, self-assembly into different structures has been observed. In 1986, Pusey and van Megen showed that hard spheres, i.e. non-attractive particles with only excluded volume repulsion, spontaneously form ordered crystals at high concentrations (Fig. 1.1a) [17]. More complex structures, such as liquid crystals, are obtained by using particles with an anisotropic shape, such as rods and platelets [18, 19, 20, 21] (Fig. 1.1b). Another approach is to create spherical particles with anisotropic or *directional* interactions. These Janus particles have distinct surface regions that are mutually attractive, so-called sticky patches [22, 23, 24, 25], and self-assemble, for example, into open lattices [26] (Fig. 1.1c). In the last decade, these two approaches have been combined

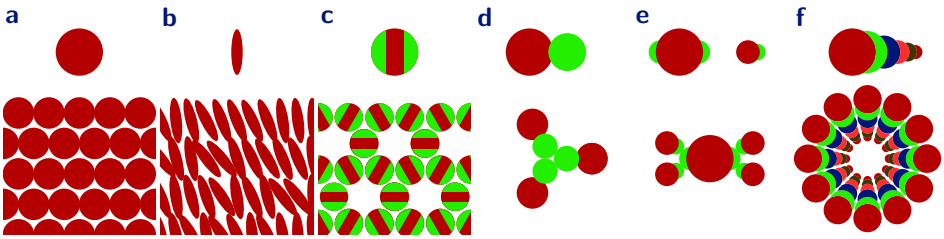

Figure 1.1. Colloidal model systems for self-assembly. Hard spheres (**a** ●) form crystals at high concentrations. Particles with an anisotropic shape (**b**) can form liquid crystals, while particles with anisotropic mutual attraction (**c** ●) can self-assemble into open lattices. Particles with an anisotropic shape as well as anisotropic interactions can form colloidal equivalents of micelles (**d**) and molecules (**e**). Self-assembly into monolayer microcapsules (**f**) has been predicted for particles with four orthogonally attractive lobes (●●●●).

using particles with an anisotropic shape as well as anisotropic interactions [27]. This resulted in, for instance, colloidal equivalents of micelles and molecules, and self-assembled tubes [28, 29, 30] (Fig. 1.1d–e). Finally, computer simulations predict the formation of monolayer microcapsules for particles that have four orthogonally attractive lobes [31] (Fig. 1.1f). Fig. 1.1 demonstrates that the anisotropy of the building blocks dramatically increases with the complexity of the self-assembled structures. Consequently, for highly complex structures, the building blocks are challenging to obtain experimentally.

1.3. Deformability

In contrast to the previously mentioned colloidal model systems, self-assembling proteins are deformable, as they can have different conformations [32]. Furthermore, so-called conformational changes influence interactions between proteins [33, p131,154]. Enzymes, for instance, undergo conformational changes upon binding to some inhibitors, preventing the enzyme from binding to substrate proteins [33, p154]. Furthermore, the hepatitis B core protein changes its conformation upon self-assembly into a virus microcapsule [34].

Recently, deformability has been introduced into nanoparticles with a size below 10 nm [35, 36, 37]. This has been achieved by grafting polymers onto their surface, that can change their conformation. Consequently, these deformable nanoparticles self-assemble into more complex structures compared to similar non-deformable

particles [35, 36, 37]. In chapters 4–5, we study deformable colloids and observe self-assembly into colloidal microcapsules for relatively simple building blocks.

1.4. Interparticle Interactions and Near-Critical Phenomena

Another challenge in colloidal self-assembly is to obtain particles with externally tunable, directional interparticle interactions. Ideally, an external knob would control the interparticle interactions without the need of adding chemicals. Temperature, an electric field or light would switch directional attraction between particles on and off, and even control the strength of the attraction. The attraction strength should be slightly larger than the thermal energy. If the attraction is too strong, colloids become kinetically trapped in the first configuration they happen to meet each other. On the other hand, if the attraction is too weak, no interparticle bonds are formed at all, and self-assembled structures are not thermodynamically stable. The directional attraction strength should thus be tuned so that bonds break once in a while, and the entire free energy landscape can be explored.

The basic framework to describe colloidal interactions is the DLVO theory [7, p409–412, 38, 39]. This theory treats interactions between colloids as the result of attractive van der Waals forces, on the one hand, and repulsive electrostatic double layer interactions, on the other hand. This results in a primary minimum with a very strong attraction strength at close interparticle distances. Furthermore, depending on primarily the salt concentration and pH, a second minimum, at further interparticle distances can be found. More sophisticated methods to induce tunable, anisotropic attraction use hydrophobic interactions [26, 40], host-guest interactions [41], DNA hybridization [29], depletion interaction [28, 30], and metal coordination [9]. All these interactions depend on temperature, and can thus in principle be externally tuned, without the addition of chemicals. The temperature dependence, however, is very weak for most interactions. For DNA-functionalized colloids, on the other hand, the attraction strength depends strongly on the temperature [8, 42, 43]. Furthermore, anisotropic attraction has also been externally tuned by magnetic fields [44, 45, 46]. Tuning the experimental conditions to obtain attraction strengths that result in kinetically accessible, thermodynamically stable clusters, however, is still challenging.

Near the critical point of partially miscible liquids, externally tunable attraction between particles can be induced [47, 48, 49]. These near-critical-solvent-mediated interactions are also known as critical Casimir interactions, and are continuously tunable with the temperature [50, 51]. In Chapter 7, we induce these interactions

for particles with anisotropic shape and interactions, and observe thermoreversible self-assembly into micelle-like structures.

Finally, colloidal particles are not only used as models, but are also found in natural and industrial systems such as fog, blood, paint, milk, asphalt, creams and mayonnaise. The latter four are emulsions: mixtures of two immiscible liquids stabilized by an emulsifier [52, p3–4]. A so-called Pickering emulsion, for example, is stabilized as colloidal particles self-assemble at the interface between the two liquids, and consequently prevent macroscopic phase separation [53, 54]. The stability of Pickering emulsions is generally tuned by changing the size and surface chemistry of the particles, or by adding salt or surfactants to the liquids [55, 56, 57, 58]. In Chapter 6, we create emulsions of near-critical mixtures, and observe that colloidal particles thermoreversibly attach onto the surface of the droplets. Consequently, the stability of these emulsions can be conveniently tuned by temperature.

1.5. Outline of This Thesis

The main goal of this thesis is to increase our understanding of self-assembly and to study new mechanisms that direct the formation of well-defined materials. Our results are organized in three parts. In Part I, we study individual colloidal particles. First, we synthesize particles with increasing complexity, resulting in particles that are mutually attractive, anisotropic and deformable (MAD, Chapter 2). These snowman-like particles consist of a core that is grafted with hydrophilic polymers and a non-grafted protrusion, and functional groups are covalently linked to the hydrophilic polymers. Next, we describe a method to automate the analysis of microscopy images (Chapter 3). This method is used throughout this thesis to determine the geometry of colloids from transmission electron microscopy images and to determine particle positions in optical microscopy images.

In Part II, we study self-assembly of deformable particles. Chapter 4 demonstrates that mutual attraction and deformability can induce anisotropic interactions for chemically and geometrically isotropic particles. Using computer simulations we deduce that the underlying mechanism is analogous to bond hybridization in quantum chemistry. Next, we apply colloidal bond hybridization in experiments using mutually attractive, anisotropic, deformable particles (Chapter 5). These relatively simple building blocks self-assemble into spherical monolayers, that superficially resemble virus microcapsules. Furthermore, the three MAD characteristics seem sufficient for the observed directionality. Deformable particles self-assemble thus into significantly more complex structures than similar non-deformable particles.

In Part III, we study the influence of near-critical phenomena on colloidal self-assembly. We show that particles thermoreversibly attach onto the interface between near-critical phase-separated mixtures (Chapter 6), and relate these observations to theory on near-critical phenomena. Furthermore, we apply this behaviour to create Pickering-like emulsions with a temperature-controllable stability. Next, we study particles with anisotropic shape and chemistry in near-critical mixtures (Chapter 7). Anisotropic, near-critical-solvent-mediated interactions are induced, resulting in thermoreversible self-assembly into micelle-like structures. Finally, the main results in Chapters 2 to 7 are summarized.

Part I

Colloidal Synthesis and Characterisation

2

Synthesis of Functionalized and Polymer-grafted Spherical and Snowman-like Colloids

Abstract

Attaching polymers and small molecules onto the surface of colloidal particles is a common way to control their interactions. Recently, anisotropic functionalization has been shown to induce even more complex interactions. Here, we combine these approaches and obtain particles that are functionalized, anisotropic, and polymer-grafted in three steps. First, cross-linked polystyrene spheres with an acrylic acid brush are synthesized by surfactant-free emulsion polymerization. Next, the spheres are swollen with additional styrene, heated and polymerized to obtain snowman-like particles. Finally, a fluorescent dye is covalently linked onto the acrylic acid groups and functionalized, polymer-grafted, snowman-like colloids are obtained.

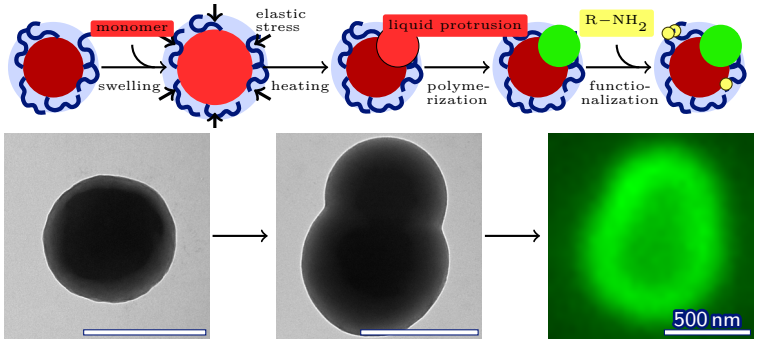

2.2

2.1. Introduction

Interactions between colloidal particles can readily be controlled by altering their surface properties. Small molecules can, for example, be bound onto particles to induce either attraction via hydrophobic interactions, or repulsion via electrostatic interactions [59, 60, 61]. Moreover, the surface of particles can be grafted with polymers to induce repulsion via steric interactions [7, p276, 52, p220-221] or attraction using DNA base pair binding [8, 29, 62]. Recently, particles have been synthesized with anisotropic or *directional* interactions. For instance, directional coating of a monolayer of particles has resulted in two-faced or *Janus* particles [22, 23, 25, 26]; clusters of particles have been swollen and polymerized to create particles with multiple patches [16, 29]; and protrusion formation has been used to create snowman-like particles and other *colloidal molecules* [13, 14, 15, 63, 64]. The last method consist of three steps. First, cross-linked polymer seed particles are swollen with additional monomer. Next, the particles are heated to induce phase separation and a liquid protrusion is formed. Finally, the liquid protrusion is polymerized and a snowman-like particle is obtained (Fig. Abstract).

In this chapter, for the first time to our knowledge, functionalization with small molecules, protrusion formation and polymer-grafting are combined. As we will discuss in Chapters 4 and 5, the resulting particles are mutually attractive, anisotropic as well as deformable (MAD), and self-assemble into surprisingly complex structures. Particles are synthesized by growing a protrusion onto polymer-grafted spheres and are subsequently functionalized. First, polymer-grafted, cross-linked poly(styrene-*co*-acrylic acid) spheres are synthesized by emulsifier-free polymerization. To study the covalent coupling of small molecules, the spheres are functionalized with a dye and observed using fluorescence microscopy. Next, non-functionalized spheres are made anisotropic by forming a protrusion onto polymer-grafted spheres. Finally, the resulting snowman-like particles are functionalized, and we obtain particles with a polymer-grafted and functionalized core and a non-functionalized protrusion.

2.2. Methods

2.2.1. Chemicals Unless stated otherwise, the following chemicals were used as received: acrylic acid (AA, 147230, 99%), aluminum oxide (Al_2O_3, puriss., 11028, ≥98%), divinylbenzene (DVB, mixture of isomers, 169099, 55%), fluoresceinamine (FlA, mixture of isomers, 46930, ≥75%), *N*-(3-dimethylaminopropyl)-*N*'-ethylcarbodiimide hydrochloride (EDC, purum, 03450, ≥98.0%), 2-(N-Morpholino)ethanesulphonic acid (MES, M3671, ≥99%), sodium phosphate dibasic (Na_2HPO_4, BioXtra, S7907, ≥99%), sodium phos-

phate monobasic dihydrate ($NaH_2PO_4 \cdot 2H_2O$, BioUltra, 71505, ≥99%), and styrene (St, ReagentPlus, S4972, ≥99%) were obtained from Sigma-Aldrich or its subsidiaries; potassium persulphate (KPS, 202015000, 99+%) and 2,2'-azobis(2-methylpropionitrile) (AIBN, 105151000, 98%) were obtained from Acros Organics; hydroquinone (puriss, 15616, ≥99.5%) was obtained from Riedel-de Haën; sodium choloride (NaCl, Emsure, 1.06404) was obtained from Merck; ethanol (100%) was obtained from Interchema; and Millipore water (MQ) was obtained with a Synergy water purification system.

2.2.2. Spherical Particles Cross-linked poly(styrene-*co*-acrylic acid) (CPSAA) spheres with a diameter of 530 ± 15 nm are prepared, where the second value indicates the standard deviation. Particles are synthesized by emulsifier-free polymerization of styrene, acrylic acid and divinylbenzene following Wang and Pang and Hu *et al.* [65, 66]. 90 ml MQ, 11 ml St passed over an Al_2O_3 column, 761 µl AA, and 55 µl DVB were added to a 250 ml three-neck round-bottom flask. The flask was constantly and vigorously stirred with a glass stirrer under nitrogen flow. Quantitatively, 0.05 g KPS was dissolved as an initiator and added to the flask with 10 ml MQ. After 15 minutes, the nitrogen inlet was raised above the liquid level, and after 15 more minutes, the flask was immersed in a 70 °C oil bath to start the polymerization. After 20 hours, a milky-white dispersion was obtained. Excess reactants were removed by washing by centrifugation (Beckman Coulter Allegra X-12R). Upon centrifugation, particles settle at the bottom of the sample, while unreacted chemicals are in the so-called supernatant. Three times, the dispersion is centrifuged at $2.1 \times 10^3\ g$ for about 2 h and the supernatant is replaced by MQ. CPSAA spheres with a diameter of 271 ± 7 nm are obtained in a virtually identical method.

Cross-linked polystyrene (CPS) spheres with a diameter of 0.41 ± 0.07 µm are prepared in a similar method. For these particles, 250 ml MQ, 23.5 ml St and 0.7 ml DVB were added to a 500 ml one-neck round-bottom flask. The flask was constantly and vigorously stirred with a PTFE coated stir bar, immersed in an 80 °C oil bath, and 0.78 g KPS in 37.5 ml MQ was added. After 24 h, a milky-white dispersion was obtained, which was washed three times by centrifugation and redispersed in MQ. By adding 50 mg NaCl to the 250 ml MQ, electrostatic repulsion can be reduced, resulting in larger particles with a diameter of 524 ± 44 nm.

2.2.3. Functionalization Fluoresceinamine is covalently linked to EDC activated carboxylic groups on spherical CPSAA particles, a method adapted from Marchand-Brynaert *et al.* [67]. In a typical synthesis, a 0.1 M MES buffer (0.49 g in 25 ml MQ), and a 0.2 M phosphate buffer (0.67 g Na_2HPO_4 and 0.041 g $NaH_2PO_4 \cdot 2H_2O$ in 25 ml MQ) were prepared. The solid mass fraction, m_s, of the dispersion was about 9% and 22 µl was brought in an Eppendorf tube. The dispersion was centrifuged ($6–10 \times 10^3\ g$, Beckman Coulter Microfuge 16), and the supernatant was replaced by an EDC/MES solution (1.16 mg EDC

in 1 ml MES buffer) to activate the AA groups. The dispersion was tumbled for one hour, and washed by centrifugation with MES buffer and twice with MQ. The dispersion was again centrifuged and the supernatant was replaced by 0.75 ml FlA/Phosphate (0.53 mg FlA in 1.5 mL phosphate buffer) to covalently bind FlA to the activated AA groups. The tube was wrapped in aluminium foil, and after tumbling for 15 h, the dispersion was washed three times with phosphate buffer, once with MES buffer, and seven times with MQ. Finally, a milky white dispersion was obtained.

Snowman-like particles are similarly functionalized using 2.5 ml dispersion with $m_s \approx 4\%$. Dispersions are brought in centrifuge tubes (VWR SuperClear Ultra-High Performance), and centrifuged using a Beckman Coulter Allegra X-12R at $2.1 \times 10^3\ g$ for 60 min (particles with a core of diameter, $d_c = 540$ nm), at $3.3 \times 10^3\ g$ for 45 min ($d_c = 626$ and 679 nm), or at $3.3 \times 10^3\ g$ for about 90 min ($d_c = 353$ nm). Typically, 45 mg EDC in 40 ml MES buffer was used to activate the AA groups, and 10 mg fluoresceinamine in 30 ml phosphate buffer is used to covalently bind FlA.

2.2.4. Snowman-like Particles To form a protrusion, non-functionalized CPSAA spheres are swollen with St, heated and polymerized, in line with Sheu *et al.*, Mock *et al.* and Kraft *et al.* [13, 14, 15]. In a typical experiment, the solid mass fraction, m_s, was determined by drying, and brought to 3–6% with MQ. About 5 ml dispersion was magnetically stirred with a PTFE coated stir bar in a glass tube. Styrene was added with a swelling ratio $S \equiv m_{St}/m_s = 3$, 5 or 7 where m_{St} and m_s are the mass of added St, and the solid mass in the dispersion. After one to two days stirring, the tube was immersed in an 80 °C oil bath for two hours under continuous stirring to form a styrene protrusion. Next, 500 µl of an aqueous hydroquinone solution (45 mg/50 mL) and 5 mg AIBN in 250 µl St were added, and the tube was immersed in the 80 °C oil bath for 24 h to polymerize the protrusion. Finally, a milky white dispersion was obtained. A mm-sized solid white aggregate was often found, which could easily be removed.

2.2.5. Characterization Transmission electron microscopy (TEM) images were taken with a Philips TECNAI 10 at 100 kV. Samples were prepared by drying a diluted dispersion droplet on a polymer coated copper grid under illumination with a heat lamp. The shape of the particles was characterized by Hough circle transformation as described in Chapter 3. To increase contrast, image levels were linearly rescaled using ImageMagick, so that 99.9% of all values were between the lower and upper level thresholds. The rescaling is indicated by the vertical bars in each image.

Infrared spectra were measured with a PerkinElmer Frontier FT-IR Spectrometer equipped with an ATR sampling accessory. A dispersion droplet was dried on an aluminum cup, and three times, the ATR unit was cleaned, part of the white solid was put on the crystal, and a spectrum was recorded. The spectra were baseline corrected and normalized

with the minimum transmittance between 1500 and 1400 cm^{-1} set to $T = 32\%$. Finally, the mean for the three spectra was calculated.

Fluorescence and reflected light microscopy images were captured with a Nikon Ti-E Inverted Microscope. Typically, a sample was prepared by bringing 0.5–2 µl dispersion between a microscope slide (Menzel-Gläser), and a #1.5 cover slip (Menzel-Gläser) with two #0 cover glasses (VWR) as spacers. Before use, the slides were cleaned with MQ, ethanol and Kimtech precision wipes, and cells were sealed with scotch tape. The microscope is operated with a Nikon TIRF 100×/1.49 objective, intermediate magnification of 1.5×, and a Hamamatsu ORCA Flash camera. For reflected light microscopy, a Nikon Intensilight C-HGFI light source was used with a Nikon D-FLE filter block. For fluorescence microscopy, the same light source was used with a Semrock FITC-3540C filter block. Image levels were linearly rescaled using ImageMagick from zero to the value of the brightest pixel.

2.3. Results and Discussion

2.3.1. Spherical Particles Polymerization of styrene, acrylic acid (AA) and divinylbenzene, results in cross-linked poly(styrene-*co*-acrylic acid) spheres with a diameter, $d = 530 \pm 15\,\mathrm{nm}$ (Fig. 2.1a–b). Here, the first value indicates the mean diameter, while the second value is the standard deviation or polydispersity over 1107 measured particles. The relative polydispersity is 2.8% and the particles indeed have a fairly uniform size (Fig. 2.1a). The mean sizes of different batches, however, vary significantly. Under virtually identical conditions, even particles with $d = 271 \pm 7\,\mathrm{nm}$ are prepared. More research is necessary to predictively control the size of the particles by the synthesis conditions. Here, the time that acrylic acid has been exposed to air seems to be an important variable.

Using infra-red spectroscopy, we verified that acrylic acid is incorporated into the particles (Fig. 2.1c). Spectra are obtained after washing by centrifugation to remove excess reactants. The spectrum of CPSAA particles (Fig. 2.1c—) is compared to the spectrum of cross-linked polystyrene particles that are polymerized without acrylic acid (Fig. 2.1c--). The two spectra are almost identical except for the fingerprint region at $\tilde{\nu} < 1500\,\mathrm{cm}^{-1}$ [68, p407]. At $1705\,\mathrm{cm}^{-1}$, however, an additional peak is found for CPSAA, that can be attributed to a C=O stretch vibration [68, p408]. This indeed indicates the presence of acrylic acid. Furthermore, a very broad O−H stretch band is expected at 3500–2500 cm^{-1} [68, p408], but here only a weak decrease in transmittance is observed.

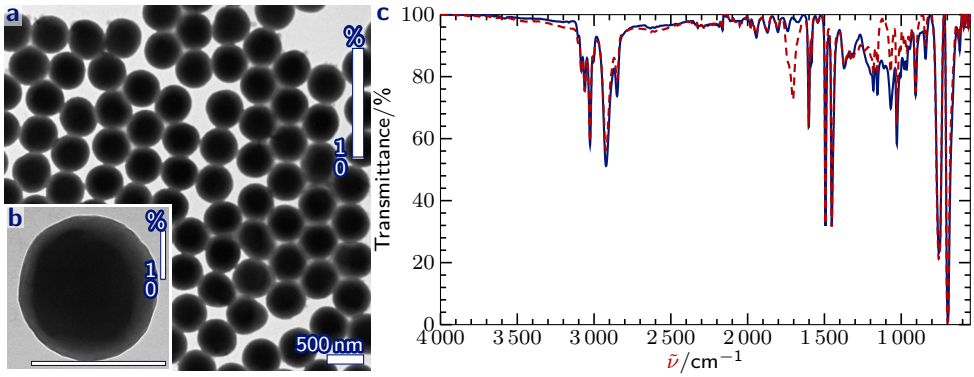

Figure 2.1. CPSAA spheres. TEM images of cross-linked poly(styrene-*co*-acrylic acid) (CPSAA) spheres with a diameter of 530 nm (**a–b**), and normalized infra-red transmittance as a function of the wavenumber, $\tilde{\nu}$, for CPSAA spheres (**c—**) and cross-linked polystyrene spheres (**c--**). In **a–b**, image levels are linearly rescaled from 0% to 1% as indicated by the vertical bars.

Acrylic acid and styrene are incorporated at different stages in the polymerization [65]. Hence, the particles consist of a hydrophobic polystyrene-rich interior and are grafted with a hydrophilic poly(acrylic acid)-rich (pAA) brush (App. 5.B). In the electron microscopy images, the colloids also have a dark interior and a more transparent shell (Fig. 2.1b). This, however, can also be due to the longer distance electrons have to travel through the centre of the spheres compared to the side.

Finally, the CPSAA spheres are synthesized without any surfactant and stabilized without an external stabilizer. Hence, no surfactants or stabilizers can desorb into the solvent. Furthermore, water can be used to dilute dispersions without loosing colloidal stability.

2.3.2. Functionalized Spherical Particles Fluoresceinamine (FlA) is covalently bound to acrylic acid groups on the CPSAA spheres. First, acrylic acid is activated with EDC which introduces a good leaving group [69, 70] (Fig. 2.2 1–3). Next, fluoresceinamine, is covalently linked forming an amide (Fig. 2.2 3–5).

CPSAA spheres that are functionalized as described in Subsection 2.2.3, appear bright in fluorescence microscopy (Fig. 2.3a,e). The particles have been washed eleven times by centrifugation to remove excess fluoresceinamine. Still, FlA might have adsorbed onto the particles instead of being covalently bound. In contrast to

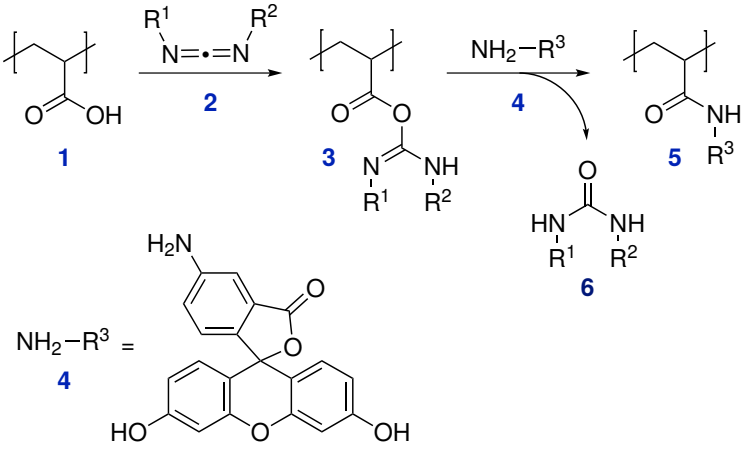

Figure 2.2. Activation and functionalization of acrylic acid. Acrylic acid groups in the cross-linked poly(styrene-*co*-acrylic acid) chains (AA, **1**) are activated with *N*-(3-dimethylaminopropyl)-*N'*-ethylcarbodiimide hydrochloride (EDC, **2**) resulting in an intermediate with a good leaving group (**3**). The intermediate reacts with fluoresceinamine (FlA, **4**) resulting in a functionalized acrylic acid group (**5**) and a urea byproduct (**6**).

the fluorescent dye fluorescein (FITC), however, fluoresceinamine is a self-quenching dye, and its fluorescence is only restored upon conversion of its amine group to an amide [71]. Hence, the clear signal in Fig. 2.3a suggests that an amide bond is formed and that fluoresceinamine is covalently bound.

We verify that fluoresceinamine is indeed covalently bound to acrylic acid by varying the synthesis method. All images in Fig. 2.3a–d are acquired under virtually identical illumination, and the fluorescence intensity strongly depends on the synthesis method. In Fig. 2.3e–f, the fluorescence intensity is given relatively to the maximum intensity per pixel, the full-well capacity of 30 000 electrons. By treating particles as described in Subsection 2.2.3, but without addition of FlA, the fluorescence intensity is not significantly larger than the noise values, indicating that FlA causes the fluorescence signal (Fig. 2.3d,f▲). For particles without AA (Fig. 2.3b,f●) or for which AA groups are not activated (Fig. 2.3c,f□), the intensity is about 40 times lower than for particles with activated AA groups (Fig. 2.3a,e∗). The lower intensity indicates that the amine group of FlA was not converted into an amide or that only a low quantity of FlA molecules is present. The fluorescence

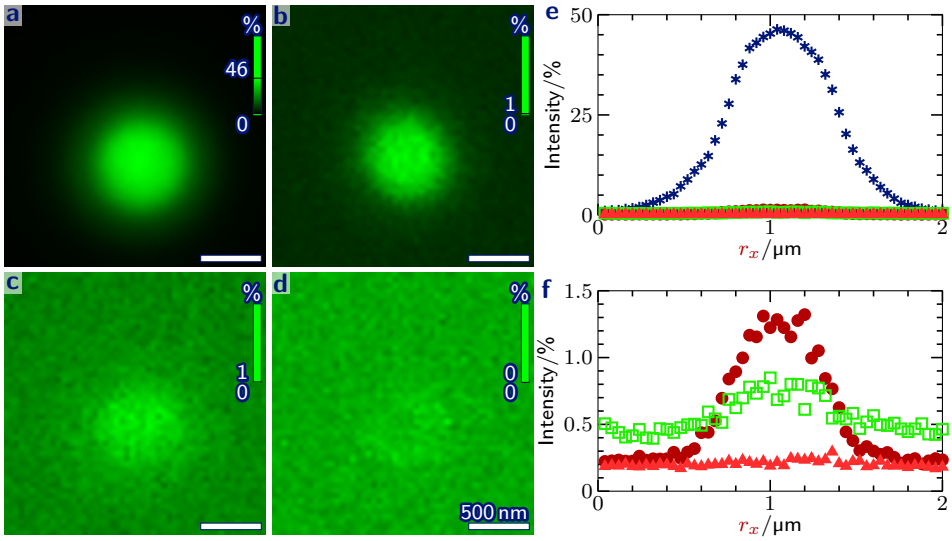

Figure 2.3. Functionalized CPSAA spheres. Fluorescence microscopy images for variations on the fluoresceinamine (FlA) coupling method (**a–d**), and fluorescence intensity relative to the maximum intensity per pixel on the horizontal line through the fluorescence maximum (**e–f**). Images are obtained for cross-linked poly(styrene-*co*-acrylic acid) (CPSAA) spheres activated with EDC and functionalized with FlA as described in Subsection 2.2.3 (**a**∗), activated and functionalized polystyrene spheres (**b**●), CPSAA without EDC addition (**c**□), and CPSAA without FlA addition (**d**▲). In **a–d**, image levels are rescaled from zero to the brightest pixel of each image.

intensity is, however, larger than without addition of FlA (compare Fig. 2.3f● and □ to ▲), so FlA probably adsorbed onto the surface in Fig. 2.3b–c. Without AA, the intensity is higher than with unactivated AA (compare Fig. 2.3f● to □). This is likely because AA groups prevent adsorption of FlA, either due to electrostatic repulsion or because the AA groups are relatively hydrophilic and FlA is relatively hydrophobic. Both without AA and with unactivated AA the fluorescence intensity is much lower than for activated AA (compare Fig. 2.3f● and f□ to e∗). Hence, we conclude that in Fig. 2.3a, fluoresceinamine is not adsorbed, but covalently binds to activated AA groups.

2.3.3. Snowman-like Particles Upon swelling CPSAA with styrene, heating and polymerizing, snowman-like particles are obtained (Fig. Abstract). The particles

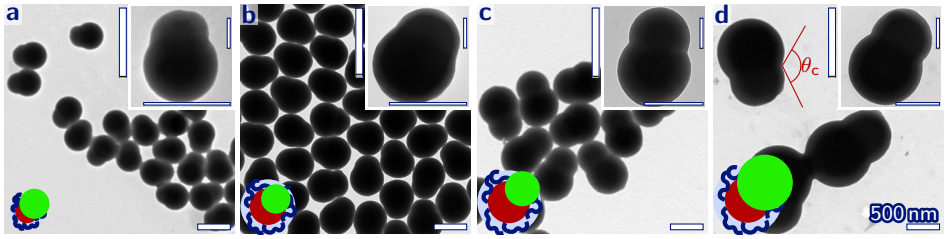

Figure 2.4. Snowman-like particles. By swelling, heating and polymerizing, snowman-like particles with a polymer-grafted (∿) cross-linked poly(styrene-*co*-acrylic acid) core (●) and a polystyrene protrusion (●) are synthesized with cores of diameters, $d_c = 353$ (**a**) 540 (**b**) 626 (**c**) and 679 nm (**d**). θ_c is the contact angle between the surface of the core and the surface of the protrusion (**d**).

Table 2.1. Properties of snowman-like particles. Swelling ratio, S, and mean, μ, and polydispersity, σ, of the diameter of the seed, d_0, diameter of the core, d_c, diameter of the protrusion, d_p, centre-to-centre distance r_{cc}, relative volume increase ΔV_r, and contact angle θ_c. The first value is the average over seven groups of measurements, the second value gives the standard deviation, and the value in brackets gives σ/μ. Finally, the ratio of d_c over d_0, and the number of measured particles, N_p is given.

S	d_0/nm		d_c/nm		d_p/nm		d_c/d_0
	μ	σ	μ	σ	μ	σ	
5	270.9 ± 2.6	6.8 ± 0.7 (2.5%)	353 ± 4	22 ± 5 (6.3%)	445 ± 5	12 ± 3 (2.6%)	1.30
5	530 ± 3	15 ± 4 (2.8%)	540 ± 17	22 ± 6 (4.1%)	435 ± 15	25 ± 5 (5.9%)	1.02
3	530 ± 3	15 ± 4 (2.8%)	626 ± 8	19 ± 3 (3.1%)	519 ± 6	19 ± 5 (3.7%)	1.18
7	530 ± 3	15 ± 4 (2.8%)	679 ± 20	57 ± 26 (8%)	827 ± 26	$(5 \pm 4) \times 10^1$(6%)	1.28

S	r_{cc}/nm		ΔV_r		θ_c/°		N_p
	μ	σ	μ	σ	μ	σ	
5	157 ± 3	20 ± 3 (12.5%)	4.31 ± 0.15	0.36 ± 0.09 (8.3%)	135.2 ± 1.0	7.1 ± 1.6 (5.3%)	561
5	163 ± 7	23.9 ± 2.8 (14.7%)	0.24 ± 0.10	0.12 ± 0.04 (50%)	142.7 ± 2.9	7.1 ± 0.8 (5.0%)	125
3	279 ± 8	26 ± 4 (9.2%)	1.19 ± 0.08	0.14 ± 0.04 (12%)	122.5 ± 1.3	6.8 ± 0.7 (5.5%)	195
7	360 ± 12	34 ± 21 (9%)	4.0 ± 0.4	0.8 ± 0.6 (20%)	124.0 ± 1.2	3.8 ± 1.7 (3.1%)	32

are studied with electron microscopy and their geometries are characterized as described in Subsection 3.2.6. By varying the synthesis conditions, particles of different geometries are obtained (Fig. 2.4 and Table 2.1).

For Fig. 2.4b, CPSAA spheres with a diameter of 530 nm are used as seed particles and swollen with styrene in a swelling ratio $S \equiv m_{St}/m_s = 5$, where m_{St} and m_s are the mass of added styrene, and the solid mass in the dispersion.

The resulting snowman-like particles consist of lobes of 540 nm and 435 nm, i.e. a lobe that is slightly larger than the seed particle, and a lobe that is significantly smaller (Fig. 2.4b). Hence, the 540 nm lobe corresponds to the CPSAA seed, which we define as the core, while the small lobe is the polystyrene protrusion (Table 2.1). Upon using CPSAA seeds with a diameter of 271 nm, however, both lobes are larger than the original seed particles (Table 2.1). Hence, the identity of each lobe can not be determined based on the size argument. Close inspection of transmission electron microscopy images (Fig. 2.4a), however, shows that the edge of the large lobe is a smooth arc, while the edge of the small lobe has some bumps. Polystyrene protrusions are formed by polymerizing a styrene droplet with a smooth surface, while the seed particle is gradually grown by emulsion polymerization and subsequently swollen and heated. Hence, the smooth large lobe corresponds to the polystyrene protrusion, while the small lobe is the core (Table 2.1). For Fig. 2.4c–d, 530 nm CPSAA seeds are used with $S = 3$ and 7, and similar arguments are used to determine which lobes correspond to the core and the protrusion (Table 2.1).

The relative volume increase,

$$\Delta V_\mathrm{r} \equiv \frac{V_\mathrm{s} - V_0}{V_0}, \tag{2.1}$$

with V_s and V_0 the volume of a snowman-like and a seed particle is calculated using Eq. 3.9. The volume of snowman-like particles is larger than the volume of seeds due to swelling with styrene. Furthermore, previous experiments have shown that ΔV_r increases with the swelling ratio, S [64]. The relative volume increase, however, is slightly smaller than the swelling ratio, as not all added styrene is incorporated into the particles (Table 2.1). This also explains the solid white aggregate, that is often found after polymerization. For seeds with $d_0 = 530$ nm and $S = 5$, however, ΔV_r is much lower than S (Table 2.1). Here, part of the styrene might have evaporated before the polymerization or more styrene might have been incorporated into the aggregate.

In all cases, the cores are significantly larger than the original seeds. Furthermore, the ratio between the diameter of the cores and the protrusions, d_c/d_0, increases with the relative volume increase, ΔV_r (Table 2.1). Upon heating, an equilibrium exist between styrene in the liquid protrusion and styrene in the cross-linked network [13, 63]. The observations in Table 2.1 suggest that for our particles, the equilibrium shifts to styrene in the cross-linked network at large ΔV_r.

The contact angle between the surface of the core and the surface of the protrusion, θ_c (Fig. 2.4d), is determined by the wetting properties of the unpolymerized styrene droplet on the surface of the cores. Upon increasing the hydrophobicity of the seed, for example, wetting of the core by the styrene droplet increases, resulting in a higher contact angle and—after polymerization—a less pronounced protrusion [14, 64]. Even though similar seeds are used for each synthesis, the contact angles are not constant (Table 2.1). We discuss two possible explanations for this observation. First, as we saw above, the relative size of core, d_c/d_0, increases with the relative volume increase, ΔV_r. Hence, upon increasing ΔV_r, more of the acrylic acid surface groups might be covered with polystyrene, resulting in a more hydrophobic surface of the cores and a larger contact angle. However, for $d_0 = 530\,\text{nm}$, θ_c decreases with ΔV_r, suggesting that the surface is less hydrophobic for larger particles. An alternative explanation arises from the pH dependence of the surface properties. At high pH, acrylic acid surface groups deprotonate, resulting in a more negative surface charge (App. 5.B) and a decrease in the hydrophobicity. Synthesis was performed in Millipore water without controlled pH. Consequently, a decrease of pH due to dissolution of CO_2 from air into water could explain a non-constant contact angle.

The contact angle and the diameters of the core and the protrusion are well-defined with polydispersities of about 5% (Table 2.1). The relative volume increase ΔV_r and the distance between the centres of the core and the protrusion, r_{cc}, however, are less well-defined with higher polydispersities. The parameters are obtained by fitting each lobe in the microscopy images to a circle (Subsection 3.3.2). The measurement error in ΔV_r and r_{cc}, are probably relatively large as they depend on properties of two circles. Furthermore, ΔV_r depends on the cubed value of both diameters. For particles with $d_c = 530\,\text{nm}$, the measurement error in ΔV_r is even higher as the difference between V_s and V_0 is relatively low.

By varying the synthesis conditions, we obtain particles with diameters of cores ranging from 353 to 679 nm, and with varying ratios between the size of the cores and the protrusions (Fig. 2.4). We thus obtained dispersions of snowman-like particles that are fairly different, but each well-defined. More systematic studies are, however, necessary to predictively control the properties of the particles by the synthesis conditions.

Finally, the dispersions with snowman-like particles of $d_c = 540$ and $626\,\text{nm}$, also contain particles with three lobes (Fig. 2.5). These particles can be formed when the liquid protrusions of two snowman-like particles coalesce before polymerization [15].

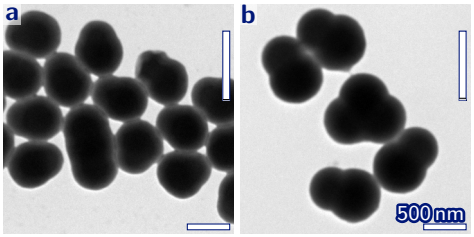

Figure 2.5. **Three-lobed particles.** Electron microscopy images of particles with three lobes surrounded by snowman-like particles with $d_c = 540$ (**a**) and 626 nm (**b**). As the number of three-lobed particles is very low, these images are not representative for the ratio between the number of three-lobed and snowman-like particles.

As expected, the diameters of the outer lobes of the three-lobed particles, seem to be similar to the diameter of cores of the snowman-like particle (Fig. 2.5). The number of three-lobed particles, however, is orders of magnitude lower than the number of snowman-like particles, so in the remainder of this thesis, three-lobed particles are ignored.

2.3.4. Functionalized Snowman-like Particles Snowman-like particles are functionalized with fluoresceinamine and studied using fluorescence microscopy. The method of Subsection 2.2.3 is followed, and the edge of the resulting particles appears bright in fluorescence microscopy images indicating covalent coupling of FlA (Fig. 2.6a–d). Furthermore, by comparing fluorescence microscopy images with reflected light microscopy images, we verify that all particles are functionalized (compare Fig. 2.6a–d to e–h). Here, immobilized particles are studied to obtain microscopy images using both techniques. Some particles happened to be immobilized at the microscopy glass which is probably due to Van der Waals forces. Other particles are immobilized close to the contact line between the dispersion, the air and the microscopy glass, due to the coffee stain effect as in Fig. 5.6a [72].

The fluorescence intensity decreases upon increasing the ratio between the diameter of the cores and the diameter of the seed particles, d_c/d_0 (compare Fig. 2.6a–d, insets to Table 2.1). All fluorescence microscopy images in Fig. 2.6 are acquired under identical illumination, and the maximum relative fluorescence intensity decreases from 38% to 6% when d_c/d_0 increases from 1.02 when $d_c = 530$ nm to 1.30 when $d_c = 353$ nm. For the snowman-like particles of 353 nm, the core is much larger than the original seed, and probably, the acrylic acid groups on the surface

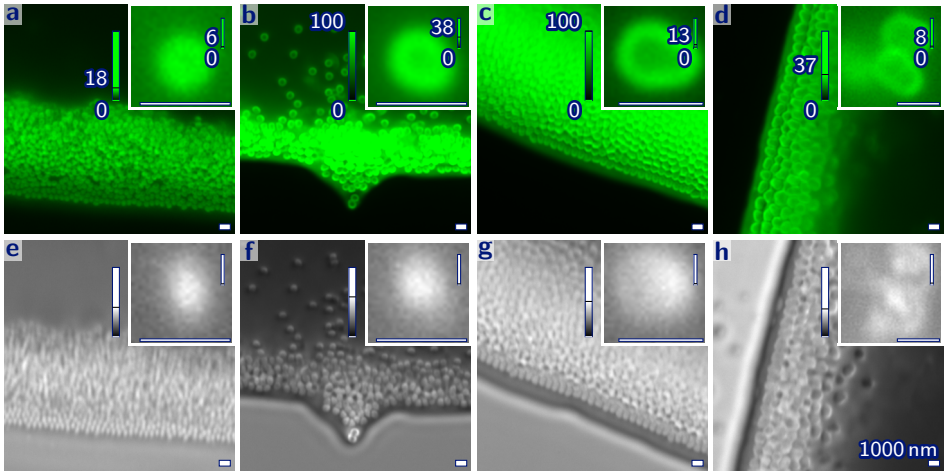

Figure 2.6. Functionalized snowman-like particles. Snowman-like particles with cores of diameter of **a,e**) 353 **b,f**) 540 **c,g**) 626 and **d,h**) 679 nm are functionalized with fluoresceinamine. The particles are studied with fluorescence microscopy (**a–d**) and reflected light microscopy (**e–h**). Particles are immobilized at the contact line or on the microscopy glass (insets). Image levels are rescaled from zero to the brightest pixel as indicated by the vertical bars, where the numbers give the thresholds as a percentage of the maximum intensity per pixel.

of the seeds are partly covered by additional polystyrene. Hence, upon increasing d_c/d_0, the acrylic acid groups seem to become more difficult to functionalize, resulting in a lower fluorescence intensity.

For snowman-like particles with $d_c = 626$ and 679 nm, both the core and the protrusion appear to be fluorescent, while for the other particles, the lobes are to small to be distinguished. We discuss three possible explanations for this observation. First, fluoresceinamine might have adsorbed onto the polystyrene protrusion. As we saw in Fig. 2.3b, fluoresceinamine can adsorb onto polystyrene surfaces, but the resulting fluorescence intensity is about 40 times lower than for covalent binding to acrylic acid (compare Fig. 2.3e* to f●). Onto the polystyrene protrusion, however, more fluoresceinamine might adsorb as the protrusion is polymerized using a non-ionic initiator, while the polystyrene spheres are polymerized using an anionic initiator. Consequently, the surface of the protrusion contains less charged groups than the particles in Fig. 2.3f●, and decreasing the number of charges seems

to increase the fluorescence (compare Fig. 2.3f● to f□). However, the brightness of the protrusion and the core are similar, and it seems unlikely that the quantity of adsorbed FlA onto the protrusion is equal to the quantity of covalently bound FlA to the core. A second explanation is that acrylic acid groups might have migrated to the protrusions allowing for covalent fluoresceinamine binding at both the core and the protrusion. Even though the polymer network is cross-linked, the particles are still highly deformable, and acrylic acid groups can expand on the order of 100 nm into the solution as we will see in App. 5.B. To cover the entire protrusion in Fig. 2.6d, however, the AA groups have to migrate much larger distances of at least 400 nm. This seems unlikely to result in a homogeneous acrylic acid and FlA distribution. The third explanation is that the brightness of the protrusion is an optical effect. The protrusion might, for example, act as a lens. This effect could possibly be prevented by studying the particles in a medium with a refractive index similar to that of polystyrene. Furthermore, the size of the particles is close to the wavelength of the excited and emitted light of about 500 nm. Hence, the exact location of fluoresceinamine on the particle surface can not be definitely verified using conventional optical microscopy. However, given the arguments above, it seems likely that at least more fluoresceinamine is present on the core than on the protrusion.

2.4. Conclusion

Prior work has shown that functionalization, polymer-grafting and anisotropy can greatly alter particle interactions. Here, we combine these approaches into polymer-grafted and functionalized snowman-like particles. First, we synthesize polymer-grafted spheres; next, we grow a protrusion onto the spheres; and finally, the polymers are covalently functionalized. Eventually, spherical and snowman-like particles with a variety of geometries and surface properties are obtained. In Chapters 5 to 7, we discover the structures into which they self-assembly.

2.5. Acknowledgement

Bas van Ravensteijn is thanked for help with the synthesis of cross-linked polystyrene particles and useful discussion. Hans Meeldijk and Chris Schneijdenberg are thanked for help with electron microscopy and Kanvaly Lacina is thanked for useful discussion.

3

Automated Image Analysis using Hough Circle Transformations

Abstract

Extracting information about the size, shape and position of particles in microscopy images can be a laborious task. Here, we describe an automated method to extract such properties using Hough circle transformations. The accuracy of this method is verified, and it is implemented in a graphical user interface. The versatility of our approach is demonstrated by characterizing spherical and snowman-like particles, and detecting the position of colloids in a time series.

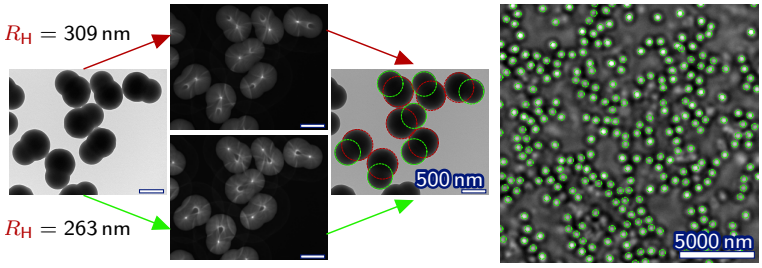

3.1. Introduction

Microscopy techniques, like optical microscopy, electron microscopy and holographic microscopy, are probably the most used techniques to characterize colloidal particles. Translating microscopy images into quantitative information about the morphology and positions of particles, however, is often a time-consuming task. A common method to measure the diameter of colloidal spheres, for example, requires visual identification of three edge pixels per sphere. This method is not only laborious, but also subjective, and the resolution is limited to a single pixel.

The Hough transformation can be used in an automated approach to pattern recognition. This method is based on a 1962 patent by Hough *et al.* [73], and was originally developed to recognize tracks of subatomic particles. The initial ideas of Hough have been extended to detect curves [74] and finally arbitrary shapes [75]. Nowadays, this computationally efficient algorithm is likely the most widely used procedure in computer vision [76]. In colloid sciences, these and similar transformation have been used to track the positions of particles in optical microscopy images [77, 78, 79, 80, 81].

In this chapter, we use Hough transformations to measure the size and position of particles in transmission electron microscopy images. First, we describe the basics of the method and verify its accuracy for test images. Next, we demonstrate that this method can be used to characterize the morphology of spherical and snowman-like colloids from electron microscopy images. Furthermore, we show that our application can also be used to detect particle positions in optical microscopy.

3.2. Methods

3.2.1. Hough Circle Transformation The basic principle of the Hough circle transformation can be visualized by simple geometry (Fig. 3.1a–b). First, we draw a circle with radius, R, and we randomly select 10 points at positions, $\vec{r}_i$ on the circle (Fig. 3.1a). Next, for each point, we draw a so-called Hough circle with radius $R_\mathrm{H} = R$ and centre $\vec{r}_i$ (Fig. 3.1b). The centre of the original circle can now be identified as the point where all Hough circles intersect.

The Hough circle transformation applies this property to transform an image of a circle into a Hough image. The transformation is demonstrated for a simple $13\,\mathrm{px} \times 13\,\mathrm{px}$ test image of a circle with position of its centre, $\vec{r}_\mathrm{c} = (7\,\mathrm{px}, 7\,\mathrm{px})$, and radius, $R = 3\,\mathrm{px} \pm \frac{1}{2}\,\mathrm{px}$ (Fig. 3.1c). Here, an image of a circle with $R = 3\,\mathrm{px} \pm \frac{1}{2}\,\mathrm{px}$ is defined as an image where the brightness of a pixel at position $\vec{r}_i$ is either 1 (white) if it is on the circle or 0 (black)

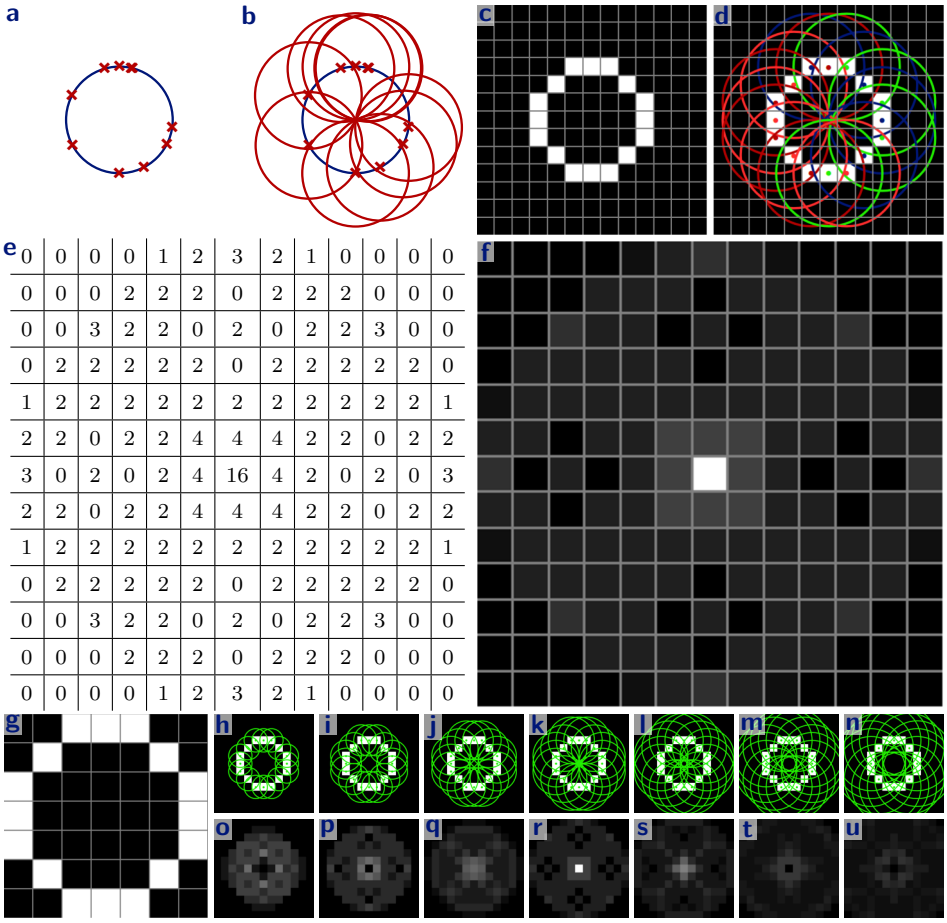

0	0	0	0	1	2	3	2	1	0	0	0	0
0	0	0	2	2	2	0	2	2	2	0	0	0
0	0	3	2	2	0	2	0	2	2	3	0	0
0	2	2	2	2	2	0	2	2	2	2	2	0
1	2	2	2	2	2	2	2	2	2	2	2	1
2	2	0	2	2	4	4	4	2	2	0	2	2
3	0	2	0	2	4	16	4	2	0	2	0	3
2	2	0	2	2	4	4	4	2	2	0	2	2
1	2	2	2	2	2	2	2	2	2	2	2	1
0	2	2	2	2	2	0	2	2	2	2	2	0
0	0	3	2	2	0	2	0	2	2	3	0	0
0	0	0	2	2	2	0	2	2	2	0	0	0
0	0	0	0	1	2	3	2	1	0	0	0	0

Figure 3.1. **Hough circle transformation.** For random positions, $\vec{r}_i$, on a circle with radius, R (**a**), all Hough circles with centres at $\vec{r}_i$ and radii $R_\mathrm{H} = R$ intersect at the centre of the original circle (**b**). For an image of a circle with $R = 3\,\mathrm{px} \pm \frac{1}{2}\,\mathrm{px}$ and centre position, $\vec{r}_\mathrm{c} = (7\,\mathrm{px}, 7\,\mathrm{px})$ (**c**), Hough circles are drawn with centres at the circle pixels and radii, $R_\mathrm{H} = R$ (**d**). The number of Hough circles crossing each pixel (**e**) gives after normalization the Hough value, H, which is the brightness in the Hough image (**f**). The position for which H is maximum corresponds to the centre of the original circle. The Hough image can also be obtained by convolving **c** with a circle matrix with $R_\mathrm{H} = 3 \pm \frac{1}{2}\,\mathrm{px}$ (**g**). The number of Hough circles crossing each pixel at $R_\mathrm{H} = 1.5$; 2.0; 2.5; 3.0; 3.5; 4.0 and 4.5 px (**h–n**), can be converted into Hough images with these radii (**o–u**). The radius of the original circle corresponds to the image with the highest maximum hough value (**r**).

otherwise,

$$B(\vec{r}_i) = \begin{cases} 1 & \text{if } R - \frac{1}{2}\,\text{px} \leq |\vec{r}_i - \vec{r}_\text{c}| \leq R + \frac{1}{2}\,\text{px} \\ 0 & \text{otherwise .} \end{cases} \tag{3.1}$$

The first step in the transformation involves counting the number of Hough circles crossing each pixel. For each of the centres of the 16 circle pixels, $\vec{r}_i$, we draw a Hough circle with $R_\text{H} = 3\,\text{px}$ and centre $\vec{r}_i$ (Fig. 3.1d). Next, for all pixels, the number of Hough circles crossing that pixel gives the Hough value, H (Fig. 3.1e). Zero Hough circles cross the corner pixels, and H increases towards the centre of the image. The maximum Hough value is 16 at (7 px,7 px), i.e. the centre of the original circle is crossed by all 16 Hough circles. Here, we define a pixel at $\vec{r}_j$ to be crossed by a Hough circle with centre $\vec{r}_i$ and radius R_H if,

$$R_\text{H} - \tfrac{1}{2}\,\text{px} \leq |\vec{r}_j - \vec{r}_i| \leq R_\text{H} + \tfrac{1}{2}\,\text{px}. \tag{3.2}$$

In the second step, the Hough values are normalized by the number of pixels per position $\vec{r}_i$ for which Eq. 3.2 is valid. After normalization, all values lie between 0 and 1. $H = 0$ if all pixels in the original image at a distance $R_\text{H} \pm \frac{1}{2}\,\text{px}$ are black, and $H = 1$ if all these pixels are white. For our test image, the normalization constant is 16, and the maximum Hough value is indeed 1.

The final Hough image is obtained by converting the matrix of normalized Hough values into an image (Fig. 3.1f). Here, brightness increases linearly with H from black at $H = 0$ to white at $H = 1$. For our test image, the resulting Hough image has a clear maximum at (7 px,7 px), that corresponds to the centre of the original circle, $\vec{r}_\text{c}$ (Fig. 3.1f).

The transformation is implemented in Mathematica using a convolution algorithm. Here, the original image is convolved with a matrix whose elements are 1 at a distance $R_\text{H} - \frac{1}{2}\,\text{px} \leq r_{ij} \leq R_\text{H} + \frac{1}{2}\,\text{px}$ from the centre and 0 otherwise (Fig. 3.1g).

If the radius of the circle is unknown, Hough images can be calculated for different radii, R_H, (Fig. 3.1o–u). When R_H is small, the Hough circles do not reach the centre of the original circle, while for large values of R_H, the Hough circle are to large to cross the centre (Fig. 3.1h–n). As expected, most circles cross the centre pixel for $R_\text{H} = R = 3\,\text{px}$ (Fig. 3.1k,r).

From the global maximum of all Hough images, both the centre and the radius of the original circle can be obtained. The radius corresponds to the value of R_H for which the maximum H is the global maximum. The coordinates of the global maximum of H give the position of the centre of the original circle, $\vec{r}_\text{c}$ (Fig. 3.1r).

3.2.2. Detection of a Disk For an image of a disk, the position and the size of the disk were measured in two steps. First, an image of the edge of the disk was calculated from the gradient in the brightness. Next, the edge image was transformed into Hough

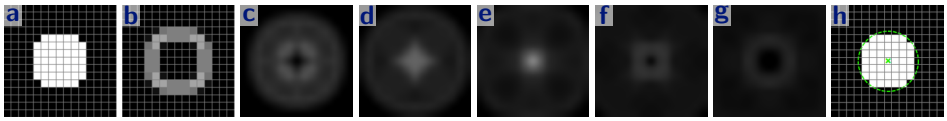

Figure 3.2. Detection of a disk. For a test image of a disk with radius, $R = 4\,\text{px}$, and position $\vec{r}_\text{c} = (8\,\text{px}, 8\,\text{px})$ (**a**), edges are detected from the gradient in the brightness (**b**). The edge image is transformed into Hough images with $R_\text{H} = 2$; 3; 4; 5 and 6 px (**c–g**). From the global maximum of the Hough images, the radius and the position of the centre of the original disk are obtained (**h**).

images, and the global Hough maximum gave the radius and the position of the centre of the disk.

This procedure is illustrated for a test image (Fig. 3.2a). An artificial $15\,\text{px} \times 15\,\text{px}$ image of a disk was constructed with brightness at position $\vec{r}_i$,

$$B(\vec{r}_i) = \begin{cases} 1 & \text{if } |\vec{r}_i - \vec{r}_\text{c}| < R \\ 0 & \text{if } |\vec{r}_i - \vec{r}_\text{c}| \geq R \end{cases}, \tag{3.3}$$

where $\vec{r}_\text{c} = (8\,\text{px}, 8\,\text{px})$ was the position of the centre of the disk, and $R = 4\,\text{px}$ was the radius of the disk (Fig. 3.2a).

An image of the edge of the disk was obtained by calculating the magnitude of the gradient in the brightness for each pixel, $|\nabla B|$. We refer to $|\nabla B|$ as the gradient, and it was calculated using Wolfram Mathematica's GradientFilter algorithm, using discrete derivatives of a Gaussian with radius $R_\text{grad} = 1\,\text{px}$ (Fig. 3.2b).

In the second step, the edge image was Hough circle transformed. Hough images were calculated with $R_\text{H} = 2$; 3; 4; 5 and 6 px (Fig. 3.2c–g). The global maximum Hough value was obtained for $R_\text{H} = 4\,\text{px}$ at (8 px,8 px). These values correspond to the radius and position of the centre of the original image (Fig. 3.2h).

Using this method, radii and positions were determined with resolution below the size of a pixel. This was achieved by rescaling the edge image and Hough transforming the rescaled image. The method is demonstrated for a test image of a $R = 15.4\,\text{px}$ disk (Fig. 3.3). To detect a disk at resolution R_res, the size of the edge image was increased to $1\,\text{px}/R_\text{res}$ times its original size using Gaussian resampling (Fig. 3.3b). Next, Hough images were calculated with scaled Hough radii, R_H/R_res, at intervals of R_res (Fig. 3.3c–h). The Hough radius, R_H, which results in the global maximum Hough value, corresponded to the radius of the disk, R (Fig. 3.3e). The coordinates of the global maximum were multiplied with R_res to obtain the position of the centre of the disk, $\vec{r}_\text{c}$.

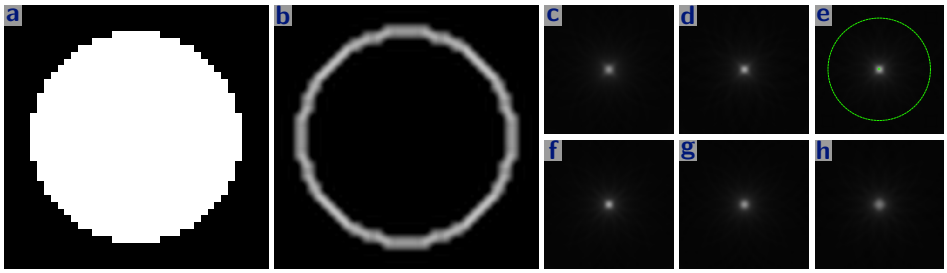

Figure 3.3. Detection of a disk at sub-pixel resolution. For a test image of a disk with radius, $R = 15.4$ px (**a**), the edge image was Gaussian rescaled to 5 times its original size (**b**). The rescaled edge image was transformed into Hough images with $R_H = 15; 15.2...15.8; 16$ px (**c–h**), and from the global maximum Hough value, the radius and the position of the original disk were obtained (**e**).

3.2.3. Optimized Detection of a Disk The method of the previous subsection was optimized to increase the calculation speed. Convolving a megapixel image for all possible radii is computationally expensive. To save computation time, first, a region of interest was selected, secondly, an estimate of the radius and centre of the disk was obtained, and thirdly, more accurate values for the position and radius were determined iteratively. Finally, the output position and radius were obtained by interpolation.

The procedure is demonstrated for a 200 px × 200 px image of a random disk (Fig. 3.4a). The radius of the disk was a pseudorandom real number taken from a normal distribution of $R = 32 \pm 4$ px. Here, 32 px was the mean of the distribution, and 4 px was the standard deviation. The coordinates of the centre of the disk, $\vec{r}_c$, were at pseudorandom numbers between 32 and 168 px. The pseudorandom numbers were not truly random, as they were generated by a deterministic Mathematica algorithm; they showed, however, statistical randomness. To demonstrate the robustness of the circle transformation, noise was added to the final image. The binary brightness of each pixel was randomly switched with a probability of 10%, i.e. 10% of the black pixels were turned white, and 10% of the white pixels were turned black.

In the first step, regions of interest were defined as regions with bright pixels, of a minimum size, and with a minimum gradient in the brightness. Initial regions were obtained by binarizing the original image using Otsu's cluster variance maximization method, and selecting regions of connected pixels with value 1. The initial guess for the radius was $R_0 = 32$ px, and the expected maximum deviation was $\Delta R_{\max} = 16$ px. Hence, regions with an area smaller than $\pi(R_0 - \Delta R_{\max})^2$ were ignored. Furthermore, for each region, the maximum magnitude of the gradient in the brightness, $|\nabla B_{\mathrm{ROI,max}}|$, for radius $R_{\mathrm{grad,ROI}} = 5$ px was calculated, and regions for which $|\nabla B_{\mathrm{ROI,max}}| < |\nabla B_{\mathrm{ROI,min}}| = 0.05$

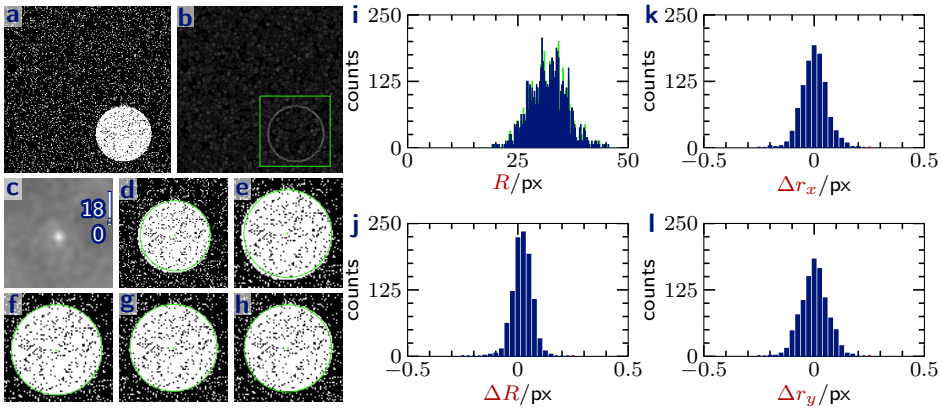

Figure 3.4. Detection of randomly generated disks. For a noisy image of a disk with a pseudorandom radius and position (**a**), the edge image was calculated and the region of interest was determined (**b** ☐). The region of interest was scaled to $\frac{1}{4}\times$ its original size, and Hough transformations (**c**) gave an estimate of the radius and position of the disk at resolution 4 px (**d** ◌). These estimates were used to iteratively determine the radius and position with resolution, $R_{\text{res}} = 2\,\text{px}$, 1 px, $\frac{1}{2}$ px and $\frac{1}{4}$ px (**e–h**). The histograms of the input radii (**i** ▮) and the measured radii (▮), R, were calculated for 1000 images. The differences between the measured and the input value for the radius, ΔR (**j**), for the corrected x-position, Δr_x (**k**), and for the corrected y-position, Δr_y (**l**) were mostly less than half the resolution (▮), while for some images the deviation was larger (▮). In **c**, image levels were linearly rescaled from Hough value 0 to the maximum Hough value at 0.18.

were ignored. Finally, a margin was added to each region of $\Delta l_{\text{ROI}} = 8\,\text{px}$, overlapping regions were merged, and the rectangular area which includes all pixels of the region was selected (Fig. 3.4b ☐).

In the second step, the radius and the position of the centre of the disk were measured with a resolution of $R_{\text{res},1} = 4\,\text{px}$, where $R_{\text{res},1}$ was an integer power of two. First, the edge image was calculated as previously described with $R_{\text{grad}} = 2\,\text{px}$. The size of the edge image was increased $1\,\text{px}/R_{\text{res},1}$ times using Gaussian resampling, and the region of interest was selected. From the rescaled edge image, Hough images were calculated with $R_{\text{H}} = R_0 - \Delta R_{\max}$ to $R_{\text{H}} = R_0 + \Delta R_{\max}$ with steps $R_{\text{res},1}$, where R_0 was the initial estimate for the radius, and $\Delta R_{\max}$ was the expected maximum deviation. The highest maximum of the Hough images gave a first estimate for the radius, R_1, and for the position of the centre, $\vec{r}_{\text{c},1}$ of the disk (Fig. 3.4c–d).

3.2

In the third step, the results from the first set of Hough images were used to iteratively find the radius and position of the centre with a final resolution of $R_{\mathrm{res,f}} = \frac{1}{4}\,\mathrm{px}$. Each step, i, resolution $R_{\mathrm{res},i}$ was multiplied with $\frac{1}{2}$,

$$R_{\mathrm{res},i} = R_{\mathrm{res},1} 2^{-(i-1)}, \tag{3.4}$$

until $R_{\mathrm{res},i} = R_{\mathrm{res,f}}$. So here, $R_{\mathrm{res},2} = 2\,\mathrm{px}$, $R_{\mathrm{res},3} = 1\,\mathrm{px}$, $R_{\mathrm{res},4} = \frac{1}{2}\mathrm{px}$, $R_{\mathrm{res},5} = R_{\mathrm{res,f}} = \frac{1}{4}\mathrm{px}$.

Each step, a squared area of the edge image was selected of length $\frac{5}{2}R_{i-1} + 1\,\mathrm{px}$ centred at $\vec{r}_{\mathrm{c},i-1}$, where R_{i-1} and $\vec{r}_{\mathrm{c},i-1}$ were the estimates for the radius and the position of the centre from the previous step. This edge image was rescaled to $1\,\mathrm{px}/R_{\mathrm{res},i}$ times its original size, and Hough images were calculated for $R_{\mathrm{H}} = R_{i-1} - R_{\mathrm{res},i}$, R_{i-1} and $R_{i-1} + R_{\mathrm{res},i}$. In the Hough images, the values within a distance R_{H} from the edge of the region of interest were set to 0. The maximum of the Hough images, gave the next estimate of the disk radius, R_i, and centre position, $\vec{r}_{\mathrm{c},i}$, at resolution $R_{\mathrm{res},i}$ (Fig. 3.4e–h). This was continued until $R_{\mathrm{res},i} = R_{\mathrm{res,f}}$.

In the last step, the final radius, R_{f}, and position of the centre, $\vec{r}_{\mathrm{c,f}}$, were obtained by interpolation. At resolution $R_{\mathrm{res,f}}$, Hough images were calculated for $R_{\mathrm{H}} = R_{i-1} - R_{\mathrm{res,f}}$, R_{i-1} and $R_{i-1} + R_{\mathrm{res,f}}$, and the maximum Hough value, $H_{\max}(R_{\mathrm{H}})$, was determined for each R_{H}. A least-squares fit of a parabola, $H_{\max}(R_{\mathrm{H}}) = c_{\mathrm{a}}{R_{\mathrm{H}}}^2 + c_{\mathrm{b}}R_{\mathrm{H}} + c_{\mathrm{c}}$, through the three points of $H_{\max}(R_{\mathrm{H}})$ was calculated. The final radius was given by R_{H} for which $H_{\max}(R_{\mathrm{H}})$ was maximum, $R_{\mathrm{f}} = \frac{-c_{\mathrm{b}}}{2c_{\mathrm{a}}}$. If $c_{\mathrm{a}} \geq 0$, no maximum was obtained and R_{f} was R_{H} for which the global maximum was obtained. If the value for which the parabola was maximum was smaller than $R_{i-1} - R_{\mathrm{res,f}}$, $R_{\mathrm{f}} = R_{i+1} - R_{\mathrm{res,f}}$, and if this value was larger than $R_{i+1} + R_{\mathrm{res,f}}$, $R_{\mathrm{f}} = R_{i+1} + R_{\mathrm{res,f}}$, Similarly, the final position of the centre, $\vec{r}_{\mathrm{c,f}}$, was calculated from the neighbours in the Hough image for R_{f}.

To test this procedure, 1000 noisy images of random disks were analysed. The histograms of the measured radii and the input radii were very similar (Fig. 3.4i). The measured mean radius was $31.9 \pm 0.6\,\mathrm{px}$, and virtually identical to the mean of the input radii, $31.9 \pm 0.5\,\mathrm{px}$. Here, the error is the standard deviation for ten means of groups of 100 images.

For each image, the error in the radius is defined as the difference between the input radius, and the measured radius. The histogram of these differences, shows that 993 values are within the measured interval from $R_{\mathrm{f}} - \frac{1}{2}R_{\mathrm{res,f}}$ to $R_{\mathrm{f}} + \frac{1}{2}R_{\mathrm{res,f}}$ (Fig. 3.4j). Furthermore, for all images, the absolute value of the error is smaller than $R_{\mathrm{res,f}}$. The mean and standard deviation in the error is $0.00 \pm 0.05\,\mathrm{px}$. There is thus no significant difference between the measured and original radii.

The difference between the measured and input coordinates, is $0.38 \pm 0.05\,\mathrm{px}$ and $0.38 \pm 0.06\,\mathrm{px}$. These relatively high differences, seem to be due to a systematic error, as the standard deviation is much lower than the mean of the difference. After subtracting

0.375 px from the measured positions, the differences are 0.00 ± 0.05 px and 0.00 ± 0.06 px. The histogram of the errors, also shows that most input values lie within the corrected measured interval (Fig. 3.4k–l). Furthermore, even without this correction, the systematic error has no effect on interparticle positions as all values are off by the same value. Finally, this error only seems to occur at resolutions below 1 px. For a resolution of $R_{\mathrm{res,f}} = 1$ px, the difference are 0.0 ± 0.3 px and 0.01 ± 0.29 px for the x and y-positions.

We conclude that this method is well-suited to accurately determine the size and position of disks with a resolution well below the size of a pixel.

3.2.4. Detection of Multiple Disks To analyse images with multiple disks, the method of the previous subsection was modified so multiple disks could be detected in each region of interest.

The method is demonstrated for noisy images with multiple randomly generated disks (Fig. 3.5). The images were 1000 px × 1000 px with 100 random disks each. The radii and positions of the centres of the disks were generated similarly and with the same parameters as in the previous subsection. Now however, the coordinates of the disks were at pseudorandom numbers between 0 and 1000 px.

We prevented disks from overlapping too much. For each newly generated disk, the centre-to-centre distance to all other disks was calculated. If for any pair, ij, this distance was less than a threshold value, the disk was not added. Here, a threshold of $\sqrt{0.6}(R_i + R_j)$ was chosen, where R_i and R_j were the radii of disk i and j. This procedure was continued until the total number of disks is 100. Finally, noise was added as described in the previous subsection

First, regions of interest were determined (Fig. 3.5a □), and next, scaled Hough images were obtained for each region. In both steps, the method and parameters as described in the previous subsection were used. R_{grad}, however, was increased to 3 px to decrease the effect of noise and consequently reduce the number of misfits, and $R_{\mathrm{grad,ROI}} = \Delta l_{\mathrm{ROI}} = 4$ px.

Here, each region could contain multiple disks, so multiple maxima were to be found in the Hough images. Furthermore, maxima could also be found in the shoulder of neighbouring disks (Fig. 3.5c→). Such local maxima, that were outside disks, should not be identified as centres of disks. Hence, the initial transformations were pixel-wise multiplied with the original images to obtain the final Hough images. Before multiplication, the original image was Gaussian filtered with radius $R_{\mathrm{Gauss}} = 10$ px to reduce the effect of noise.

The disks in a certain region were detected from the local maxima in the Hough images. The global maximum for the Hough images gave the first estimate for the position of the centre, $\vec{r}_{\mathrm{c},1,1}$, and for the radius, $R_{1,1}$, of the first disk (Fig. 3.5d). The input image did not contain disks that overlap more than a threshold value. Hence, the disk

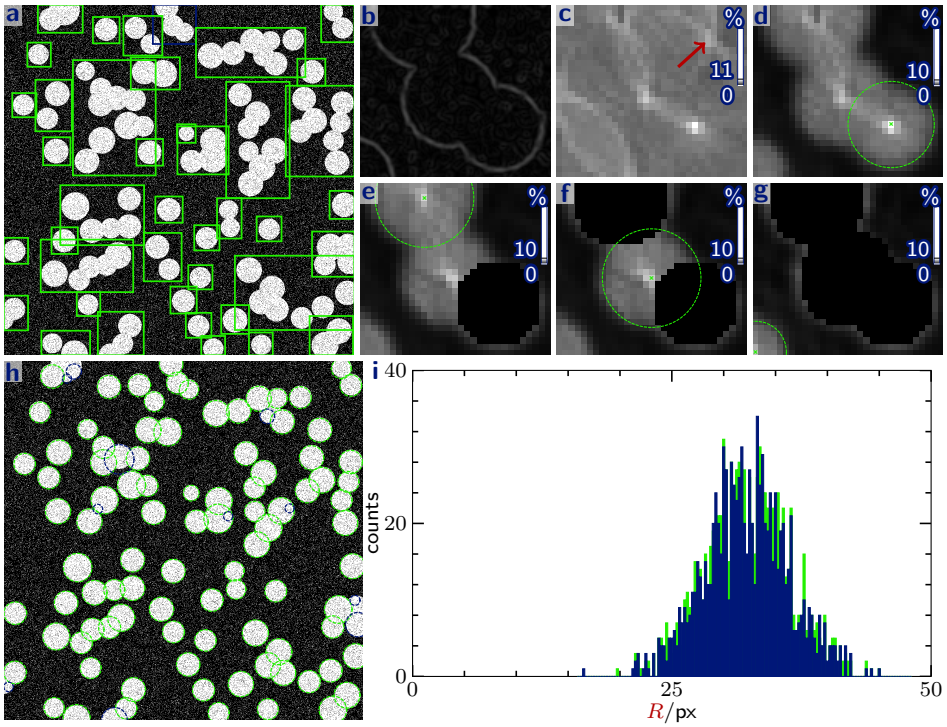

Figure 3.5. Detection of multiple disks. Regions of interest were selected in a randomly generated image of 100 disks (**a** □). For the blue region in a, the edge image (**b**) and scaled Hough images were calculated. The Hough image with $R_H = 28$ px has a local maximum outside the disks (**c** →). Such maxima were masked by multiplying with the original image, and the global maximum at $R_H = 28$ px gave the position of the centre of the first disk (**d**). Each next disk was given by the global maxima after masking the Hough values in all previously found disks (**e–g**), until the global maximum was lower than $H_{min,1}$. After iteratively finding the circles at resolution $R_{res,f} = \frac{1}{4}$ px, $H_{min,f}$ was determined which separated correctly detected disks (**h** ◌), from misfits (**h** ◌). Finally, the histogram of the input radii (**i** ▮) and measured radii (▮), R, was calculated for ten images. For **c–g**, image levels were linearly rescaled from zero to the global maximum Hough value.

with centre $\vec{r}_{c,1,1}$ and radius $x_{ij,\min}R_{1,1}$ was determined, where $x_{ij,\min}$ was the minimum relative distance between two disks. Next, for all Hough images, the values of pixels within this disk were set to 0 (Fig. 3.5e). For our test image we only expected disks with a centre-to-centre distance larger than $\sqrt{0.6}(R_i + R_j)$, and we set $x_{ij,\min} = 1$. The global maximum after masking out the first disk, gave the position and radius of the second disk. This procedure was repeated until the global maximum was lower than $H_{\min,1} = 0.05$, or the number of detected disks reached $N_{p,\max} = 200$ (Fig. 3.5e–g).

Misfits can arise as a region of interest sometimes contained only a part of a disk (Fig. 3.5g). Most of these misfits were removed by ignoring for each pair with a centre-to-centre distance less than $x_{ij,\min}(R_{i,1} + R_{j,1})/2$, the disk with the lowest Hough value. Such misfits, however, could also be prevented by selecting the entire image as region of interest (Fig. 3.9d).

The resulting radii and positions of the centres were used as starting values to iteratively determine the radii and positions of the centres with $R_{\mathrm{res,f}} = \frac{1}{4}$ px. The method of the previous subsection was followed, but each Hough image was now multiplied with the Gaussian filtered and scaled original image. The identified disks were sorted based on the value of the Hough image at the position of their centre, H_{f}. By visual inspection, the threshold Hough value $H_{\min,\mathrm{f}}$ was determined for which the disks with $H_{\mathrm{f}} > H_{\min,\mathrm{f}}$ did not contain misfits (Fig. 3.5h).

For the example image, 93 disks were identified (Fig. 3.5h). This procedure was repeated for nine additional random images, and 969 of the 1000 input disks were identified. Particles which were not correctly detected overlapped with another disk or were partly outside the image. Both factors resulted in incomplete circles in the edge image, and hence in a low Hough value. Many disks which overlap with either other disks or the image boundary, however, were identified.

The histogram of the measured radii agrees well with the original radii (Fig. 3.5i). The mean radius is 32.2 ± 0.4 px for both the input and detected disks. Here, the error is the standard deviation for the ten means of each image. The standard deviation for the radii in each image gives the polydispersity, σ. The polydispersity is 4.04 ± 0.25 px and 4.0 ± 0.3 px for the input and detected disks. Both the measured mean radius and polydispersity are nearly identical, and this method is thus well suited to objectively analyse images with multiple disks.

3.2.5. Detection of a Snowman-like Shape Snowman-like shapes consist of two partly overlapping disks, that were detected in two steps. First, the largest disk was iteratively detected using Hough circle transformations as described above. Next, the edge of the first disk was masked, and the other disk is similarly detected.

This method is illustrated for a noisy test image of 200 px × 200 px (Fig. 3.6). Test images were generated similarly as for the previously described method. The coordinates

of the centre of the first disk were pseudorandom numbers between 64 and 136 px, and the centre of the second disk was at a random position at 32 ± 2 px from the first centre. The radii of the two disks were pseudorandom numbers taken from a normal distribution of 32 ± 4 px. The largest radius of the two was defined as R_l, while the smaller radius was R_s.

The region of interest was selected (Fig. 3.6b) and the large disk was detected iteratively using the same parameters and method as in the previous subsection. The initial estimates, R_0 and ΔR_max were now replaced by $R_{\mathrm{l},0} = 32$ px and $\Delta R_{\mathrm{l,max}} = 16$ px.

The final radius, $R_{\mathrm{l,f}}$, and position of the centre, $\vec{r}_{\mathrm{c,l,f}}$, of the large disk were used to mask the pixels of the edge image which were on the edge of the large disk (Fig. 3.6c). Pixels at $\vec{r}_i$ for which,

$$R_{\mathrm{l,f}} - \Delta r_\mathrm{mask}/2 < |\vec{r}_{\mathrm{c,l,f}} - \vec{r}_i| \leq R_{\mathrm{l,f}} + \Delta r_\mathrm{mask}/2, \tag{3.5}$$

were identified as on the edge of the large disk, where $\Delta r_\mathrm{mask} = 2$ px was the width of the mask. In the edge image, these pixels were set to zero.

The position, $\vec{r}_{\mathrm{c,s,f}}$, and radius, $R_{\mathrm{s,f}}$, of the small disk were measured iteratively, using the masked edge image. As region of interest, a squared area centred at the position of the large disk was selected. The length of the sides of this region were $2(r_{\mathrm{cc},0} + \Delta r_{\mathrm{cc,max}} + R_{\mathrm{s},0} + \Delta R_{\mathrm{s,max}}) + 1$ px, where $r_{\mathrm{cc},0} = 32$ px was the initial estimate for the distance between the centre of the large disk and the centre of the small disk, $\Delta r_{\mathrm{cc,max}} = 8$ px was the estimated maximum deviation in $r_{\mathrm{cc},0}$, $R_{\mathrm{s},0} = 32$ px was the initial estimate for the radius of the small disk, and $\Delta R_{\mathrm{s,max}} = 16$ px was the estimated maximum deviation in $R_{\mathrm{s},0}$. To prevent misfits, the method of the previous subsection was slightly modified. The input distance between the centre of the small disk and the centre of the large disk was 32 ± 2 px. The Hough maximum of the small disk was thus expected on a 32 px ring around the maximum of the large disk. Hence, the Hough image was masked, with all Hough values at $\vec{r}_i$ which do not fulfil,

$$r_{\mathrm{cc},0} - \Delta r_{\mathrm{cc,max}} \leq |\vec{r}_{\mathrm{c,l,f}} - \vec{r}_i| \leq r_{\mathrm{cc},0} + \Delta r_{\mathrm{cc,max}}, \tag{3.6}$$

set to zero (Fig. 3.6e).

Furthermore, we made sure there was no edge between the centres of the large and the small disk. In the masked edge image, all pixels on the line of thickness 1 px between the two centres were identified (Fig. 3.7f). If any of these pixels had a value above $|\nabla B_{\mathrm{cc,max}}|$, the detected small disk was rejected; all pixels in the Hough images which were part of the rejected small disk were masked; and the next maximum was tried. This procedure was continued until a small disk was found which belonged to the same snowman-like shape or the total number of tries reached 10. Here, $|\nabla B_{\mathrm{cc,max}}| = 1$, because the noise caused a high gradient in the brightness even inside the image.

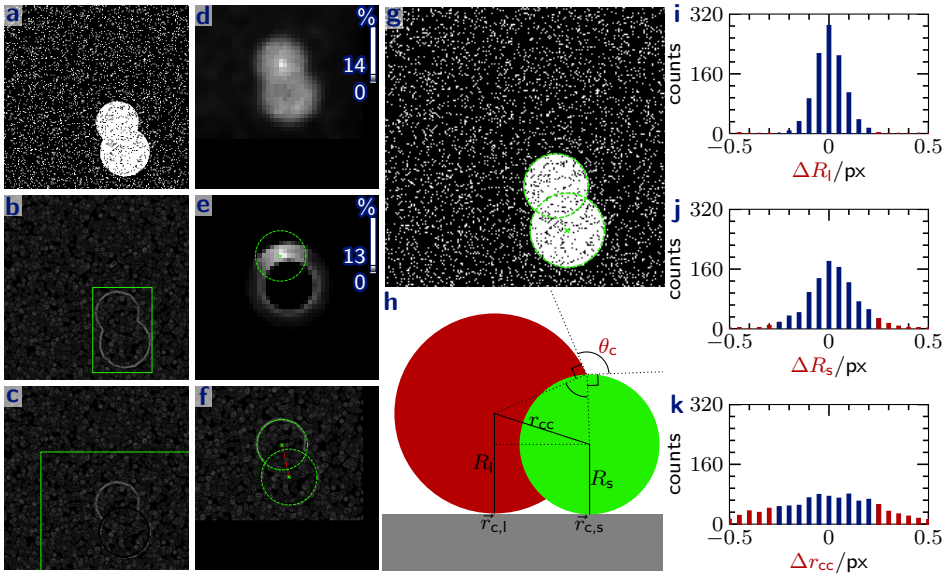

Figure 3.6. Detection of snowman-like shapes. A noisy image of a snowman-like shape was generated from two randomly generated overlapping disks (**a**). The region of interest was selected (**b**), and the first disk was detected as before. Next, the edge of the first disk was masked in the edge image, and the region around the centre of the first disk was selected as region of interest (**c**). To prevent identification of maxima too far from or too close to the centre of the first disk, the Hough image (**d**) was masked (**e**) and its maximum corresponds to the position and size of the second disk (**e** ◌). The pixels in the masked edge image on the line between the two centres were identified (**f** —). And the maximum value of these pixels was below $|\nabla B_{cc,max}|$. Using the final Hough maximum, the shape was fully characterized (**g**). Side view of a snowman-like particle on a substrate with the positions, $\vec{r}_{c,l}$ and $\vec{r}_{c,s}$, and radii, R_l and R_s, of the large lobe and the small lobe, the centre-to-centre distance, r_{cc}, and the contact angle, θ_c (**h**). For 1000 images, histograms of the difference between the measured and input values for the radius of the large disk, ΔR_l (**i**), the radius of the small disk, ΔR_s (**j**) and the centre-to-centre distance, Δr_{cc} (**k**) were calculated. Most values are within the measured interval (▮), while other values are outside the measured interval (▮). For **c–d**, image levels were linearly rescaled from zero to the global maximum Hough value.

Usually, the largest disk had the highest Hough value and was thus identified first. This may seem surprising, as the normalized Hough value does not depend on the radius of the disk. The Hough value, however, depends on the completeness of the circular edge. For the edge image of a snowman-like shape, both circles are incomplete, but the fraction of the circle which is missing is smallest for the largest disk. Hence, the Hough value of the large disk is highest, and this lobe was identified first. If, however, the second identified lobe had a larger radius than the first lobe, the second lobe was identified as the large disk and the first lobe as the small disk.

From the measured radii and positions of the centres, the centre-to-centre distance,

$$r_{cc} = \sqrt{|\vec{r}_{c,l} - \vec{r}_{c,s}|^2 + (R_l - R_s)^2}, \tag{3.7}$$

was calculated. Here, the last term in the square root corrects for the 2D projection of a three-dimensional snowman-like particle lying on a flat surface (Fig. 3.6h).

The contact angle between the surface of the two lobes of a snowman-like particle, θ_c (Fig. 3.6h), was calculated using the law of cosines [82, p1713],

$$\theta_c = 180° - \cos^{-1}\left[\frac{{R_l}^2 + {R_s}^2 - {r_{cc}}^2}{2R_lR_s}\right]. \tag{3.8}$$

Finally, the total volume of a snowman-like particle is the volume of the two spheres with radii R_l and R_s minus the volume of the intersection of the spheres [82, p2778],

$$\begin{aligned} V_s =& \frac{4\pi({R_l}^3 + {R_s}^2)}{3} \\ &- \frac{\pi(R_l + R_s - r_{cc})^2\left({r_{cc}}^2 + 2R_lr_{cc} - 3{R_l}^2 + 2R_sr_{cc} + 6R_lR_s - 3{R_s}^2\right)}{12r_{cc}}. \end{aligned} \tag{3.9}$$

Using this method, 1000 randomly generated images were analysed. The differences between the input value and the measured value for R_l, R_s and r_{cc} are plotted in Fig. 3.6i–k. Most values lie within the measured interval. For the small disk diameter, however, the agreement is not as good as for single disks (compare Fig. 3.6j to Fig. 3.4j). This can be explained as incomplete circles are more difficult to detect. As we have seen before, the edge of the large disk is a more complete circle than the edge of the small disk. Hence, the error in the radius of the large disk is smaller than in the radius of the small disk. The error in the centre-to-centre distance is larger than for the radii (compare Fig. 3.6k to i–j). This can be explained as errors in the positions of centres as well as in the radii for each disk contribute to the final error in r_{cc}. For 970 out of 1000 snowman-like shapes, the errors in R_l, R_s and r_{cc} are all smaller than 1 px, and large errors can easily be removed by visual inspection. Even without removing the misfits, however, the mean and polydispersity are very similar for the input and measured values (Table 3.1).

Table 3.1. Results for single snowman-like shapes. Mean, μ, and polydispersity, σ, of the radius of the large disk, R_l, the radius of the small disk, R_s, the centre-to-centre distance, r_cc, and the contact angle, θ_c, for the input and the detected snowman-like shapes. The first value is the average over ten means of 100 images, and the second value gives the standard deviation.

	R_l/px		R_s/px		r_cc/px		θ_c/°	
	μ	σ	μ	σ	μ	σ	μ	σ
Input	34.3±0.3	3.23±0.23	29.74±0.22	3.26±0.18	32.48±0.29	2.15±0.09	119.1±0.9	7.7±0.6
Detected	34.25±0.29	3.23±0.24	29.5±0.3	3.55±0.29	32.7±0.3	2.47±0.25	118.3±0.8	9.2±1.5

3.2.6. Detection of Multiple Snowman-like Shapes

Images with multiple snowman-like shapes were analysed using a similar method as in the previous subsection. Here, however, multiple shapes were to be found. This was implemented by masking the edge of each detected disk.

The method is demonstrated for a randomly generated 1000 px × 1000 px image with 100 snowman-like shapes (Fig. 3.7). Particles were randomly generated with the same parameters as in the previous subsection, but now positions of the centres of the first disks are pairs of pseudorandom numbers between 32 and 936 px. New shapes were added if they do not overlap with existing snowman-like shapes until the total number of shapes was 100 (Fig. 3.7a).

To demonstrate that multiple shapes can be found in a region, the entire image was identified as region of interest. Furthermore, this also reduced the number of misfits, which often arise from shapes which overlap with the edge of a region.

The same parameters and method as in the previous subsection were used to find the first snowman-like shape. Upon finding the second disk at $R_\mathrm{res,f}$, its edge was masked in the edge image, and the next shape was detected. This procedure was continued, until the global maximum of the Hough images for the large disk was lower than $H_\mathrm{min,1} = 0.02$ or the number of found shapes reached $N_\mathrm{p,max} = 110$.

Next, overlapping snowman-like shapes were removed, and the shapes were sorted based on the geometric mean of the final Hough value of the large and the small disk $H_\mathrm{f} = \sqrt{H_\mathrm{l,f} H_\mathrm{s,f}}$. Finally, the threshold $H_\mathrm{min,f}$ was determined above which no clear misfits were presents (Fig. 3.7a).

For ten randomly generated images, 975 out of 1000 shapes are detected, and the input and measured histograms of the shape properties overlap (Fig. 3.7b–e). Furthermore, the properties of the input snowman-like shapes are nearly identical to those for the detected shapes (Table 3.2).

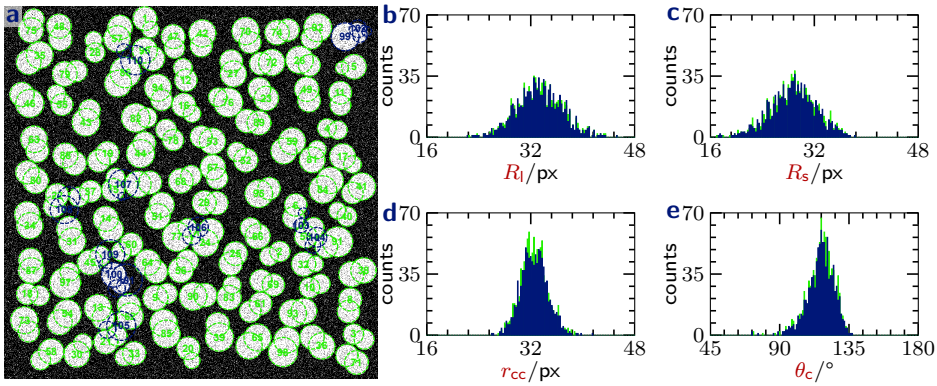

Figure 3.7. Detection of multiple snowman-like shapes. Snowman-like shapes were detected in a randomly generated image with 100 shapes (**a**). $H_{min,f}$ was determined which separates correctly detected snowman-like shapes (**a**) from misfits ( ). For 10 images, the distribution of the measured ( ) and input ( ) values for the radius of the large disk, R_l (**b**), the radius of the small disk, R_s (**c**), the centre-to-centre distance, r_{cc} (**d**), and the contact angle, θ_c (**e**), were calculated.

Table 3.2. Results for multiple snowman-like shapes. Mean, μ, and polydispersity, σ, of the radius of the large disk, R_l, the radius of the small disk, R_s, the centre-to-centre distance, r_{cc}, and the contact angle, θ_c, for the input and the detected snowman-like shapes. The first value is the average over ten images, and the second value gives the standard deviation.

	R_l/px		R_s/px		r_{cc}/px		θ_c/°	
	μ	σ	μ	σ	μ	σ	μ	σ
Input	33.4±0.3	3.51±0.22	28.8±0.4	3.4±0.3	32.49±0.19	2.01±0.14	116.9±0.7	8.3±0.7
Detected	33.3±0.3	3.48±0.21	28.7±0.4	3.5±0.4	32.55±0.20	2.11±0.18	116.6±0.8	8.8±1.4

3.2.7. Measuring Interparticle Interactions

From the positions of particles with respect to each other, the two-dimensional radial distribution function $g(r_{ij})$ was calculated. Furthermore, the average of $g(r_{ij})$ was converted into the effective pair potential.

Distributions of interparticle distances should be corrected for the average number of pixels at a certain distance, r_{ij}. For small interparticle distances, the number of pixels increases with $2\pi r_{ij}$. Due to the finite size of a microscopy image, however, the number of pixels decreases when r_{ij} becomes close to the image length (Fig. 3.8).

To correct for these effects the histogram of distances between many random pairs was calculated (Fig. 3.8). 10^7 times, two pseudorandom positions, $\vec{r}_i$ and $\vec{r}_j$ on a microscopy

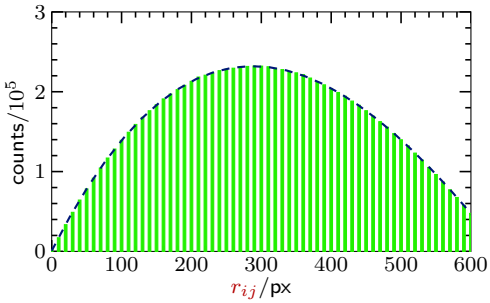

Figure 3.8. Normalization of interparticle distance histograms. For 10^7 randomly generated pairs of positions on a 600 px × 600 px image, the histogram of the distance between the pairs, r_{ij}, was calculated (▮). The histogram was fitted to a third order polynomial (- -), that was used to normalized histograms of interparticle distances obtained from equally sized images.

image were chosen, and the distance between the positions, $r_{ij} = |\vec{r}_i - \vec{r}_j|$ was calculated. A polynomial of order three was fitted through the histogram of these distances (Fig. 3.8- -). For a 600 px × 600 px image, this polynomial was $0.00151{r_{ij}}^3 - 3.668{r_{ij}}^2 + 1734 r_{ij} + 786$.

To obtain the two-dimensional radial distribution function, $g(r_{ij})$, the histogram was normalized by dividing the counts with the fitted polynomial. Furthermore, $g(r_{ij})$ was scaled so $g(r_{ij}) \approx 1$ at large interparticle distances.

Finally, if particles undergo Brownian motion, the effective two-dimensional pair potential can be calculated using $w(r_{ij})/k_\mathrm{B}T = -\ln\left\langle g(r_{ij})\right\rangle$, where k_B is the Boltzmann constant, T is the temperature, and $\left\langle g(r_{ij})\right\rangle$ is the time average or ensemble average of the radial distribution function.

3.3. Results and Discussion

3.3.1. Characterization of Spherical Particles Using the method of Subsection 3.2.4, electron microscopy images of cross-linked poly(styrene-*co*-acrylic acid) (CPSAA) spheres are analysed (Fig. 3.9).

Cross-linked poly(styrene-*co*-acrylic acid) spheres are synthesized as described in Subsection 2.2.2, and electron microscopy images are obtained as described in Subsection 2.2.5. For images with pixels of length, $l_\mathrm{px} = 9.73\,\mathrm{nm}$, the image levels are linearly rescaled so that 99.9% of all values are between the lower and upper level thresholds, and the entire image is selected as region of interest (Fig. 3.9a).

The edge image is calculated with $R_\mathrm{grad} = 5\,\mathrm{nm}$ (Fig. 3.9b). Defining the edge of the particles is non-trivial, and often subjective. Here, we calculate the edge

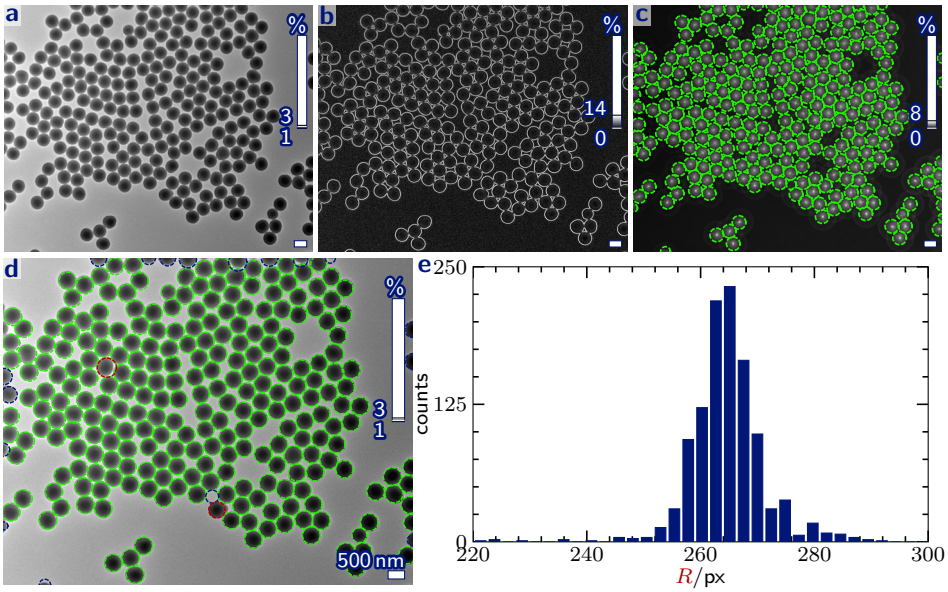

Figure 3.9. Characterisation of spherical particles. Transmission electron microscopy images of colloidal spheres (**a**) are transformed into edge images (**b**). From these, Hough images are calculated at resolution $R_{\text{res,1}} = 38.9\,\text{nm}$ (**c**). The maxima in the Hough images give estimates of the radii and positions of the centres of the particles (**c** ◌). These estimates are used to iteratively determine the radii and positions of the centres at $R_{\text{res,f}} = 2.4\,\text{nm}$ (**d** ◌), and particles with a Hough value below a threshold (◌) and misfits (◌) are ignored. Finally, for five images, a histogram of the radii, R, is calculated. Image values are linearly rescaled as indicated by the vertical bars. The QR code links to an interactive demonstration of characterisation of this image (phd.chrisevers.com/3qr9.html)

image from the magnitude of the gradient in the brightness. Using this method, the only free parameter is the radius over which the gradient is determined, R_{grad}. Increasing this radius reduces noise, but decreases the magnitude of the gradient. The location of the maximum in the gradient, however, does not vary strongly with R_{grad}. Unlike methods which depend on cut-off values for the brightness, the edge position in the gradient image is thus fairly parameter independent.

Furthermore, in the original image, the brightness is high in the top left corner, while the bottom right corner is dark (Fig. 3.9a). The edge image, however, depends only on the gradient of the brightness, and the edges are as bright in each corner.

The radii and positions of the centres are obtained iteratively using the parameters in App. Table 3.1, where most parameters are integer multiples of l_{px}. First, the Hough image is calculated at resolution $R_{\mathrm{res},1} = 38.9\,\mathrm{nm}$ (Fig. 3.9c). Because the particles are dark in the original image, the initial Hough image is in this case multiplied with the negative of the original image. Next, the maxima in the Hough image give the first estimates for the radii and positions of the centres of the particles (Fig. 3.9c). These values are used as input values to iteratively detect the particles at resolution $R_{\mathrm{res,f}}$ (Fig. 3.9d). Finally, by visual inspection, the threshold Hough value $H_{\mathrm{min,f}}$ is determined to remove most misfits (Fig. 3.9d). Remaining clear misfits are manually removed (Fig. 3.9d).

Using this method, all particles that are completely in the original image are recognized. Particles which overlap with the border of the image, however, are often incorrectly detected; although even some of these particles seem to be correctly identified. Finally, two particles that do not overlap with the border are incorrectly detected (Fig. 3.9d). This can be explained by their irregular shape.

For TEM images of dried colloids on a polymer coating, the bottom of each particle is at the top of the coating. Hence, if the polydispersity of the particles is low, the centres of all particle are at approximately the same height and in the same focal plane. Consequently, we can measure the radius of multiple particles from a single image.

The calculation time increases dramatically with the resolution. For a $1280\,\mathrm{px} \times 1024\,\mathrm{px}$ image (Fig. 3.9) the first estimates at $R_{\mathrm{res},1} = 4\,\mathrm{px}$, are calculated in 19 s on a Intel Core i5 laptop. Refining the results at $R_{\mathrm{res}} = 2$, 1, $\frac{1}{2}$, and $\frac{1}{4}$ px takes 0.8, 1.7, 5.8 and 18.0 min The total analysis time thus strongly depends on $R_{\mathrm{res,f}}$ and is 27 min for $R_{\mathrm{res,f}} = \frac{1}{4}$ px. Even though we optimized our method as described in Subsection 3.2.3, smarter algorithms or GPU processing could reduce the calculation speed even further.

Five images with the same magnification are analysed and 1107 particles are identified. A sharp histogram of radii of the particles is obtained (Fig. 3.9e). The mean radius is $264.8 \pm 1.7\,\mathrm{nm}$ and the polydispersity is $7.4 \pm 2.0\,\mathrm{nm}$. Here, the second values denote the standard deviations over the values for the five images. Both the radius and polydispersity are thus determined with a resolution well below $l_{\mathrm{px}} = 9.73\,\mathrm{nm}$.

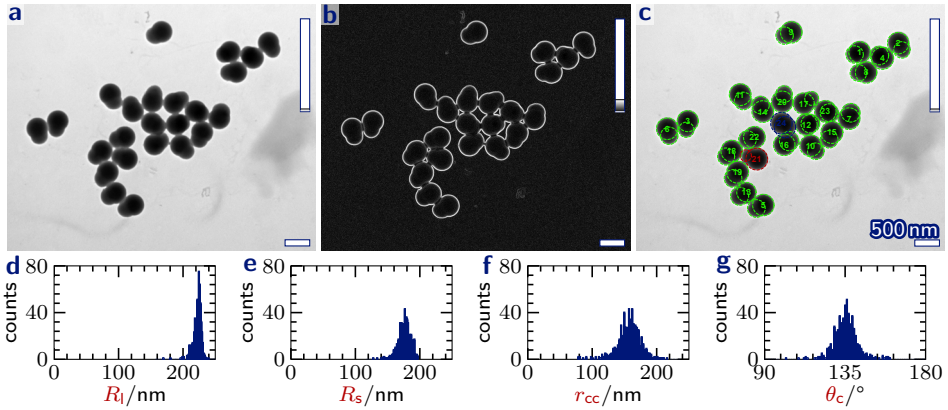

Figure 3.10. Characterization of snowman-like particles. Transmission electron microscopy images of colloidal snowman-like particles (**a**) are transformed into edge images (**b**). From these, radii and positions of the centres of each lobe are determined iteratively (**c**). Particles with low Hough values are ignored and other misfits are manually removed. For 58 images, histograms for the radius of the large lobe, R_l (**d**), the radius of the small lobe, R_s (**e**), the centre-to-centre distance, r_{cc} (**f**), and the contact angle, θ_c (**g**) are plotted. The QR code links to an interactive demonstration of characterisation of snowman-like particles (phd.chrisevers.com/3qr10.html)

3.3.2. Characterization of Snowman-like Particles Electron microscopy images of snowman-like particles are analysed using the method of Subsection 3.2.6 (Fig. 3.10). Snowman-like particles are prepared as described in Subsection 2.2.4, and transmission electron microscopy images with a pixel length, $l_{px} = 4.9\,\text{nm}$, are obtained (Fig. 3.10a). The images are analysed with parameters as defined in App. Table 3.2. The radii and positions of the centres of each lobe of the snowman-like particles are determined, and particles with low Hough values and other misfits are ignored (Fig. 3.10a–c). The number of misfits is relatively large, because particles tend to cluster on the TEM grid due to drying effects (Fig. 3.10c). Hence, edges of particles often touch resulting in even more incomplete circles than for non-touching snowman-like particles (Fig. 3.10b). Many particles that are in close contact with their neighbours are, however, correctly identified (Fig. 3.10c).

Table 3.3. Properties of snowman-like particles. Mean, μ, and polydispersity, σ, of the radius of the large lobe, R_l, the radius of the small lobe, R_s, the centre-to-centre distance, r_cc, and the contact angle, θ_c, for the input and the detected snowman-like particles. The first value is the average over seven groups of 80 particles each, and the second value gives the standard deviation.

R_l/nm		R_s/nm		r_cc/nm		θ_c/°	
μ	σ	μ	σ	μ	σ	μ	σ
222.4±2.3	5.8±1.5	176.3±1.8	11.1±2.6	157±3	20±3	135.2±1.0	7.1±1.6

For 58 images, 561 particles are detected, and histograms of the particle properties are plotted (Fig. 3.10d–g), and the mean and polydispersity are calculated (Table 3.3).

For dried snowman-like particles, the centres of each lobe are at different heights. For each lobe, the bottom should be at the top of the polymer coated grid (Fig. 3.6h). Hence, the centres of the large lobes are at higher positions than the centres of the small lobes, and the particles are oriented tilted on the surface. In transmission electron microscopy, however, we observe a 2D projection, and both the centre-to-centre distance and the contact angle are corrected for the tilted orientation according to Eq. 3.7 and Eq. 3.8.

Furthermore, the tilted particle orientation could cause a problem in focusing. For particles with $R_\mathrm{l} = 222\,\mathrm{nm}$ and $R_\mathrm{s} = 176\,\mathrm{nm}$, the height difference between the centres of the large lobe and the small lobe is 46 nm. The centres of both lobes are in focus if this difference is smaller than the depth of field. Here, the depth of field is the range over which the z-position of an object can be changed, while still remaining in focus. In contrast to optical microscopy, the depth of field is usually large for electron microscopy [83]. For the particles in Fig. 3.10a, the edge of each lobe is sharp, and both lobes are indeed in focus.

Using this method, the shape of individual particles is fully characterized, resulting in accurate statistics of derived particle properties. The contact angle, θ_c for example, depends on R_l, R_s and r_cc (Eq. 3.8). In Table 3.3, θ_c is obtained by calculating its value for each particle and taking the mean and standard deviation for all 561 values. Using manual measurements, θ_c is often calculated using the means and the standard deviations for R_l, R_s and r_cc and the law of propagation of errors [82, p938]. Using this method, the mean and standard deviation would have been slightly different at 135.4° and 6.8° instead of 135.2° and 7.1° (Table 3.3). In this case, the polydispersities of R_l, R_s and r_cc are relatively low, and the difference

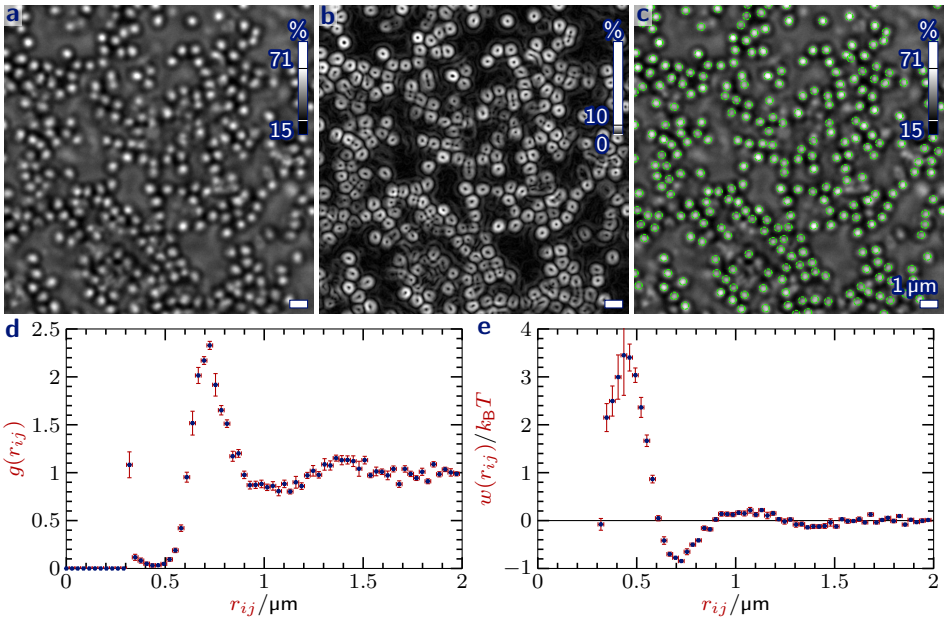

Figure 3.11. Interparticle interaction measurements. An optical microscopy image of diffusing colloids (**a**) is converted into its edge image (**b**), and the particle positions are determined (**c**). Using 151 images, the time-averaged two-dimensional radial distribution functions, $g(r_{ij})$, is obtained (**d**), which is converted into the effective two-dimensional pair potential, $w(r_{ij})$ (**e**). The error bars indicate the width of the bins and the standard deviation over seven groups of images. The QR code links to an interactive demonstration of detecting particles in an optical microscopy image (phd.chrisevers.com/3qr11.html)

between the direct and indirect measurements of θ_c is negligible. The difference might, however, become significant if, for example, the polydispersity in the radii is high, while the polydispersity in the contact angle is low.

3.3.3. Interparticle Interactions Using the method of Subsection 3.2.4, positions of particles in dispersion are determined to estimate their effective pair potential (Fig. 3.11).

A time series of reflected light microscopy images of diffusing snowman-like particles is obtained (Fig. 5.7). For each microscopy image, the edge image is

calculated and the particle positions are determined using the parameters in App. Table 3.3 (Fig. 3.11a–c).

For Fig. 3.11c, all particles that are in focus are identified. For particles just out of focus, the gradient in the brightness is low, and hence the Hough value is below $H_{\mathrm{min},1}$. By varying $H_{\mathrm{min},1}$, the depth of focus can thus be narrowed or broadened. In the software, a suitable value for $H_{\mathrm{min},1}$ can be determined by visually inspection.

For 151 images, 41568 particles are identified, and a histogram of the interparticle distances, $r_{ij} = |\vec{r}_{\mathrm{c},i} - \vec{r}_{\mathrm{c},j}|$, is calculated (Fig. 3.11d). The histogram is corrected for the finite image size and normalized (Subsection 3.2.7), resulting in the two-dimensional radial distribution function $g(r_{ij})$. At $r_{ij} < 0.5\,\mu\mathrm{m}$, the number of counts approaches zero, because particles can not penetrate each other. The peak at $0.3\,\mu\mathrm{m}$ seems to be due to misfits, and arises because a minimum interparticle distance of $x_{ij,\mathrm{min}} R_0 = 0.305\,\mu\mathrm{m}$ is used. At large distances, on the other hand, $g(r_{ij})$ becomes constant as the particles are uncorrelated at large separation. The histogram peaks at $0.725 \pm 0.015\,\mu\mathrm{m}$, which indicates an effective mutual attraction. Here, the width of the bins of the histogram is $R_{\mathrm{res,f}}$, and the error is estimated at $\frac{1}{2} R_{\mathrm{res,f}}$.

The attraction strength can be estimated by translating the radial distribution function into an effective pair potential, $w(r_{ij})$ (Fig. 3.11e). At $r_{ij} < 0.5\,\mu\mathrm{m}$, the effective pair potential becomes less accurate. This can be explained as these positions have a high effective pair potential, and are thus less likely to be sampled. Furthermore, when the interparticle distance is less than the wavelength of light, it is more difficult to distinguish the particles. At large interparticle distances, the particles do not interact, and the effective pair potential is zero. The minimum in the potential gives the effective attraction strength, $-0.845 \pm 0.018\,k_{\mathrm{B}}T$, where the second value is the standard deviation over the minima of seven groups of about 22 images each. Relatively high particle concentrations can cause long-range features in the effective pair potential. This results in a positive peak at $r_{ij} \approx 1.1\,\mu\mathrm{m}$, followed by a second minimum at $r_{ij} \approx 1.4\,\mu\mathrm{m}$. The measured effective pair potential differs from the actual pair potential, due to the high concentration, because we assume all particles to have the same height, and because we only measure in a two-dimensional slice. Hence, the error in the measured attraction strength is much larger than the low standard deviation suggests. Finally, we verified that optical effects due to close proximity of the particles as described by Baumgartl and Bechinger [84] do not seem to change our results significantly.

3.4. Conclusion

In this chapter, the Hough circle transformation is used to measure sizes and positions of particles in microscopy images. We verified the accuracy of this method and optimized it to allow analysis in the order of minutes on a laptop. Measurements require only a few input parameters. Of these, H_{min} is the only cut-off parameter, which final value is determined by visual inspection. By tuning the parameters, particle positions in electron and optical microscopy were obtained. Furthermore, both spherical and snowman-like particles were characterized. Our method is more objective and less time-consuming than visual inspection, and can be extended to characterize arbitrary shapes and even 3D objects.

3.5. Acknowledgement

Hans Meeldijk and Chris Schneijdenberg are thanked for help with electron microscopy. David Grier, Mark Hannel and Jos van Rijssel are thanked for useful suggestions and discussion.

3.A. Appendix Figures and Tables

The described method is implemented in a graphical user interface using Wolfram Mathematica (App. Fig. 3.1). This program is freely available at (phd.chrisevers.com/3qr12.html).

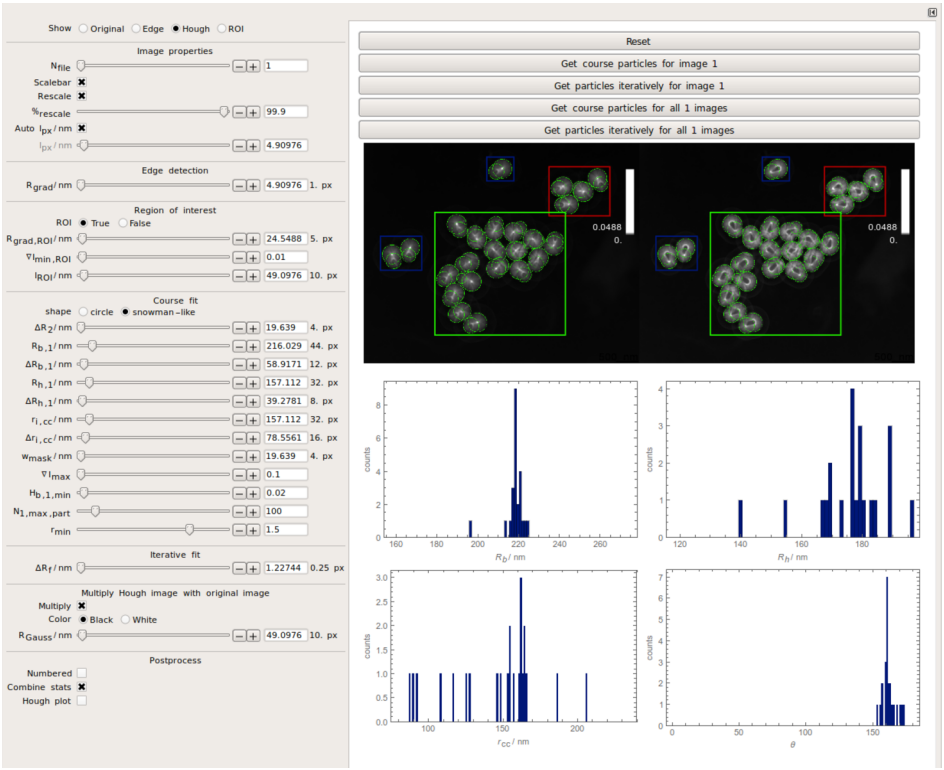

Appendix Figure 3.1. Screenshot of the graphical user interface.

Appendix Table 3.1. Parameters to detect spherical particles in Fig. 3.9.

R_{grad}/nm	R_0/nm	ΔR_{max}/nm	$R_{\mathrm{res,1}}$/nm	$R_{\mathrm{res,f}}$/nm
9.7	272.4	116.8	38.9	2.4
$x_{ij,\mathrm{min}}$	$H_{\mathrm{min,1}}$	$N_{\mathrm{p,max}}$	R_{Gauss}/nm	
1.5	0.02	300	48.6	

Appendix Table 3.2. Parameters to detect colloidal snowman-like particles in Fig. 3.10.

$R_{\mathrm{grad,ROI}}$/nm	$\lvert\nabla B_{\mathrm{ROI,min}}\rvert$	Δl_{ROI}/nm	R_{grad}/nm	$R_{\mathrm{l,0}}$/nm	$\Delta R_{\mathrm{l,max}}$/nm
24.5	0.01	49.1	4.9	216.0	58.9
$R_{\mathrm{s,0}}$/nm	$\Delta R_{\mathrm{s,max}}$/nm	$R_{\mathrm{res,1}}$/nm	$r_{\mathrm{cc,0}}$/nm	$\Delta r_{\mathrm{cc,max}}$/nm	Δr_{mask}/nm
157.1	39.3	19.6	157.1	78.6	19.6
$\lvert\nabla B_{\mathrm{cc,max}}\rvert$	$H_{\mathrm{min,1}}$	$N_{\mathrm{p,max}}$	$x_{ij,\mathrm{min}}$/nm	$R_{\mathrm{res,f}}$/nm	R_{Gauss}/nm
0.1	0.02	100	1.5	1.2	49.1

Appendix Table 3.3. Parameters to detect interparticle interactions in Fig. 3.11.

R_{grad}/nm	R_0/nm	ΔR_{max}/nm	$R_{\mathrm{res,1}}$/nm	$x_{ij,\mathrm{min}}$	$H_{\mathrm{min,1}}$	$N_{\mathrm{p,max}}$	R_{Gauss}/nm
87	203	0	29	1.5	0.024	500	58

Part II

Self-assembly of Deformable Colloids

4

Colloidal Bond Hybridization in Spherical and Snowman-like Particles

Abstract

In colloidal bond hybridization, anisotropic interactions are induced for deformable particles. Here, we model deformable particles as mutually attractive, hard spheres with mobile satellite spheres. Using this simple model, we show that even for isotropic particles, anisotropic interactions are induced. Anisotropy arises as satellite spheres redistribute when the particles bind each other; a process that is analogous to redistribution of electrons in the formation of chemical bonds. Furthermore, we show that the valency of the particles can be tuned by the size and the number of satellite spheres. Finally, by implementing colloidal bond hybridization for snowman-like particles, we show that the combination of mutual attraction, anisotropy and deformability can stabilize curved monolayers.

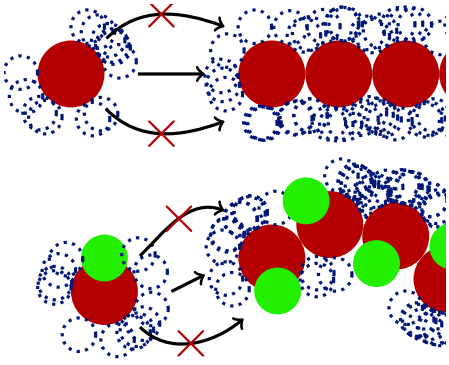

4.1. Introduction

4.2

Particles with anisotropic or *directional* interactions are promising building blocks for new functional materials and models for biological structures [24, 27, 85]. One way of inducing anisotropic interactions is by functionalizing part of the surface of particles with mutually attractive groups. The resulting particles are anisotropic or *patchy*, and can self-assemble into open lattices and colloidal equivalents of molecules and micelles [26, 28, 29]. Another approach is to anchor flexible surface groups onto the surface of the particles. The resulting particles are deformable; their overall shape changes when the surface groups alter their conformation. Mutually attractive, deformable particles self-assemble into more complex structures than expected for similar non-deformable particles. Upon grafting polymers onto the surface of spherical nanoparticles, for example, finite-size, isotropic clusters can be obtained [35]. Moreover, polymer-grafting can even induce anisotropic interactions resulting in self-assembled strings, sheets, and large vesicles [36, 37]. The combination of anisotropy and deformability, however, has–to the best of our knowledge–not been studied yet.

In this chapter, we develop a simple model for deformable particles and demonstrate that combining mutual attraction, anisotropy and deformability induces the stabilization of curved structures. We model deformable particles as mutually attractive central spheres with penetrable hard satellite spheres. We expect anisotropic interactions to arise as the satellite spheres redistribute upon binding. This process is analogous to bond hybridization in quantum chemistry. When two hydrogen atoms bind and form H_2, for example, the electrons around each atom redistribute, i.e. two isotropic orbitals hybridize into the molecular orbitals of H_2. Similarly, when mutually attractive, deformable particles bind, flexible surface groups redistribute, resulting in anisotropic interactions. We refer to this process as colloidal bond hybridization.

Using Monte Carlo simulations, we verify this mechanism. In the first part of this chapter, we study mutually attractive, isotropic, deformable (MID) particles. We show that the valency of MID particles, that we measure as the average number of bonds, can be tuned by the size and the number of satellite spheres. Next, we combine these two parameters into the covered surface fraction, that—with the initial configuration—dictates both the valency as well as the morphology of the observed structures. In the second part, we study mutually attractive, anisotropic, deformable (MAD) particles. Here, colloidal bond hybridization is combined with anisotropy, resulting in mechanically stable, curved monolayers.

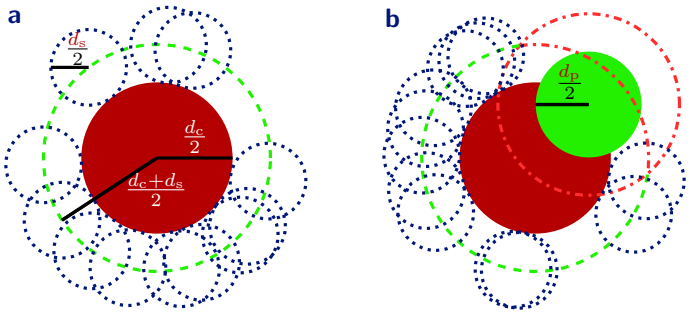

Figure 4.1. Deformable particles. Schematic diagrams of spherical and snowman-like, deformable particles. Mutually attractive, isotropic, deformable (MID) particles (**a**) are modelled as mutually attractive, hard central spheres with diameter d_c (●) and penetrable hard satellite spheres with diameter d_s (⋱). The satellite spheres can move at a distance $(d_c + d_s)/2$ from the centre of the central sphere (- -). Mutually attractive, anisotropic, deformable (MAD) particles (**b**) are modelled as MID particles with a rigid protrusion (●). Due to the protrusion, part of the surface of the central sphere is inaccessible for satellite spheres (- ··).

4.2. Methods

4.2.1. Deformable Particles We develop simple models for spherical and snowman-like particles. Mutually attractive, isotropic, deformable (MID) spheres are modelled as central hard spheres with N_s satellite spheres each (Fig. 4.1a). The central spheres have diameter d_c, and are mutually attractive, which can be due to for example hydrophobic effects in an experimental system. The satellite spheres model flexible surface groups like solvophilic polymers. These spheres have diameter d_s, and can move at a distance $d_s/2$ from the surface of the central sphere. The mobile spheres are penetrable hard spheres that can interpenetrate each other, but have excluded volume interactions with other particles. Penetrable hard spheres are frequently used to model polymers [86, 87, 88].

Mutually attractive, anisotropic, deformable (MAD) snowman-like particles are modelled by adding a rigid, hydrophobic sphere to a MID particle (Fig. 4.1b). The second sphere is a so-called *protrusion* with diameter d_p, and its presence makes the deformable particle anisotropic. The protrusion has a short-range attraction with other protrusions and central spheres that corresponds to for example hydrophobic effects of non-functionalized polystyrene. Finally, the relative sizes of the satellite spheres and the protrusion are $x_s = d_s/d_c$ and $x_p = d_p/d_c$.

4.2

4.2.2. Monte Carlo Simulations The models of deformable spherical and snowman-like particles are implemented in Monte Carlo computer simulations. The central spheres have a square well interaction potential,

$$w_{\mathrm{cc}}(r_{ij}) = \begin{cases} \infty & \text{if } r_{ij} \leq d_{\mathrm{c}}, \\ -\varepsilon_{\mathrm{cc}} & \text{if } d_{\mathrm{c}} < r_{ij} \leq d_{\mathrm{c}} + \xi, \\ 0 & \text{if } r_{ij} > d_{\mathrm{c}} + \xi, \end{cases} \tag{4.1}$$

where r_{ij} is the distance between the centres of the spheres, and ξ is the width of the square well.

The satellite spheres can move at a fixed distance $(d_{\mathrm{c}} + d_{\mathrm{s}})/2$, from the centre of the particle, and have penetrable hard sphere interactions: satellite spheres are free to overlap each other, i.e. $w_{\mathrm{ss}} = 0$, but they have hard sphere interactions with the central spheres,

$$w_{\mathrm{cs}}(r_{ij}) = \begin{cases} \infty & \text{if } r_{ij} \leq (d_{\mathrm{c}} + d_{\mathrm{s}})/2, \\ 0 & \text{if } r_{ij} > (d_{\mathrm{c}} + d_{\mathrm{s}})/2. \end{cases} \tag{4.2}$$

Snowman-like particles have one protrusion each and the hydrophobicity of the protrusions is captured by a weak square-well mutual attraction with strength $w_{\mathrm{pp}} = -\varepsilon_{\mathrm{pp}}$ over the range $d_{\mathrm{p}} < r_{ij} \leq d_{\mathrm{p}} + \xi$. The central spheres and protrusions interact through a square-well potential with depth $w_{\mathrm{cp}} = -\sqrt{\varepsilon_{\mathrm{cc}}\varepsilon_{\mathrm{pp}}}$ over the range $(d_{\mathrm{c}} + d_{\mathrm{p}})/2 < r_{ij} \leq (d_{\mathrm{c}} + d_{\mathrm{p}})/2 + \xi$. Finally, the protrusions have hard-sphere interactions with the satellite spheres,

$$w_{\mathrm{ps}}(r_{ij}) = \begin{cases} \infty & \text{if } r_{ij} \leq (d_{\mathrm{p}} + d_{\mathrm{s}})/2, \\ 0 & \text{if } r_{ij} > (d_{\mathrm{p}} + d_{\mathrm{s}})/2. \end{cases} \tag{4.3}$$

The model is used in Monte Carlo simulations in the canonical ensemble. Two different initial configurations are used: 1) unbound particles with increasing interaction strength from $\varepsilon_{\mathrm{cc}} = 3$ to $9k_{\mathrm{B}}T$ in steps of $1k_{\mathrm{B}}T$, and 2) a square monolayer in a hexagonal packing arrangement with fixed interaction strength $\varepsilon_{\mathrm{cc}} = 9k_{\mathrm{B}}T$. In the latter initial configuration, the protrusions are randomly oriented below and above the midplane of the monolayer and the distance between the centres of neighbouring central spheres is $d_{\mathrm{c}} + \xi/2$. The number of deformable particles is 98, the box length is set such that the total volume fraction of the central spheres equals 0.001, and periodic boundary conditions apply in all directions. The protrusions have a diameter $d_{\mathrm{p}} = 0.7d_{\mathrm{c}}$, a weak attraction strength $\varepsilon_{\mathrm{pp}} = \varepsilon_{\mathrm{cc}}/5$, and their centres are at a distance $d_{\mathrm{c}}/2$ from the centre of the central sphere. Finally, the square well width is set to $\xi = 0.1d_{\mathrm{c}}$.

For each particle shape and initial configuration, we perform simulations for every combination of number of satellite spheres, $N_{\mathrm{s}} \in \{2, 4, 6, 8, 10, 12\}$, and satellite sphere size, $x_{\mathrm{s}} = d_{\mathrm{s}}/d_{\mathrm{c}} \in \{0.20, 0.25, ..., 0.70\}$. The simulations that had a hexagonal monolayer

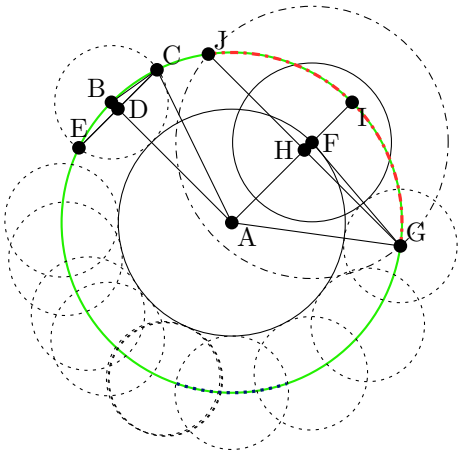

Figure 4.2. Covered surface fraction. The covered surface fraction, x_{cs} (Eq. 4.4), is the number of satellite spheres, N_{s}, times the covered area per satellite spheres, A_{s} (⋯), divided by the total available area in the absence of a protrusion, A_0 (—), minus the area excluded by a protrusion, $A_{\mathrm{ex,p}}$ (- - -).

as the initial configuration are repeated an additional four times, and all resulting data plots and morphologies are averages over these runs. To measure the valency, we calculate the average number of bonds per particle, $\langle N_{\mathrm{b}} \rangle$, where we define particles to be bound when the centre-centre distance between their central spheres, r_{cc}, is less than $d_{\mathrm{c}} + \xi$.

4.2.3. Covered Surface Fraction The number of satellite spheres, N_{s}, and the relative size of the satellite spheres, x_{s}, can be combined into the covered surface fraction, x_{cs}. The covered surface fraction is defined as the surface area covered by satellite spheres, divided by the total available surface area in the absence of neighbouring particles,

$$x_{\mathrm{cs}} = \frac{N_{\mathrm{s}} A_{\mathrm{s}}}{A_0 - A_{\mathrm{ex,p}}}, \tag{4.4}$$

where A_{s} is the surface area that is covered by each satellite sphere (Fig. 4.2⋯), A_0 is the surface area over which satellite spheres can move in the absence of a protrusion or any neighbouring particles (Fig. 4.2—), and $A_{\mathrm{ex,p}}$ is the area that is excluded by a protrusion (Fig. 4.2- - -). x_{cs} is thus a single particle property and overlap between covered surface areas of satellite spheres is ignored.

The available area over which a satellite sphere can move in the absence of a protrusion and any neighbouring particles (Fig. 4.2—) is the surface area of a sphere with diameter

$d_c + d_s$,

$$A_0 = \pi \left(d_c + d_s\right)^2 . \tag{4.5}$$

4.3

The area covered by a satellite sphere (Fig. 4.2⋯) is the spherical cap with radius, $R_{cap} = AB = (d_c + d_s)/2$, and height, $h_{cap} = BD$, where AB and BD denote the lengths of the line segments from point A to B and B to D in Fig. 4.2. The height of the cap can be found using basic geometry and the law of cosines [82, p1713],

$$h_{cap} = AB - AC\cos\measuredangle BAC = \frac{BC^2}{2AB} = \frac{{d_s}^2}{4(d_c + d_s)}, \tag{4.6}$$

where $\measuredangle BAC$ is the angle between B, A and C in Fig. 4.2. The resulting area per satellite sphere is [82, p2794],

$$A_s = 2\pi R_{cap} h_{cap} = \pi \frac{{d_s}^2}{4}. \tag{4.7}$$

Similarly, the excluded area by the protrusion (Fig. 4.2-⋯) is the spherical cap with radius $R_{cap} = AI = (d_c + d_s)/2$ and height,

$$h_{cap} = AI - AG\cos\measuredangle GAF = \frac{FG^2 - (AG - AF)^2}{2AF} = \frac{d_p(d_p + 2d_s)}{4d_c}. \tag{4.8}$$

Consequently, the excluded surface area is,

$$A_{ex,p} = \pi \frac{d_p(d_p + 2d_s)(d_c + d_s)}{4d_c}. \tag{4.9}$$

The expressions for the different surface areas are used to obtain the covered surface fraction by inserting Eq. 4.5, 4.7 and 4.9 into Eq. 4.4,

$$x_{cs} = \frac{N_s d_c {d_s}^2}{(d_c + d_s)(2d_c - d_p)(2d_c + d_p + 2d_s)} \tag{4.10}$$

$$= \frac{N_s {x_s}^2}{(1 + x_s)(2 - x_p)(2 + x_p + 2x_s)}, \tag{4.11}$$

where we inserted the dimensionless satellite sphere diameter, $x_s = d_s/d_c$, and protrusion diameter, $x_p = d_p/d_c$ in the second equation. For spherical particles, $d_p = 0$, and the covered surface fraction reduces to,

$$x_{cs} = \frac{N_s {d_s}^2}{4(d_c + d_s)^2} = \frac{N_s {x_s}^2}{4(1 + x_s)^2}. \tag{4.12}$$

The covered surface fraction increases thus with both the number and the size of the satellite spheres.

4.3. Results and Discussion

4.3.1. Mutually Attractive, Isotropic, Deformable Particles The clusters of mutually attractive, isotropic, deformable (MID) particles, are studied using Monte Carlo simulations. MID particles are modelled as central spheres with N_s satellite spheres that model flexible surface groups (Fig. 4.1a). The particles are mutually attractive due to a square well potential between their central spheres. Furthermore, the particles as a whole are deformable; their shape can change as a result of migration of the satellite spheres over the surface of the central sphere. In the simulations, two different initial configurations are used, 1) unbound particles and 2) particles in a hexagonal monolayer. In the first case, the mutual attraction between the central spheres, ε_{cc}, is stepwise increased to $9k_BT$, while in the latter case ε_{cc} is constant at $9k_BT$.

Using computer simulations, we determine the average number of bonds per particle, $\langle N_b \rangle$, that we take as measure for the valency (Fig. 4.3). Here, the number of bonds per particle is defined as the number of neighbours within the range of the mutual attraction. The value of the valency results from a competition between attractive interactions and excluded volume effects. Attraction between the central spheres promotes the formation of bonds, until the number of bonds reaches the so-called kissing number, that is the maximum number of twelve spheres that can be placed in contact with a central sphere [89]. When bonds are formed, however, part of the surface becomes inaccessible for the satellite spheres due to hard sphere interactions between satellite spheres and central spheres of neighbouring particles (Fig. 4.4a-···). Hence, the entropy of the satellite spheres decreases with the number of bonds, and these excluded volume effects favour unbound particles. To accommodate both effects, we expect the satellite spheres to rearrange when particles bind each other. Consequently, bonds are formed in plane, while satellite spheres move out of plane (Fig. 4.4a). As a consequence, even isotropic particles, i.e. spheres without patches or shape-anisotropy, form anisotropic bonds, and the valency is greater than zero, but smaller than twelve (Fig. 4.3).

This process is analogous to bond hybridization in quantum chemistry. When two hydrogen atoms bind and form the hydrogen molecule H_2, for example, the electrons around each atom redistribute, i.e. two isotropic orbitals hybridize into the molecular bonding orbital of H_2 (Fig. 4.4b—). Similarly, in colloidal bond hybridization, the redistribution of satellite spheres induces anisotropic bonds.

The valency decreases with the relative size of the satellite spheres, x_s, and the number of satellite spheres, N_s (Fig. 4.3). Increasing the size of the satellite spheres

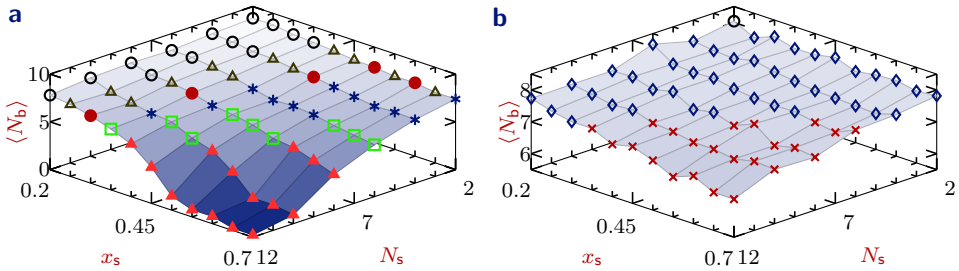

Figure 4.3. Valency of MID particles. The average number of bonds, $\langle N_b \rangle$, per mutually attractive, isotropic, deformable (MID) particle is determined using Monte Carlo simulations. The initial configurations of the simulations are unbound particles (**a**) and hexagonal monolayers (**b**). $\langle N_b \rangle$ decreases with the dimensionless diameter of the satellite spheres, x_s, and the number of satellite spheres, N_s. The symbols correspond to the in Fig. 4.6 defined morphologies. Note the different $\langle N_b \rangle$-range in **a** and **b**.

results in an increase in the fraction of the surface that becomes excluded when a bond is formed (App. 4.A and compare Fig. 4.5a to b). Consequently, the loss of entropy upon forming a bond increases with x_s, and the valency decreases with x_s (Fig. 4.3). Increasing the number of satellite spheres, N_s, results in more satellite particles that each lose entropy when a bond is formed. Hence, the valency also decreases with N_s (Fig. 4.3). We conclude that the valency can be tuned by the size and the number of satellite spheres.

Many-body interactions are expected to have a strong influence on the valency. For example, if three deformable particles bind, the particles might arrange in a way that creates overlap between their excluded surface areas (Fig. 4.5c). In this arrangement, the available surface area for the satellite spheres increases, and the total entropy might be higher than without overlap. Another many-body phenomenon is that no more than twelve spheres can be placed in contact with a central thirteenth sphere as we discussed above. Many-body interactions are difficult to incorporate in analytical models, and at this point, we have not been able to formulate an analytical theory to compare with the results from simulations.

The valency strongly depends on the initial configuration if the number and the size of the satellite spheres is large (compare Fig. 4.3a to b). For simulations with unbound particles as the initial configuration, the valency decreases from 8.8 for a few, small satellite spheres to 0.2 for many, large satellite spheres (Fig. 4.3a). When

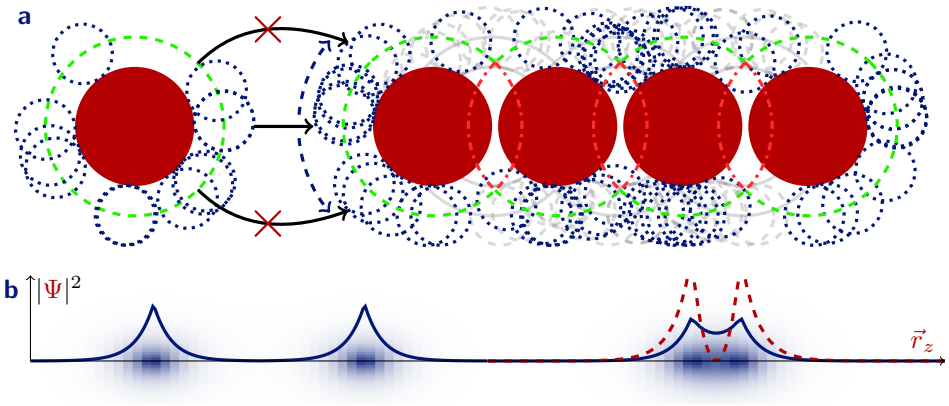

Figure 4.4. Bond hybridization. In colloidal bond hybridization (**a**) anisotropic interactions can be induced for mutually attractive, isotropic, deformable particles. Upon binding, satellite spheres (⋱) redistribute (⇢). Consequently, mutually attractive central spheres (●) interact in plane, while satellite spheres move out of plane, resulting in anisotropic interactions (→). This process is analogous to bond hybridization in quantum chemistry (**b**) where the electrons redistributes upon binding, and atomic orbitals of hydrogen atoms (left) hybridize into bonding (—) and antibonding (- -) molecular orbitals of the hydrogen molecule, H_2 (right). Here, the lines give the electron density, $|\Psi|^2$, as a function of the position in the z-direction, r_z, and the background gives a two-dimensional plot of the electron density as calculated in App. 4.B.

the initial configuration is a hexagonal monolayer, on the other hand, the valency has a similar value of 8.2 for a few, small satellite spheres. The decrease in the valency upon increasing the size and the number of satellite spheres, however, is much smaller, and the minimum valency is 6.7 (Fig. 4.3b). To understand why the valency depends on the initial configuration, we take a look at the morphologies of the clusters.

When unbound particles are used as the initial configuration, a large variation in morphologies of clusters (Fig. 4.6a,c–h) is observed. This is in agreement with the large variation in the valency in Fig. 4.3a. Furthermore, we compare our results with results for a more detailed model. Akcora *et al.* [36] have simulated nanoparticles with flexible polymers anchored onto their surface. Their model of MID particles also consists of mutually attractive central spheres. The flexible surface groups, however, are modelled as tethered chains of hard spheres, instead

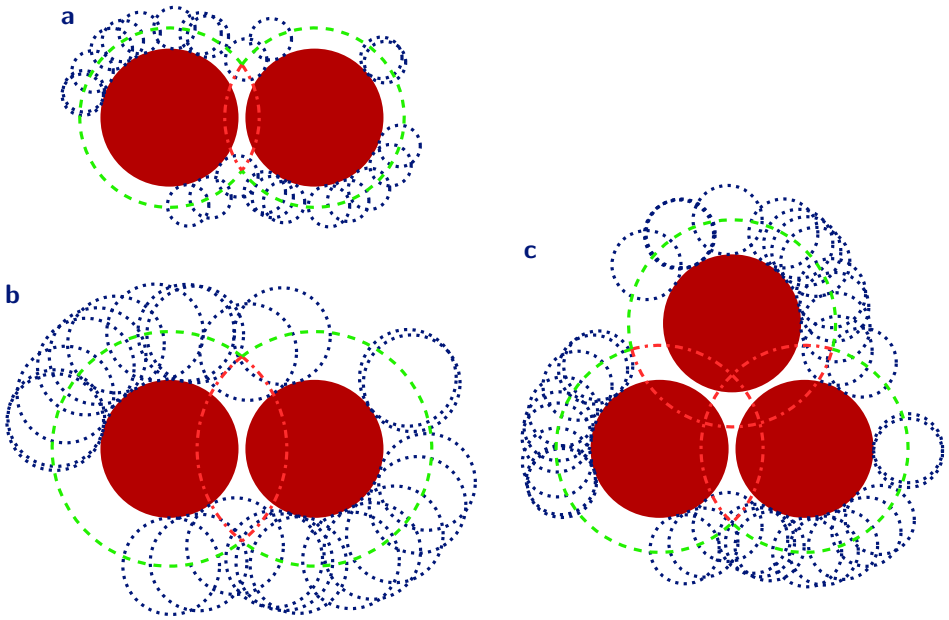

Figure 4.5. Excluded surface area. The excluded surface area (···) depends on both the size of the satellite spheres, x_s, and the number of bonds, N_b. For small satellite spheres (**a**) the fraction of the surface area that becomes excluded when a bond is formed is smaller than for large satellite spheres at the same centre-to-centre distance (**b**). If three particles are in contact (**c**), the particles can arrange in such a way that their excluded surface areas overlap.

of mobile, penetrable hard satellite spheres [36]. For both models, the particles reorganize into compact aggregates when the number and the size of the tethered chains or satellite spheres is small (Fig. 4.6c). This configuration maximizes the potential energy due to attractive interactions between the central spheres. Excluded volume effects become more important for more or larger chains or satellite spheres. Consequently, we expect the satellite spheres to redistribute upon binding, and snapshots of the simulations show that satellite spheres indeed move to the outside of the clusters (Fig. 4.6d–g●). Excluded volume effects induce more complex structures and a decrease in the dimensionality. Hence, for both models, flattened and elongated clusters, and finally unbound particles are observed (Fig. 4.6d–h). Our model thus qualitatively reproduces the more detailed model, which justifies that anchored flexible surface groups can be modelled as mobile penetrable hard

spheres. Furthermore, this suggests that also for the more detailed model, the main ingredients that induce anisotropic interactions are mutual attraction and deformability. As our model does not contain any molecular details, we expect this behaviour to be generic for mutually attractive, deformable particles. This expectation is in line with experimental results for polymer-grafted nanoparticles, where both mutual attraction and deformability can be identified and anisotropic interactions are induced [36, 37].

The behaviour is remarkably different when the initial configuration is a hexagonal monolayer. Similar to simulations where the initial configuration consists of unbound particles, the particles reorganize into compact aggregates if the number and the size of satellite spheres is small (Fig. 4.6b,i). Upon increasing these two quantities, however, the satellite spheres redistribute out of plane and mechanically stable bilayers and monolayers are observed (Fig. 4.6b,j–k). For many and large satellite spheres, the observed morphologies thus strongly depend on the initial configuration. Only unbound particles are found when unbound particles are used as the initial configuration, whereas monolayers are observed when monolayers are used as the initial configuration for $x_\mathrm{s} \gtrsim 0.55$ and $N_\mathrm{s} \gtrsim 8$ (compare Fig. 4.6h to k). This suggests that at least one of the initial configurations results in kinetically trapped structures. Sampling the disintegration from a monolayer into unbound particles should be easier than the formation of a monolayer from unbound particles. This becomes clear as many translations of particles at the edge of a monolayer result in an unbound particle. The formation of a new bond, however, requires the redistribution of many satellite spheres, and even more so if the number and the size of the satellite spheres is large (Fig. 4.4a). For a monolayer as the initial configuration, on the other hand, breaking the bonds between the central spheres is difficult as the interaction strength is $9k_\mathrm{B}T$. Hence, both morphologies are mechanically stable, and free energy calculations are necessary to verify which morphology corresponds to the free energy minimum. Moreover, when $x_\mathrm{s} = 0.7$, the diameter of the satellite spheres, $d_\mathrm{s} = 0.7d_\mathrm{c}$, is much larger than the range of the square well attraction between the central spheres, $\xi = 0.1d_\mathrm{c}$. Accordingly, rearrangement of satellite spheres is already necessary at distances much larger than the range of the attraction. Hence, a smoother attractive potential could perhaps prevent kinetic trapping. In experimental systems, potentials are by definition smoother than a square well potential, but kinetic trapping might still occur. Hence, external potentials could possibly be necessary to guide assembly into monolayers.

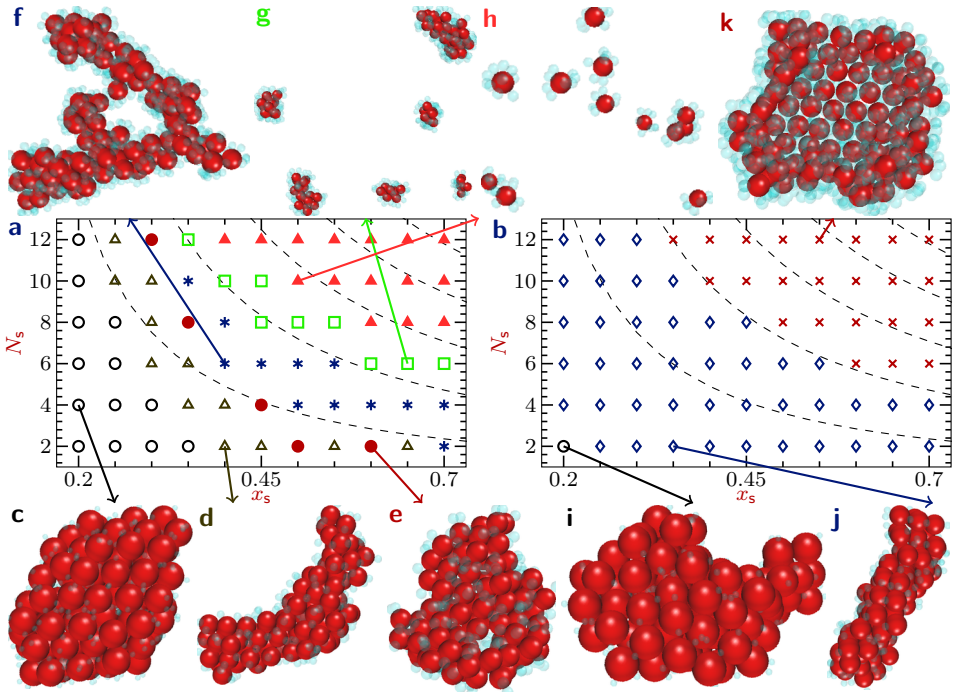

Figure 4.6. Clusters of MID particles. Morphology diagrams of clusters of mutually attractive, isotropic, deformable (MID) particles as a function of the dimensionless diameter of the satellite spheres, x_s, and the number of satellite spheres, N_s (**a–b**), and representative snapshots with central spheres (**c–k** ●) and satellite spheres (●). When unbound particles are used as the initial configuration (**a**) and x_s and N_s are increased, compact (**c** ○), cylindrical (**d** △), flattened (**e** ●), rod-like (**f** ∗) and finite-size (**g** □) clusters as well as unbound particles (**h** ▲) are found. When the initial configuration is a hexagonal monolayer (**b**), compact clusters (**i** ○), bilayers (**j** ◇) and monolayers (**k** ×) are observed. The dashed lines indicate where the covered surface fraction, x_{cs}, is 0.1, 0.2, 0.3, 0.4 and 0.5.

As expected, a strong correlation between the valency and the morphology of the clusters is observed (compare symbols to surface plots in Fig. 4.3). Hence, kinetic trapping can also explain the difference in the valency upon starting with unbound particles or hexagonal monolayers. For unbound particles with large and many satellite spheres, bond formation is prevented and the valency is close to

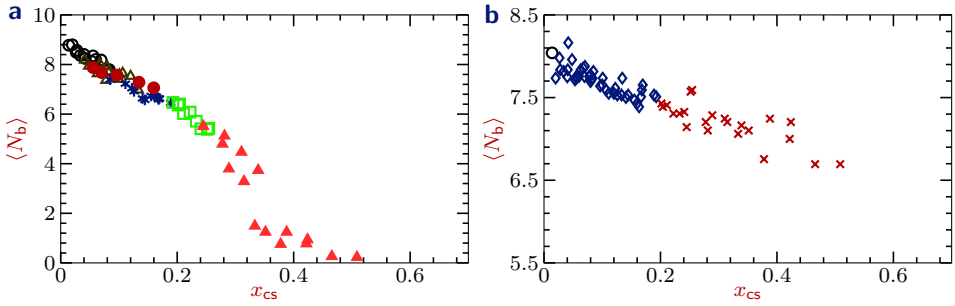

Figure 4.7. Valency versus covered surface fraction for MID particles. The average number of bonds per mutually attractive, isotropic, deformable (MID) particle, $\langle N_b \rangle$, is given as a function of the covered surface fraction, x_{cs}. $\langle N_b \rangle$ is determined using Monte Carlo simulations with unbound particles (**a**) and hexagonal monolayers (**b**) as initial configurations. The symbols correspond to the in Fig. 4.6 defined morphologies. Note the different $\langle N_b \rangle$-range in **a** and **b**.

zero. Upon starting with monolayers for such particles, however, the monolayers do not disintegrate resulting in a higher average number of bonds.

The covered surface fraction, x_{cs}, incorporates both the size and the number of satellite spheres in a single quantity (Eq. 4.12), and we expect this quantity to correlate with the valency and the morphology of the structures. Indeed, the contour lines of x_{cs} are virtually parallel to the transitions in the morphology diagrams (Fig. 4.6a–b). Furthermore, the morphologies also strongly correlate with the covered surface fraction (Fig. 4.7, symbols). Finally, upon plotting the valency as a function of x_{cs}, all curves collapse onto single curves that depend on the initial configuration (Fig. 4.7). Hence, we conclude that the covered surface fraction and the initial configuration dictate the morphology and the valency.

4.3.2. Mutually Attractive, Anisotropic, Deformable Particles We study the combination of colloidal bond hybridization and anisotropy, by adding rigid spheres or *protrusions* to the deformable spheres of the previous subsection (Fig. 4.1b). The resulting snowman-like particles are mutually attractive, anisotropic and deformable (MAD), and consist of mutually attractive, deformable cores, and slightly attractive, rigid protrusions (Fig. 4.1b). The core corresponds to a lobe with flexible surface groups as in the previous subsection. The protrusion, on the other hand, corresponds to a non-functionalized lobe in experiments. Non-functionalized

surfaces are typically hydrophobic, and this is captured by a short-range attraction with other protrusions or central spheres.

The dependence of the valency on the size and the number of satellite spheres for MAD particles mimics the behaviour for MID particles (compare Fig. 4.3 to Fig. 4.8a–b). For MAD particles, we measure the valency as the average number of bonds for the central spheres with other central spheres. Furthermore, similar to MID particles, the values for the valency collapse onto a single curve as a function of the covered surface fraction (Fig. 4.8c–d). For MAD particles, the valency is thus also dictated by the covered surface fraction. The central spheres of the MAD particles, however, form on average about one bond less than for MID particles (compare Fig. 4.8c–d to Fig. 4.7). This can be explained as the protrusion covers a section of the surface of the central sphere making that section inaccessible for other central spheres (Fig. 4.1b-···).

Using unbound particles as the initial configuration, the morphologies for MAD particles are similar to those for MID particles (compare Fig. 4.9a,c–h to Fig. 4.6a,c–h). The morphology diagram, however, is shifted to the lower left corner for MAD particles. For anisotropic particles, each structure is thus found for smaller and fewer satellite spheres than for MID particles. This can be understood as the addition of a protrusion reduces the available surface area for the satellite spheres (Fig. 4.1b-···). Consequently, the covered surface fraction increases (Eq. 4.11), and its isolines are shifted to the lower left corner of the morphology diagram (compare Fig. 4.6a- - to Fig. 4.9a- -). Hence, the transitions between morphologies occur at similar x_{cs}-values for both MID and MAD particles.

Using hexagonal monolayers as the initial configuration, different morphologies are obtained for MAD particles than for isotropic particles (compare Fig. 4.9b,i–n to Fig. 4.6b,i–k). Similar to MID particles, compact clusters are observed for MAD particles with a few small satellite spheres, and bilayers and flat monolayers are obtained upon increasing the size or the number of satellite spheres (Fig. 4.9i–k). Upon increasing these parameters further, however, curved monolayers with protrusions pointing in plane (Fig. 4.9l,QR) are observed. Moreover, for even larger and more satellite spheres, we obtain curved monolayers with all protrusions pointing inwards (Fig. 4.9m–n). Furthermore, for non-attractive protrusions, we also obtain curved monolayers, but now, for all sizes and numbers of satellite spheres, protrusions are pointing inwards (data not shown). The difference between the two initial configurations is again striking. When the initial configuration is a monolayer, curved structures are obtained for many and large satellite spheres,

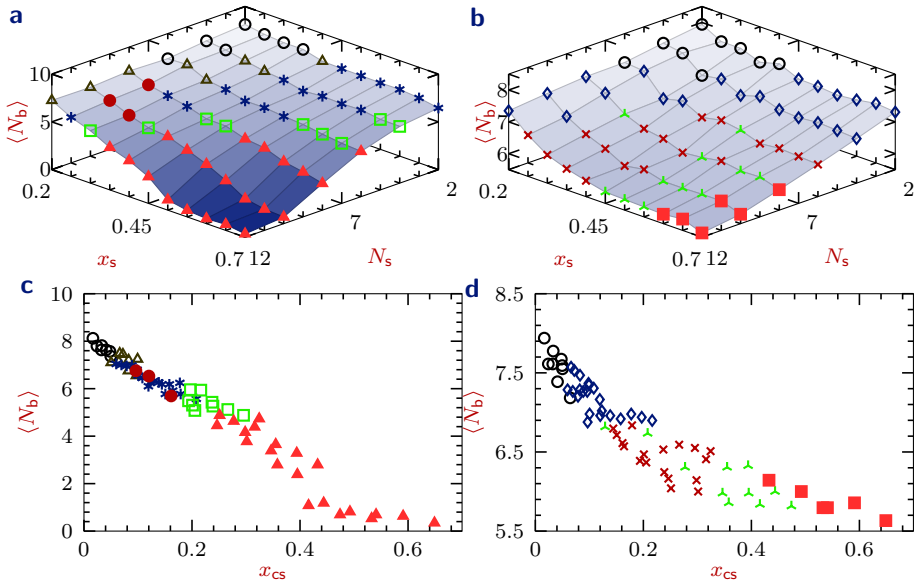

Figure 4.8. Valency of MAD particles. The average number of bonds, $\langle N_b \rangle$, per mutually attractive, anisotropic, deformable (MAD) particle is determined using Monte Carlo simulations with unbound particles (**a,c**) and hexagonal monolayers (**b,d**) as the initial configurations. $\langle N_b \rangle$ decreases with the dimensionless diameter of the satellite spheres, x_s, the number of satellite spheres, N_s, and the covered surface fraction, x_{cs}. The symbols correspond to the in Fig. 4.9 defined morphologies. Note the different $\langle N_b \rangle$-range in **a,c** and **b,d**.

whereas particles remain unbound when the initial configuration consists of unbound particles (compare Fig. 4.9l–n to h). Following the same reasoning as in the previous subsection, both morphologies could be kinetically trapped, but could be mechanically stable in experiments as well. For simulations of MID particles, no curved structures are observed (Fig. 4.6). The introduction of a protrusion breaks the symmetry of the building blocks and this induces a shift from flat to curved structures. The transition between flat and curved monolayers occurs at a less well-defined value for the covered surface fraction than for other transitions (Fig. 4.8d× ⅄). This is most likely the result of the small difference between these morphologies. Nevertheless, a strong correlation between the morphologies of the clusters and the covered surface fraction is observed (Fig. 4.8c–d). Similar to MID

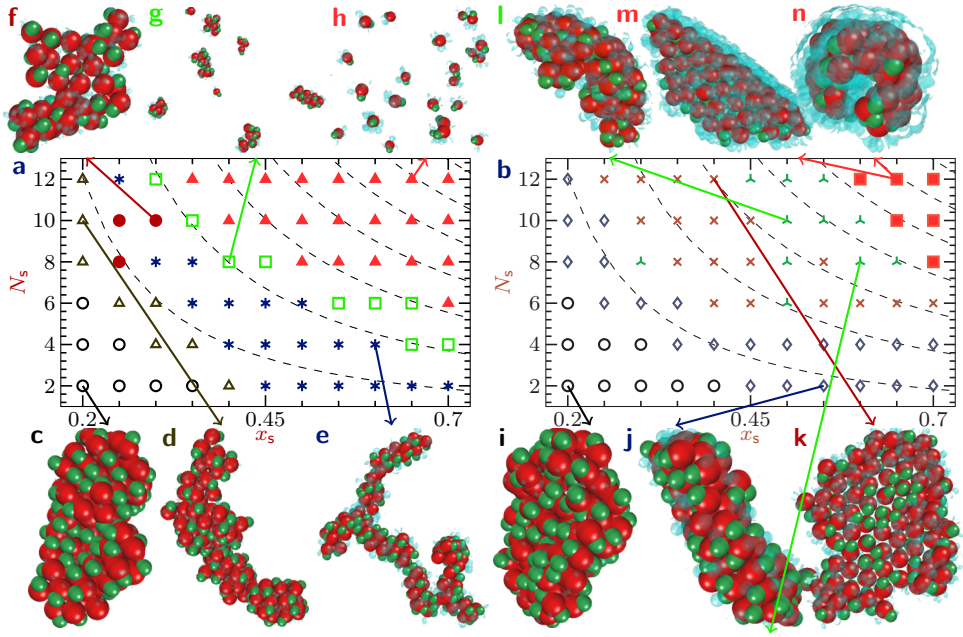

Figure 4.9. Clusters of MAD particles. Morphology diagrams of clusters of mutually attractive, anisotropic, deformable (MAD) particles as a function of the dimensionless diameter of the satellite spheres, x_s, and the number of satellite spheres, N_s (**a–b**), and representative snapshots with central spheres (**c–n** ●), protrusions (●) and satellite spheres (●). When unbound particles are used as the initial configuration (**a**), increasing x_s and N_s results in compact (**c** ○), cylindrical (**d** △), rod-like (**e** ∗), flattened (**f** ●) and finite-size (**g** □) clusters as well as unbound particles (**h** ▲). When the initial configuration is a hexagonal monolayer (**b**), compact clusters (**i** ○), bilayers (**j** ◇), flat monolayers (**k** ×), curved monolayers with in plane protrusions (**l** ⅄) and curved monolayers with out of plane protrusions (**m–n** ■) are found. The dashed lines indicate where the covered surface fraction, x_{cs}, is 0.1 to 0.7 and the QR code links to a movie where a curved monolayer at $x_s = 0.6$ and $N_s = 8$ is rotated (phd.chrisevers.com/4qr9.mp4).

particles, the covered surface fraction and the initial configuration thus dictate the morphology of the obtained clusters.

4.4. Conclusion

In this chapter, we developed a simple model for attractive, deformable particles: mutually attractive hard spheres with mobile satellite spheres. The satellite spheres cause an effective repulsion that competes with a short-range attraction between the hard spheres. Consequently, the satellite spheres redistribute upon binding. This process is analogous to the formation of the simplest chemical bond, where two isotropic orbitals hybridize into the molecular orbital of H_2. Using Monte Carlo simulations, we demonstrate that in colloidal bond hybridization, anisotropic interactions are induced for isotropic particles. The valency can be tuned by both the size and the number of the satellite spheres, resulting in a variety of different structures. For mutually attractive, isotropic, deformable (MID) particles, these results are in qualitative agreement with simulations using a more detailed model, justifying our simple model. Moreover, we show that the fraction of the surface of the central sphere that is covered by satellite spheres determines both the morphology of the clusters as well as the valency of the particles. Furthermore, extending our model to mutually attractive, anisotropic, deformable (MAD) particles shows that even curved monolayers can be stabilized by a combination of colloidal bond hybridization and anisotropy. Translating properties of experimental particles into the parameters used in our simulations is challenging, and sampling all configurations is troublesome. Hence, to predict self-assembled structures from experimentally determined properties, more theoretical work is needed for which work of Asai *et al.* [90] could be extended.

4.5. Acknowledgements

This work is a collaboration with Jurriaan Luiken and Peter Bolhuis. Both are thanked for their contribution in developing the model for deformable particles, and Jurriaan is thanked for performing the computer simulations and the collaboration in analysing the data.

4.A. Excluded Surface Fraction

We calculate the fraction of the available surface area that is excluded upon the formation of a bond. Surface area is excluded if the surface-to-surface distance, r_{ss}, is smaller than the diameter of a satellite sphere, d_s (Fig. 4.5). The excluded area is the area of the spherical cap with radius, $R_{cap} = (d_c + d_s)/2$, and height, $h_{cap} = (d_c + d_s)/2 - (d_c + r_{ss})/2$ (Fig. 4.5···) [82, p2794],

$$A_{ex} = \begin{cases} 2\pi R_{cap} h_{cap} = \frac{\pi}{2}(d_c + d_s)(d_s - r_{ss}) & \text{if } r_{ss} < d_s \\ 0 & \text{if } r_{ss} \geq d_s, \end{cases} \tag{4.13}$$

where d_c is the diameter of the central sphere.

The excluded surface fraction is,

$$\frac{A_{ex}}{A_0} = \begin{cases} \frac{d_s - r_{ss}}{2(d_c + d_s)} = \frac{x_s - x_{ss}}{2(1 + x_s)} & \text{if } x_{ss} < x_s \\ 0 & \text{if } x_{ss} \geq x_s, \end{cases} \tag{4.14}$$

where $x_{ss} = r_{ss}/d_c$ is the dimensionless surface-to-surface distance, and x_s is the dimensionless diameter of a satellite sphere.

Finally,

$$\frac{\partial A_{ex}/A_0}{\partial x_s} = \frac{1 + x_{ss}}{2\,(1 + x_s)^2} > 0 \quad \text{if } x_{ss} < x_s, \tag{4.15}$$

and the excluded surface fraction thus increases with the relative size of the satellite spheres, x_s.

4.B. Calculation of Electron Densities

The electron density, $|\Psi(\vec{r})|^2$, at a volume element at position $\vec{r}$ is plotted for hydrogen atoms and the hydrogen molecule, H_2, in Fig. 4.4b. For the hydrogen atom, we take the electron density as the squared radial wave function of the 1s orbital [91, p88],

$$|\Psi(\vec{r})|^2 = \left[c \exp\left(-|\vec{r} - \vec{r}_n|/R_B\right)\right]^2, \tag{4.16}$$

where c is a normalization constant, $\vec{r}_n$ is the position of the nucleus, and $R_B = 52.9\,\text{pm}$ is the Bohr radius, where little error is introduced as the mass of the electron is used instead of the reduced mass of the electron.

For the hydrogen molecule, we ignore interactions between the electrons and assume that the bonding and antibonding orbitals are linear combinations of atomic

1s orbitals of the hydrogen atom [91, p258-259]. The resulting probability density for each electron is,

$$|\Psi(\vec{r})|^2 = \left[c\exp\left(-|\vec{r}-\vec{r}_{\mathrm{n},1}|/R_{\mathrm{B}}\right) \pm c\exp\left(-|\vec{r}-\vec{r}_{\mathrm{n},2}|/R_{\mathrm{B}}\right)\right]^2, \tag{4.17}$$

where the two terms are summed for a bonding orbital, and subtracted for an antibonding orbital, and the two nuclei are at $\vec{r}_{\mathrm{n},1}$ and $\vec{r}_{\mathrm{n},2}$, and $|\vec{r}_{\mathrm{n},1} - \vec{r}_{\mathrm{n},2}| = 1.4R_{\mathrm{B}}$ [91, p259]. Finally, as the hydrogen atom has two electrons, the total electron density is obtained by multiplying the result in Eq. 4.17 with 2.

5

Self-Assembly into Microcapsules via Colloidal Bond Hybridization and Anisotropy

Abstract

In material sciences, anisotropic interactions have been induced by distributing mutually attractive domains anisotropically over the surface of colloids, or by making mutually attractive nanoparticles deformable. In biology, however, proteins incorporate mutual attraction, anisotropy as well as deformability, and self-assemble, for example, into virus microcapsules. Here, we combine these three characteristics into model particles that self-assemble into colloidal microcapsules. In the previous chapter, we showed that mutual attraction and deformability induce anisotropic interactions via colloidal bond hybridization. Here, this mechanism induces self-assembly of isotropic spheres into planar monolayers, while anisotropic snowman-like particles self-assemble into monolayer microcapsules. A modest change of the building blocks thus results in a significant leap in the complexity of the self-assembled structures.

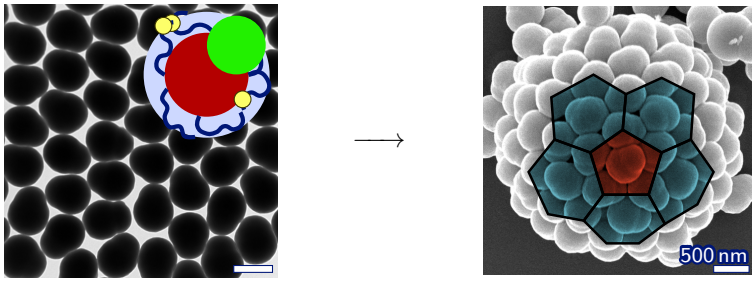

5.1. Introduction

In protein self-assembly, biomolecules spontaneously form structures ranging from simple dimers to icosahedral microcapsules enclosing viral DNA [92, p63-64]. Self-assembling proteins are mutually attractive, anisotropic and deformable, and we abbreviate these three characteristics as MAD. Mutual attraction is commonly induced via hydrophobic interactions. Anisotropy is the second characteristic, and can, for example, be recognized in proteins that form complexes. These proteins contain hydrophobic parts that are in contact with other proteins, and hydrophilic parts that are exposed to the solution [33, p43]. Finally, deformability or *floppiness* is the result of structural rearrangements during self-assembly [32]. The hepatitis B core protein, for example, changes its conformation upon assembly into a virus monolayer microcapsule [34].

For micrometer-sized colloidal particles, mutual attraction and anisotropy have recently been combined using attractive domains or *patches*. The resulting *patchy* particles self-assemble, for instance, into open lattices and colloidal equivalents of molecules and micelles [26, 28, 29]. In self-assembly of nanoparticles, on the other hand, mutual attraction and deformability have recently been coupled by grafting flexible polymers onto the surface of mutually attractive particles. This results in isotropic clusters [35], and self-assembled strings, sheets, and large vesicles [36, 37]. To the best of our knowledge, anisotropy and deformability have not been combined in a colloidal model systems. Furthermore, self-assembly into monolayer microcapsules has not been experimentally observed by applying either anisotropy or deformability. Such structures have been predicted for cone-shaped particles with four orthogonally attractive patches [31] (Fig. 1.1f). Unfortunately, these building blocks are challenging to synthesize and have not been experimentally realized yet.

In this chapter, we show that colloidal particles that are relatively easy to synthesize can also self-assemble into microcapsules. The design of these particles is inspired by MAD proteins, i.e. particles that are mutually attractive, anisotropic, as well as deformable. We discuss our results in four parts. First, we study particles with two of the three characteristics: mutually attraction and deformability. In the previous chapter, we introduced colloidal bond hybridization, a mechanism that induces anisotropic interactions for mutually attractive and deformable particles. Here, we implement colloidal bond hybridization in an experimental model system and observe planar monolayers for chemically and geometrically isotropic particles. In the second part, we combine colloidal bond hybridization with anisotropy, using

MAD particles, with all previously mentioned characteristics. We achieve this combination using snowman-like particles that consist of a deformable core and a non-deformable second lobe or *protrusion*. These relatively simple particles self-assemble into microcapsules and we discuss their similarities with the structure of viruses. Furthermore, they also form spherical cavities at high particle concentrations, as discussed in the third part. In the last part, we propose a mechanism for the formation of microcapsules with cavities as intermediates.

5.2. Methods

5.2.1. Chemicals and Colloidal Particles Unless stated otherwise, the following chemicals were used as received: *tert*-butylamine (tBA, 391433, ≥99.5%), fluoresceinamine (FlA, mixture of isomers, 46930, ≥75%), and fluorescein sodium salt (Fl, F6377), were obtained from Sigma-Aldrich or its subsidiaries; potassium chloride (KCl, 196770010, p.a.) was obtained from Acros; potassium hydroxide (KOH, 1.05033), sodium hydroxide (NaOH, 1.06498), and hydrochloric acid (HCl, 1.00317 37%) were obtained from Merck; glycerol (262447, Ph. Eur.) was obtained from Bufa; ethanol (100%) was obtained from Interchema; and Millipore water (MQ) was obtained with a Synergy water purification system. Salt solutions were prepared by mixing weight amounts of salt with MQ.

Mutually attractive, isotropic, deformable (MID) cross-linked poly(styrene-*co*-acrylic acid) particles with a diameter of 530 nm were synthesized as described in Subsection 2.2.2. Mutually attractive, anisotropic, deformable (MAD) snowman-like particles with a cross-linked poly(styrene-*co*-acrylic acid) core, a polystyrene protrusion, and core diameters of 353, 540, 626 and 679 nm are synthesized and functionalized with fluoresceinamine as described in Subsections 2.2.3 and 2.2.4. For Fig. 5.5h,m,r, we modified the latter synthesis method and added the same molar amount of *tert*-butylamine instead of fluoresceinamine. Furthermore, particles similar to MAD particles that are isotropic were synthesized by functionalizing MID particles with fluoresceinamine as described in Subsection 2.2.3. The synthesis of fluoresceinamine functionalized, polystyrene snowman-like particles, i.e. mutually attractive, anisotrotropic, non-deformable particles, is previously described by van Ravensteijn *et al.* [11]. Cross-linked polystyrene (CPS) particles with a diameter of 0.41 µm were prepared as described in Subsection 2.2.2.

5.2.2. Optical Microscopy Typically, a sample was prepared by bringing 0.5–2 µl dispersion between a microscope slide (Menzel-Gläser), and a #1.5 cover slip (Menzel-Gläser) with two #0 cover glasses (VWR) as spacers. Before use, the slides were cleaned with MQ, ethanol and Kimtech precision wipes, and the dispersions of colloids in water were washed as described in Section 2.2, and diluted with MQ. Furthermore, cells were sealed with glue (Norland NOA81, cured with a UVP UVGL-58 lamp) or adhesive tape.

Evaporating droplets between two glass slides (Fig. 5.6h–l) were studied in similar cells, but without sealing the sides of the cell. Evaporating droplets on a glass slide (Fig. 5.6b–f, 5.9a–d and App. Fig. 5.4), on the other hand, were studied by bringing 0.5 µl dispersion on a similarly cleaned #1.5 cover slip (Menzel-Gläser). Droplets evaporated spontaneously and for each dispersion four times (twice for non-deformable particles) a time series was obtained of a 89×89 µm area. Samples with a high concentration of colloids (Fig. 5.7) were obtained by preparing a cell as described above and subsequent sedimentation in the earth gravitational field. Thin cells as in Fig. 5.8, Fig. 5.9e–r and App. Fig. 5.3 were prepared in a capillary and sealed with glue, while preventing contact between uncured glue and the dispersion. For this aim, a $0.02 \times 0.2 \times 50\,\mathrm{mm}^3$ capillary (VitroCom 5002-050) was filled half with dispersion. Next, the cell was pressed on a microscopy slide (Menzel-Gläser) with tweezers and a foam cushion, and nitrogen gas was blown from the filling side to push the dispersion to the middle of the cell. While blowing, the other side was sealed and fixated on the microscopy slide with a glue droplet (Norrland NOA81) to prevent the dispersion from flowing back. Finally, the other side was sealed with glue, the glue was cured with UV light (UVP UVGL-58), and the cells were centrifuged (Beckman Coulter Allegra X-12R) in centrifuge tubes (VWR SuperClear Ultra-High Performance). Fig. 5.8e–f and Fig. 5.9e–l are obtained after centrifugation at $2.1 \times 10^3\,g$.

Bright field, fluorescence and reflected light microscopy images were captured with a Nikon Ti-E Inverted Microscope unless stated otherwise. The Nikon Ti-E is operated with a Nikon TIRF 100×/1.49 objective, intermediate magnification of 1.5×, and a Hamamatsu ORCA Flash camera. For reflected light microscopy, a Nikon Intensilight C-HGFI light source was used with a Nikon D-FLE filter block. For fluorescence microscopy, the same light source was used with a Semrock FITC-3540C filter block. The microscopy images in Fig. 5.7 and App. Fig. 5.2 were obtained with a Nikon Ti-U inverted Microscope with a Nikon Plan Apo VC 100×/1.40 objective, intermediate magnification of 1.5×, and a Lumenera Infinity X camera. The images in App. Fig. 5.1 were obtained with the same set-up with an intermediate magnification of 1×. The bright field microscopy images in Fig. 5.8, Fig. 5.9e–r and App. Fig. 5.3 were obtained with a Nikon Eclipse LV100POL microscope with its focal plane parallel to the gravitational field, a Nikon Plan Fluor ELWD 40×/0.6 objective, and a QImaging MicroPublisher 5.0 camera. Finally, confocal microscopy images were captured with a Nikon TE2000-U, with a Nikon Plan Apo 100×/1.40 objective and a 488 nm laser. For confocal fluorescence microscopy (Fig. 5.2i–k), a detector at 590 nm was used and fluorescein sodium salt was added to the dispersion, while for confocal reflected light microscopy (Fig. 5.2l), a detector at 515 nm was used.

To increase contrast, image levels were linearly rescaled using ImageMagick and the rescaling is indicated by the vertical bars in each image. For bright field, fluorescence and confocal microscopy, image levels were rescaled from zero to the value of the brightest pixel unless stated otherwise. For reflected light microscopy and the bright field images in

Fig. 5.8c,f,i and Fig. 5.9i–k,p–r however, contrast was increased further by linearly rescaling with a lower threshold at the value of the darkest pixel instead of at zero. Finally, for Fig. 5.8b,e,h, Fig. 5.9e–g,m–o and App. Fig. 5.3, the threshold values for the cropped versions in Fig. 5.8c,f,i and Fig. 5.9i–k,p–r were used.

The effective two-dimensional radial distribution function, $g(r_{ij})$, and the effective pair potential (Fig. 5.7f–g) were obtained by analysing reflected light microscopy time series as explained in Subsection 3.3.3. For particles in a microcapsule (Fig. 5.2n), the positions of the particles are similarly determined and the number of counts was plotted as a function of the interparticle distance with its maximum normalized to 1.

5.2.3. Electron Microscopy After freeze-drying or sintering, self-assembled structures could be studied using scanning electron microscopy. For freeze-drying, 1 µl dispersion was brought on a polymer coated copper grid. The grid was vitrified in liquid nitrogen and mounted on a cryo transfer unit which was brought under vacuum of about 10^{-4} Pa. Temperature was increased to −90 °C at 5 °C/min and kept constant for about six hours to allow the water to sublimate.

For sintering, the sample was heated above the glass transition temperature of polystyrene at about 100 °C [6, p13-13]. First, the dispersion was centrifuged and redispersed in 1:1 glycerol:water. Next, the dispersion was immersed in a 105 °C oil bath for 30 minutes. Additional MQ was added to decrease the viscosity, and the dispersion was washed three times with MQ by centrifugation. Finally, 1 µl washed dispersion was brought on a polymer coated copper grid, and after drying, the sample was coated with a ∼6 nm platinum layer.

Both samples were studied with a FEI XL30 FEG scanning electron microscope operated at 5–10 kV. Image levels were linearly rescaled using ImageMagick, from the value of the darkest pixel to the brightest pixel.

Finally, transmission electron microscopy images were obtained as described in Subsection 2.2.5, and characterised following Subsection 3.2.6. Unless stated otherwise, the size of the particles refers to the in this way obtained diameters.

5.2.4. Dynamic Light Scattering and Laser Doppler Electrophoresis The hydrodynamic radius and the zeta potential were measured with a Malvern Zetasizer Nano ZS using dynamic light scattering and laser doppler electrophoresis. 5 µl washed dispersion with a solid content, m_s, of about 10%, was added to 8 ml salt solution resulting in a solid content of about 0.006%. The diluted dispersion was immediately equilibrated at 25 °C for five minutes in a folded capillary cell (Malvern DTS1060). The mean, μ, and the standard deviation or polydispersity, σ, in the hydrodynamic diameter, d_{hd}, were measured seven consecutive times by dynamic light scattering. Measurements were performed at a scattering angle of 173° and data was analysed using the cumulant method

of the Zetasizer software. Next, seven consecutive times, μ and σ were determined for the zeta potential, ζ, by laser Doppler electrophoresis at 173° using the general purpose mode. The radii of the particles, R, were about 250 nm, while the Debye screening length, κ^{-1} was about 10 nm. Hence, $R\kappa \gg 1$ and the Smoluchowski model was used to analyse the data [7, p430-432]. For each value, the trend was calculated as the slope of a least squares linear fit normalized by the mean value.

To measure the hydrodynamic diameter at small pH intervals, a Malvern MPT-2 autotitrator was used with the Zetasizer. In a typical experiment, 5 µl washed dispersion was added to 8 ml 1 mM KOH, and 1 mM HCl was used as titrant. For App. Fig. 5.6∗, 1 mM NaOH was used instead of KOH, and for App. Fig. 5.6●, 9 mM KCl was added to both the dispersion and the titrant. The autotitrator tubes, titrant vial and capillary cell were thoroughly flushed with MQ and salt solution and pumped dry. The diluted dispersion was magnetically stirred with a PTFE coated stir bar and circulated through the autotitrator and the capillary cell. Next, the hydrodynamic diameter was determined seven consecutive times as described above. Now, however, the dispersion was circulated through the autotitrator between each measurement, and pH was measured using an electrode. After each series of seven measurements, titrant was added, the dispersion was stirred and recirculated and a new series was measured until pH was below 3.7.

5.3. Results and Discussion

5.3.1. Planar Monolayers We create isotropic as well as anisotropic building blocks that are mutually attractive and deformable. Before discussing the more complex anisotropic particles, we consider a basic implementation of colloidal bond hybridization using mutually attractive, isotropic, deformable (MID) particles. These poly(styrene-*co*-acrylic acid) spheres are synthesized by copolymerizing acrylic acid and styrene in water (Fig. 5.1a–b, Subsection 2.2.2), and their deformable nature arises as acrylic acid and styrene are incorporated at different stages in the polymerization process [65, 66] (App. 5.B). Hence, the particles consist of a hydrophobic styrene-rich core and a hydrophilic acrylic acid-rich brush. The particles are mutually attractive as hydrophobic polystyrene groups are present both in the interior of the particles as well as in the acrylic acid-rich brush. Furthermore, dynamic light scattering shows that the brush can rearrange on the order of 0.1 µm, rendering the particles deformable (App. 5.B).

Mutually attractive, isotropic, deformable (MID) particles self-assemble into planar monolayers in water (Fig. 5.1c–d). These clusters translate and rotate randomly in the solution (Fig. 5.1QR). When clusters are oriented horizontally, the

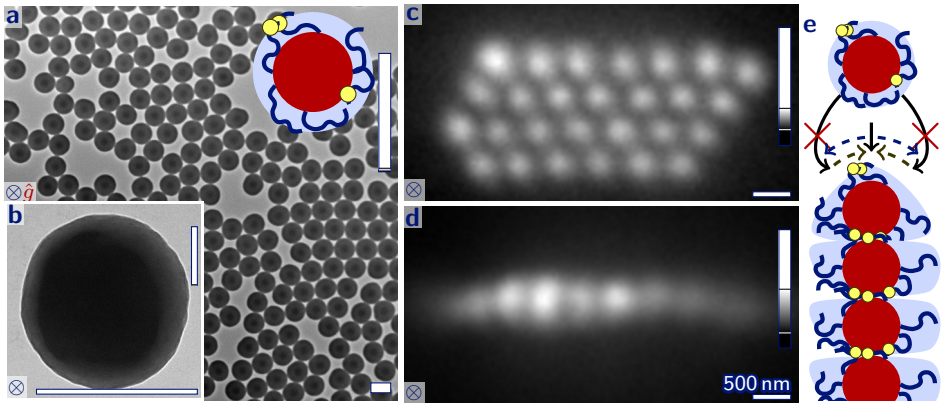

Figure 5.1. Self-assembled planar monolayers. Mutually attractive, isotropic, deformable (MID) particles (**a–b**, transmission electron microscopy) consist of a styrene-rich core (●), a deformable acrylic acid-rich brush (∿) and mutually attractive moieties (●). In water, the particles self-assemble into planar hexagonal monolayers (**c–d**, top and side view, reflected light microscopy). In colloidal bond hybridization (**e**), surface groups of deformable particles redistribute upon binding: mutually attractive moieties (●) move towards the contact area, while hydrophilic chains (∿) move into the solution. The direction of the gravitational field is indicated by $\hat{g}$ and image levels are rescaled as indicated by the vertical bars. The QR code links to a movie of a bright field microscopy time series of a randomly translating and rotating planar monolayer (phd.chrisevers.com/5qr1.mp4).

hexagonal orientation of the particles can be observed (Fig. 5.1c), while a vertically oriented cluster shows that it is indeed only one layer thick (Fig. 5.1d).

We propose that a colloidal equivalent of quantum chemical bond hybridization drives the formation of monolayers. In Subsection 4.3.1, we saw that anisotropic interactions can be induced for MID particles, as surface groups redistribute upon binding. The poly(styrene-*co*-acrylic acid) spheres also incorporate the three MID characteristics, and can also change their configuration upon binding. The polymer brush contains mutually attractive styrene groups as well as hydrophilic acrylic acid groups (Fig. 5.1e ● and ∿). Attraction between the hydrophobic groups promotes compact structures, while excluded volume effects of the hydrophilic parts favour unbound particles. To accommodate both effects, the polymer brush rearranges

upon binding: hydrophobic parts interact in plane, while hydrophilic parts expand out of plane. Consequently, anisotropic interactions are induced for chemically and geometrically isotropic particles and planar monolayers are formed (Fig. 5.1e).

5.3

The planar monolayers have a similar morphology as the structures that are found in computer simulations of MID particles (compare Fig. 5.1c–d to Fig. 4.6k) Our observations are also in line with results for polymer-grafted nanoparticles that are mutually attractive, isotropic and deformable [36, 37, 90, 93]. In our system, however, anisotropic interactions are induced for particles that are two orders of magnitude larger than in previous work. Furthermore, these larger particles allow visualization of self-assembled structures in solution using optical microscopy without freezing in liquid nitrogen or drying. Additionally, DNA coated colloids can also form crystalline monolayers [94], but for these particles, a functionalized surface induces anisotropic interactions.

Finally, the segregation of hydrophobic and hydrophilic moieties in the polymer brush (Fig. 5.1e) is similar to phase segregation in self-assembly of block copolymers [95]. In our system, however, copolymers are anchored to the surface of µm-sized particles. Consequently, molecular segregation of the polymers induces anisotropic interactions on the colloidal length scale.

5.3.2. Monolayer Microcapsules In the remainder of this chapter, we combine colloidal bond hybridization with anisotropy, which results in fundamentally new behaviour. Anisotropic building blocks are synthesized by growing a rigid protrusion onto the MID particles of Fig. 5.1a–b. The protrusion is grown by swelling with additional styrene [13, 14, 15] (Subsection 2.2.4). Furthermore, we increase the attraction between the deformable cores by functionalizing the acrylic acid-rich brush with hydrophobic groups [67] (Subsection 2.2.3). Next, the particles are washed by centrifugation, which is a crucial step as we will see in Subsection 5.3.4. Finally, we obtain mutually attractive, anisotropic, deformable (MAD) particles that consist of a deformable core (Fig. 5.2a ●∿) and a non-deformable protrusion (Fig. 5.2a ●).

The MAD particles self-assemble into monolayer microcapsules (Fig. 5.2c–m). In Fig. 5.2, we study particles with a diameter of the core of 540 nm and a diameter of the protrusion of 435 nm. As the size of the particles is similar to the wavelength of light, we can study self-assembled structures in solution using optical microscopy. The microcapsules randomly translate and rotate over the glass substrate due to Brownian motion (Fig. 5.2QR1). As their gravitational length is about 0.5 µm

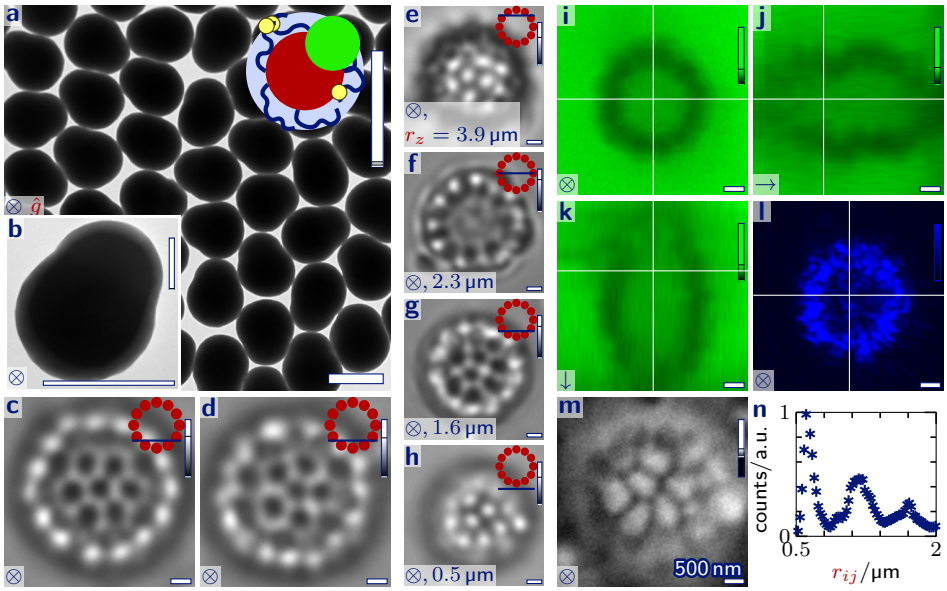

Figure 5.2. Self-assembled microcapsules. Mutually attractive, anisotropic, deformable (MAD) particles (**a–b**, transmission electron microscopy) consist of a core (**a** ●) with hydrophilic (∿) and hydrophobic (○) moieties and a rigid protrusion (●). These particles self-assemble into monolayer microcapsules in water (**c–h**, bright field microscopy) where each particle has six (**c**) or five nearest neighbours (**d**), and cross-sections can be obtained at different heights, r_z (**e–h**). In **c–h**, the height of the focal plane (—) is schematically indicated with respect to the MAD particles (●). Adding a water-soluble dye, shows that microcapsules are water-filled (**i–k**, confocal fluorescence microscopy, **l**, confocal reflected light microscopy) where the white lines indicate the positions of the orthogonal slices through the three-dimensional image. Using reflected light microscopy, the orientation of the particles is observed (**m**), and a histogram of the interparticle distances, r_{ij}, is obtained with a maximum at 0.63 µm (**n**). Image levels are rescaled as indicated by the vertical bars, and the gravitational field is indicated by $\hat{g}$. The QR codes link to a movie of the time series at the bottom of the microcapsule of **c–d** (phd.chrisevers.com/5qr2a.mp4) and the height series of **e–h** (phd.chrisevers.com/5qr2b.mp4).

(App. 5.C), they can even move about one particle diameter in the vertical direction. Consequently, different slices of the microcapsule come into focus in Fig. 5.2QR1, even though the focal plane of the microscope remains at the same height. When the bottom of the microcapsule is just below the focal plane, we observe particles that are either darker or brighter than the background (Fig. 5.2c–d). The dark particles are just below focus, and form the bottom of the microcapsule. We observe that most particles have six nearest neighbours (Fig. 5.2c). Pentagons, however, occur frequently as expected from the Euler characteristic of a sphere (Fig. 5.2d). The bright particles, on the other hand, are just above the focal plane. A ring with a thickness of one particle diameter is observed, that corresponds to a slice above the bottom of the microcapsule. The distance between the dark and the bright particles is estimated from a height series of a microcapsule (Fig. 5.2e–h,QR2). The bottom most particle of this microcapsule happened to be stuck on the glass slide. Hence, particles remain at the same position, and we can measure the distance between focal planes where the particles are dark and bright, which is 1 µm (compare Fig. 5.2g to h). As expected, this distance is comparable to the theoretical axial resolution, $2\lambda n_{\mathrm{D}}/\mathrm{NA}^2 = 0.7\,\mu\mathrm{m}$ [96, p207], where $\lambda = 5 \times 10^2\,\mathrm{nm}$ is the wavelength of light, $n_{\mathrm{D}} = 1.515$ is the refractive index of the immersion oil, and $\mathrm{NA} = 1.49$ is the numerical aperture of the objective. Upon increasing the focal plane further, the centre and the top of the microcapsule can be observed (Fig. 5.2f,e). The centre shows a monolayer ring of particles, while the top of the microcapsule consists of particles with again five or six neighbours. Furthermore, the distance between the top and the bottom layer is comparable to the horizontal diameter of the monolayer rings. From these observations, we conclude that the structures are spherical monolayers microcapsules.

We verify that the microcapsules are water-filled. Bright field microscopy shows that most microcapsules do not contain other particles (Fig. 5.2f). In the interior of some microcapsules, however, other particles are found. Furthermore, in the rare occasion that microcapsules have vacancies, particles can freely move into and out of the microcapsule (App. Fig. 5.2d–m). This suggests that the interior and the exterior of the microcapsule consist of the same solvent, water. Next, we study the microcapsules after adding a water-soluble dye to the dispersion. In confocal fluorescence microscopy, the particle monolayer can be distinguished as a dark region due to the absence of dye in the interior of the particles (Fig. 5.2i–k). In confocal reflected light microscopy, on the other hand, the monolayer appears bright as light is reflected due to the difference in the refractive index between the particles

and water (Fig. 5.2l). Fluorescence is observed with a similar intensity both inside and outside the microcapsule. Hence, we conclude that the microcapsules indeed are water-filled. Furthermore, fluorescence inside the microcapsules also demonstrates that molecules can freely diffuse into the microcapsules. From the geometry of the particles, we expect that interstitial space is present between the self-assembled particles, and the microcapsules are thus not molecularly impenetrable.

In contrast to previously obtained microcapsules of colloidal particles, so-called colloidosomes [97], the microcapsules observed here are self-assembled without a template. Colloidosomes are formed by adsorbing particles onto a template of emulsion droplets. In the previous paragraph, we verified that no emulsion droplet is present when we study the microcapsules. One might, however, suggest that such a droplet was present during the formation of the microcapsules. The synthesis of the particles involves polymerization of styrene. Consequently, small droplets of unreacted styrene could have served as a template for spherical structures. However, microcapsules are only observed after covalently linking fluoresceinamine onto the particles, and the particles are washed five times by centrifugation before addition of fluoresceinamine. Hence, excess styrene is removed, and when microcapsules are formed, no droplets are present that could serve as a template.

The histogram of the interparticle distances in a microcapsule, shows a maximum at $r_{ij}^* = 0.63\,\mu\text{m}$ (Fig. 5.2n). As expected, r_{ij}^* is between the diameter of the core of the snowman-like particles of 540 nm and their total length of 651 nm. Furthermore, an additional broad peak is observed at $1.9r_{ij}^*$, and another peak at $2.7r_{ij}^*$. These values correspond well to the hexagonally dominated orientation of the particles where peaks are expected at 1, 1.7, 2, and $2.6r_{ij}^*$. The decrease of the height of the peaks can be ascribed to the curvature of the microcapsules. The curvature makes it less likely that pairs with a large interparticle distance are both in focus.

We estimate the number of particles in our microcapsules from optical microscopy images. We measure the outer diameter of the monolayer ring (Fig. 5.2f), resulting in a diameter of the microcapsules $d_\text{m} = 3.7 \pm 0.8\,\mu\text{m}$, where 0.8 is the standard deviation over thirty microcapsules. With an interparticle distance of $0.63\,\mu\text{m}$, this results in about 1.3×10^2 particles per microcapsule (App. 5.D). One might expect the protrusions to point into the microcapsules, and that consequently, the shape of the particles determines the diameter of the microcapsules, d_m (App. Fig. 5.7). This would result in $d_\text{m} \approx 2.2\,\mu\text{m}$ (App. 5.D). The expected diameter for this configuration is thus much smaller than the measured diameter. Moreover, in App. 5.D, we assumed the hydrophilic brush to be fully collapsed, and d_m is

even smaller if the diameter of the core increases due to swelling of the brush. The protrusions are, however, not necessarily pointing into the interior of the microcapsules, as can be observed using reflected light microscopy. We observe that protrusions do not point inwards, but most MAD particles align tangentially to the surface of the microcapsules (Fig. 5.2m).

In order to observe the self-assembled particles in greater detail, the water medium has to be removed as required for scanning electron microscopy. Removing the medium is non-trivial as the microcapsules collapse upon evaporating water (App. Fig. 5.1). This can be explained by the large interfacial tension of water, $\gamma = 72\,\mathrm{mN/m} = 1.8 \times 10^7 k_\mathrm{B}T/\mu\mathrm{m}^2$, where $k_\mathrm{B}T$ is the thermal energy. The collapse of the structures can be prevented by either sintering or freeze drying. By sintering, we follow Dinsmore *et al.* [97] by heating particles above the glass transition temperature of polystyrene, $T_\mathrm{g} = 100\,^\circ\mathrm{C}$ [6, p13-13] (Fig. 5.3a–b). As a result, neighbouring particles partly merge, and the structure strengthens. Alternatively, water can be removed as a vitrified solid. First, we quench a sample in liquid nitrogen, and next, increase the temperature to $-90\,^\circ\mathrm{C}$ under vacuum so that water sublimates (Fig. 5.3k–l). Microcapsules withstand drying using either method.

The orientation of the particles in the dried samples is studied using scanning electron microscopy. Again, most particles are surrounded by six neighbours, while some particles have five neighbours (compare Fig. 5.3d,n * to □). We define a face as a group of particles with a common neighbour. By distinguishing hexagonal and pentagonal faces, we see similarities with a truncated icosahedron (compare Fig. 5.3f to g). A truncated icosahedron has 12 pentagonal faces and 20 hexagonal faces, and is the structure of buckminsterfullerene, soccer balls and many viruses.

The monolayer microcapsules thus resemble microcapsules or *capsids* of icosahedral viruses, but important details are different. Most viruses have an icosahedral symmetry, while helical structures are also common [33, p667]. Similar to our structures, most icosahedral virus capsids consist of identical building blocks that self-assemble into hollow, monolayer microcapsules with pentagonal and hexagonal faces [98]. Unlike virus microcapsules, however, the colloidal microcapsules show no overall icosahedral symmetry. The red hexagons in Fig. 5.3f, for example, should have been pentagons in a perfect truncated icosahedron. Furthermore, in a virus microcapsules, all subunits are in equivalent, or at least similar or *quasi-equivalent* environments [99, 100, p122]. Consequently, each subunit of a virus has a similar number of neighbours. In Fig. 5.3f, however, both particles with five and six neighbours are found. Furthermore, in order for all subunits to have similar

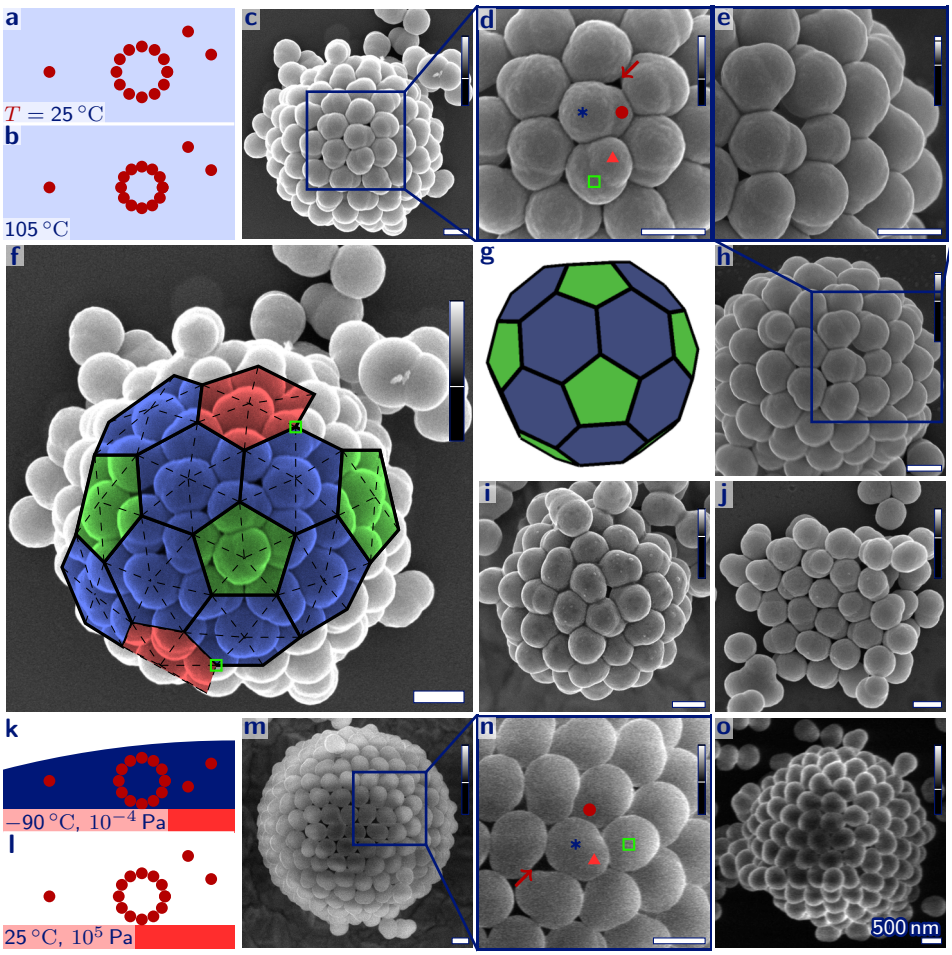

Figure 5.3. Scanning electron microscopy images of self-assembled microcapsules. To prevent disintegration upon drying, microcapsules are studied after sintering (**a–j**) or freeze-drying (**k–o**). Upon sintering, the solvent (●) is heated in order to partly merge the particles (●) (**a–b**). Upon freeze-drying, vitrified water (●) is sublimated on a polymer coated copper grid (●) under vacuum (**k–l**). Particles in the microcapsules have six (**d,n** *) or five (□) neighbours, and interstitial spaces are found between the particles (→). Furthermore, both protrusions that point slightly inwards (●) and outwards (▲) are found. The structure of **c** is compared with a truncated icosahedron (**f–g**). Centres of particles are connected (**f- -**), and local pentagonal (●), hexagonal (●), hexagonal instead of pentagonal (●) and pentagonal instead of hexagonal (□) ordering is indicated. Besides microcapsules, also planar monolayers (**j**) are observed. Image levels are rescaled as indicated by the vertical bars.

environments, the number of subunits per microcapsule should fulfil $N_p = 60T$, where $T = 1, 3, 4, 7, ...$ is the triangulation number [99, 100, p122]. We estimated the number of particles in the colloidal microcapsules, $N_p \approx 1.3 \times 10^2$ (App. 5.D). This could correspond to a structure with similar local environments if the number of quasi-equivalent subunits is 60, i.e. $T = 1$, as $T = 2$ is forbidden. A number of subunits of 60 could be achieved if the snowman-like particles self-assemble as dimers. Fig. 5.3f, however, does not give any indications for the formation of dimers. Furthermore, the large standard deviation of the measured diameters, $d_m = 3.7 \pm 0.8\,\mu m$, suggests that—unlike virus capsids—microcapsules have no well-defined number of subunits.

Using scanning electron microscopy, we can easily distinguish the cores and the protrusions of the particles. As already observed using reflected light microscopy (Fig. 5.2m), the particles align tangentially to the surface of the microcapsules (Fig. 5.3). The polystyrene protrusions are thus in contact with neighbouring particles, which suggests that they are attracted to other protrusions and cores. The protrusions are polymerized with a non-ionic initiator, and should thus have a hydrophobic surface which explains the attraction. Furthermore, most protrusions point slightly towards the interior or towards the exterior of the microcapsules (compare Fig. 5.3d,n ● to ▲).

As discussed before, the particles do not form an impenetrable microcapsule, and indeed, interstitial space is observed between the particles (Fig. 5.3d–n→). The interstitial space in the sintered microcapsules, however, seems to be slightly smaller than in the freeze-dried structures, as the particles partly fill the holes upon heating (compare Fig. 5.3d to n) [97]. By sintering even longer, the interstitial space is expected to decrease further, and the microcapsules might become suitable for molecular encapsulation. Aside from the difference in the size of the interstitial space, the geometry of microcapsules that have been sintered and freeze-dried is similar. This suggests that sintering and freeze-drying do not alter the structure of the microcapsules. The resolution for the freeze-dried images, however, is lower as this sample was not coated with platinum, and consequently became charged.

Particles that self-assemble into microcapsules have three characteristics that we abbreviate as MAD, they are 1) mutually attractive as they are functionalized with hydrophobic moieties, 2) anisotropic due to the presence of a protrusion, and 3) deformable as the hydrophilic brush can change its conformation (Fig. 5.4a). By systematically varying the complexity of the particles, we identify that in our system, these three characteristics are required for self-assembly into microcapsules

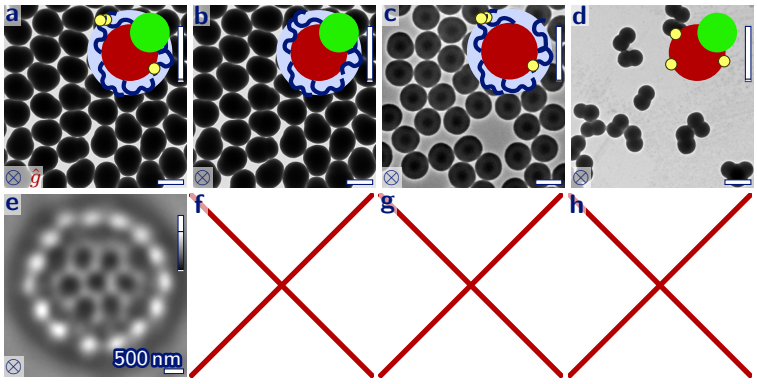

Figure 5.4. Microcapsule formation upon varying the complexity of the particles. The synthesis of MAD particles (**a**) that are functionalized with mutually attractive groups (), anisotropic () and deformable () is modified resulting in non-functionalized particles (**b,f**), isotropic particles (**c,g**) and non-deformable particles (**d,h**). Microcapsules are only found in the first case (**e**). The direction of the gravitational field is indicated by $\hat{g}$ and image levels are rescaled as indicated by the vertical bars.

(Fig. 5.4). First, before functionalization with mutually attractive groups, no microcapsules are found for any of the anisotropic, deformable particles in Fig. 5.5a–c, indicating that mutual attraction is essential in the formation of microcapsules (Fig. 5.4b,f). Second, for similar particles that are functionalized with mutually attractive groups and deformable, but lack a protrusion, also no microcapsules are found (Fig. 5.4c,g). Finally, we study non-deformable particles with a similar geometry as the MAD particles and functionalized with identical hydrophobic moieties. For these non-deformable particles, no microcapsules are observed either (Fig. 5.4d,h), showing that deformability is another requirement. These three characteristics seem sufficient to induce self-assembly into monolayer microcapsules, and are relatively easy to experimentally implement. In contrast, particles with four orthogonally attractive patches, that have previously been predicted to form microcapsules, have not been experimentally realized yet [31] (Fig. 1.1f).

The self-assembling tendency is robust, as microcapsules are found for particles with different sizes and functional groups (Fig. 5.5). We prepare MAD particles with diameters of the cores ranging from $d_c = 353$ to 679 nm (Subsection 2.3.3). Even though the size ratio between the lobes is very different (compare schematics in Fig. 5.5a–d), microcapsules are observed for particles with cores of 353, 540

and 626 nm (Fig. 5.5a–c,j–l). For particles with cores of 679 nm, however, no microcapsules are observed. This can be understood as the particles with $d_c = 540$, 626 and 679 nm are all obtained by swelling deformable spheres with a diameter of 530 nm with additional styrene (Subsection 2.2.4). Consequently, for the largest snowman-like particles, the about 0.1 µm long deformable brush might be covered by polystyrene. Hence, these particles might not be deformable enough to induce self-assembly into microcapsules. Another difference compared to the particles with $d_c = 540$ and 626 nm, is that the rigid protrusion of the particles with $d_c = 679$ nm is much larger than the deformable core (compare schematics in Fig. 5.5b–c to d). Particles with $d_c = 353$ nm, however, have a similar size ratio, and do self-assemble into microcapsules (compare Fig. 5.5a,j to d,n). Additionally, we functionalize snowman-like particles using both fluoresceinamine and *tert*-butylamine. These molecules have very different molecular structures, but the solubility in water is 0.05 g/kg for both fluorescein and isobutane [6, p5-171], where we ignored the amine groups as these react to form covalent bonds. Hence, both moieties have a similar hydrophobicity, and functionalization with either moiety is expected to result in a similar mutual attraction strength. Indeed, coupling fluoresceinamine and *tert*-butylamine both induce the formation of microcapsules (Fig. 5.5l–m).

Besides microcapsules, we also observe other structures and unbound particles. Other well-defined structures we found are planar hexagonal monolayers (Fig. 5.5o–r and Fig. 5.3j), that are very similar to the structures in the previous subsection. The total yield of microcapsules is very low, as only 1 in every 10^4 MAD particles is found in such a structure. The low yield is probably due to the formation mechanism of the microcapsules to be discussed in Subsection 5.3.4.

5.3.3. Cavities At high particle concentrations, MAD particles form curved hollow structures or *cavities*, and presumably, these are intermediates in the formation of microcapsules. The tendency to form cavities is robust, as similar structures are observed at five different experimental conditions. In this subsection we first describe the observations for each experimental condition, before discussing the relation between cavities and microcapsules in Subsection 5.3.4.

The first experimental condition where cavities are found is at the edge of an evaporating droplet on a glass slide (Fig. 5.6a–f). Evaporation of a droplet of particles in water causes a flow of particles towards the glass/water/air contact line that is known as the coffee stain effect [72] (Fig. 5.6a). Consequently, a dense three-dimensional layer is formed near the contact line. For MAD particles,

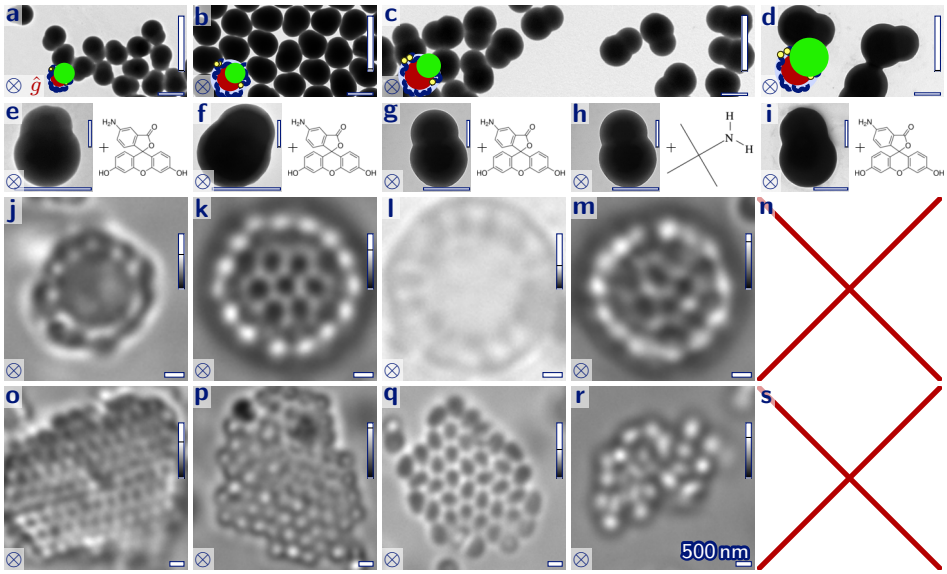

Figure 5.5. Varying the size and functionalization of the building blocks. Transmission electron microscopy images of mutually attractive (●), anisotropic, deformable (∿) (MAD) particles with diameters of the core (●) and the protrusion (●) of 353 and 445 nm (**a,e**), 540 and 435 nm (**b,f**), 626 and 519 nm (**c,g–h**) and 679 and 827 nm (**d,i**). For particles with core diameters of 353, 540 and 626 nm, and upon functionalization with both fluoresceinamine (**j–l,o–q**) and *tert*-butylamine (**m,r**), self-assembled microcapsules (**j–m**) and monolayers (**o–r**) are observed using bright field microscopy. The direction of the gravitational field is indicated by $\hat{g}$ and image levels are rescaled as indicated by the vertical bars.

hemispherical regions with almost no particles, i.e. cavities, are spontaneously formed inside this layer (Fig. 5.6b–f). The second experimental condition where we observe cavities is in an evaporating droplet that is confined between two parallel glass slides (Fig. 5.6g–l). Again, flow is induced towards the contact line, but now a two-dimensional monolayer is formed in which circular cavities are found. Initially, reversible bonds are formed, as we see both the formation and breaking of bonds (compare Fig. 5.6i–j to k). Furthermore, a movie of the time series shows that bound particles at the edge of the layer can still wiggle and rotate their protrusions (Fig. 5.6QR). Further away from the edge of the layer, however, no bonds are broken

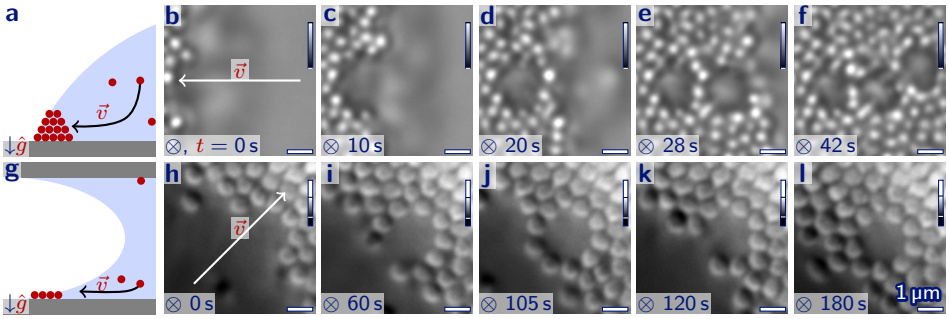

Figure 5.6. Cavity formation near the contact line. At the edge of an evaporating droplet (**a** ●) on a glass slide (●), a flow of particles (●) towards the contact line between the glass, the water and the air (○) is induced that results in a dense three dimensional layer (**a**). For MAD particles, hemispherical regions with almost no particles, so-called cavities, are formed inside this layer (**b–f**, bright field microscopy). For an evaporating droplet that is confined between two glass slides, a monolayer is formed near the contact line (**g**). Inside this monolayer, circular cavities are formed (**h–l**, reflected light microscopy). The direction of the particle flow is indicated by $\vec{v}$ and the gravitational field by $\hat{g}$. The QR code links to a movie of the time series of **h–l** (phd.chrisevers.com/5qr6.mp4).

and less translations and rotations are observed. This can be explained as such translations would require the movement of more particles.

The third experimental condition is at high particle volume fractions, $\phi \approx 0.2$, where a *cavity phase* is formed (Fig. 5.7). In this phase, we observe coexisting regions on the order of 1–10 µm with either high particle concentrations or virtually no particles, i.e. dense curved structures around cavities (Fig. 5.7a). Furthermore, the particles are very mobile, reversible bonds between the particles are formed and break, and consequently cavities form and disappear (Fig. 5.7b–e,QR). We translate the positions of the particles into an effective two-dimensional radial distribution function, $g(r_{ij})$, which we use to estimate the effective interparticle potential, $w(r_{ij})$ (Fig. 5.7f–g). The minimum of the potential corresponds to the strength of the attraction which is about $-0.8 k_B T$ (Fig. 5.7g). This strength corresponds to the formation of reversible bonds, and agrees well with the observations in Fig. 5.7b–e,QR.

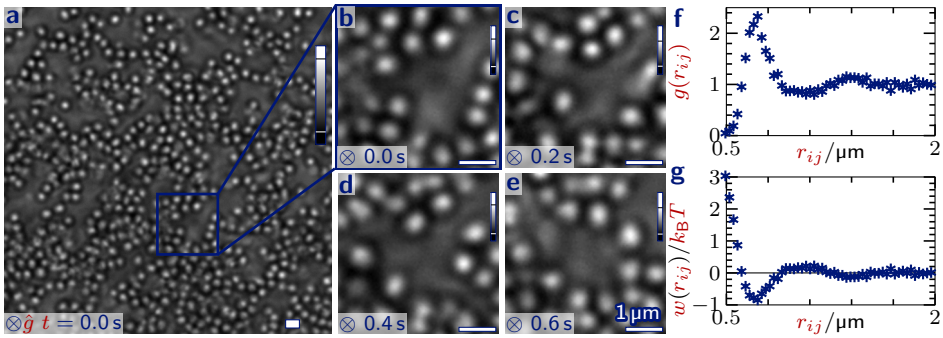

Figure 5.7. Cavity formation at high volume fractions. For MAD particles at a volume fraction of about 0.2, regions with almost no particles, or cavities, are observed (**a–e**, reflected light microscopy). The effective two-dimensional radial distribution function of this cavity phase, $g(r_{ij})$ (**f**), peaks at an interparticle distance, $r_{ij} = 0.73\,\mu\text{m}$, and the corresponding effective pair potential, $w(r_{ij})$ (**g**), has a minimum of $-0.8 k_\text{B}T$. The gravitational field is indicated by $\hat{g}$ and the QR code links to a movie of the time series of **a–e** (phd.chrisevers.com/5qr7.mp4).

The fourth experimental condition in which cavities are observed is upon sedimentation (Fig. 5.8a–f). MAD particles in water are brought in a cell with a height of 5 cm, that was glued on both sides (Fig. 5.8a). We carefully prevented contact between the dispersion and uncured glue, to avoid interactions between monomers in the glue and the MAD particles. Upon leaving the cell undisturbed for a few days, particles sedimented to the bottom of the cell as their gravitational length, $l_\text{g} \approx 50\,\mu\text{m}$, is much smaller than the height of the cell (App. 5.C). By using a cell with a thickness of 20 µm, we can study the concentrated sample using bright field microscopy. In the sediment, we observe bright regions, in a dark background (Fig. 5.8b–c). A high brightness indicates a low particle concentration, and the bright regions corresponds thus to cavities. The cavities have a diameter on the order of 1 µm–10 µm, and are thus smaller than the thickness of the cell. Consequently, dense regions are still present behind or in front of the cavities, and the contrast is poor. To compensate this, we change both the upper and the lower image level thresholds, as indicated by the vertical bars in Fig. 5.8. After centrifugation at $2.1 \times 10^3\,g$, the same position is studied again. The cavities withstand the large centrifugal force (Fig. 5.8d–f and App. Fig. 5.3a). Moreover,

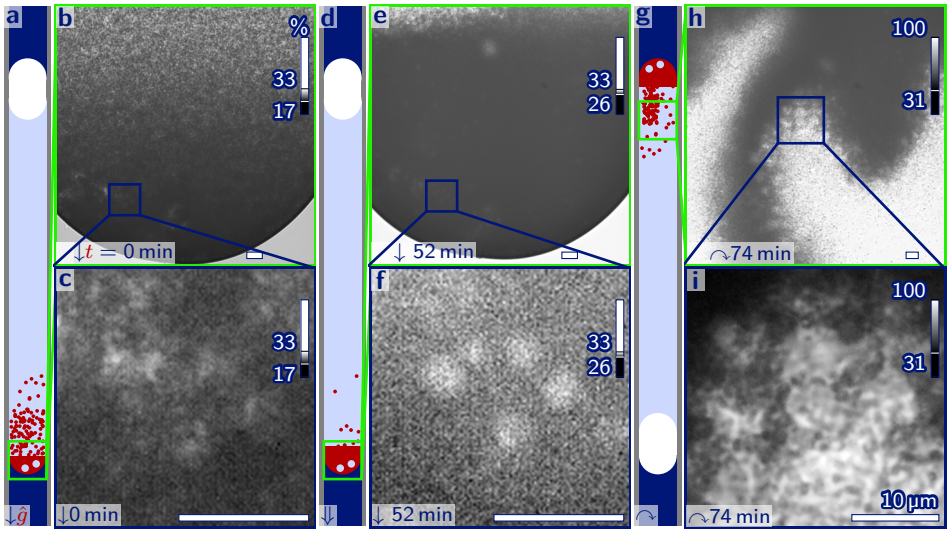

Figure 5.8. Cavity formation upon densification. MAD particles (●) in water (●) are studied using bright field microscopy in a thin cell (●) that is glued on both sides (●). In the earth gravitational field, a sediment is formed in which cavities are observed (**a–c**, bright regions), and these cavities become more spherical after centrifugation (**d–f**). Upon turning the cell upside down (**g–i**), cavities are observed in the diluting sediment. A magnification of **e** can be found in App. Fig. 5.3a, the gravitational field is indicated by $\hat{g}$, and the QR code links to a movie of the time series of **h–i** (phd.chrisevers.com/5qr8.mp4). Both the upper and the lower image level thresholds are changed as indicated by the vertical bars.

they became more spherical and their edges became more well-defined (compare Fig. 5.8c to f). The final experimental condition where cavities are observed is upon diluting the sediment (Fig. 5.8g–i). After turning the cell upside-down, particles move to the bottom of the cell and the density of the sediment decreases. In the diluting sediment, again bright spherical regions are observed that correspond to cavities (Fig. 5.8g–i,QR).

We study the formation of cavities upon varying the complexity of the building blocks, similarly as for the formation of microcapsules in Fig. 5.4. As discussed above, MAD particles are mutually attractive, anisotropic and deformable, and form spherical cavities at the edge of an evaporating droplet, upon centrifugation,

and upon diluting a sediment (Fig. 5.9a,e,i,m,p). Similar particles that are non-deformable or non-functionalized, however, show no cavities (Fig. 5.9b,d,f,h,j,l,n,q), while isotropic particles show fewer cavities (Fig. 5.9c,g,k,o,r). Non-deformable particles lack a hydrophilic brush, and hence stick to the edge of the cell. Consequently, no sediment is obtained (Fig. 5.9h,l), that can be diluted. We conclude that—as for the formation of microcapsules—mutual attraction, anisotropy and deformability all strongly influence the formation of cavities. Furthermore, we observe that both the size of the cavities, as well as their dependence on the complexity of the particles are independent of the experimental conditions (compare rows in Fig. 5.9). Hence, the formation of cavities seems to be driven by densification, while the influence of other effects—such as flow near the contact line in Fig. 5.6—should be small.

5.3.4. Formation Mechanism of Microcapsules We have strong indications that microcapsules do not spontaneously form at low particle concentrations. First of all, the minimum in the effective pair potential between unbound MAD particles is similar to the thermal energy, $k_\mathrm{B}T$ (Fig. 5.7g), and unbound particles do not form lasting bonds upon collision (Fig. 5.7QR). Particles that self-assembled into a microcapsule, on the other hand, are irreversible bounded as no exchange is observed. In the rare occasion that a microcapsule has some vacancies, these vacancies are stable for days (App. Fig. 5.2a–c). Even bonds at the edge of the vacancy, where particles have only two or three neighbours, do not break, and each bond is thus much stronger than $k_\mathrm{B}T$. Additionally, even after days, no vacancy has been filled by an unbound particle (App. Fig. 5.2c). Hence, it seems that a kinetic barrier prevents the formation of irreversible bonds, and thus self-assembly into microcapsules.

More evidence for a kinetic barrier is obtained by taking a closer look at the interparticle distance distribution. For self-assembled particles, this distribution peaks at a 0.1 µm shorter distance than for particles that form reversible bonds (compare Fig. 5.2n to Fig. 5.7f). The difference in the interparticle distance is comparable to the estimated size of the hydrophilic brush which is also about 0.1 µm (App. Table 5.1, App. Fig. 5.6). Hence, it seems plausible that the brush prevents the formation of strong bonds, as it needs to move out of the binding site upon bond formation (Fig. 5.1e). In the microcapsules, the brush seems to have moved out of the way, as the interparticle distance is between the diameter of the core and the total length of the snowman-like particles. Hence, the styrene-rich

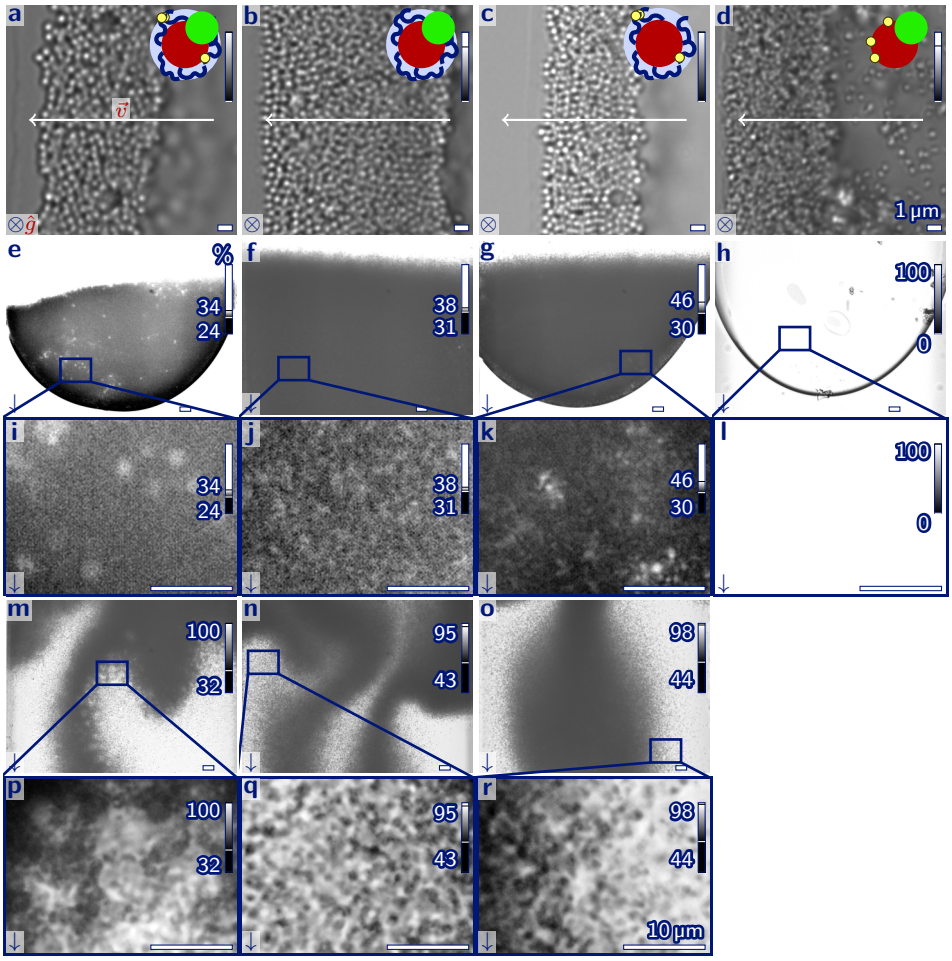

Figure 5.9. Cavity formation upon varying the complexity of the particles. We study mutually attractive, anisotropic, deformable (MAD) particles (**a,e,i,m,p**) and similar non-functionalized (**b,f,j,n,q**), isotropic (**c,g,k,o,r**) and non-deformable particles (**d,h,l**) using bright field microscopy at the edge of an evaporating droplet (**a–d**), in a sediment after centrifugation (**e–l**), and upon diluting the sediment (**m–r**). The entire images of **a–d** can be found in App. Fig. 5.4 and magnifications of **e–g** can be found in App. Fig. 5.3b–d. The direction of the particle flow is indicated by $\vec{v}$, and the gravitational field by $\hat{g}$. For **e–g,i–k,m–r**, both the upper and the lower image level thresholds are changed as indicated by the vertical bars.

cores of the MAD particles are in close proximity and the irreversible bonds are probably the result of hydrophobic or van der Waals forces between the styrene-rich cores.

A kinetic barrier due to the rearrangement of surface groups was previously discussed for Monte Carlo simulations of deformable particles (Fig. 4.6 and 4.9). The simulations also showed that unbound particles do not spontaneously form curved monolayers, even though these monolayers are mechanically stable. In the simulations, many satellite spheres need to reorganize upon bond formation, and that seemed to prevent the formation of new bonds. Similarly, in the experiments, the hydrophilic brush needs to rearrange, and that could prevent the formation of irreversible bonds. The formation of microcapsules requires, besides strong bonds, a specific orientation of many particles. This could be another factor that hinders the formation of microcapsules.

Several observations suggest that the formation of microcapsules and cavities are closely related. First of all, the structures of the cavities and the microcapsules are similar: regions with almost no particles surrounded by a curved region with a high particle concentration. Second, at all five experimental conditions, the diameters of the cavities are comparable to the diameters of the microcapsules. Finally, mutual attraction, anisotropy and deformability all strongly influence the formation of both microcapsules and cavities.

Hence, we propose that microcapsules are formed at high particle concentrations with cavities as intermediates. After coupling mutually attractive moieties onto the brush, the particles are washed by centrifugation to remove unreacted chemicals. Microscopy images show that upon centrifugation, spherical cavities are formed with a similar size and shape as the microcapsules (compare Fig. 5.8f to Fig. 5.2f). Centrifugation thus aligns the particles in a specific microcapsule-like orientation. The second step in the assembly of microcapsules is the formation of irreversible bonds. Centrifugation pushes the particles close together. Consequently, a constant force is present that prefers the hydrophilic brush to move out of the binding site. In the cavity phase of Fig. 5.7, the hydrophilic brush does not have time to rearrange upon collision of two particles. Each centrifugation step, on the other hand, takes about one hour (Subsection 2.2.3), and during this time, the brush should have a significantly greater opportunity to rearrange. Consequently, particles that surround the cavities could form irreversible bonds, and are observed as microcapsules after shaking the sediment to redisperse the particles. Regions with local hexagonal order, on the other hand, are thought to form monolayers,

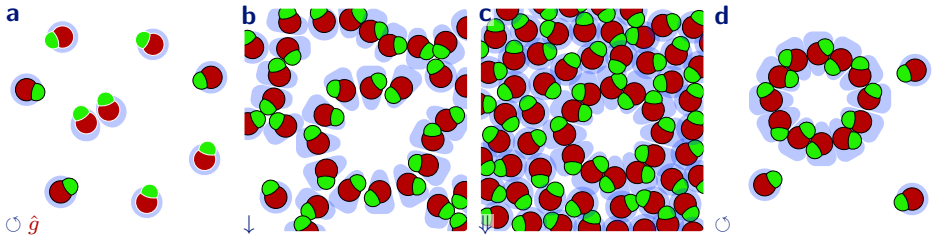

Figure 5.10. Formation mechanism of microcapsules. We propose the following formation mechanism for the microcapsules: unbound MAD particles (**a**) with a core (●) with mutually attractive and deformable surface groups (●) and a rigid protrusion (●) form a cavity phase upon densification (**b**). Upon centrifugation, the particles are pushed into close contact, and irreversible bonds are formed (**c**). Finally, after redispersion, particles that surrounded cavities are found as microcapsules (**d**). The gravitational field is indicated by $\hat{g}$.

whereas randomly oriented regions could form compact clusters. This mechanism also explains the low yield of the microcapsules, as only a few cavities are formed in the sediment (App. Fig. 5.3a). Microcapsules could thus be formed as follows: 1) particles form a dense sediment with cavities (Fig. 5.10b), 2) centrifugation pushes particles closer together and irreversible bonds are formed (Fig. 5.10c), 3) after shaking, particles that surrounded cavities are found as microcapsules (Fig. 5.10d). Additional experiments are, however, necessary to obtain real-space proof of this formation mechanism.

Finally, we compare the observations in this chapter with the results using computer simulations of the previous chapter. For isotropic particles, Monte Carlo simulations showed that mutual attraction and deformability stabilize planar monolayers by colloidal bond hybridization, which agrees well with the observations in Subsection 5.3.1 (compare Fig. 4.6k to Fig. 5.1c–d). Furthermore, simulations showed that adding a protrusion induces a shift from planar to curved structures (Fig. 4.9l–n) that correspond to the microcapsules and the cavities in Fig. 5.3 and Fig. 5.9. Moreover, the hemispherical monolayers with in plane protrusions resemble segments of the experimentally observed microcapsules (compare Fig. 4.9l,QR to Fig. 5.3). At relatively low particle concentrations, we observe in neither simulations nor experiments the formation of monolayers from unbound particles. In both cases, this can be ascribed to the rearrangement of many surface groups that is required to make irreversible bonds. In the simulations, we overcome this barrier by pre-

aligning the MAD particles before we start the simulations, and observe that curved monolayers are mechanically stable. Similarly, in the experiments, the particles are pre-aligned in cavities at high particle concentrations. The formation of the cavities seems a combined effect of mutual attraction, anisotropy and deformability (Fig. 5.9). Here, the protrusion breaks the symmetry of the building blocks, which is probably key in the formation of these structures. This hypothesis agrees well with the curving of initially planar monolayers in simulations of snowman-like particles (Fig. 4.9l–n). In the experiments, cavities are formed at high particle concentrations with a relatively low yield (App. Fig. 5.3a). To verify that mutual attraction, anisotropy and deformability also induces the formation of cavities in simulations would require many particles at a very high concentration, which is computationally quite challenging.

5.4. Conclusion

In this chapter, we translate the mutually attractive, anisotropic and deformable (MAD) nature of self-assembling proteins into colloidal MAD particles. On the one hand, mutual attraction and deformability cause surface groups to rearrange upon binding, which is a colloidal equivalent of bond hybridization; anisotropy, on the other hand, induces curvature. These three characteristics are most likely sufficient to induce self-assembly into monolayer microcapsules, a process that—to the best of our knowledge—had not been realized before in a colloidal model system. This suggests that, while details are different, these properties could be important in the assembly of virus microcapsules as well. Furthermore, the relatively simple MAD particles self-assemble into dramatically more complex structures than similar particles that are isotropic or non-deformable, and the mechanism of the self-assembly is fundamentally different from previous work where anisotropic interactions are induced by rigid patches [26, 28, 29], structural rearrangements upon changing the solvent [101], or electric fields [102]. Quantification of attraction strength, anisotropy, number of particle lobes and deformability lead to a large parameter space that remains to be systematically explored. Independently controlling these properties, however, seems impossible for proteins; colloidal particles, on the other hand, are promising building blocks to address this challenge.

5.5. Acknowledgement

Jurriaan Luiken and Peter Bolhuis are thanked for their collaboration in designing this research and discussing the results. Joris Koek is thanked for exploratory

work on the swelling of deformable particles. Bas van Ravensteijn is thanked for providing non-deformable, fluoresceinamine functionalized snowman-like particles. Sonja Castillo is thanked for taking the scanning electron microscopy images and Hans Meeldijk and Chris Schneijdenberg are thanked for help with freeze drying and transmission electron microscopy. Alfons van Blaaderen, Marjolein Dijkstra and Ernest van der Wee are thanked for useful discussion.

5.A. Appendix Figures and Tables

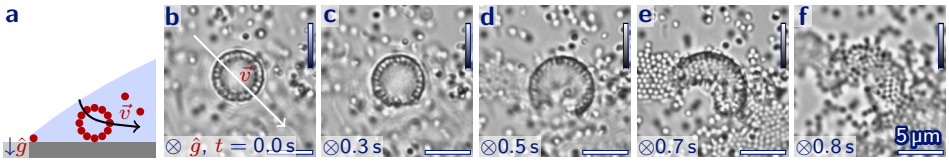

Appendix Figure 5.1. Microcapsules collapse upon evaporation. A microcapsule of MAD particles (**a** ●) near a microscopy slide (●) is observed in an evaporation dispersion droplet with an advancing interface between the water phase (●) and the air (○). Bright field microscopy images (**b–f**) show that the microcapsule collapses (**c–e**) just before the remaining water evaporated as indicated by the change of the brightness of the particles from bright to dark (**e–f**). The gravitational field is indicated by $\hat{g}$ and the direction of the water/air interface by $\vec{v}$.

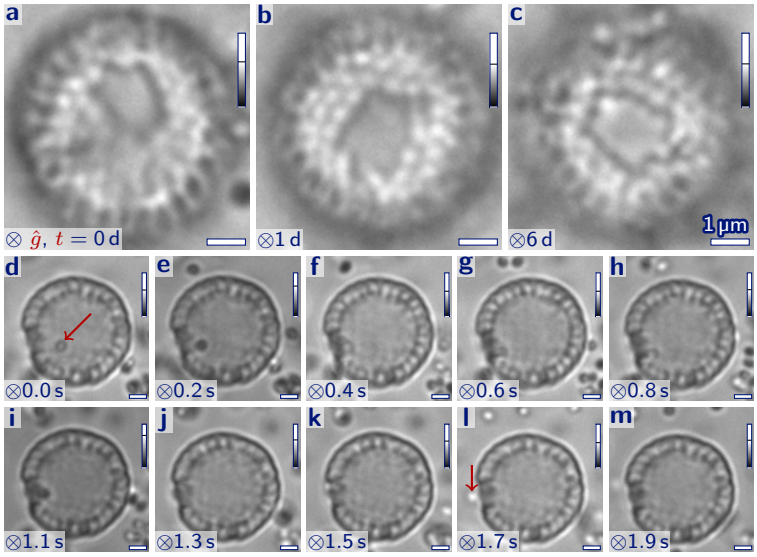

Appendix Figure 5.2. Microcapsule with vacancies. Bright field microscopy images of a microcapsule of MAD particles with vacancies. The positions of the vacancies are identical for days (**a–c**), and an unbound MAD particle (→) in the interior of the microcapsule escapes through the vacancy (**d–m**). The gravitational field is indicated by $\hat{g}$.

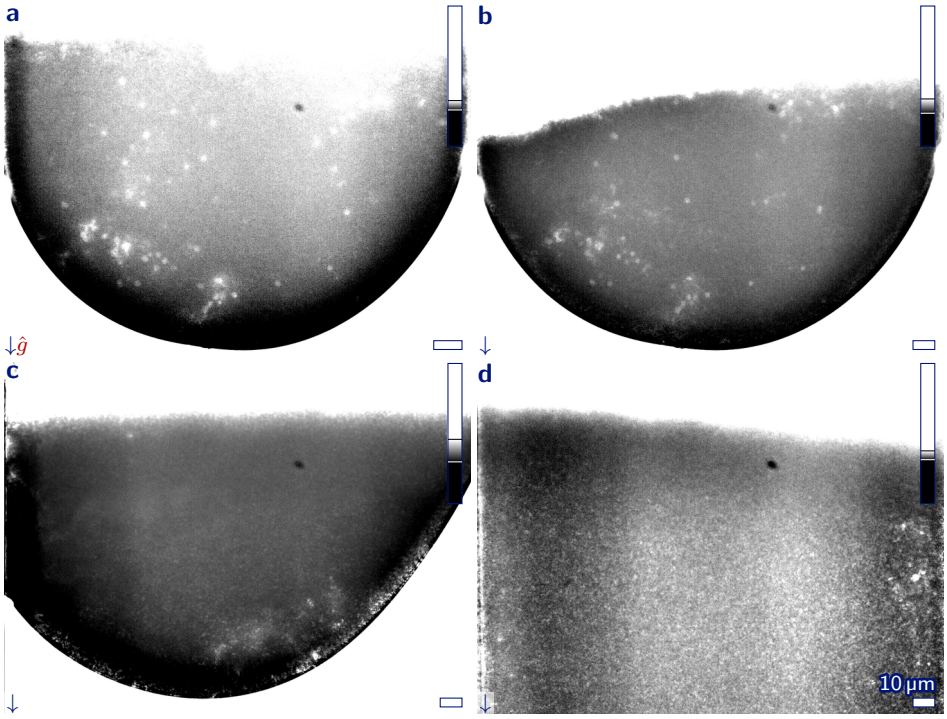

Appendix Figure 5.3. **Centrifuged sediments.** Magnifications of the bright field microscopy images Fig. 5.8e and Fig. 5.9e–g. For MAD particles, spherical cavities are observed in the sediment (**a–b**, bright regions), while the sediments of similar isotropic and non-functionalized particles show less (**c**) and no (**d**) cavities. The gravitational field is indicated by $\hat{g}$.

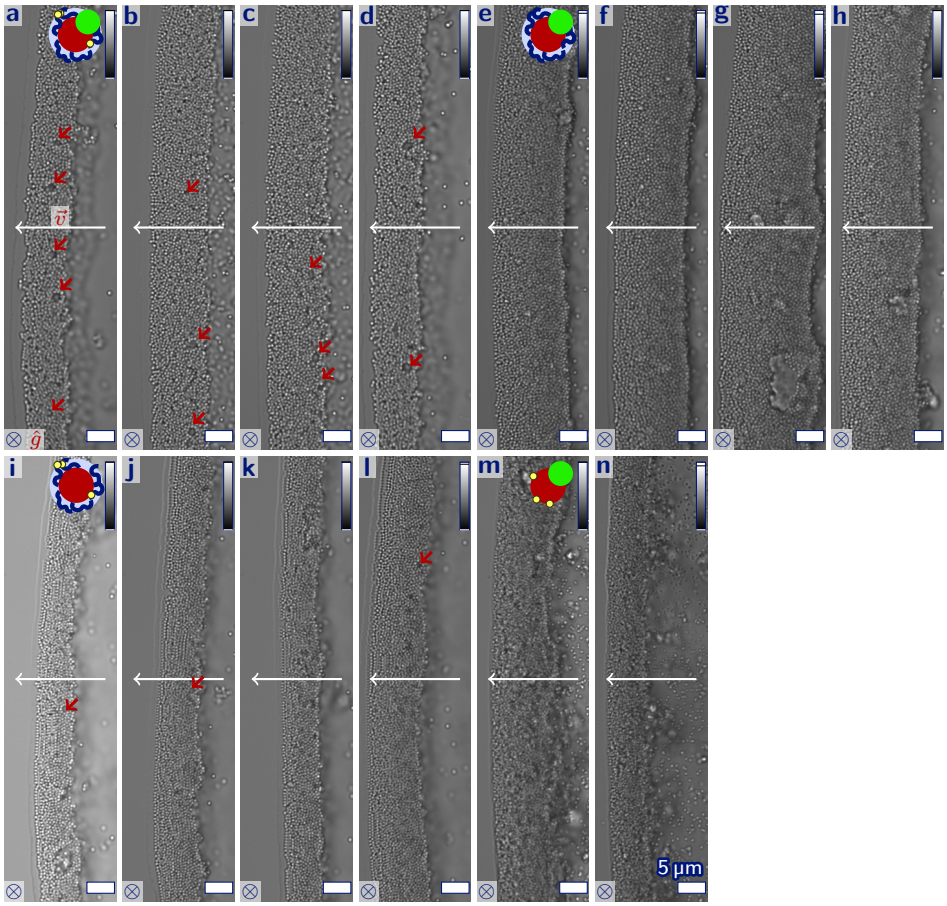

Appendix Figure 5.4. Formation of cavities at the contact line. Evaporating droplets with MAD particles (**a–d**) and similar non-functionalized (**e–h**), isotropic (**i–l**) and non-deformable particles (**m–n**) are studied. For each type, four times (twice for non-deformable particles) a part of the contact line is imaged. Many cavities are found for MAD particles(**a–d** →), while for isotropic particles the number of cavities is significantly lower (**i–l**), and the other particles did not show any cavities (**e–h,m–n**). Crops of these images can be found in Fig. 5.9a–d. The direction of the particle flow is indicated by $\vec{v}$, and the gravitational field by $\hat{g}$.

5.B. Size and Electrostatic Potential of MID particles

The hydrodynamic diameter, d_{hd}, and the zeta potential, ζ, of the particles in Fig. 5.1 are measured and their dependence on the composition of the particles and the medium is studied. We use dynamic light scattering and laser doppler electrophoresis and the results are summarized in App. Table 5.1, while more details can be found in App. Table 5.2.

For cross-linked poly(styrene-*co*-acrylic acid) (CPSAA) spheres, the strength of the mean zeta potential increase from $-40.3\,\mathrm{mV}$ to $-52.2\,\mathrm{mV}$ upon exchanging an acidic 1 mM HCl medium for a basic 1 mM KOH solution (App. Table 5.1). Upon replacing HCl with KOH the H_3O^+ concentration decreases. Consequently, the dissociation equilibrium between acrylic acid and acrylate groups,

$$\mathrm{R{-}COOH} + \mathrm{H_2O} \rightleftharpoons \mathrm{R{-}COO^-} + \mathrm{H_3O^+}, \tag{5.1}$$

shifts to the right. Hence, the number of negatively charged groups on the particles increases upon replacing HCL with KOH, which explains that a more negative zeta potential is measured.

Appendix Table 5.1. Hydrodynamic diameter and zeta potential measurements. The mean, μ, and the polydispersity, σ, in the hydrodynamic diameter, d_{hd}, and the zeta potential, ζ, are measured using dynamic light scattering and laser Doppler electrophoresis. The first value is the average over seven consecutive measurements, and the second value gives the standard deviation. Both cross-linked poly(styrene-*co*-acrylic acid) (CPSAA) and cross-linked polystyrene (CPS) particles are measured in different media.

Particles	Medium	d_{hd}/nm		ζ/mV	
		μ	σ	μ	σ
CPSAA	1 mM HCl	573±6	(15±4)×10^1	-40.3±2.5	4.72±0.20
CPSAA	1 mM KOH	807±10	(21±4)×10^1	-52.2±0.4	5.81±0.18
CPSAA	1 mM HCl/9 mM KCl	578±6	194±17	-25±4	8.2±1.6
CPSAA	1 mM KOH/9 mM KCl	720±12	(23±8)×10^1	-54.9±2.0	9±4
CPS	1 mM HCl	495±13	232±21	-46.8±2.6	5.22±0.26
CPS	1 mM KOH	488±7	205±14	-78.4±0.4	7.42±0.17

We take a closer look at the equilibrium in Eq. 5.1 by defining the acid dissociation constant at logarithmic scale [6, p5-94, 103, p136, 68, p45],

$$\mathrm{p}K_\mathrm{a} \equiv -\log\left(\frac{[\mathrm{H_3O^+}][\mathrm{R{-}COO^-}]}{[\mathrm{R{-}COOH}]\,\mathrm{mol\,l^{-1}}}\right) \iff \frac{[\mathrm{R{-}COO^-}]}{[\mathrm{R{-}COOH}]} = 10^{\mathrm{pH}-\mathrm{p}K_\mathrm{a}}, \qquad (5.2)$$

where $[\mathrm{H_3O^+}]$, $[\mathrm{R{-}COO^-}]$ and $[\mathrm{R{-}COOH}]$ are the concentrations of $\mathrm{H_3O^+}$, of protonated sites, and of deprotonated sites in $\mathrm{mol\,l^{-1}}$, and the concentration and activity of $\mathrm{H_3O^+}$ are assumed to be equal. From the second equation it follows that at $\mathrm{pH} = \mathrm{p}K_\mathrm{a}$, half of the protonatable sites are deprotonated while the other half is protonated. Furthermore, at $\mathrm{pH} \gg \mathrm{p}K_\mathrm{a}$ almost all acid groups are deprotonated and negatively charged, while at $\mathrm{pH} \ll \mathrm{p}K_\mathrm{a}$ almost no groups are charged. For acrylic acid, $\mathrm{p}K_\mathrm{a} = 4.25$ [6, p5-95], which is between the pH values of the HCl and KOH media at $\mathrm{pH} \approx 3$ and 11. Hence, in 1 mM HCl, most acrylic acid groups are expected to be uncharged, while in 1 mM KOH, most acrylic acid groups should be charged. This agrees well with the observation that the zeta potential becomes more negative upon replacing HCl with KOH. Finally, the negative zeta potential for particles in 1 mM HCl arises from sulphonate groups. These are residues of the polymerization initiator and have a $\mathrm{p}K_\mathrm{a}$ of about 2 [6, p5-93]. Hence, the sulphonate groups are negatively charged in both 1 mM HCl and KOH.

Before discussing the dependence of the hydrodynamic diameter on the medium, we take a closer look at the composition of the particles. The particles are synthesized by polymerization of 89 mol-% styrene, 10 mol-% acrylic acid and 0.4 mol-% divinylbenzene, and the polymerization is initiated in the water phase by 0.2 mol-% potassium persulphate (Subsection 2.2.2). Styrene has a solubility of 0.003 M in water, while acrylic acid is miscible with water, and its concentration is 0.11 M [6, p5-185,p3-8]. Hence, initially, mainly acrylic acid is expected to be incorporated in the polymer chains. Once the polymer chains grow longer and become cross-linked by divinylbenzene groups, however, they nucleate and the nucleus swells with styrene. Consequently, in the second step, mainly styrene should be incorporated. Finally, when most styrene has been polymerized, the remaining acrylic acid should be incorporated. The polymers should thus consist of 1) an acrylic acid-rich part 2) a styrene-rich part, and 3) an acrylic acid-rich part. These expectations are in line with infra-red spectroscopy measurements by Wang and Pan [65]. They show that the ratio between the acrylic acid peak and the styrene peak first decreases and subsequently increases as a function of the

reaction time. As acrylic acid-rich parts are more hydrophilic than styrene-rich parts, we expect the acrylic acid-rich parts to form a hydrophilic brush around the styrene-rich core. Finally, the length of the polymer chains is estimated from the molar ratios of the monomers and the initiator, where each initiator molecule is assumed to induce the formation of two polymer chains. This results in about 259 styrene, 30 acrylic acid, and one divinylbenzene groups per chain.

We propose that an expansion of the hydrophilic, acrylic acid-rich brush causes an increase of the hydrodynamic diameter with pH. In 1 mM HCl, the hydrodynamic diameter is 573 nm and slightly larger than the dried diameter of 530 nm (App. Table 5.1). This can be explained because in solution, the hydrophilic brush is swollen with water, and because of the relatively high polydispersity as will be discussed later. Upon exchanging HCl with KOH, pH becomes higher, and the number of charged acrylic acid groups in the hydrophilic brush increases. Consequently, more electrostatic repulsion between charged groups in the brush is induced, the brush swells, and the hydrodynamic diameter increases from 573 nm to 807 nm (App. Table 5.1). The maximum end-to-end distance of a polymer that consists of 30 acrylic acid groups is estimated to be about 60 times the length of a C−C-bond, 9 nm [6, p9-48], where we ignore the influence of bond angles. The extension of a single polymer chain is thus much smaller than the increase in the hydrodynamic radius from 287 to 404 nm. The polymer chains are, however, cross-linked, and the extension of the network is expected to be much larger than the extension of a single chain. Here, the extension of the network should thus be on the order of 10^2 nm.

By increasing the salt concentration, and measuring particles without acrylic acid, we verify that the increase of the size is indeed induced by electrostatic repulsion of acrylic acid groups. Upon adding 9 mM KCl, the total salt concentration or ionic strength, I, increases from 1 mM to 10 mM, and the Debye screening length, κ^{-1}, decreases from 10 nm to 3 nm [7, p134]. Hence, the range of the electrostatic repulsion decreases, and we expect the expansion of the brush to decrease. Indeed, the measured hydrodynamic radius decreases from 807 nm to 720 nm upon increasing I from 1 mM to 10 mM in 1 mM KOH (App. Table 5.1). The increase of the size is thus induced by electrostatic interactions. In 1 mM HCl, on the other hand, the acrylic acid groups are deprotonated, and the hydrodynamic diameter remains virtually constant at 573 nm and 578 nm upon increasing I (App. Table 5.1). Furthermore, for similar cross-linked polystyrene (CPS) particles without acrylic acid, the hydrodynamic diameter remains virtually constant at

495 nm and 488 nm upon exchanging 1 mM HCl with KOH (App. Table 5.1). This indicates that, indeed, acrylic acid groups cause the increase of the size. Hence, we conclude that electrostatic repulsion in the cross-linked, acrylic acid-rich brush causes the increase in the hydrodynamic radius. In other words, the hydrophilic brush can undergo structural rearrangements on the order of 10^2 nm, rendering the particles deformable.

Next, we take a closer look at the zeta potential. With other parameters held constant, the zeta potential of CPSAA is invariably weaker in HCl than in KOH, $-40.3\,\mathrm{mV}$ and $-52.2\,\mathrm{mV}$ at $I = 1\,\mathrm{mM}$ and $-25\,\mathrm{mV}$ and $-54.9\,\mathrm{mV}$ at $I = 10\,\mathrm{mM}$ (App. Table 5.1). This can be explained as the acrylic acid groups have a higher charge in a basic environment than in an acidic environment as we discussed before. Furthermore, increasing the ionic strength for CPSAA in HCl results in a decrease of the strength of the zeta potential from $-40.3\,\mathrm{mV}$ to $-25\,\mathrm{mV}$, whereas the hydrodynamic diameter does not significantly change (App. Table 5.1). This can be explained by taking a closer look at the definition of the zeta potential. The zeta potential is the potential at the so-called slip plane, which is some distance, r_{slip}, from the surface of the particle (App. Fig. 5.5) [7, p429]. Here, the slip plane is defined such that at a distance from the surface $r_{\mathrm{s}} < r_{\mathrm{slip}}$, the fluid flows with the particle, while at $r_{\mathrm{s}} > r_{\mathrm{slip}}$, the fluid does not move with the particle. Upon increasing the ionic strength, the Debye length decreases, and more counter ions are found between the slip plane and the surface of the particle. Hence, the electrostatic potential at the slip plane decreases (compare App. Fig. 5.5— to —), and the strength of the measured zeta potential decreases from $-40.3\,\mathrm{mV}$ to $-25\,\mathrm{mV}$ upon increasing I (App. Table 5.1). Increasing the ionic strength for CPSAA in KOH, on the other hand, results in a slightly stronger zeta potential, i.e. ζ decreases from $-52.2\,\mathrm{mV}$ to $-54.9\,\mathrm{mV}$ (App. Table 5.1). In KOH, the hydrophilic brush is significantly expanded, and the expansion decreases upon increasing the ionic strength. Consequently, the position of the slip plane changes with I. Furthermore, the number of charged groups in the brush also depends on the ionic strength. In the polymer brush, the protonatable sites are close together. Consequently, there is an additional electrostatic energy cost to deprotonated a group close to an already deprotonated group, an effect that is known as charge regulation [104, 105]. Upon increasing the ionic strengths, electrostatic interactions are screened, and it becomes easier for protonated groups to become charged close to already deprotonated groups. The surface potential is thus expected to become more negative upon increasing I. Hence, the Debye length, the position

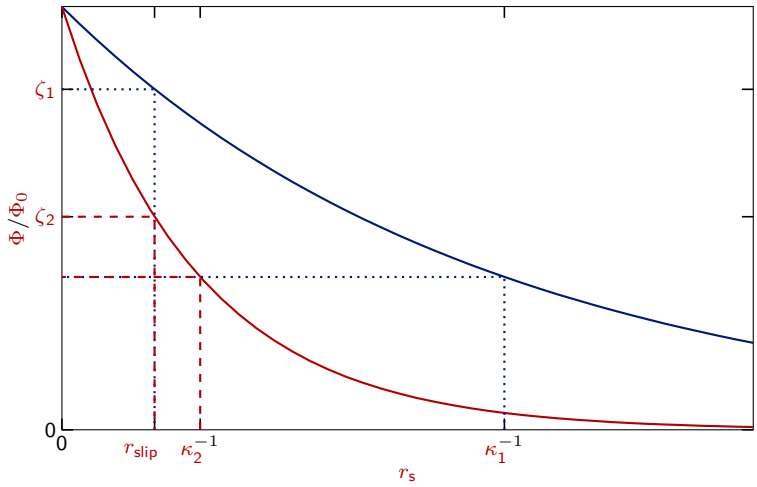

Appendix Figure 5.5. Zeta potential. Schematic representation of the electrostatic potential, Φ, as a function of the distance from the particle surface, r_s. Φ is normalized by the surface potential, Φ_0, and calculated using the Gouy–Chapman theory [7, p138]. The potential at the slip plane, which is at a distance r_{slip} from the surface, is the zeta potential, ζ. At low salt concentrations (—), the Debye length, κ^{-1}, is large and the zeta potential is strong; at high salt concentrations (—), κ^{-1} is small, and ζ is weak.

of the slip plane and the surface potential all change with I. As the measured zeta potential remains almost constant, it seems that these three effects cancel. Finally, for CPS particles, the zeta potential also becomes more negative upon replacing HCl with KOH, and decreases from −46.8 nm to −78.4 nm. Similarly as for acrylic acid groups in the brush, deprotonation of sulphonate groups close to already deprotonated groups is energetically expensive, and not all sulphonate groups are expected to be deprotonated in 1 mM HCl. Upon replacing HCl with KOH, however, the dissociation equilibrium (similar as in Eq. 5.1) shifts further to the right, and the number of deprotonated sulphonate groups increases. This could thus explain the more negative zeta potential upon replacing HCl with KOH.

Finally, the polydispersity, σ, in the hydrodynamic diameter is about 2×10^2 nm in all media (App. Table 5.1) and much larger than the polydispersity measured from transmission electron microscopy images, $\sigma = 15$ nm (Subsection 2.3.1). This is probably due to cluster formation, which is observed without added salt in Fig. 5.1.

Upon adding salt, even more clustering is expected, as the electrostatic repulsion is more screened. The measured hydrodynamic diameter is expected to increase when clusters are formed. In 1 mM HCl, however, d_{hd} is only 50 nm larger than the dried diameter, which is partly due to swelling of the hydrophilic brush of water. The effect of clusters on the mean values should thus be low. For CPSAA, σ is higher in KOH than in HCl. The dimensionless polydispersity index, $\mathrm{PdI} = (\sigma/\mu)^2$ (App. Table 5.2), however, does not significantly change upon replacing KOH with HCl. The polydispersity increases thus because the particles become larger, and not because of an increase in the number of clusters. Upon increasing the ionic strength, however, PdI increases. This can be explained, as electrostatic repulsions become more screened, resulting in a decrease of the stabilization of the particles. The mean hydrodynamic radius, however, does not significantly increase with I in 1 mM HCl, and decreases with I in 1 mM KOH due to the decrease of the size of the brush (App. Table 5.1). Consequently, the influence of the formation of clusters is much smaller than the influence of the swelling of the brush. Furthermore, the formation of clusters resists the observed trends in the hydrodynamic diameter, and the actual increase of the size of the brush might thus be even larger. Additionally, the trends in the measured values are low (App. Table 5.2), which also suggests that the influence of the formation of cluster is small. For some zeta potential measurements, the trends in both the mean zeta potential, and the count range are larger than 1% (App. Table 5.2). Probably, the electric field, that needs to be applied in laser Doppler electrophoresis measurements, affects the particles, resulting in trends in the measured zeta potential. For cross-linked poly(styrene-*co*-acrylic acid) (CPSAA) spheres in 1 mM KOH/9 mM KCl, the dispersion contained gas bubbles after analysis and the last two zeta potential measurements clearly deviated. The reported values are thus obtained from the first five measurements.

To study the pH dependence in more detail, samples are prepared at 1 mM KOH, and measured while 1 mM HCl is added stepwise. Consequently, $[\mathrm{K}^+]$, decreases with the same rate as $[\mathrm{Cl}^-]$ increases. Added H^+, however, reacts with OH^- into $\mathrm{H_2O}$ with [68, p46],

$$[\mathrm{H}^+][\mathrm{OH}-] = 1.0 \times 10^{-14}\,(\mathrm{mol/l})^2. \tag{5.3}$$

Hence, without any other added salt, the initial ionic strength, I_0 is 1 mM, I goes through a minimum of 0.5 mM at pH 7 and finally I increases again. The corresponding Debye lengths are 10 nm and 14 nm [7, p134]. Upon adding KCl,

however, initially $I_0 = 10\,\mathrm{mM}$, while the minimum is $I = 9.5\,\mathrm{mM}$ and the Debye length is about 3 nm in both cases. In the previous measurements we noted that the applied electric field required for zeta potential measurements eventually seems to disturb the sample. Hence, only the hydrodynamic radius is measured as a function of pH.

For CPSAA spheres with $I_0 = 1\,\mathrm{mM}$, the mean hydrodynamic diameter decreases from 787 nm at pH 9.75 to 568 nm at pH 3.80 (App. Fig. 5.6∗), which agrees well to the results in App. Table 5.1. The hydrodynamic diameter decreases gradually with pH. The steepest decrease is at pH ≈ 8, while the diameter is more or less stable at pH < 6. This might seem surprising as pK_a of acrylic acid is 4.25. As discussed before, however, electrostatic repulsion prevents deprotonation of all groups in the charged brush. Hence, already at pH ≈ 10, a decrease of pH results in less protonated groups, which explains the observed decrease of the hydrodynamic radius (App. Fig. 5.6∗). Upon decreasing pH further, the number of charged groups becomes gradually lower, and the distance between the charges increases. Finally, at pH < 6, the distance between the charged groups seems to be so large, that electrostatic repulsion does not expand the brush any more (App. Fig. 5.6∗). The salt concentration decreases upon decreasing pH from 10 to 7 (Eq. 5.3), and a decrease in the salt concentration results in an increase in the hydrodynamic diameter (App. Table 5.1). If the salt concentration would have been constant at all pH values, the decrease of the measured hydrodynamic diameter with pH (App. Fig. 5.6∗), might thus have been steeper.

Finally, upon increasing the ionic strength, the dependence of the hydrodynamic diameter on pH is much smaller (App. Fig. 5.6●), and for CPS spheres, d_hd is virtually constant (App. Fig. 5.6□). Both observations agree well with results in App. Table 5.1. The polydispersity index, PdI, on the other hand, is—excluding a few outliers—constant with pH for all three cases, indicating that the influence of cluster formation is again low.

In this appendix, we measured the hydrodynamic diameter and the zeta potential of spherical particles upon varying the composition of the particles and the medium, and explained our observations using physical chemical theory. Based on these observations, we conclude that the cross-linked poly(styrene-*co*-acrylic acid) spheres of Fig. 5.1 have an acrylic acid-rich brush, that can expand on the order of 0.1 µm into the solution.

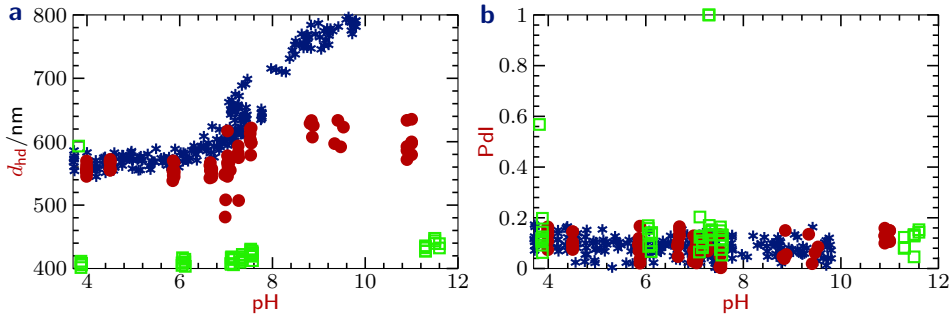

Appendix Figure 5.6. pH dependence of the hydrodynamic diameter. For cross-linked poly(styrene-*co*-acrylic acid) (CPSAA) and cross-linked polystyrene (CPS) spheres, the hydrodynamic diameter, d_{hd} (**a**), and the polydispersity index, PdI (**b**), are measured as a function of pH. CPSAA spheres are dispersed in a 1 mM (*) and a 10 mM (●) salt solution, while CPS spheres are measured in a 1 mM salt solution (□).

5.C. Gravitational Length

The competition between Brownian motion and gravity can be expressed using the gravitational length [88, p1],

$$l_g = \frac{k_B T}{N_p m g} = \frac{k_B T}{N_p(\rho_p - \rho_m)V g}, \tag{5.4}$$

where $k_B T$ is the thermal energy, N_p is the number of particles in a cluster, m is the effective mass of a particle, g is the gravitational acceleration, ρ_p and ρ_m are the densities of the particles and the medium, and V is the volume of a particle. Furthermore, if $\rho_p > \rho_m$, $l_g > 0$ and the particles sediment, while if $\rho_p < \rho_m$, the particles cream. The density of polystyrene is 1.06–1.12 g cm^{-3} [6, p15-93], while the density of water is 1.00 g cm^{-3} [6, p4-98]. The volume of a snowman-like particles with $d_c = 540$ nm, $d_p = 435$ nm and $r_{cc} = 163$ nm is $V = 0.096\,\mu m^3$ (Eq. 3.9). Hence, for a single particle, $l_g \approx 49\,\mu m$, while for a microcapsule of about 100 particles (App. 5.D), $l_g \approx 0.5\,\mu m$.

5.D. Number of Particles per Microcapsule

We estimate the number of particles per microcapsule using two methods: 1) using optical microscopy measurements and 2) from the geometry of the particles.

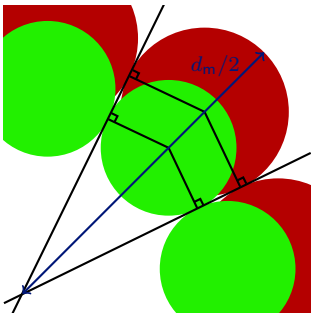

Appendix Figure 5.7. Predicting the size of a microcapsule from the geometry of its building blocks. The diameter of a microcapsule, d_m, with close contact between neighbouring cores (●) and between neighbouring protrusions (●), is determined from the intercept of the common tangents of the core and the protrusion.

Using the first method, the number of particles per microcapsule is estimated from the distance between particles in microcapsules and the diameter of the microcapsules. We take the distance between neighbouring particles from the first peak in the interparticle distance histogram for particles in a microcapsule, $r_{ij}^* = 0.63\,\text{nm}$ (Fig. 5.2n). The mean diameter of the microcapsules is obtained from Hough circle transformations of 30 microcapsules following Subsection 3.2.3, $d_m = 3.7 \pm 0.8\,\mu\text{m}$. If we assume that the particles are oriented hexagonally and cover the entire surface of the microcapsules, we obtain for the number of particles per microcapsule [82, p1366],

$$N_p = \frac{\pi {d_m}^2}{(\sqrt{3}/2){r_{ij}^*}^2} \approx 125, \tag{5.5}$$

where we divided the estimated surface area of a microcapsule by the surface area per particle.

Using the second method, we assume that the shape of the snowman-like particles determines the size of the microcapsules (App. Fig. 5.7). For a particle with a core of diameter, $d_c = 540\,\text{nm}$, a protrusion with diameter, $d_p = 435\,\text{nm}$, and distance between the centres of the core and the protrusion, $r_{cc} = 163\,\text{nm}$, the intercept of the common tangents of the protrusion and the core gives $d_m = 2.2\,\mu\text{m}$. We obtain the number of particles for a microcapsule with this geometry by inserting this value and $r_{ij} = d_c = 540\,\text{nm}$ into Eq. 5.5, resulting in $N_p = 61$.

Appendix Table 5.2. Hydrodynamic diameter and zeta potential. The mean, μ, and the polydispersity, σ, in the hydrodynamic diameter, d_{hd}, and the zeta potential, ζ, are measured using dynamic light scattering and laser Doppler electrophoresis. The polydispersity index, PdI, is calculated from μ and σ in the hydrodynamic diameter and for each measurement, the derived count rate is given in thousand counts per seconds. The first value is the average over seven consecutive measurements, the second value gives the standard deviation and the value in brackets is the trend. Both cross-linked poly(styrene-*co*-acrylic acid) (CPSAA) and cross-linked polystyrene (CPS) particles are measured in different media.

Particles	Medium	d_{hd}/nm	
		μ	σ
CPSAA	1 mM HCl	573±6 (+0.25%)	(15±4)×10^1 (+1.7%)
CPSAA	1 mM KOH	807±10 (+0.10%)	(21±4)×10^1 (+2.7%)
CPSAA	1 mM HCl/9 mM KCl	578±6 (-0.08%)	194±17 (+3%)
CPSAA	1 mM KOH/9 mM KCl	720±12 (-0.23%)	(23±8)×10^1 (+4%)
CPS	1 mM HCl	495±13 (+0.25%)	232±21 (+1.6%)
CPS	1 mM KOH	488±7 (-0.4%)	205±14 (+0.4%)

Particles	Medium	PdI	Derived count rate (kcps)
CPSAA	1 mM HCl	0.07±0 .04 (+3%)	(63.7±1 .0)×10^3 (+0.7%)
CPSAA	1 mM KOH	0.073±0 .025 (+5%)	(58.7±1 .2)×10^3 (-0.19%)
CPSAA	1 mM HCl/9 mM KCl	0.114±0 .021 (+6%)	(627±6)×10^2 (+0.03%)
CPSAA	1 mM KOH/9 mM KCl	0.12±0 .06 (+8%)	(577±4)×10^2 (+0.21%)
CPS	1 mM HCl	0.220±0 .028 (+2.7%)	(277±4)×10^2 (+0.4%)
CPS	1 mM KOH	0.177±0 .024 (+1.6%)	(54.7±1 .5)×10^3 (-1.0%)

Particles	Medium	ζ/mV	
		μ	σ
CPSAA	1 mM HCl	-40.3±2.5 (+2.8%)	4.72±0.20 (+0.17%)
CPSAA	1 mM KOH	-52.2±0.4 (+0.12%)	5.81±0.18 (-0.8%)
CPSAA	1 mM HCl/9 mM KCl	-25±4 (+4%)	8.2±1.6 (-0.7%)
CPSAA	1 mM KOH/9 mM KCl	-54.9±2.0 (+0.11%)	9±4 (+20%)
CPS	1 mM HCl	-46.8±2.6 (+2.2%)	5.22±0.26 (-0.7%)
CPS	1 mM KOH	-78.4±0.4 (+0.10%)	7.42±0.17 (-0.3%)

Particles	Medium	Derived count rate (kcps)
CPSAA	1 mM HCl	(19.7±2 .5)×10^4 (+1.1%)
CPSAA	1 mM KOH	(17±5)×10^4 (+10%)
CPSAA	1 mM HCl/9 mM KCl	(15.2±2 .9)×10^4 (-1.9%)
CPSAA	1 mM KOH/9 mM KCl	(15±6)×10^4 (+14%)
CPS	1 mM HCl	(8.0±1 .1)×10^4 (-1.2%)
CPS	1 mM KOH	(11.8±2 .5)×10^4 (-0.3%)

Part III

Colloids in Near-Critical Mixtures

6

Pickering-like Emulsions by Thermoreversible Attachment of Colloids onto Near-Critical Interfaces

Abstract

Emulsions are ubiquitous in consumer and industrial products. Their formation usually requires high shear and tuning their stability commonly involves changing particles or adding chemicals. Here, we use temperature to induce emulsification and control stability. We study near-critical mixtures of liquids with lower phase-separation temperatures. Below these temperatures, the liquids are fully miscible, while above these temperatures, two coexisting phases with temperature-dependent compositions are formed. Hence, the properties of this system are easily tunable, and as a consequence, colloidal particles thermoreversibly attach onto the interface between the phases. We make use of this property to create and destabilize Pickering-like emulsions by changing the temperature. Finally, we prepare hollow shells by simply heating followed by cooling.

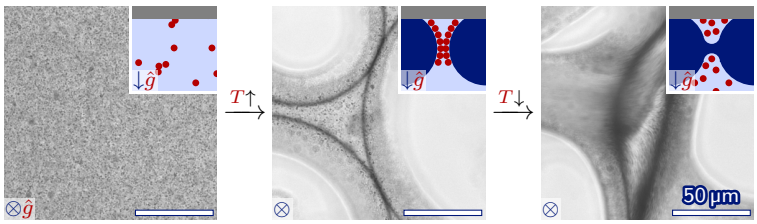

6.1. Introduction

An emulsion is a mixture of two immiscible liquids that is kinetically stabilized by an emulsifier. Emulsions are found in many foods, cosmetics and pharmaceuticals, and usually, droplets of oil are dispersed in water or the other way around [56, 106]. Merging or *coalescence* of droplets is commonly prevented by surfactants, polymers or solid particles [7, p539]. In the latter case, a so-called Pickering emulsion is formed [53, 54]. These emulsion are kinetically stable as particles attach onto the surface of droplets, and hence molecular contact between the droplets is prevented [7, p577]. The stability of a Pickering emulsion depends strongly on the attachment energy of particles onto the interface and is generally tuned by changing either the size and surface properties of the particles, or by adding salt or surfactants to the liquids [55, 56, 57, 58]. The preparation of an emulsion requires the formation of interfacial areas, for which energy is typically provided by turbulent flow-induced shear [7, p569-575]. Other emulsification techniques require a chemical non-equilibrium state, and even spontaneous formation of thermodynamically stable Pickering emulsions and so-called microemulsions has been described [7, p550, p573-574, 107].

In this chapter, we create emulsion droplets by temperature-induced phase separation, and stabilize the droplets by thermoreversible attachment of particles onto their surface. For this purpose, we use partially miscible liquids with lower and upper phase separation temperatures. Between these temperatures, phase separation occurs, while below the lower and above the upper phase separation temperature, the liquids are fully miscible. The phase separation temperatures depend on the composition of the liquid and were previously determined for the mixtures used in this chapter (Fig. 6.1a). The phase separation temperatures form a closed loop in which the two components phase separate. Furthermore, at the top and the bottom of each loop, critical points are found (Fig. 6.1b*). Close to a critical point, a temperature change of a few degrees results in a significant change in the compositions of the coexisting phases (compare Fig. 6.1b— to —). Similar mixtures have previously been used to induce the formation of bicontinuous Pickering emulsions, so-called bijels [108, 109]. In bijel formation, quenching deep into the closed loop results in spinodal decomposition. At the bottom of the closed loop, however, near-critical phenomena occur. To the best of our knowledge, the effect of near-critical behaviour on Pickering emulsions, and more specifically, on the attachment of particles onto interfaces has not been studied yet.

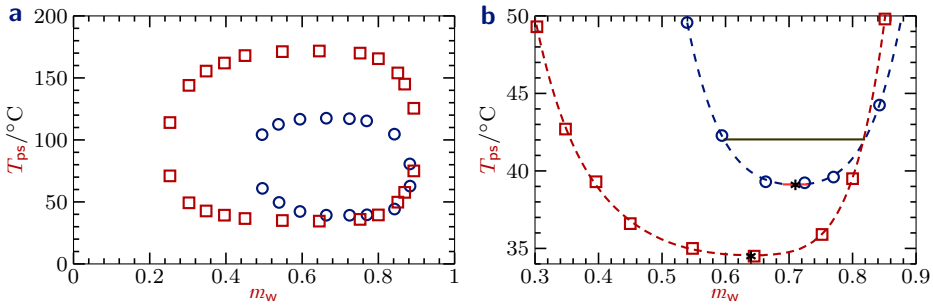

Figure 6.1. Phase separation of partially miscible mixtures. Phase separation temperatures, T_{ps}, as a function of the mass fraction of heavy or normal water, m_w, for mixtures of 3-methylpyridine and heavy water (3MP/D_2O ○ Cox [110]) and 1-propoxy-2-propanol and normal water (PnP/H_2O □ Cox *et al.* [111]). The mixtures have both lower and upper phase separation temperatures (**a**), between which the liquids phase separate into a water-poor and a water-rich phase. Outside this closed loop, on the other hand, the liquids are fully miscible. Close to the lower critical points (**b** ∗), the composition of each phase depends strongly on the temperature. This is illustrated for 3MP/D_2O at $m_w = 0.69$. At the lower phase separation temperature, the mixture phase separates into phases with similar compositions (—), while at higher temperatures, the difference in the composition increases (—). The dashed lines are fits to fourth (- -) and sixth (- -) order polynomials resulting in critical points at $m_w = 0.71$ and $T^* = 39.1\,°C$, and $m_w = 0.64$ and $T^* = 34.5\,°C$ (∗).

This chapter consist of three parts. First, we verify that close to the critical point, the interfacial properties of phase-separated droplets can be tuned by the temperature. Next, we add colloidal particles and observe thermoreversible attachment of colloids onto the surface of the droplets. We propose two explanations for this behaviour, that are discussed using theory on near-critical phenomena. Finally, when the surface of the droplets is covered by colloids, coalescence is prevented. Consequently, Pickering-like emulsion form upon increasing the temperature, and are destabilized when the particles detach from the surface upon decreasing the temperature. In contrast to conventional methods, that create emulsions by shear and control their stability by exchanging particles or adding chemicals, we simply change the temperature to create and control Pickering-like emulsions. Finally, we demonstrate that this approach can also be used to form hollow shells through merely heating and cooling particles in a near-critical mixture.

6.2. Methods

6.2.1. Chemicals The following chemicals were used as received: fluorescein sodium salt (F6377), 3-methylpyridine (3MP, 236276, ≥99.5%), 1-propoxy-2-propanol (PnP, 424927, 99%), and rhodamine B (R6626, ≥95%) were obtained from Sigma-Aldrich or its subsidiaries; deuterium oxide (heavy water, D_2O, DLM-4-1000. 99.9%) was obtained from Cambridge Isotope Laboratories; Millipore water (H_2O) was obtained with a Synergy water purification system.

6.2.2. Sample Preparation Samples of colloidal particles in near-critical mixtures were prepared in thin glass cells. Cross-linked polystyrene particles with a diameter of 524 ± 44 nm were prepared as described in Subsection 2.2.2 and washed by centrifugation. Dispersions were obtained by mixing weighed amounts of either 3MP, D_2O and colloids washed in D_2O; or PnP, H_2O and colloids washed in H_2O. After vortexing the dispersions (Labotech TMO1), $0.05 \times 0.5 \times 50\,\mathrm{mm}^3$ glass tubes (VitroCom 5005-050) were filled by capillary action. Next, both ends of the tubes were sealed first in a flame (Prodont Holliger Microtorch II) and next with glue droplets (Norland NOA81) that were cured with a UV lamp (UVP UVGL-58).

6.2.3. Microscopy Unless stated otherwise, samples were studied with a Nikon Ti-U inverted optical microscope in bright field mode. The microscope was operated with Plan Fluor ELWD 40×/0.60 (Fig. 6.2, 6.3 and 6.6a–i) and CFI Plan Fluor 60×/0.70 (App. Fig. 6.4) objectives, no intermediate magnification, and a Lumenera Infinity X camera. Samples were fixated with adhesive tape on a Linkam THMS600 heating stage that was operated with a Linkam TP 93 controller. We report the temperature of the heating stage relative to the temperature at which phase separation is observed, $\Delta T_{\mathrm{ps}} = T - T_{\mathrm{ps}}$.

App. Fig. 6.4 is obtained using snowman-like particles with a core of diameter 679 nm (Subsection 2.3.3) and a Linkam FTIR 600 heating stage. Fig. 6.6k is obtained using a purpose-built heating stage that caused no temperature gradient in the imaging plane (App. Fig. 6.1c–d). A Peltier element (Quick-Cool, QC-18-0.6-1.2M) was mounted on a $2.2 \times 3.0 \times 1.3\,\mathrm{cm}^3$ metal block that acted as a heat reservoir. Temperature was controlled by a stepwise variable resistor (Dr. C.E. Bleeker NV) between the power source (Delta Elektronika E 018-0.6 D) and the Peltier element. The Peltier controller (Quick-Cool, QC-PC-CO-CH1 with a Altai HEP-613 power source) was set to 100% and used to measure the temperature at the heat reservoir. A Nikon Ti-E inverted optical microscope with a Nikon CFI Plan Fluor 40×/0.75 objective, no intermediate magnification, and a Hamamatsu ORCA Flash camera was used for imaging. As the absence of a hole in the heating stage made bright field microscopy impossible, samples were studied using reflected light microscopy, with a Nikon Intensilight C-HGFI light source and a Nikon

D-FLE filter block. Finally, transmission electron microscopy images were obtained as described in Subsection 2.2.5.

6.2.4. Contact Angle Measurements The contact angle, θ_c, is the angle between two interfaces at the three-phase contact line (Fig. 6.2d). If one of the phases is a solid, the Young equation gives the contact angle between 1) the interface of the solid and the dispersed phase, and 2) the interface of the continuous and the dispersed phase [7, p.53-55],

$$\theta_c = \cos^{-1}\left(\frac{\gamma_{sc} - \gamma_{sd}}{\gamma_{cd}}\right), \tag{6.1}$$

where the interfacial tensions are between a) the solid and the continuous phase, γ_{sc}, b) the solid and the dispersed phase, γ_{sd}, and c) the continuous phase and the dispersed phase, γ_{cd}.

The contact angles of droplets that attach to the edge of a cell were determined by optical microscopy. We studied the droplets in bright field mode, where light passes through the entire thickness of the sample, and for each droplet, two concentric circles were observed (Fig. 6.2a–c). The radius of the outer circle corresponds to the radius of the droplet, R_d, while the radius of the inner circle corresponds to the radius of the circular three-phase contact line, R_c (Fig. 6.2d). These radii were measured using Olympus analySIS FIVE, and the contact angle, θ_c, between the glass, the continuous phase and the dispersed phase was calculated (Fig. 6.2d),

$$\theta_c = \cos^{-1}\left(\frac{R_d}{R_c}\right) + 90°. \tag{6.2}$$

6.3. Results and Discussion

6.3.1. Near-Critical Phase-Separated Mixtures We study phase-separated mixtures of 3-methylpyridine and heavy water (3MP/D_2O) using optical microscopy. 3MP and D_2O are partially miscible: they mix at room temperature, and phase separate above the lower phase separation temperature, T_{ps}. The phase separation temperature depends on the mass fraction of water, m_w, and above T_{ps}, droplets nucleate, and subsequently grow by coalescence and presumably Ostwald ripening. We measure the temperature of the heating stage at which phase separation is observed, $T_{ps} = 40.0\,°C$, for a mass fraction of heavy water, $m_w = 0.69$. Fitting the previously measured phase separation temperatures (Fig. 6.1b- -), however, shows that $T_{ps} = 39.1\,°C$ at $m_w = 0.69$. The temperature of the heating stage is generally slightly higher than the temperature inside the measurement cell due to cooling by

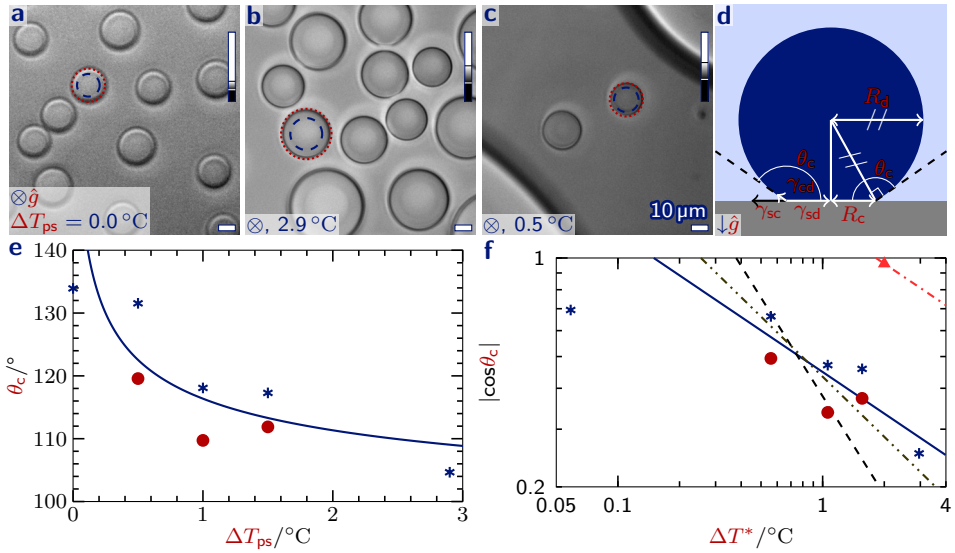

Figure 6.2. Near-critical phase-separated mixtures. Microscopy images of a 3MP/D_2O mixture with mass fractions of water of 0.69 (**a–c**). At or above the lower phase separation temperature, $\Delta T_{ps} \geq 0$, droplets are formed that attach to the glass wall of the cell. The contact angle, θ_c, depends on the interfacial tensions between 1) the solid glass (**d** ●) and the continuous phase (●), γ_{sc}, 2) the solid glass and the dispersed phase (●), γ_{sd}, and 3) the continuous phase and the dispersed phase, γ_{cd}. θ_c can be obtained from the radius of the droplet, R_d (**a–c** - -), and the radius of the contact circle, R_c (**a–c** ·····). The contact angle decreases upon increasing ΔT_{ps} (**e** ∗), and increases upon decreasing ΔT_{ps} again (e ●). The absolute value of the cosine of the contact angle $|\cos\theta_c|$ is fitted as an exponential function of the temperature relative to the critical temperature, $\Delta T^* = T - T^*$ (**f** —), and for a fixed exponent of -1 (- -) and -0.61 (-·-). Finally, a fit through 164° at $\Delta T^* = 2\,°C$ (▲) with the same exponent as — is given (-·-). To increase contrast, image levels are rescaled as indicated by the vertical bars and rhodamine B is added. The direction of the gravitational field is indicated by $\hat{g}$.

surrounding air. To minimize the deviation between the temperature of the heating stage and the temperature of the sample, we report the measured temperature relative to the temperature at which phase separation is observed, $\Delta T_{ps} = T - T_{ps}$.

The contact angle of phase-separated droplets is determined from the microscopy images. Droplets are observed in a thin glass cell and attach to the edge of the

cell (Fig. 6.2a–c). The contact angle between a) the interface of the dispersed phase and the glass wall of the cell and b) the interface of the dispersed phase and the continuous phase, θ_c (Fig. 6.2d), is determined from the radii of circles in microscopy images as described in Subsection 6.2.4.

The contact angle increases upon decreasing the temperature relative to the lower phase separation temperature, ΔT_{ps} (Fig. 6.2e). The value of the contact angle is the result of the force balance between the three interfacial tensions at the contact line (Fig. 6.2d, Eq. 6.1), and the interfacial tensions depend on the compositions of each phase. These compositions can be estimated from the phase diagram. At $\Delta T_{ps} = 2.9\,°C$, the compositions of the coexisting phases are given by the intersects of the horizontal tie line at $\Delta T_{ps} = 2.9\,°C$ with the phase separation temperature, $m_w = 0.59$ and 0.82 (Fig. 6.1b—). At the phase separation temperature, however, the composition of the two phases are $m_w = 0.69$ and 0.73 (Fig. 6.1b—). In other words, upon decreasing the temperature, the system approaches the lower critical point, and the difference in the composition between the phases diminishes. Hence, we expect the difference in the interfacial tensions between a) the glass and the continuous phase and b) the glass and the dispersed phase, $\gamma_{sc} - \gamma_{sd}$, to approach zero. The interfacial tension between the continuous and the dispersed phase, γ_{cd}, however, is also expected to approach zero. Hence, both the numerator as well as the denominator in Eq. 6.1 vanish. We observe that the contact angle deviates from 90°. This suggests that γ_{cd} approaches zero more rapidly than $\gamma_{sc} - \gamma_{sd}$. This results in the counter-intuitive behaviour that close to the critical point—where the two phases are most similar—the contact angle deviates from 90°.

We compare these observation to work by Cahn [112] on the contact angle near the critical point. At the critical concentration, previous experiments and theory show that γ_{cd} approaches zero as $|\Delta T^*|^\mu$ where ΔT^* is the temperature relative to the lower critical solution temperature, i.e. the temperature at the critical point, $T - T^*$, and $\mu = 1.3$ is the critical exponent of the interfacial tension [113, 114, 114, 115, 116, 117, p33]. $\gamma_{sc} - \gamma_{sd}$, on the other hand, should approach zero as the difference in the composition and thus as $|\Delta T^*|^{0.33}$ [112, 113, 118, 119]. Cahn inserted these relations into Eq. 6.1 and showed that $|\cos\theta_c|$ should diverge as $\Delta T^{*-1.0}$ [112]. If the temperature approaches the lower phase separation temperature, $|\cos\theta_c|$ increases, and the contact angle should thus deviate from 90° which is in qualitative agreement with our measurements.

Next, we quantitatively compare our measurements to the prediction by Cahn [112]. The fit in Fig. 6.1b shows that the phase separation tempera-

ture, T_{ps}, at $m_{\mathrm{w}} = 0.69$ is 0.06 °C above the critical temperature, T^*. Using $\Delta T^* = \Delta T_{\mathrm{ps}} + 0.06\,^{\circ}\mathrm{C}$, we fit our data to an exponential function resulting in (Fig. 6.2f—),

$$|\cos\theta_{\mathrm{c}}| = 0.45|\Delta T^*/^{\circ}\mathrm{C}|^{-0.42}. \tag{6.3}$$

6.3

We only measured over a small temperature-range, but the critical exponent of −0.42 deviates significantly from the value of −1.0 as predicted by Cahn (Fig. 6.2f- -). The value at $\Delta T_{\mathrm{ps}} = 0.0\,^{\circ}\mathrm{C}$ corresponds to $\Delta T^* = 0.06\,^{\circ}\mathrm{C}$, and is ignored in the fit, as the resolution of the heating stage is only 0.1 °C. The uncertainty in $\log \Delta T^*$ is thus relatively large at $\Delta T^* = 0.06\,^{\circ}\mathrm{C}$. Furthermore, at $\Delta T^* < 0.15\,^{\circ}\mathrm{C}$, $|\cos\theta_{\mathrm{c}}| > 1$. This corresponds to a wetting transition, i.e. below this temperature one phase completely wets the solid surface as previously predicted and observed by Cahn [112] and Moldover and Cahn [120]. The temperature difference between the wetting transition temperature, and the phase separation temperature is only 0.1 °C, and comparable to the resolution of the heating stage. Hence, no wetting transition has been experimentally observed.

The deviation between the measured and theorical exponent becomes less alarming by considering data on mixtures of 2,6-lutidine and water. These mixtures also have a closed-loop phase diagram, and a similar molecular structure. Grattoni *et al.* [121] interpolated measurements of the interfacial tension in these mixtures resulting in,

$$\gamma_{\mathrm{cd}}/\mathrm{mN\,m^{-1}} = 0.043(\Delta T^*/^{\circ}\mathrm{C})^{0.88}. \tag{6.4}$$

We note that the measured critical exponent, $\mu = 0.88$, deviates from the critical exponent for the interfacial tension as measured and predicted for other systems at $\mu = 1.3$. The critical exponent of the difference in the composition, on the other hand, is 0.27 and similar to the previously reported value of 0.33 (App. Fig. 6.2). Furthermore, these critical exponents should result in a critical exponent for the contact angle of −0.61, which is in much better agreement with our data (Fig. 6.2f-···). We speculate that a lower value of μ could possibly be due to hydrogen bonding or the amphiphilic character of 2,6-lutidine, resulting in adsorption of these molecules onto the interface. These effects might also occur in 3MP/D_2O, and measurements of the interfacial tension would verify if μ is about 0.9 in our system as well. We may safely conclude, however, that the interfacial properties of 3MP/D_2O depend strongly on the temperature. More specifically, in a phase-separated, near-critical mixture, the contact angle deviates from 90° upon approaching the phase separation temperature, while the interfacial tension decreases.

The contact angle is measured upon first increasing the temperature, and then decreasing the temperature again (Fig. 6.2e). The observed hysteresis in the contact angle is probably due to pinning of the droplet on the glass. By allowing more time for the droplets to equilibrate, the equilibrium contact angle should be reached, and the hysteresis could presumably be reduced. The number of droplets, however, decreases with time due to coalescence and possibly Ostwald ripening. Hence, even for these measurements, only a few small droplets were left at the final temperature. Increasing the equilibration time even further, while still retaining good statistics is therefore challenging. Furthermore, droplets attach both to the bottom and the top of the cell, and in the latter case, lensing effects could result in measurement errors. Additionally, in the studied temperature regime, deformation of the shape of the droplets by gravity should be small (App. 6.B). Finally, a horizontal gradient in the temperature is due to the hole in the heating stage that allowed bright field microscopy (App. Fig. 6.1a–b). Using a purpose build set-up (App. Fig. 6.1c–d), uniform heating in the imaging plane could be achieved. That set-up resulted in similar behaviour, but did not allow bright field microscopy. Hence, unless stated otherwise, the set-up with a gradient in the imaging plane is used.

6.3.2. Thermoreversible Interfacial Attachment Cross-linked polystyrene colloids are added to the near-critical mixtures and their attachment onto phase-separated droplets is studied (Fig. 6.3). We study colloidal particles in 3MP/D_2O as well as in PnP/H_2O. The colloids have a diameter of 524 ± 44 nm, and crucially, they are synthesized without addition of surfactants or stabilizers to prevent interactions between surface-active molecules and the mixtures (Subsection 2.2.2).

After the addition of colloids, 3MP/D_2O and PNP/H_2O phase-separate at $T_{ps} = 39.0\,^{\circ}C$ and $32.2\,^{\circ}C$. Remarkably, for PNP/H_2O, the observed phase separation temperature is well below the interpolated value using previous measurements by Cox *et al.* [111], $T_{ps} = 34.6\,^{\circ}C$ at $m_w = 0.60$ (Fig. 6.1b). The lower temperature we measure, might be due to the presence of the particles or a deviation in the temperature sensor. Just above the phase separation temperature, particles are found in the continuous phase (Fig. 6.3a,f). Occasionally, particles reside for some seconds at the interface but no durable attachment is observed. Remarkably different behaviour is observed upon increasing the temperature further to more than $2\,^{\circ}C$ above the lower phase separation temperature. These temperatures are deeper in the phase separation region (Fig. 6.1), and particles permanently attach onto the interface (Fig. 6.3b,g). Upon decreasing the temperature again below the

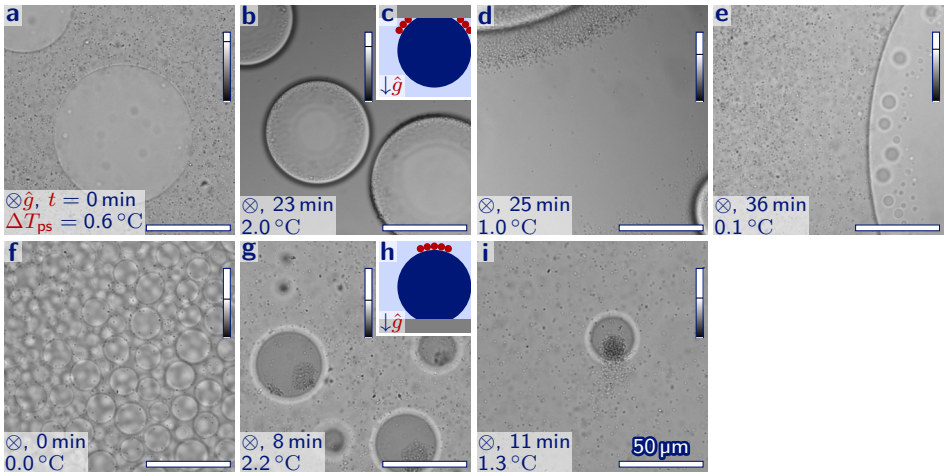

Figure 6.3. Thermoreversible interfacial attachment. Microscopy images of cross-linked polystyrene particles in a 3MP/D_2O mixture with $m_w = 0.71$ (**a–e**), and a PnP/H_2O mixture with $m_w = 0.60$ (**f–i**). Above the lower phase separation temperature, $\Delta T_{ps} > 0$ (**a,f**), the mixtures phase separate and particles are found in the continuous phase. Upon increasing the temperature (**b,g**), particles attach to the interface in a ring-like (**b**) or island-like (**g**) configuration. These configurations are sketched (**c,h**) at the edge of the cell (●) with the particles (●) creaming at the interface between the continuous (●) and the dispersed (●) phase. Upon decreasing the temperature again (**d,i**), particles detach from the interface, and eventually (**e**) are homogeneously dispersed in the continuous phase. To both mixtures, a rhodamine dye was added to increase contrast and the direction of the gravitational field is indicated by $\hat{g}$.

attachment temperature at 2 °C, the particles leave the interface and move back into the continuous phase (Fig. 6.3d–e,i).

To explain thermoreversible attachment, we consider the free energy change upon adsorption of particles onto the interface, ΔG_{ad}. We hypothesize that ΔG_{ad} is too small for particles to attach just above T_{ps}, while ΔG_{ad} should be large enough for attachment at $\Delta T_{ps} \geq 2\,°C$. For spherical particles, the free energy change upon adsorption is [122, p8],

$$\Delta G_{ad} = -\pi {R_p}^2 \gamma_{cd}(T) \left[1 - \left|\cos\left(\theta_c(T)\right)\right|\right]^2, \tag{6.5}$$

where R_p is the radius of the particle, γ_{cd} is the interfacial tension between the continuous and the dispersed phase, θ_c is the contact angle between a) the interface of the particle and the dispersed phase and b) the interface of the continuous and the dispersed phase, and we explicitly state that both γ_{cd} and θ_c are temperature-dependent. In the previous subsection, we saw that upon approaching T_{ps}, γ_{cd} decreases (Eq. 6.4), while $|\cos\theta_c|$ increases (Fig. 6.2f). Even though we measured the contact angle at a glass surface, an increase of $|\cos\theta_c|$ upon approaching the phase separation temperature should be general as discussed before. Hence, upon approaching the phase separation temperature, a decrease of the adsorption energy is expected (Eq. 6.5). Consequently, just above the lower phase separation temperature, the adsorption strength, $|\Delta G_{ad}|$, might be comparable to the thermal energy, $k_B T$, and thus too small for permanent attachment; while at higher temperatures, ΔG_{ad} becomes stronger, and might be about $-6 k_B T$, resulting in permanent attachment.

We estimate the adsorption energy as a function of the contact angle for the experimental system in Fig. 6.3b and d (compare Fig. 6.4a–b-- to —). The particles have a radius of 262 nm and are immersed in 3MP/D_2O at $m_w = 0.71$. We calculate the adsorption energy at $\Delta T_{ps} = 2\,°C$, where particles attach, and at $\Delta T_{ps} = 1\,°C$ where no permanent attachment is observed. The mass fraction of water, $m_w = 0.71$, is virtually identical to the critical mass fraction (Fig. 6.1b), and hence, $T_{ps} \approx T^*$, and $\Delta T_{ps} \approx \Delta T^*$. We take values for the interfacial tensions using the previously mentioned interpolation for mixtures of 2,6-lutidine and water (Eq. 6.4). Even though the components in our system are different, we expect the difference in the interfacial tension for both systems to be smaller than a factor of two as the mixtures have similar phase behaviour and molecular structures. At $\Delta T_{ps} = 1\,°C$, the resulting adsorption energy is weaker than the thermal energy, $k_B T$, if $\theta_c \geq 168°$ (Fig. 6.4b—). Hence, if the contact angle at $\Delta T_{ps} = 1\,°C$ is about 168°, no attachment of particles onto the interface is expected. At $\Delta T_{ps} = 2\,°C$, the adsorption is stronger than $6\,k_B T$ if $\theta_c \leq 164°$ (Fig. 6.4b--). Hence, if the contact angle at $\Delta T_{ps} = 2\,°C$ is about 164°, we expect particles to attach onto the interface. At the glass surface, we observe a decrease in the contact angle of about $10\,°/°C$ (Fig. 6.2e). A similar decrease in the contact angle at the surface of the particles from about 168° at 1 °C to 164° at 2 °C could thus explain a transition from no attachment to permanent attachment.

The critical exponent of the contact angle is used to obtain an expression of the adsorption energy as a function of the temperature (Fig. 6.4c). In Fig. 6.2f—,

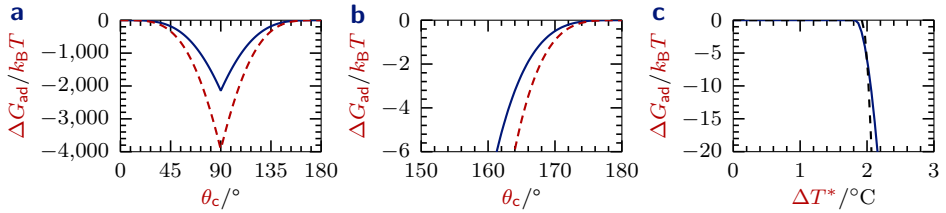

Figure 6.4. Adsorption energy of a particle onto an interface. The change in the free energy upon adsorption of a sphere with radius 262 nm onto an interface, ΔG_{ad}, is estimated for an interface of phase-separated 3MP/D_2O. ΔG_{ad} is calculated using Eq. 6.5 (**a–b**) as a function of the contact angle between the interface and the surface of the particle, θ_c. The interfacial tensions are estimated at 1 °C above the critical temperature (—) and at $\Delta T^* = 2\,°C$ (- -) using Eq. 6.4. We plot both the entire range of θ_c (**a**), as well as the regime where a transition from reversible ($\Delta G_{ad} \approx -k_BT$) to irreversible adsorption ($\Delta G_{ad} \ll -k_BT$) is observed (**b**). The adsorption energy as a function of the temperature relative to the critical temperature, ΔT^*, is calculated by inserting Eq. 6.4 and Eq. 6.6 into Eq. 6.5 (**c** —), and by assuming a critical exponent of the contact angle of -1 (- -).

we determined a relation between the temperature and the absolute value of the cosine of the contact angle on the glass. To obtain a similar expression for the contact angle on the particles, we assume 1) that the contact angle is 164° at $\Delta T_{ps} = 2\,°C$, so $\Delta G_{ad}(\Delta T_{ps} = 2\,°C) = -6k_BT$, and 2) $|\cos(\theta_c)|$ increases with a critical exponent of -0.42 as in Eq. 6.3 (Fig. 6.2f-···),

$$|\cos(\theta_c)| = \begin{cases} 1.3(\Delta T^*/°C)^{-0.42} & \text{if } \Delta T^* \geq 1.8\,°C \\ 1 & \text{if } \Delta T^* < 1.8\,°C, \end{cases} \tag{6.6}$$

where a wetting transition is predicted at $\Delta T^* = 1.8\,°C$. Inserting Eq. 6.4 and 6.6 into Eq. 6.5 gives a very steep increase of the strength of the adsorption energy from -1.2 to -6 and $-14k_BT$ upon increasing the temperature from $\Delta T_{ps} = 1.9$ to 2.0 and 2.1 °C (Fig. 6.4c—). These predictions are in good agreement with the sharp transition from no attachment to permanent attachment upon changing the temperature with 0.1 °C as we will see in Fig. 6.6h–j. Furthermore, the increase in the adsorption strength would have been even steeper for a critical exponent of $|\cos(\theta_c)|$ of -1 (Fig. 6.4c- -).

For a transition from adsorption to desorption, the values of the contact angle at the particles should be larger than those measured at the glass substrate (compare Fig. 6.2f-··· to —). Using the interpolation in Fig. 6.2f—, we estimate that at $\Delta T^* = 1\,°\mathrm{C}$, θ_c at the glass substrate is only about 117°, which would result in an adsorption energy of about $-6.5 \times 10^2 k_B T$ (Eq. 6.5 and Fig. 6.4a—). Additional measurements should verify if the contact angles of the near-critical mixtures on sulphonated polystyrene surfaces are indeed larger than on a glass substrate. These measurements, however, are challenging as the radius of the particles is smaller than the wavelength of light. Larger particles or particles adsorbed onto an interface as in [123] could perhaps resolve this issue.

A relatively large contact angle, could also be due to pinning of the interface on the particle surface. The surface of the cross-linked polystyrene particles is irregular (App. Fig. 6.3). Hence, upon adsorption onto the interface between the continuous and the dispersed phase, the particles can get trapped before reaching their equilibrium position. This results in a so-called pinned contact angle. As the particles approach the interface from the continuous phase, pinning should result in a higher value of θ_c than the equilibrium contact angle. If the pinned angle at $\Delta T_{ps} = 2\,°\mathrm{C}$ is about 164°, particles attach to the interface. As the contact angle should be pinned at a higher value than the equilibrium value, a small decrease in the temperature should not result in an increase of the contact angle. Hence, for a pinned contact angle, the adsorption energy only decreases with the temperature due to a decrease of the interfacial tension. At a fixed contact angle, the decrease in the adsorption energy with the temperature, however, might only result in an attachment transition if $\theta_c \approx 165°$, where $\Delta G_{ad} \approx 4.6 k_B T$ at $\Delta T_{ps} = 2\,°\mathrm{C}$, and $\Delta G_{ad} \approx 2.5 k_B T$ at $\Delta T_{ps} = 1\,°\mathrm{C}$ (Fig. 6.4b). It seems unlikely that pinning results in such a well-defined contact angle for all particles. Hence, pinning can not explain the transition from attachment to no attachment. The flattened edges of the particles (App. Fig. 6.3), on the other hand, could result in a smaller or larger interfacial area that is covered by particles compared to perfect spheres at the same contact angle. This effect changes the adsorption energy with respect to the estimate for perfect spheres, and makes desorption either more or less likely.

We observe that attached particles cluster at the interface. At droplets that attach to the top of the cell, the colloids assemble into ring-like structures (Fig. 6.3b–c), while at the bottom of the cell, island are formed (Fig. 6.3g–h). Polystyrene particles, however, have a density above the densities of the mixtures (App. Table 6.1). Buoyancy of the particles seems thus unlikely to explain creaming to the

top of the droplets. Another explanation is thermophoresis or the Soret effect. In a temperature gradient, bombardment of colloids with relatively hot, fast molecules on one side, and cold, slow molecules on the other side can result in a net force towards the cold side [124, 125, 126]. In our sample cell, a temperature gradient is also expected as the cell is only heated from above (App. Fig. 6.1b). The particles, however, cluster at the top of the cell, where the temperature is highest, while a temperature gradient is expected to result in a net force towards the bottom of the cell. Examples of thermophoresis in the opposite direction, however, have been previously described [127, 128], and preliminary results show that for a temperature gradient in the horizontal direction, particles also move to the hot side of a cell (App. Fig. 6.4). A final explanation is that the hydrophobic polymer network inside the particles is swollen by the more hydrophobic component of the mixture. The densities of the relatively hydrophobic 3MP and PnP are well below those for D_2O and H_2O (App. Table 6.1). We estimate that in PnP/H_2O at $m_w = 0.60$, each particle should be swollen with PnP to more than 3× its original mass for the densities of the particles to be lower than the density of the liquid. Here, we assumed the density of the liquid to be the mass weighed average of the densities of the pure components. Additional experiments should verify if the particles are indeed swollen with PnP or 3MP.

Only particles that are attached to an interface cream, while unattached particles are found over the entire thickness of the cell. Hence, creaming is most likely a two-step process. First, particles form clusters at the interface, next, clusters cream to the top of the cell as an upward gravitational or Soret force is higher for clusters than for single particles. Formation of clusters could be induced due to so-called capillary attraction. Capillary attraction is induced if the surface of the particles is irregular and distorts the interface (App. Fig. 6.3) [129, 130]. We estimate the capillary attraction in our system, and due to the high contact angle and low interfacial tension, the attraction might be too small to induce the formation of clusters (App. 6.D).

Alternatively, thermoreversible attachment and formation of clusters might be explained by contactless attachment of particles, i.e. without touching the interface. Competition between repulsive and attractive forces has been shown to induce contactless attachment of particles onto oil/water interfaces [131, 132, 133]. In our system, particles are negatively charged due to sulphate surface groups. If the particles are dispersed in the water-rich phase, that could result in a negative image charge in the dispersed phase (Fig. 6.5a). Consequently, repulsion by the image

charge could prevent interfacial adsorption. An unequal distribution of potassium counter-ions over both phases, on the other hand, could generate a positive charge or Donnan potential over the interface (Fig. 6.5a). As a consequence, an attraction between the positively charged interface and the negatively charged particles could be generated. Experiments by Wang *et al.* [132] suggest that competition between repulsion by an image charge and attraction to a charged interface could result in an attractive secondary minimum, and a repulsive barrier that prevents adsorption. In Fig. 6.5b and App. 6.C, we estimate the resulting interaction potential for our system upon varying the interfacial potential. These estimates show that the image charge repulsion is too weak to explain our observations. In Fig. 6.5, the interface between the continuous and the dispersed phase is assumed to be flat. As the interfacial tension is only about 0.1 mN/m, the interface might, however, deform. A deformation of the interface could increase both the attraction to the charged interface and the repulsion by the image charge. Further calculations should indicate if for a deformed interface, the attraction is strong enough for attachment, while the repulsion is sufficient to prevent adsorption. Additionally, these calculations should also take van der Waals interactions into account. Furthermore, we speculate that a deformation of the interface should also result in capillary attraction, and might explain the formation of clusters. Finally, the contactless attachment energy seems to be much less sensitive to temperature changes than the adsorption energy (compare App. Fig. 6.5 and Fig. 6.4c). Hence, even with deformability taken into account, contactless attachment does not seem to explain the sharp transition from attachment to detachment in Fig. 6.6h–j.

Finally, similar behaviour is observed for both 3MP/D_2O and PnP/H_2O, and both attachment transitions are observed at $\Delta T^* = 2\,°C$. This suggests that thermoreversible attachment could be generically induced for near-critical, partially miscible liquids. In 3MP/D_2O, however, all particles are found at the interface, while in PnP/H_2O, particles are also found in the continuous phase. We have not found an explanation for this difference yet, but measurements of the charge of particles in either mixture might help to understand these observations. At $\Delta T^* > 2\,°C$, however, attached particles have not been observed to leave the interface for all studied compositions.

6.3.3. Temperature-Controlled Pickering-like Emulsions At a high particle concentration, increasing the temperature of near-critical mixtures induces the formation of particle-stabilized droplets (Fig. 6.6). Similarly as in the previous subsection,

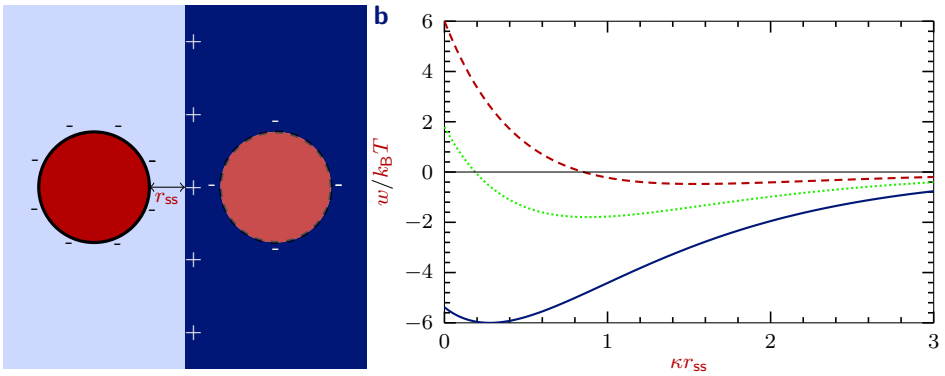

Figure 6.5. Contactless attachment. **a**) A negatively charged particle (●) is attracted to a positively charged interface and repelled by its image charge (●) if the dielectric constant of the host medium (●) is higher than that of the medium on the other side of the interface at a distance r_{ss} (●). **b**) The interaction potential, w, for 3MP/D_2O at a mass fraction of water of $m_w = 0.71$ is estimated as a function of the ratio of the surface-to-surface distance of the particle from the interface, r_{ss}, and the Debye length, κ^{-1}. At 2 degrees above the phase separation temperature, the maximum attraction is $-6k_BT$, if the potential at the interface, ψ_{int}, is 1.3 mV (—), while the maximum repulsion is $6k_BT$ at $\psi_{int} = 0.4$ mV (- -). The strength of the maximum attraction is equal to the maximum repulsion if $\psi_{int} = 0.7$ mV at $1.8k_BT$ (····).

we observe 1) phase separation at $T_{ps} \approx 32\,°C$, 2) attachment of particles onto the interface at $\Delta T_{ps} \approx \Delta T^* \geq 2\,°C$, and 3) coalescence of droplets that are in contact (Fig. 6.6a–e). In this case, however, large droplets in contact do not coalesce and are kinetically stable for minutes (Fig. 6.6f–h). This can be understood as the coverage by particles increases with the size of the droplets. With each coalescence event, the interfacial area to volume ratio of the droplets decreases, and consequently, the density of particles on the interface increases. Hence, whereas for relatively small droplets, only the top of the droplets is covered by a ring of particles, for large droplets, a larger part of the surface is covered by particles (compare Fig. 6.6d to g). Apparently, for the Pickering-like emulsion in Fig. 6.6f–h, the ring of particles extends down to the middle of the droplets, and coalescence is prevented. Unlike conventional Pickering emulsions, only part of the surface of the droplets thus needs to be covered by particles to prevent coalescence. In a much larger cell, however,

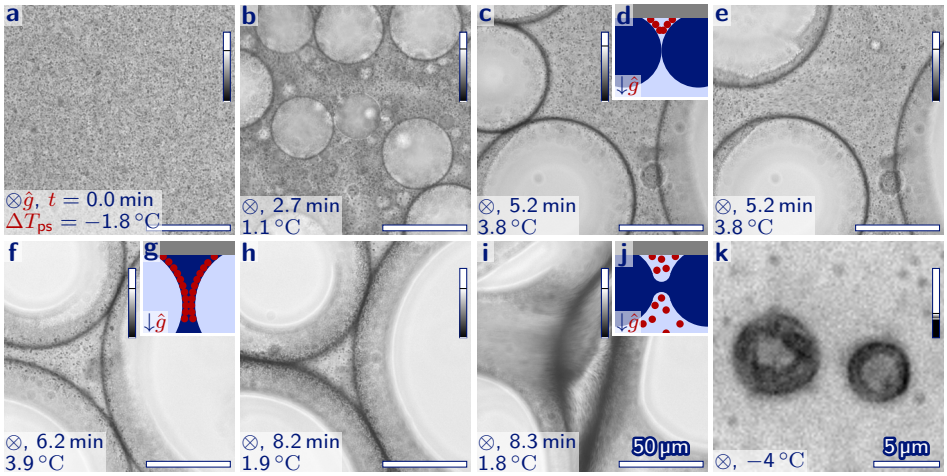

Figure 6.6. Pickering-like emulsion with temperature-controlled stability. Microscopy images of cross-linked polystyrene particles in a PnP/H_2O mixture with $m_w = 0.68$. Below the lower phase separation temperature, $\Delta T_{ps} < 0$, particles are dispersed in the mixture (**a**). At $\Delta T_{ps} \geq 0$, droplets are formed, and particles are found in the continuous phase (**b**). Upon increasing the temperature further, particles attach onto the surface of the droplets (**c**), but droplets still coalesce (**c–e**) as probably, particles (**d** ●) do not fully cover the interface between the continuous (●) and dispersed (●) phase. After more coalescence events, droplets that are in contact do not coalesce for minutes (**f–h**), until the relative temperature is decreased below 1.9 °C (**i–j**, artist impression). Finally, after cooling down to $\Delta T_{ps} < 0$ (**h**), hollow spherical shells are found. The last image is obtained for a sample with $m_w = 0.60$, and for the other images, fluorescein is added to increase contrast. The QR code links to a movie of the time series of **a–i** (phd.chrisevers.com/6qr6.mp4).

relatively less droplets attach to the wall, and we expect coalescence to continue until droplets are fully covered and a real Pickering emulsion should be obtained.

Upon decreasing the temperature, particles detach from the interface and droplets that are in contact coalesce (Fig. 6.6h–j). In the previous subsection, we observed a threshold temperature for particle attachment at $\Delta T^* = 2\,°C$. Here, we again observe a transition at this temperature. Above 2 °C, kinetically stable droplets are observed, whereas droplets coalesce upon decreasing the temperature

only 0.1 °C (compare Fig. 6.6h to i). Close inspection of the time series (Fig. 6.6QR) reveals that just before coalescence, many particles detach from the interface and move back into the continuous phase. Detachment of the particles thus seems to destabilizes the droplets. This strongly supports the idea that the emulsion is stabilized by thermoreversible attachment of particles. Consequently, the stability of the emulsions can be controlled by temperature.

The emulsification is not fully thermoreversible. After decreasing the temperature of a Pickering-like emulsion below the phase separation temperature, a continuous phase is obtained with many aggregates of colloidal particles. We hypothesize that these aggregates are formed when particles are pushed together at the surface of shrinking droplets. We verify that droplets indeed shrink upon decreasing the temperature. Using the lever rule, the mass ratio between the coexisting phases can be estimated from the phase diagram (App. 6.E). From the estimated mass ratios, we conclude that upon decreasing the temperature from $\Delta T_{\mathrm{ps}} = 4\,^{\circ}\mathrm{C}$ to $2\,^{\circ}\mathrm{C}$, the volume of the continuous phase increases, while the droplets shrink. During the shrinking of the droplets, the particles are still attached onto the interface. As we saw before, the coverage of the interface by particles is high, and the particles are pushed even closer together as the droplets shrink. Consequently, the electrostatic repulsive barrier between neighbouring particles might be overcome, leading to the formation of irreversible van der Waals bonds and eventually aggregates. For droplets at lower particle concentrations and lower maximum temperatures, particles leave the interface unclustered (Fig. 6.3d–e,i), and no large aggregates are found. These observation can be explained as the number of attached particles in Fig. 6.3 is lower than in Fig. 6.6. Consequently, the particles might be able to redistribute on the surface of the shrinking droplet, instead of being pushed through their repulsive barrier. Furthermore, in Fig. 6.3, the temperature is increased to only $\Delta T^{*} \approx 2\,^{\circ}\mathrm{C}$ instead of $4\,^{\circ}\mathrm{C}$ in Fig. 6.6, Hence, the volume decrease of the droplets before the particles leave the interface is low, and the force that pushes the particles together cannot overcome the electrostatic repulsion. By keeping Pickering-like droplets at temperatures just above $2\,^{\circ}\mathrm{C}$, fully thermoreversible emulsions might thus be created. Another approach is to increase the interparticle repulsion. A common method to increase the repulsion is to adsorb surfactants or polymers onto the surface of the particles. These could, however, detach from the interface and influence the phase behaviour. To prevent this effect, chemically grafting hydrophilic polymers onto the surface of particles seems the most promising route towards fully thermoreversible Pickering emulsions.

Aggregation of particles on the interface of shrinking droplets, results—besides ill-defined clusters—also in hollow shells (Fig. 6.6k). These shells are probably formed upon shrinking small, fully covered droplets. This is similar to the formation of colloidosomes where 1) an emulsion is created by shear and particles adsorb onto the interface of emulsion droplets, 2) irreversible bonds between particles are formed by addition of salt or by sintering, and 3) the continuous phase is replaced by the same phase as the dispersed phase [97]. In our method, similar structures are obtained by merely increasing and subsequently decreasing the temperature. As discussed before, the interface of most droplets is not fully covered by particles. Hence, the yield of colloidosomes is low. In a larger container, the number of droplets at the wall of the cell decreases, and a higher yield is expected. To obtain shells with a small polydispersity in their size, however, uniform heating is probably required, which might be challenging at a larger scale.

As an outlook, we note that the temperature dependence of the size of near-critical droplets has the potential to induce more complex structures. Buckled structures have been shown to form upon either shrinking shells, shrinking a microgel onto which particles are adsorbed, or shrinking Pickering emulsion droplets [134, 135, 136, 137]. Using our system, similar buckled structures might be formed by a mere temperature change. At temperatures far above the lower phase separation temperature, colloids attach onto the interface of phase-separated droplets. In a large container, this should result in fully covered droplets. Upon decreasing the temperature again, while remaining above the temperature at which particles detach, the droplets shrink, while the particles remain attached onto the interface. A decrease of the temperature should thus result in a decrease of the volume of the droplets, whereas the particles prevent a decrease of the surface area of the droplets. Hence, we expect the droplets to buckle, and hollow buckled structures could in principle thus be obtained by simply increasing and decreasing the temperature.

Furthermore, by applying a temperature gradient in the imaging plane, more complex behaviour is observed. At a constant gradient, some preliminary results simultaneously show nucleation of droplets, attachment of particles onto the interface, directed flow, and bursting of droplets (App. Fig. 6.4). We expect that these observations are the result of an interplay between phase separation, thermophoresis and thermoreversible attachment, but more research is needed to fully understand this behaviour.

Most observations in this chapter have been explained using existing theories on near-critical phenomena. A number of open questions, however, remain. First

of all, additional experiments on the near-critical behaviour of the interface and the contact angle of our mixtures are necessary. These should verify 1) if the critical exponent of the interfacial tension, μ, is about 0.9, instead of 1.3 as expected from theory, 2) if our preliminary results for the critical exponent of the contact angle can be reproduced over a larger temperature range, and 3) if the contact angle on the surface of the particles is indeed much larger than on a glass surface. Second, we propose two explanations for thermoreversible attachment, adsorption and contactless attachment. The plausibility of the first explanation can be verified using the results of above mentioned experiments. To asses the contactless attachment, deformation of the interface and van der Waals forces should be taken into account to estimate the interaction energy, and the phase in which the particles preferentially reside needs to be identified. Furthermore, the creaming behaviour of particles needs to be systematically investigated using particles that are less irregular, and additional experiments should elucidate why above the attachment temperature, many particles in PNP/H_2O are still found in the continuous phase. Finally, we made progress towards thermoreversible Pickering emulsions. We expect that by using a larger container and either a smaller temperature increase or more repulsive particles, in principal, truly thermoreversible Pickering emulsification could be achieved.

6.4. Conclusion

We study colloids in near-critical, partially miscible liquids with lower and upper phase separation temperatures. Above the lower phase separation temperature, two coexisting phases are found and their composition changes sensitively with the temperature. Hence, interfacial properties can easily be controlled, and particles thermoreversibly attach onto the surface of phase-separated droplets. We make use of this property to create and control the stability of Pickering-like emulsions and create colloidosomes by simply changing the temperature. Increasing the temperature results in an increase in the interfacial tension between the phases, and a contact angle closer to 90°. Hence, an increase in the adsorption energy with the temperature could explain these effects. The formation of clusters on the interface, however, is not explained. Consequently, an alternative mechanism involving contactless attachment needs to be further investigated.

Our Pickering-like emulsions are conveniently prepared by increasing the temperature without the need of high shear. Furthermore, thermoreversible attachment is demonstrated for two different near-critical mixtures with a lower phase sepa-

ration temperature. We expect that thermoreversible attachment, however, can be employed in more common partially miscible liquids with only an upper phase separation temperature as well. In fact, those mixtures might be even more straightforwardly applicable, as—in the presence of colloids—merely heating above the upper phase separation temperature and cooling back to room temperature, should already result in a Pickering emulsion.

6.5. Acknowledgement

Micah van der Vaart is thanked for performing most of the experiments described in this chapter. Joost Wolters is thanked for taking the transmission electron microscopy images. Jan Groenewold, Jeffrey Everts, Nina Elbers and Mark Vis are thanked for useful discussions.

6.A. Appendix Figures and Tables

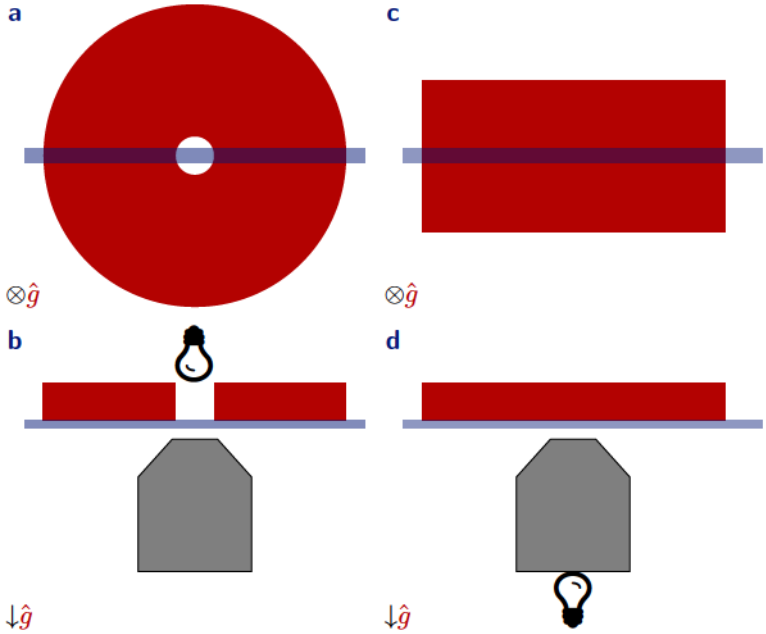

Appendix Figure 6.1. Microscopy set-up. Schematic illustrations of microscopy set-ups from above (**a**,**c**) and the side (**b**,**d**). For bright field microscopy (**a**–**b**), a sample cell (●) is fixated on a Linkam heating stage (●) with a circular hole. The sample is illuminated from above and studied with an objective from below (●). For reflected light microscopy (**c**–**d**), the sample cell is heated with a metal block (●) and illuminated from below. The direction of the gravitational field is indicated by $\hat{g}$.

Appendix Table 6.1. Densities, ρ, of used compounds.

Name	ρ/g cm^{-3}	Reference
H_2O	1.00	[6, p4–98]
D_2O	1.10	[6, p4–98]
PnP	0.89	[6, p3–468]
3MP	0.96	[6, p3–394]
polystyrene	1.06–1.12	[6, p15–93]

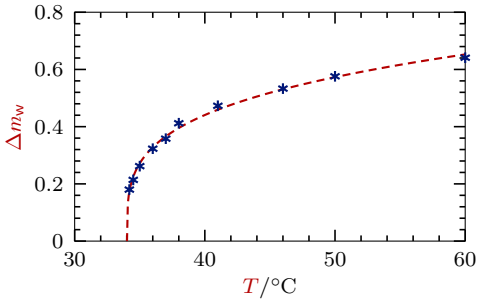

Appendix Figure 6.2. Composition difference. The difference in the mass fractions of water, Δm_w, for phase-separated 2,6-lutidine and water are plotted as a function of the temperature, T, using composition measurements of Grattoni *et al.* [121] (*). The values are fitted to an exponential function, $0.27(\Delta T^*/°C)^{0.27}$, with $T^* = 34.0\,°C$ (--).

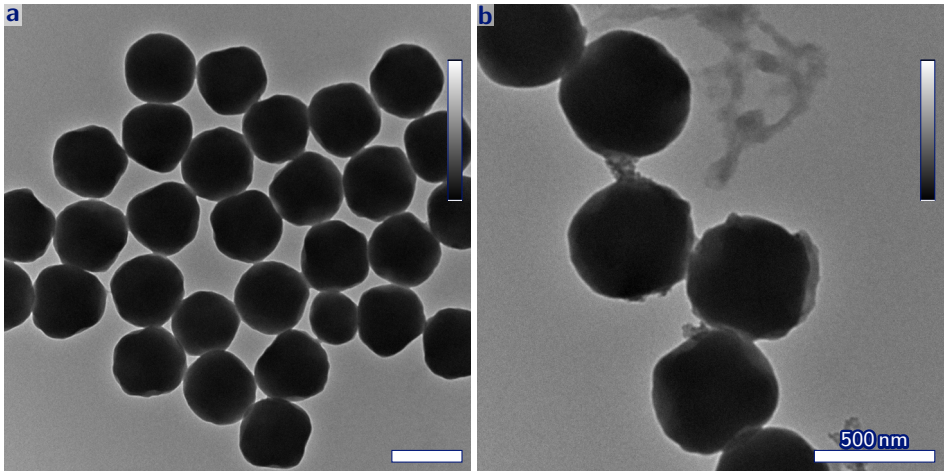

Appendix Figure 6.3. Cross-linked polystyrene particles. Transmission electron microscopy images of cross-linked polystyrene particles with a diameter of 524 ± 44 nm.

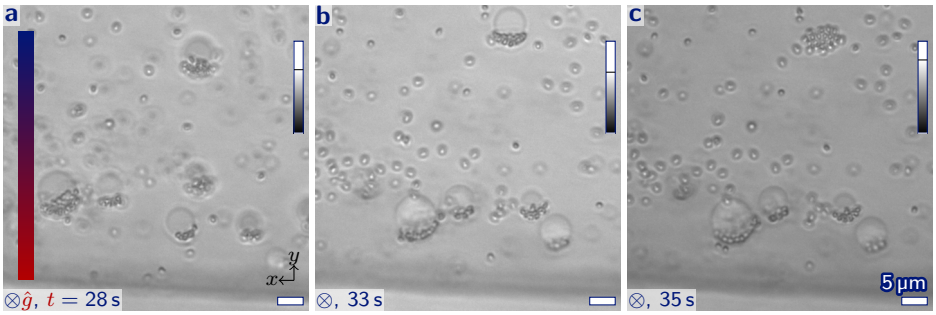

Appendix Figure 6.4. Attachment of particles and bursting of droplets in a temperature gradient. Colloidal snowman-like particles are studied in 3MP/D_2O with a mass fraction of water, $m_w = 0.66$. The sample is heated from the direction of the bottom of the images, resulting in a temperature gradient in the y-direction. At the bottom of the images, where the temperature is highest, phase-separated droplets nucleate. Particles attach onto the interface of the droplets and cluster at the bottom of the droplets. Furthermore, unattached particles move towards the bottom of the image, while droplets move in the opposite direction. Once the droplets reach the top of the image, where the temperature is lowest, the droplets burst and the attached particles are released (**b–c**). Image levels are rescaled as indicated by the grey vertical bars, the temperature gradient is indicated by the coloured vertical bar, and the direction of the gravitational field is indicated by $\hat{g}$. The QR code links to a movie of the complete time series (phd.chrisevers.com/6qrA4.mp4).

6.B. Deformation of Droplets by Gravity

In the earth gravitational field, a competition is expected between gravity that flattens droplets and interfacial tension that prefers a spherical geometry. The gravitational energy depends on the difference in the density of the continuous and the dispersed phase, $\Delta\rho_{cd}$, while the interfacial energy depends on the interfacial tension between these phases, γ_{cd}. The capillary length denotes above which length scale gravity becomes important [138, p33],

$$l_c = \sqrt{\frac{\gamma_{cd}}{\Delta\rho_{cd} g}}, \tag{6.7}$$

where $g = 9.8\,\mathrm{m\,s^{-2}}$ is the gravitational acceleration in the earth gravitational field. Close to the critical point, both γ_{cd} and $\Delta\rho_{cd}$ approach zero.

We estimate the capillary length in Fig. 6.2 at 0.05 °C and 3 °C above the critical point. We assume values for γ_{cd} and $\Delta\rho_{cd}$ using interpolations of previous measurements of 2,6-lutidine and water [121]; Eq. 6.4 and,

$$\Delta\rho_{cd}/\mathrm{kg\,m^{-3}} = 7.3(\Delta T^*/°\mathrm{C})^{0.47}, \tag{6.8}$$

where ΔT^* is the temperature relative to the critical temperature. At $\Delta T^* = 0.05\,°\mathrm{C}$, $\gamma_{cd} = 0.0031\,\mathrm{mN/m}$ and $\Delta\rho_{cd} = 1.8\,\mathrm{kg\,m^{-3}}$, while at $\Delta T^* = 3\,°\mathrm{C}$, $\gamma_{cd} = 0.11\,\mathrm{mN/m}$ and $\Delta\rho_{cd} = 12\,\mathrm{kg\,m^{-3}}$. The resulting capillary lengths are 420 µm at $\Delta T_{ps} = 0.05\,°\mathrm{C}$ and 971 µm at $\Delta T_{ps} = 3\,°\mathrm{C}$. Even for droplets with a diameter equal to the thickness of the cell, 50 µm, the effect of gravity is thus expected to be small. Finally, by inserting Eq. 6.4 and 6.8 into Eq. 6.7, we expect that the capillary length approaches zero upon approaching the critical temperature as $\Delta T^{*0.2}$. Gravity becomes thus more important near the critical point.

We estimate the geometry of the droplets from the interfacial and the gravitational energy. The interfacial energy is the product of the interfacial tension and the interfacial area, A,

$$U_s = \gamma_{cd} A. \tag{6.9}$$

We assume that gravity deforms a droplet into an oblate spheroid, that has a interfacial area [82, p2052],

$$A = 2\pi {R_e}^2 + \frac{\pi {R_p}^2}{e} \ln\left(\frac{1+e}{1-e}\right), \tag{6.10}$$

where R_e is the equatorial radius, R_p is the polar radius, and e is the ellipticity,

$$e \equiv \sqrt{1 - {R_p}^2/{R_e}^2}. \tag{6.11}$$

6.B

The gravitational energy is obtained by integrating the gravitational energy of an infinitesimal thin disk with mass m at height h from the bottom of the spheroid to the top of the spheroid,

$$U_g = \int_{h=0}^{2R_p} mgh \, \mathrm{d}h = \int_{h=0}^{2R_p} \Delta\rho_{cd}\pi[R(h)]^2 gh \, \mathrm{d}h = \frac{4}{3}\pi {R_p}^2 {R_e}^2 \Delta\rho_{cd} g, \tag{6.12}$$

where the radius is [82, p2052],

$$R(h) = R_e\sqrt{1 - \left(\frac{h - R_p}{R_p}\right)^2}. \tag{6.13}$$

The volume of an oblate spheroid is [82, p2052],

$$V = \frac{4}{3}\pi {R_e}^2 R_p. \tag{6.14}$$

Upon deformation, the volume should be conserved, and hence, R_p can be expressed in terms of R_e and V,

$$R_p = \frac{3V}{4\pi {R_e}^2}. \tag{6.15}$$

Furthermore, we define the relative equatorial radius,

$$x_e = \frac{R_e}{R} = \sqrt[3]{\frac{4\pi}{3V}} R_e, \tag{6.16}$$

where R is the radius of sphere with volume V.

Finally, the total energy is given by the sum of the interfacial energy (Eq. 6.9) and the gravitational energy (Eq. 6.12),

$$U_{tot} = U_s + U_g. \tag{6.17}$$

Using these equations, we calculate the shape of droplets at 0.05 °C and 3 °C above the critical point. We take values for the interfacial tension and the difference in the density as defined above, the volume is the volume of a sphere with a diameter of 50 µm, i.e. equal to the thickness of the measurement cells. Inserting these

values and Eq. 6.9 to 6.12 and 6.15 to 6.16 into Eq. 6.17, and minimizing the sum numerically for x_e using Wolfram Mathematica 10, gives $x_e = 1.00074$ at $\Delta T_{ps} = 0.05\,°C$ and $x_e = 1.00014$ at $\Delta T_{ps} = 3\,°C$. Even close to the critical point and for droplets as big as the diameter of the cell, the equatorial radius is thus virtually identical to the radius of a sphere with the same volume. Hence, deformation of droplets due to gravity can be neglected.

6.C. Contactless Attachment Energy on a Flat Interface

Similar to Wang *et al.* [132], the free energy of a spherical particle near a flat charged interface is estimated as the sum of 1) attraction to an interfacial charge and 2) repulsion by an image charge (Fig. 6.5a).

For the attraction to an interfacial charge, we use the electrostatic double layer interaction potential for a spherical particle at a surface-to-surface distance, r_{ss}, from a flat interface in the so-called linear superposition approximation [139, p317],

$$w_{int}(r_{ss}, \psi_p, \psi_{int}) = R_p \mathcal{Z}(\psi_p, \psi_{int}) e^{-\kappa r_{ss}}, \tag{6.18}$$

where ψ_p is the surface potential of the particle, ψ_{int} is the potential over the interface, R_p is the radius of the particle, κ is the inverse Debye length, $r_{ss} \ll R_p$, and $\mathcal{Z}$ is the electrostatic double layer interaction constant [7, p238, 139, p316],

$$\mathcal{Z}(\psi_1, \psi_2) = 64\pi \frac{{k_B}^2 T^2}{e^2} \varepsilon_0 \varepsilon_r \tanh\left(\frac{e\psi_1}{4k_B T}\right) \tanh\left(\frac{e\psi_2}{4k_B T}\right), \tag{6.19}$$

where k_B is the Boltzmann constant, T is the temperature, e is the electron charge, ε_0 is the vacuum permittivity, ε_r is the relative permittivity, and ψ_1 and ψ_2 are surface potentials. Here, we assumed monovalent salt and as the radius of the droplets is much larger than the radius of the particles, we assumed the interface to be flat. As expected, the interaction potential is positive and thus repulsive if the potentials have the same sign, and the potential is attractive for an oppositely charged particle and surface.

Next, we calculate the interaction with an image charge. A charge density, σ, at a distance r_{ss} from an interface experiences an interaction as if there was an image charge density [139, p258],

$$\sigma_{img} = \sigma \frac{\varepsilon_{r,c} - \varepsilon_{r,d}}{\varepsilon_{r,c} + \varepsilon_{r,d}}, \tag{6.20}$$

at a distance r_{ss} on the other side of the interface. Here, $\varepsilon_{r,c}$ is the relative permittivity of the continuous phase in which the charge resides and $\varepsilon_{r,d}$ is the relative permittivity of the dispersed phase. If $\varepsilon_{r,c} > \varepsilon_{r,d}$, the sign of the image charge is equal to the sign of the original charge, and repulsion is induced, while for $\varepsilon_{r,c} < \varepsilon_{r,d}$, the interaction is attractive. The Grahame equation relates a charge density to the surface potential [7, p135, 139, p308],

$$\sigma(\psi_1) = \sqrt{8\varepsilon_0\varepsilon_r k_B T I}\sinh\left(\frac{e\psi_1}{2k_B T}\right), \tag{6.21}$$

where I is the ionic strength, ψ_1 is the original surface potential, and we again assume monovalent salt. The image charge potential can be calculated by solving Eq. 6.21 for the surface potential and inserting Eq. 6.20 and 6.21,

$$\psi_{img}(\psi_1) = \frac{2k_B T}{e}\sinh^{-1}\left(\frac{\sigma_{img}(\psi_1)}{\sqrt{8\varepsilon_0\varepsilon_r k_B T I}}\right) \tag{6.22}$$

$$= \frac{2k_B T}{e}\sinh^{-1}\left(\frac{\varepsilon_{r,c}-\varepsilon_{r,d}}{\varepsilon_{r,c}+\varepsilon_{r,d}}\sinh\left(\frac{e\psi_1}{2k_B T}\right)\right). \tag{6.23}$$

Next, the electrostatic interaction of a charged flat surface with an image charged surface at a surface-to-surface distance, $2r_{ij}$, from the original surface is given by [139, p317],

$$\frac{w_{img}(r_{ij},\psi_1)}{A} = \frac{\kappa}{2\pi}\mathcal{Z}(\psi_1,\psi_{img}(\psi_1))e^{-2\kappa r_{ij}}. \tag{6.24}$$

where A is the area of the surfaces. To obtain the interaction potential for a sphere with its image sphere, we use the Derjaguin approximation for two interaction spheres, and integrate the result with integration boundaries that result in zero potential at infinite separation [139, p216],

$$w_{img}(r_{ss},\psi_p) = \int_{r_{ij}=r_{ss}}^{\infty}\pi R_p\frac{w_{img}(r_{ij},\psi_p)}{A}\,\mathrm{d}r_{ij} = \tfrac{1}{4}R_p\mathcal{Z}(\psi_p,\psi_{img}(\psi_p))e^{-2\kappa r_{ss}}, \tag{6.25}$$

where we inserted Eq. 6.24, and $\psi_1 = \psi_p$.

Finally, we take the total interaction potential as the sum of Eq. 6.18 and Eq. 6.25,

$$w(r_{\mathrm{ss}}, \psi_{\mathrm{p}}, \psi_{\mathrm{int}}) = w_{\mathrm{int}}(r_{\mathrm{ss}}, \psi_{\mathrm{p}}, \psi_{\mathrm{int}}) + w_{\mathrm{img}}(r_{\mathrm{ss}}, \psi_{\mathrm{p}}) \tag{6.26}$$

$$= R_{\mathrm{p}} \left[\mathcal{Z}(\psi_{\mathrm{p}}, \psi_{\mathrm{int}}) e^{-\kappa r_{\mathrm{ss}}} + \tfrac{1}{4} \mathcal{Z}(\psi_{\mathrm{p}}, \psi_{\mathrm{img}}(\psi_{\mathrm{p}})) e^{-2\kappa r_{\mathrm{ss}}} \right] \tag{6.27}$$

The surface-to-surface distance at which the interaction potential has the strongest attraction, r_{ss}^*, is found by taking the derivative of Eq. 6.27 with respect to r_{ss},

$$\frac{\partial w(r_{\mathrm{ss}}, \psi_{\mathrm{p}}, \psi_{\mathrm{int}})}{\partial r_{\mathrm{ss}}} = 0 \iff \kappa r_{\mathrm{ss}} = \ln \left(\frac{-\mathcal{Z}(\psi_{\mathrm{p}}, \psi_{\mathrm{img}}(\psi_{\mathrm{p}}))}{2\mathcal{Z}(\psi_{\mathrm{p}}, \psi_{\mathrm{int}})} \right), \tag{6.28}$$

where the signs of ψ_{p} and ψ_{img} should be opposite to the sign of ψ_{int}. Furthermore, the interaction potential at r_{ss}^* is,

$$w(r_{\mathrm{ss}}^*, \psi_{\mathrm{p}}, \psi_{\mathrm{int}}) = -R_{\mathrm{p}} \frac{\mathcal{Z}(\psi_{\mathrm{p}}, \psi_{\mathrm{int}})^2}{\mathcal{Z}(\psi_{\mathrm{p}}, \psi_{\mathrm{img}}(\psi_{\mathrm{p}}))}, \tag{6.29}$$

while the interaction potential at contact is,

$$w(r_{\mathrm{ss}} = 0, \psi_{\mathrm{p}}, \psi_{\mathrm{int}}) = R_{\mathrm{p}} \left[\mathcal{Z}(\psi_{\mathrm{p}}, \psi_{\mathrm{int}}) + \tfrac{1}{4} \mathcal{Z}(\psi_{\mathrm{p}}, \psi_{\mathrm{img}}(\psi_{\mathrm{p}})) \right]. \tag{6.30}$$

We qualitatively estimate the shape of the total interaction potential. The surface potential of the particles, ψ_{p}, should be negative due to sulphate groups at the particle surface. We did not add additional salt, so the surface potential on the interface should be mainly due to positively charged counterions. These could have a preference for the dispersed phase, resulting in a positive potential over the interface, ψ_{int}. Hence, we expect the electrostatic double layer interaction constant, $\mathcal{Z}(\psi_{\mathrm{p}}, \psi_{\mathrm{int}})$, to be negative (Eq. 6.19). The first term in the square brackets of Eq. 6.27, describes the particle-interface interaction, and is thus expected to result in attraction. For contact-less adsorption, the attraction should be counter-acted by a strong short-range repulsion to prevent adsorption onto the interface. The range of the second term, that describes the image charge interaction, $1/2\kappa$, is indeed shorter than for the interface interaction, $1/\kappa$. Furthermore, the image charge interaction is repulsive if the image charge potential, ψ_{img}, has the same sign as the potential of the particle, that is, if $\varepsilon_{\mathrm{r,c}} > \varepsilon_{\mathrm{r,d}}$ (Eq. 6.23). Hence, if the

interfacial attraction and image charge repulsion are strong enough, the potential of Eq. 6.27 could induce contactless attachment.

We estimate the values for the parameters in above equations for the experiment in Fig. 6.3b. The mean radius of the particles is 262 nm. For 3MP/D_2O at $m_w = 0.71$, the attachment transition is observed at 2 °C above the critical point, i.e. at 41.1 °C. The mass fractions of water at 41.1 °C are 0.61 and 0.81 (Fig. 6.1b- -), and we assume the relative permittivities to be the mass weighed averages of the permittivities of 3MP and D_2O. Hence, $\varepsilon_r = \varepsilon_{r,c} = 61$ and $\varepsilon_{r,d} = 48$, where we used temperature dependent permittivities for 3MP and normal water [6, p6-188,p6-196]. We assumed the continuous phase to be the water-rich phase, so that $\varepsilon_{r,c} > \varepsilon_{r,d}$, and the image charge interaction is repulsive (Eq. 6.20). We take the zeta potential as a measure for the surface potential. In water in 1 mM salt, the zeta potential of similar cross-linked polystyrene particles is about −50 to −80 mV (App. Table 5.1). In a 3MP/D_2O medium, the zeta potential is expected to be lower as 3MP is less polar. It is, however, sufficiently high to prevent aggregation, and, hence, we estimate $\psi_p = -30$ mV. Substituting these values into Eq. 6.23 and Eq. 6.19 gives $\psi_{img}(\psi_p) = -3.5$ mV and $\mathcal{Z}(\psi_p, \psi_{img}(\psi_p)) = 0.16 k_B T/\text{nm}$.

Using these parameters, we estimate if contactless attachment can explain the attachment of particles in Fig. 6.3b. We expect contactless attachment if both the depth of the interaction potential as well as the strength of the repulsion at contact are sufficiently strong, say $w(r^*_{ss}, \psi_p, \psi_{int}) \leq -6 k_B T$ and $w(r_{ss} = 0, \psi_p, \psi_{int}) \geq 6 k_B T$. Inserting the estimated values of the previous paragraph into Eq. 6.29 and solving for the potential at the interface gives $\psi_{int} \geq 1.3$ mV for the first condition (Fig. 6.5b—). For the second condition, however, $\psi_{int} \leq 0.4$ mV (Fig. 6.5b- -). Clearly, both conditions can not be fulfilled at the same time.

The interfacial potential at which the strength of the attraction and the repulsion are equal is obtained using Eq. 6.29 and Eq. 6.30,

$$w(r^*_{ss}, \psi_p, \psi_{int}) = -w(r_{ss} = 0, \psi_p, \psi_{int}) \tag{6.31}$$

$$\mathcal{Z}(\psi_p, \psi_{int}) = -\frac{\sqrt{2}-1}{2} \mathcal{Z}(\psi_p, \psi_{img}(\psi_p)), \tag{6.32}$$

where the interaction constants have opposite sign. Inserting this result into Eq. 6.29 gives an attraction strength of,

$$w(r^*_{ss}, \psi_p, \psi_{int}) = -\frac{3-2\sqrt{2}}{4} R_p \mathcal{Z}(\psi_p, \psi_{img}(\psi_p)). \tag{6.33}$$

Inserting the estimated values for 3MP/D_2O at $\Delta T^* = 2\,°C$ shows that the strength of the attraction and the repulsion are equal at $-1.8k_BT$ and $1.8k_BT$ respectively if the surface potential is $\psi_{int} = 0.7\,mV$ (Fig. 6.5b⋯). These interaction strengths are not nearly enough for permanent attachment. The image charge repulsion is thus too weak to compensate an interfacial attraction that is sufficient for attachment of particles. Hence, we conclude that contactless attachment on a flat interface can not explain the observations in Fig. 6.3.

Next, we study the critical behaviour of the extremes in the interaction potential. As the surface potentials are relatively small, $|\psi_i| < 4k_BT/e$, we can assume $\tanh x = x$ in Eq. 6.19, resulting in,

$$w(r_{ss}^*, \psi_p, \psi_{int}) = -\frac{4\pi R_p \varepsilon_0 \varepsilon_r \psi_p {\psi_{int}}^2}{\psi_{img}(\psi_p)} = -\frac{c_1(\Delta T^{*0.3})^2}{\Delta T^{*0.3}} = -c_1 \Delta T^{*0.3}, \tag{6.34}$$

$$w(r_{ss} = 0, \psi_p, \psi_{int}) = 4\pi R_p \varepsilon_0 \varepsilon_r \psi_p \left[\psi_{int} + \tfrac{1}{4}\psi_{img}(\psi_p)\right] = c_2 \Delta T^{*0.3}, \tag{6.35}$$

where we inserted Eq. 6.19 into Eq. 6.29 and Eq. 6.30, assumed the interfacial potential and the potential of the image charge to approach the critical point as the difference in the composition (App. Fig. 6.2), assumed all other variables, including ε_r and ψ_p to be constant, and gathered the constants in c_1 and c_2. The minimum attraction strength as well as the maximum repulsion approach the critical point with the same exponent, and are zero at the critical point, as expected. Furthermore, if we assume the attraction and the repulsion to be $-1.8k_BT$ and $1.8k_BT$ at 2 °C, we obtain the temperature dependent attachment energy (App. Fig. 6.5). The contactless attachment energy is less sensitive to the temperature than the adsorption energy (compare App. Fig. 6.5 to Fig. 6.4c). This seems to be in contrast with a transition from attachment to no attachment upon increasing the temperature with 0.1 °C (Fig. 6.6h–j).

Finally, we check if our approximations are valid. For the Derjaguin approximation, r_{ss} should be much smaller than R_p. The range of interest is from $r_{ss} = 0$ to $2/\kappa$ (Fig. 6.5b), so this condition is fulfilled if $\kappa^{-1} \ll 130\,nm$ which even without added salt should be the case. Furthermore, in the linear superposition approximation, we assumed the midplane potentials to be small. As both ψ_{img} and ψ_{int} are small, this condition should also be met. Finally, we assumed the interface to be flat. As the interfacial tension is very low, we expect the interface to deform upon attachment to increase the attractive interaction with the particles. Hence,

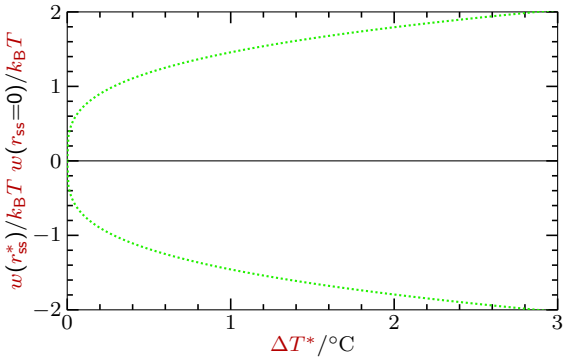

Appendix Figure 6.5. Contactless attachment energy. The contactless maximum attraction strength, $w(r_{ss}^*)$ (negative values), and maximum repulsion, $w(r_{ss}=0)/k_BT$, (postive values) are given as a function of the temperature above the critical temperature, ΔT^*, for $\psi_{int} = 0.7\,\mathrm{mV}$.

the attraction and repulsion are expected to be stronger, and further work should verify if they are strong enough for permanent attachment onto the interface.

6.D. Capillary Attraction Energy

We estimate the strength of the attraction between the particles in Fig. 6.3b. We assume that the particles are adsorbed onto the interface with contact angle, $\theta_c = 164°$, at which the adsorption energy is $-6k_BT$. Capillary attraction arises due to deformation of the interface by the irregular surface of the particles. For spherical particles with irregularities of size h_c, the interaction potential between two particles is [129, 130],

$$w(r_{ij}) = -12\pi\gamma_{cd}{h_c}^2\frac{{R_c}^4}{{r_{ij}}^4}, \tag{6.36}$$

where r_{ij} is the distance between the centres of the two particles, γ_{cd} is the interfacial tension between the continuous and the dispersed phase, and R_c is the radius of the contact line. Here, the particles are assumed to be oriented in such a way that their attraction is maximized. To derive Eq. 6.36, Stamou *et al.* [129] only take the second order, or quadrupole term of the height of the interface into

account,

$$h_{\mathrm{int}}^{(2)}(r,\theta) = h_{\mathrm{c}} \cos\left[2(\theta-\theta_0)\right] \left(\frac{R_{\mathrm{c}}}{r}\right)^2, \tag{6.37}$$

where r and θ are polar coordinates with the origin at the centre of the particle, θ_0 is the angle at which the contact line has its maximum height, and h_{c} is the height of the undulations of the contact line, i.e. the size of the irregularities. This assumption is valid if r_{ij} is much larger than R_{c} as lower order terms are not allowed, and the terms decay with the inverse power of their multipole order, i.e. higher order terms decay more rapidly.

For phase-separated 3MP/D2O, at $\Delta T^* = 2\,°\mathrm{C}$, we estimate the interfacial tension using Eq. 6.4, resulting in $\gamma_{\mathrm{cd}} = 0.079\,\mathrm{mN/m}$. Furthermore, the radius of the contact line, $R_{\mathrm{c}} = R_{\mathrm{p}} \cos(\theta_{\mathrm{c}} - 90°) = 72\,\mathrm{nm}$, is determined similar as in Fig. 6.2d and Eq. 6.2, but now for $\theta_{\mathrm{c}} = 164°$ and a particle with radius $R_{\mathrm{p}} = 262\,\mathrm{nm}$ instead of a droplet with radius R_{d}. Finally, we calculate the energy at close contact between the particles, $r_{ij} = 2R_{\mathrm{p}}$.

We insert these values into Eq. 6.36, and find that the strength of the interaction energy is larger than the thermal energy, $k_{\mathrm{B}}T$, if $h_{\mathrm{c}} \geq 6 \times 10\,\mathrm{nm}$. This value is relatively large, but comparable to the height of the irregularities in App. Fig. 6.3. An interaction strength of about $-k_{\mathrm{B}}T$ might result in the formation of clusters, as the particles are confined to a relatively small two-dimensional surface, and can make six bonds each.

The size of the irregularities, however, is comparable to the contact radius R_{c}, and the theory is probably not valid in this limit. Furthermore, close to the critical point, the thickness of the interface increases as $\Delta T^{*-0.6}$ [113], and this could also influence the capillary attraction potential. Finally, we check the assumption that only the quadrupole term of the height of the interface is taken into account (Eq. 6.37). Due to the large contact angle, the contact radius is an order of magnitude lower than the interparticle distance at contact and $R_{\mathrm{p}} \gg R_{\mathrm{c}}$. Hence, for a crude estimation, it seems valid to only take this term into account, as other terms decay more rapidly. We conclude, however, that more work is needed to more accurately estimate the capillary interaction potential.

6.E. Phase Diagram Analysis

For a phase separating system, the fraction between the total masses of each phase can be determined using the lever rule. This rule relates the total mass of

each phase, m_i, with the distances along the horizontal tie line, l_i [140, p.178],

$$m_c l_c = m_d l_d, \tag{6.38}$$

where the indexes refer to the continuous and dispersed phase, and we rewrote the equation for masses instead of molar amounts. For our mixtures, the tie line length is the difference in the mass fraction of water before and after phase separation, $l_i = |m_{w,i} - m_{w,0}|$.

6.5

The relative amount of each phase can be estimated for a given temperature and initial mole fraction by fitting the lower phase separation temperatures (Fig. 6.1b--). For the PnP/H_2O mixture at $m_w = 0.68$ in Fig. 6.6, the phase separation temperature is estimated to be 34.6 °C. At $\Delta T_{ps} = 4$ °C, the estimated compositions of each phase are $m_{w,c} = 0.79$ and $m_{w,d} = 0.40$, resulting in an estimated total mass ratio of $m_d/m_c = 0.41$. At $\Delta T_{ps} = 2$ °C, however, $m_{w,c} = 0.77$ and $m_{w,d} = 0.46$, resulting in an estimated total mass ratio of $m_d/m_c = 0.39$, where we assumed the phase with the lowest mass to be the dispersed phase. Neglecting the change in the density of each phase, the volume of the droplets thus shrinks upon decreasing the temperature.

7

Thermoreversible Self-Assembly into Micelle-like Structures in Near-Critical Mixtures

Abstract

Particles with directional interactions can self-assemble into new materials and are used to model interactions between biomolecules. Here, we use near-critical-solvent-mediated interactions to induce thermoreversible directional bonds between snowman-like particles. We demonstrate that in a water poor, near-critical mixture, hydrophilic spheres aggregate with an externally tunable attraction strength. Similar hydrophobic spheres, on the other hand, are only slightly attractive. Consequently, snowman-like particles that consist of a hydrophilic core and a hydrophobic protrusion have externally tunable, directional interactions. Furthermore, by changing the composition of the mixture, thermoreversible self-assembly into either oblate spheroidal or cylindrical micelle-like structures is induced.

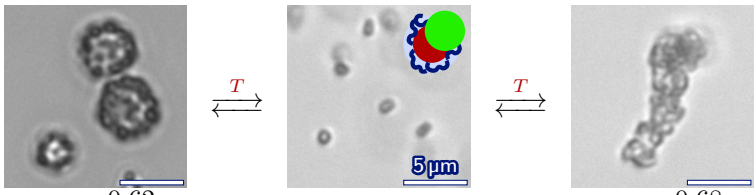

7.1. Introduction

Patchy particles have distinct surface regions with specific properties. Using mutually attractive patches, directional interactions can be induced, resulting in self-assembling materials and candidate models for biological structures [24, 27, 85]. Patchy attraction has previously been induced using depletion interaction, hydrophobic attraction, and complementary DNA hybridization [26, 28, 29]. Attraction between DNA functionalized patchy particles can be externally switched on and off with temperature [8, 29]. These particles are, however, challenging to synthesize, and tuning the experimental conditions to obtain kinetically accessible, thermodynamically stable clusters is still challenging.

Thermoreversible attractions can also be induced by near-critical-solvent-mediated interactions that are often referred to as critical Casimir forces [47, 48, 49]. The resulting attraction between solids in near-critical mixtures is explained as a result of either solvent fluctuations or a wetting transition [112, 141]. Even though the origin of the interaction is debated, attraction has been observed in both experiments [50, 51, 142] and explicit computer simulations [143]. Furthermore, the degree of the hydrophobicity of the surface strongly influences the strength and even the sign of the interaction, and attraction strengths of several times the thermal energy, $k_{\mathrm{B}}T$, can be obtained [50, 144]. Hence, thermo-reversible directional interactions can be induced for anisotropically functionalized Janus particles [145]. For shape-anisotropic particles, however, only preliminary results of self-assembly into colloidal strings have been published [146].

Here, we use near-critical-solvent-mediated interactions to induce thermoreversible self-assembly of snowman-like particles into micelle-like structures. In the first part of this chapter, we immerse isotropic particles in a water-poor, near-critical mixture. Colloidal spheres with a hydrophilic brush have externally tunable attractions with a strength of about $-4\,k_{\mathrm{B}}T$. Similar spheres without a brush, on the other hand, have much weaker mutual attractions in this mixture. In the second part of this chapter, we study anisotropic particles. For snowman-like particles that consist of a core with a hydrophilic brush and a non-functionalized protrusion, we expect attraction between the cores. Consequently, these anisotropic particles form structures with a reduced dimensionality, and thermoreversible self-assembly into cylindrical and oblate spheroidal micelle-like structures is observed.

7.2. Methods

7.2.1. Chemicals and Synthesis The components of the binary mixture where used as received. 3-methylpyridine (3MP, 236276, $\geq 99.5\%$), was obtained from Aldrich; and deuterium oxide (heavy water, D_2O, DLM-4-1000. 99.9%) was obtained from Cambridge Isotope Laboratories. Cross-linked poly(styrene-*co*-acrylic acid) (CPSAA) spheres, cross-linked polystyrene (CPS) spheres and snowman-like particles that consist of a CPSAA core and a polystyrene protrusion were used. CPSAA spheres with a diameter of 530 nm (Fig. 2.1), and CPS spheres with a diameter of 524 nm (App. Fig. 6.3), were synthesized as described in Subsection 2.2.2. For the synthesis of snowman-like particles with a diameter of the core of 771 nm (App. Fig. 7.2), Subsection 2.2.4 was followed with swelling ratio, $S = 6.7$, and by rotating the tube at 80 rpm instead of stirring with a stir bar.

7.2.2. Sample Preparation Samples of colloidal particles in binary mixtures were prepared in thin glass cells. Dispersions were obtained by mixing weighed amounts of 3MP, D_2O and colloids washed in D_2O. After vortexing the dispersions (Labotech TMO1), $0.05 \times 1 \times 50\,mm^3$ (Fig. 7.1 and Fig. 7.2) or $0.2 \times 4 \times 50\,mm^3$ (Fig. 7.3) glass tubes (VitroCom W5005-050 or W3520-050) were filled by capillary action. Next, both ends of the tubes were sealed in a flame (Prodont Holliger Microtorch II), and the samples were sonicated before each measurement.

7.2.3. Microscopy Samples were studied with an optical microscope and heated with a heating stage. A Nikon Ti-U inverted optical microscope was used in bright field mode with a Lumenera Infinity X camera. Fig. 7.1a–h and Fig. 7.3 were obtained with a CFI Plan Fluor 60×/0.70 objective with 1.5× intermediate magnification, and Fig. 7.1i–k were obtained with the same objective with no intermediate magnification, while Fig. 7.2 was obtained with a Plan Apo VC 100×/1.40 objective with no intermediate magnification. Samples were fixated with adhesive tape on a Linkam THMS600 heating stage that was operated with a Linkam TP 93 controller. We report the temperature relative to the lower phase separation temperature, $\Delta T_{ps} = T - T_{ps}$ where T is the temperature of the heating stage, and T_{ps} is the temperature at which phase separation is observed.

Finally, transmission electron microscopy images were obtained as described in Subsection 2.2.5.

7.3. Results and Discussion

7.3.1. Spherical Particles Near-critical-solvent-mediated attraction between spherical colloids is induced in a mixture of 3-methylpyridine and heavy water ($3MP/D_2O$) (Fig. 7.1). We study particles both with and without a hydrophilic brush, and immerse the particles in mixtures with a mass fraction of water, m_w, of 0.67

and 0.66. These compositions are at the water-poor side of the critical point at $m_w = 0.71$ [110] (Fig. 6.1b*). Phase separation is observed at the lower phase separation temperature, T_{ps}, where the temperature of the heating stage is 38.8 °C and 38.5 °C for $m_w = 0.67$ and 0.66. Interpolating previously measured values, however, results in $T_{ps} = 39.3$ °C and 39.5 °C at these compositions [110] (Fig. 6.1b- -). The slightly lower temperatures we measure, might be due to the presence of the particles, contamination by for example oligomers, or a deviation in the temperature sensor. By reporting the relative temperature, $\Delta T_{ps} = T - T_{ps}$, we minimize the influence of these effects.

7.3

Just below the lower phase separation temperature, i.e. near the lower critical point, poly(styrene-*co*-acrylic acid) spheres with a hydrophilic acrylic acid-rich brush (Subsection 2.3.1) are mutually attractive and form clusters (Fig. 7.1a). As expected, the interaction strength depends strongly on the temperature. Clusters are formed upon approaching the phase separation temperature, i.e. when $|\Delta T_{ps}| \leq 0.7$ °C, and fall apart upon increasing $|\Delta T_{ps}|$ (Fig. 7.1a–d). Furthermore, the assembly and disassembly can be repeated (Fig. 7.1e–h). At $\Delta T_{ps} = -0.7$ °C, clusters grow by incorporating unbound particles and by merging with other clusters (Fig. 7.1f–g). After about one hour, only a few unbound particles are left, and large, slowly moving clusters remain. We define the width of a cluster as the size of its smallest horizontal dimension. Here, the width is about 3 µm (Fig. 7.1g), and thus much larger than the diameter of the particles of 0.53 µm. By changing the focal plane, we estimate that the thickness of the clusters, i.e. the size in the vertical direction, should also be multiple particle diameters. Consequently, we estimate that about half of the particles is at the interface of the clusters, while the other half should be fully surrounded by other particles (Fig. 7.1i).

Whereas unbound particles move in three dimensions, the clusters sediment and move in two dimensions over the bottom of the cell. This could be explained by buoyancy, as the density of polystyrene is slightly higher than the density of 3MP/D_2O (App. Table 6.1). Consequently, a single particle has a gravitational length of 1.5×10^2 µm and can thus diffuse over the entire 50 µm thickness of the cell (App. 7.B). A cluster of 1000 particles, however, has a gravitational length of 0.15 µm and can only move over the bottom of the cell. The variation in the tabulated density of polystyrene however, is 0.06 g cm^{-3}, and thus larger than the estimated difference between the density of polystyrene and the solvent, $\rho_p - \rho_m \approx 0.03$. Furthermore, our particles do not consist of pure polystyrene, but are cross-linked, have an acrylic acid brush, and the core might be swollen with

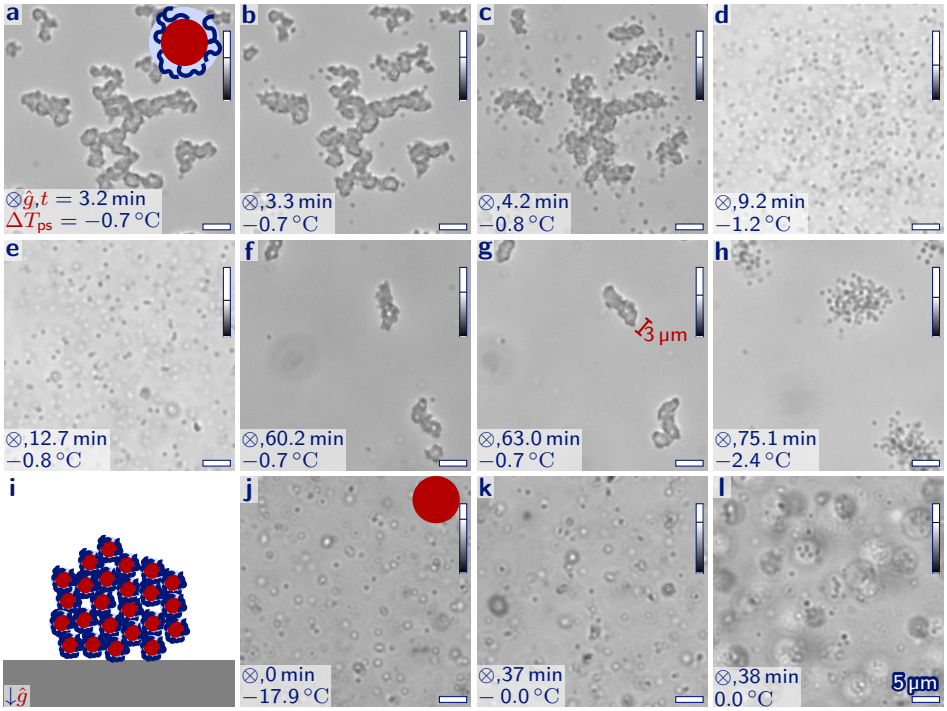

Figure 7.1. Thermoreversible self-assembly into random aggregates. Bright field microscopy images of spherical particles in near-critical 3MP/D_2O at temperatures below the phase separation temperature $\Delta T_{ps} < 0\,°C$. Poly(styrene-*co*-acrylic acid) spheres are studied in a mixture with a mass fraction of water, $m_w = 0.67$ (**a–h**). The spheres consist of a styrene-rich core (**a** ●) and an acrylic acid-rich brush (**a** ∿). Close to the lower phase separation temperature, $|\Delta T_{ps}| \leq 0.7\,°C$, these particles self-assemble into randomly shaped structures (**a**), and the clusters disassemble further away from T_{ps} (**b–d**). Upon increasing the temperature again, small clusters are formed (**e**) that subsequently grow into larger structures with a width of about 3 µm (**f–g**) and disassemble again upon cooling (**h**). The size and shape of the structures suggest that they are random aggregates (**i**) that sediment on the glass (**i** ●). Polystyrene spheres (**j** ●) in a mixture with $m_w = 0.66$, on the other hand, already form a few clusters well below the lower phase separation temperature (**j**) and the number of clusters increases only slightly (**k**) just before the medium phase separates (**l**). The direction of the gravitational field is indicated by $\hat{g}$ and the QR code links to a time series of **a–h** (phd.chrisevers.com/7qr1.mp4).

relatively hydrophobic 3MP, while the brush might be swollen with heavy water. Hence, the actual gravitational length could be very different, and one might suggest that clusters are found at the wall due to solvent-mediated attraction between particles and glass. In the second part of Fig. 7.1QR, single particles translate in two dimensions over the glass, before moving out of focus, whereas clusters remain at the glass. This suggests that a weak solvent-mediated attraction between the particles and the glass wall is present. For clusters, the solvent-mediated attraction is expected to be larger, as the contact area is larger than for a single particle. Hence, a combination of gravity and solvent-mediated attraction could explain the two dimensional movement of the clusters. To prevent effects of the wall in future experiments, the difference in the density between the particles and the medium could be brought to zero by using a mixture of 3MP/D_2O/H_2O. This, however, is challenging as the density of the mixture is temperature-dependent.

7.3

Thermoreversible aggregation in a near-critical mixture is in line with previous results for particles in bulk and near surfaces [48, 50, 51, 145]. We use near-critical mixtures with mass fractions of water of 0.67 and 0.66, while the critical mass fraction is 0.71 (Fig. 6.1b*), i.e. these mixtures are water-poor. For such mixtures, both theory and experiments have shown that attraction is induced between surfaces onto which the poor component preferentially adsorbs [48, 50]. On the water-poor side of the critical point, for example, attraction between hydrophilic surfaces and hydrophilic particles can be induced, while no attraction is observed between hydrophobic particles and hydrophobic surfaces [50]. Our mixture is also water-poor, and indeed, we observe attraction between hydrophilic particles. Furthermore, the attraction is very temperature sensitive. The first frame of Fig. 7.1QR, is obtained after equilibrating at $\Delta T_{\mathrm{ps}} = -0.5\,^{\circ}\mathrm{C}$ for 12 min and shows only one single particle, that happened to be stuck on the glass (App. Fig. 7.1a→). All other particles are aggregated, suggesting an interaction strength of at least $-4\,k_{\mathrm{B}}T$ (App. 7.C). At $\Delta T_{\mathrm{ps}} = -0.7\,^{\circ}\mathrm{C}$, on the other hand, freely moving, unbound particles are found (App. Fig. 7.1b→), suggesting an interaction strength of about $-4\,k_{\mathrm{B}}T$ (App. 7.C). These interaction strengths agree well with measurements by Hertlein *et al.* [50]. Furthermore, at $-4\,k_{\mathrm{B}}T$, bonds are expected to break once in a while. Consequently, equilibration to the lowest free energy state should be possible. At $\Delta T_{\mathrm{ps}} = -0.7\,^{\circ}\mathrm{C}$, the clusters fall apart upon decreasing the temperature less than $0.1\,^{\circ}\mathrm{C}$, which is the resolution of the heating stage (Fig. 7.1a–b). The interaction strength decreases thus significantly with only a small temperature change. Previous experiments have shown a similar transition

for particle–surface attractions. Upon decreasing the temperature with just 0.02 °C, Hertlein *et al.* [50] observed a transition from an attraction with a strength of $-3k_BT$, to no attraction.

Hydrophobic particles, on the other hand, are expected to be non-attractive in a water-poor solvent. Indeed, cross-linked polystyrene spheres show remarkably different behaviour than particles with a hydrophilic brush (compare Fig. 7.1j–l to a–h). At temperatures well below the lower phase separation temperature, already some clusters are found (Fig. 7.1j). The polystyrene particles are charge-stabilized by sulphate groups, but the electrostatic repulsion appears to be insufficient to prevent some bond formation. Most particles, however, are still unbound, so the attraction energy is only a few k_BT. Very close to the lower phase separation temperature, some additional clusters are formed (Fig. 7.1k), but still, most particles are unbound, suggesting an attraction strength slightly stronger than the thermal energy. As expected, the preferential adsorption of water onto these particles is thus much less than for spheres with a poly(acrylic acid) brush. The presence of sulphate groups on the particle surface, might result in some preferential adsorption of water, and thus a very weak solvent-mediated attraction upon approaching T_{ps}. We conclude that, in a water-poor, near-critical mixture, adding a hydrophilic brush results in a transition from very weak to relatively strong interparticle attractions.

7.3.2. Anisotropic Particles We induce directional interactions by growing a polystyrene protrusion onto the poly(styrene-*co*-acrylic acid) spheres (App. Fig. 7.2), and immersing these snowman-like particles in a near-critical mixture (Fig. 7.2). Each snowman-like particle consists of a core that corresponds to the relatively strongly attractive particles of the previous subsection, and a protrusion that corresponds to the weakly attractive particles. In contrast to the latter particles, the protrusions do not contain sulphate groups, which increases the hydrophobicity. On the other hand, the protrusions might contain some acrylic acid groups, which decrease the hydrophobicity. Hence, we expect the hydrophobicity of the protrusions and the polystyrene spheres in the previous subsection to be comparable, and their mutual attraction to be weak.

Phase separation is observed at $T_{ps} = 38.8\,°C$, which is again about 0.5 °C lower than the value obtained by interpolating previous measurements (Fig. 6.1b- -). Just below the lower phase separation temperature, snowman-like particles self-assemble into cylindrical structures (Fig. 7.2a). Analogous to the spherical particles,

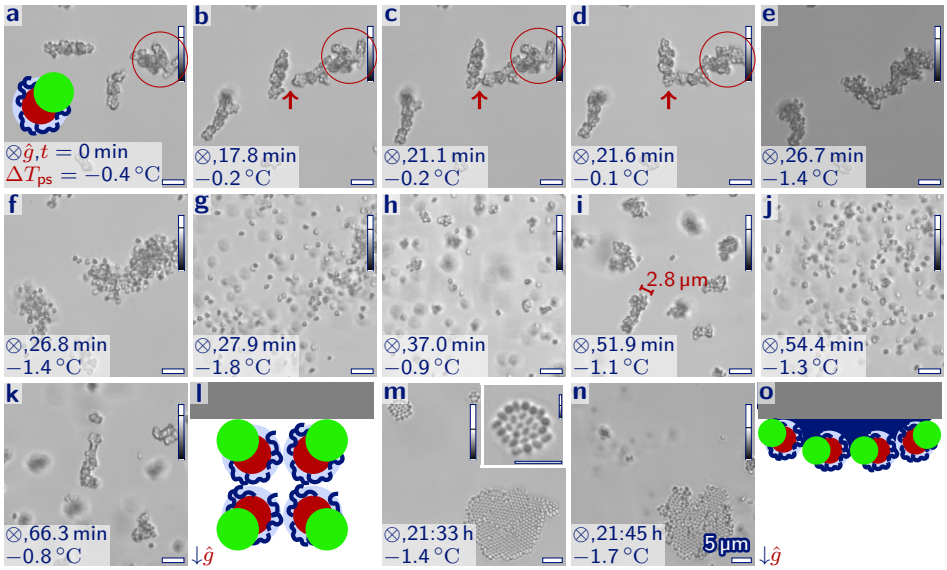

Figure 7.2. Thermoreversible self-assembly into cylindrical micelle-like structures. Bright field microscopy images of snowman-like particles in a 3MP/D_2O mixture with $m_w = 0.68$. The particles consist of a polystyrene-rich core (**a** ●) with an poly(acrylic acid)-rich brush (**a** ∿), and a polystyrene protrusion (**a** ●). Close to the lower phase separation temperature, $|\Delta T_{ps}| \lesssim 1.4\,°C$, snowman-like particles self-assemble into cylindrical structures (**a**) that merge head to tail into larger structures (**b–d** →). Upon decreasing the temperature, the structures fall apart (**e–f**) and only single particles are found (**g**). Increasing the temperature again results in small clusters (**h**) that merge into cylindrical structures (**i**). This process is repeated an additional time (**j–k**). Their size and shape suggest that the structures are cylindrical micelles (**l**) that cream to the glass (**l** ●). One day later, the cylindrical clusters reorganized into flat crystalline structures (**m–n**) which might be due to adsorption on a thin water-rich layer (**o** ●). The direction of the gravitational field is indicated by $\hat{g}$, and the QR code links to a time series of **a–k** and **m–n** (phd.chrisevers.com/7qr2.mp4).

the formation of clusters is thermoreversible, and a sharp transition between an attractive and a non-attractive regime is observed at $\Delta T_{\mathrm{ps}} \approx -1.4\,^{\circ}\mathrm{C}$ (Fig. 7.2e–f).

We find strong indications that the snowman-like particles have directional interactions. In the previous subsection, we observed that spherical particles with a hydrophilic brush are strongly mutually attractive, while similar particles without a brush are only weakly attractive. Hence, the cores with the hydrophilic brush are expected to be attractive, and should be oriented to the inside of the structures, while the protrusion should point to the outside (Fig. 7.2l). The radii of the core and the protrusion are comparable to the wavelength of light. Hence, we cannot directly observe the orientation of the particles in the microscopy images. We recognize, however, three indirect indications for this configuration. First of all, the width of the cylindrical structures is about 2.8 µm (Fig. 7.2i) and is slightly larger than twice the length of dried snowman-like particles, $l = 1.2\,\mu\mathrm{m}$ (App. Fig. 7.2). In solution, the hydrophilic brushes are expected to expand on the order of 0.1 µm (App. 5.B), and water-poor near-critical-solvent-mediated interactions have a typical range of about 0.02 µm [50], so the measured width is very close to the expected width for a core-to-core configuration of about 2.5 µm (Fig. 7.2l). Consequently, all particles seem to be at the surface of the clusters. At first sight, the structures of the clusters look rather similar for spherical and snowman-like particles (compare Fig. 7.1g to Fig. 7.2e). For spherical particles, however, the width of the clusters is about six times larger than the particle size, and only about half of the particles is at the surface of the clusters (Fig. 7.1g,i). Second, for snowman-like particles, the number of side branches is low, while for spherical particles, the structures can be very branched (compare Fig. 7.1a to Fig. 7.2e). Finally, in Fig. 7.2a–d, the merger of two clusters seems to induce large conformational changes. In these images, no unbound particles are observed and the attraction strength is thus strong. Consequently, the geometry of the clusters remains constant for minutes (Fig. 7.2a–c◯), i.e. clustered particles do not wiggle or change the relative positions to their neighbours (Fig. 7.2QR). In Fig. 7.2c–d, however, a large structural rearrangement is observed (Fig. 7.2c–d◯) exactly at the moment that two clusters merge (Fig. 7.2c–d→). This could be due to chance or an increase of the attraction strength with the temperature, but might also suggest a long-range periodicity in the structures of the clusters, i.e. that the orientation of particles inside the clusters is well-defined. These three observations all indicate that the snowman-like particles have directional interactions, resulting in cylindrical micelle-like structures.

The observed structures resemble cylindrical micelles comparable to those observed in molecular surfactants. For molecular amphiphiles, the surfactant packing parameter relates the geometry of the molecule to the structure of the micelles [147, 7, p14],

$$N_{\mathrm{sp}} = \frac{V_{\mathrm{att}}}{l_{\mathrm{att}} A_0}, \tag{7.1}$$

7.3

where V_{att} and l_{att} are the volume and the length of the mutually attractive part of the surfactant, and A_0 is the effective area of the non-attractive head group. The curvature of the self-assembled structures decreases with the surfactant number: for spherical micelles, $N_{\mathrm{sp}} \approx 0.33$, while for cylindrical micelles, $N_{\mathrm{sp}} \approx 0.5$, and for bilayers, $N_{\mathrm{sp}} \approx 1$ [7, p14]. We use the geometry of our colloidal particles, to calculate their surfactant parameter, $N_{\mathrm{sp}} = 0.65$ (App. 7.D). This value indeed corresponds best to cylindrical micelles.

After about one day, the cylindrical micelle-like structures had reorganized into crystalline monolayers (Fig. 7.2m–n). We speculate that this redistribution could be due to temperature fluctuations and subsequent adsorption of particles onto a thin water-rich layer (Fig. 7.2o). In the previous chapter, we saw that above the phase separation temperature, particles attach to the interface of phase separated droplets. The temperature of the heating stage was set to $\Delta T_{\mathrm{ps}} = -0.9\,^{\circ}\mathrm{C}$, but overnight, a temperature fluctuation of about $1\,^{\circ}\mathrm{C}$ could have induced such a transition. Previous experiments by Yu *et al.* [145], showed that when particles adsorb to a phase separated droplet, a thin water-rich layer on a glass surface could remain stable well below the phase separation temperature, and induce the formation of crystalline monolayers. Hence, when the temperature stabilized again, the particles are in a two dimensional crystal and orient parallel to the edge of the cell to cover the interfacial area (Fig. 7.2o). This suggests that unlike the relatively small and hydrophobic spheres in the previous chapter, the larger more hydrophilic snowman-like particles do not detach from the interface close to the critical point. Furthermore, the large crystalline structure is stable until $\Delta T_{\mathrm{ps}} = -1.7\,^{\circ}\mathrm{C}$ (Fig. 7.2m–n). This structure thus seems to be more stable than the cylindrical micelles, that fall apart below $\Delta T_{\mathrm{ps}} = -1.4\,^{\circ}\mathrm{C}$. Additional experiments should verify if crystalline structures indeed form upon increasing and decreasing the temperature, and if the observed increase in the stability can be reproduced.

The structure of the clusters can be changed by reducing the mass fraction of water. Whereas at $m_{\mathrm{w}} = 0.68$, cylindrical micelle-like structures are observed, similar particles form spheroidal structures at $m_{\mathrm{w}} = 0.62$ (Fig. 7.3). As before, the

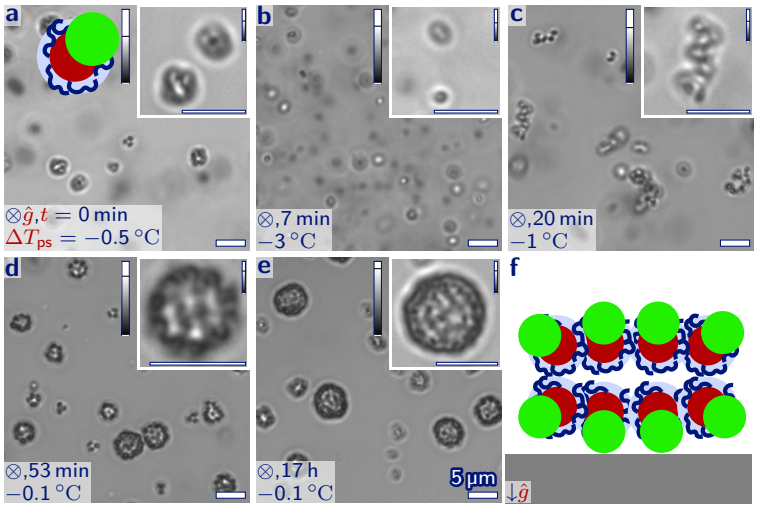

Figure 7.3. Thermoreversible self-assembly into oblate spheroidal micelle-like structures. Bright field microscopy images of snowman-like particles in a 3MP/D_2O mixture with $m_w = 0.62$. Close to the lower phase separation temperature, $|\Delta T_{ps}| \leq 1.0\,°C$, snowman-like particles self-assemble into spheroidal structures (**a**), and the clusters disassemble upon cooling (**b**). Upon increasing the temperature again, first, random aggregates are formed (**c**) that subsequently rearrange into spheroidal structures that are stable overnight (**d–e**). The size and shape of the structures suggest that the structures are oblate spheroidal micelles (**f**) that sediment to the glass (**f** ●). The direction of the gravitational field is indicated by $\hat{g}$.

formation of micelles is thermoreversible and at $\Delta T_{ps} = -1.0\,°C$, a sharp transition between an attractive and a non-attractive regime is observed. Above this threshold temperature, first, randomly shaped structures are formed, that after some minutes reorganize into spheroidal structures that are stable for many hours (Fig. 7.3c–e). The horizontal diameter of the structures is 3–5 µm and thus significantly larger than twice the length of the snowman-like particles, $l = 1.2\,µm$. By changing the position of the focal plane, the height of the clusters was estimated to be smaller than the width of the structures, but larger than the length of the particles. Hence, it seems plausible that the structures are oblate spheroidal micelle-like structures (Fig. 7.3f).

We hypothesize that a change in the interaction range could explain the difference in the morphology of the clusters upon changing the composition of the

solvent. Upon decreasing the mass fraction of water from $m_w = 0.68$ to 0.62, the distance to the critical point increases, and a transition from cylindrical to oblate spheroidal structures is observed (compare Fig. 7.2d to Fig. 7.3e). Oblate spheroidal structures are less curved than cylindrical structures. As the surfactant number, N_{sp}, decreases with the curvature of the clusters, we thus expect N_{sp} to increase upon decreasing m_w. Consequently, either the ratio of V_{att} over l_{att} increases, or A_0 decreases (Eq. 7.1). The polystyrene protrusion is rigid, and its interactions are dominated by excluded volume interactions with other particles, hence, A_0 is expected to be constant. For the poly(styrene-*co*-acrylic acid) core, however, the effective size depends on the range of the attractive potential between the cores. For a short-range attraction, the cores have to be close together, and the effective V_{att} over l_{att} ratio should be low, resulting in more curved structures. For a long-range attraction, on the other hand, V_{att}/l_{att} is larger, and structures are expected to be less curved. Hence, a change from short-range to long-range attraction upon decreasing m_w could explain the observed transition. More experiments are necessary to verify if the range of the interaction indeed increases upon decreasing m_w. Additionally, the effective size of the cores also depends on the size of the brush. The hydrophilic brush can change its configuration on the order of 0.1 µm depending on the solvent properties (App. 5.B). A decrease of the mass fraction of water is expected to result in a decrease of the size of the hydrophilic brush. Consequently, V_{att}/l_{att}, and the surfactant parameter should decrease upon decreasing m_w promoting a higher curvature. A change in the swelling of the brush is thus expected to resist the observed transition from cylindrical to oblate spheroidal structures. Measurements of the size of poly(styrene-*co*-acrylic acid) spheres as a function of m_w, however, are necessary to verify if the size of the core indeed decreases upon decreasing m_w.

The structures in Fig. 7.3d–e might, however, be small Pickering emulsion droplets. The resolution of the temperature sensor is 0.1 °C, so in Fig. 7.3d–e, the phase separation temperature might already have been reached. Consequently, phase-separated droplets could have formed and the particles could be attached onto the surface of these droplets. Additional experiments are necessary to verify if spheroidal micelle-like structures can also be formed further away from the phase separation temperature.

Furthermore, at $m_w = 0.62$ and 0.67, clusters of particles sediment to the bottom of the cell, while at $m_w = 0.68$, clusters cream to the top of the cell (compare Fig. 7.3f and 7.1i to Fig. 7.2l). This could be the result of buoyancy, if

the density of the medium, ρ_m, becomes greater than the density of the particles, ρ_p, upon increasing the heavy water concentration from 0.62 to 0.68 (Eq. 5.4). The density of the medium increase with m_w. The estimated density difference, however, $\rho_p - \rho_m = 0.04\,\mathrm{g\,cm^{-3}}$ at $m_w = 0.62$, and $0.03\,\mathrm{g\,cm^{-3}}$ at $m_w = 0.68$ (App. 7.B). The increase in ρ_m thus seems to be too small to explain a transition from sedimentation to creaming. As discussed in the previous chapter, the density of the particles might be influenced by preferential swelling. Upon increasing the mass fraction of water, swelling of the polystyrene core by 3MP is expected to decrease, resulting in an increase in ρ_p, and a stronger tendency to sediment (Eq. 5.4). Similarly, swelling of the hydrophilic brush by D_2O is also expected to increase the tendency to sediment. Hence, the expected swelling behaviour resists a shift from sedimentation to creaming upon increasing m_w. Finally, thermophoresis could also effect the sedimentation behaviour. As explained in Subsection 6.3.2, a temperature gradient can result in a net force towards the hot or the cold side of the sample (App. Fig. 6.1a). In Fig. 7.2, an oil immersion objective is used, while the other figures are obtained with a conventional objective. Direct contact between immersion oil and the bottom of the glass cell is expected to result in a larger temperature gradient than for contact with air. Consequently, the gradient induced force should be larger in Fig. 7.2 than in the other figures. This might explain that particles cream in Fig. 7.2, and sediment in Fig. 7.1 and 7.3. Further experiments are, however, necessary to fully understand the sedimentation and creaming behaviour.

Most observations in this chapter have been explained using existing theory on near-critical-solvent-mediated attraction and surfactant assembly. Additional experiments are, however, required to study the reproducibility of our observations. Furthermore, three main questions remain to be answered: 1) what causes the formation of crystalline monolayers, 2) what induces the transition from cylindrical to oblate spheroidal micelles, and 3) what causes the transition from sedimentation to creaming? In the previous discussion a number of explanations has been suggested, but further experiments are necessary to verify if these explanations are sufficient, or if new concepts are necessary to explain our results.

7.4. Conclusion

In a near-critical mixture, solvent-mediated attraction between particles is induced that strongly depends on the temperature and the hydrophobicity of the surface of the particles. Consequently, on the water-poor side of the critical point,

particles with a hydrophilic brush aggregate, while similar particles without a brush are only slightly attractive. Furthermore, the aggregation is thermoreversible, and the attraction strength is only several $k_{\mathrm{B}}T$. We use these properties to induce externally tunable, directional interactions for amphiphilic snowman-like particles. In a near-critical solvent, these particles have hydrophilic mutually attractive cores and hydrophobic, weakly attractive protrusions. Hence, these snowman-like particles self-assemble into micelle-like structures. Using concepts from surfactant self-assembly, we explain the formation of cylindrical structures. By decreasing the mass fraction of water, also oblate spheroidal clusters are formed. This suggests that the effective size of the hydrophilic core can be tuned by the composition of the liquid. However, further experiments are necessary to understand 1) the formation of oblate spheroidal micelles, 2) creaming and sedimentation of the particles, and 3) the formation of crystalline monolayers at a glass surface.

Externally tunable attraction of only several $k_{\mathrm{B}}T$ could facilitate self-assembly into structures that are up till now kinetically inaccessible. Snowman-like particles that self-assemble into micelle-like structures via anisotropic depletion interaction, for example, self-assemble into smaller structures than free energy calculations predict [28]. Finally, by exploring a larger range of compositions of the mixture, changing the size ratio between the core and the protrusion, and increasing the number of attractive cores, one might expect thermoreversible self-assembly into even more morphologies such as colloidal equivalents of surfactant bilayers, bicontinuous phases, and photonic crystals.

7.5. Acknowledgement

Anh Nguyen, Triet Dang and Peter Schall are thanked for their collaboration in designing this research and discussing the results. Anh and Triet are thanked for their help during the microscopy experiments.

7.A. Appendix Figures

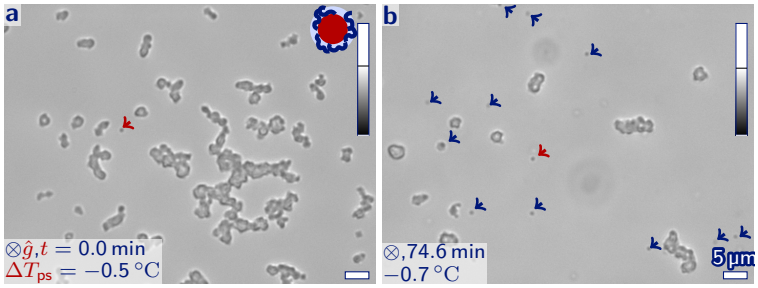

Appendix Figure 7.1. Self-assembled random aggregates. Bright field microscopy image of poly(styrene-*co*-acrylic acid) spheres in near-critical 3MP/D_2O at $m_w = 0.67$. After equilibration at $-0.5\,°C$ below the phase separation temperature for 12 min (**a**), one single particle is found (→) that was attached to the glass, whereas all other particles have aggregated. After equilibration at $\Delta T_{ps} = -0.7\,°C$ for 60 min (**b**), twelve unbound particles (→) and one single particle attached to the glass (→) were found. The spheres consist of a styrene-rich core (**a** ●) and an acrylic acid-rich brush (∿). These images are part of the time series in Fig. 7.1QR.

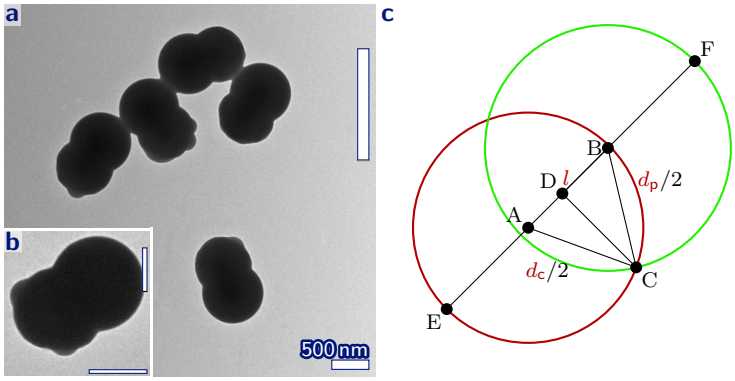

Appendix Figure 7.2. Snowman-like particles. Transmission electron microscopy images (**a–b**) and a schematic diagram (**c**) of snowman-like particles with a poly(styrene-*co*-acrylic acid) core (○) with diameter, $d_c = 771 \pm 26$ nm, a polystyrene protrusion (○) with diameter, $d_p = 823 \pm 14$ nm, and a total length, $l = 1175 \pm 26$ nm. The second values give the standard deviations over 79 particles, and the image levels are rescaled as indicated by the vertical bars.

7.B. Gravitational Length

We estimate the gravitational length following App. 5.C. The density of polystyrene is 1.06–1.12 g cm^{-3} [6, p15-93], while the density of 3MP/D_2O has previously been measured as a function of the composition at $T = 35\,°C$ [148]. By fitting these values to a second order polynomial, we estimate $\rho_p - \rho_m \approx 0.038$, 0.031 and 0.030 g cm^{-3} at $m_w = 0.62$, 0.67 and 0.68. Furthermore, the volume of the poly(styrene-*co*-acrylic acid) spheres is $\frac{4}{3}\pi R^3$, where $R = 265\,nm$ is the radius of the particles. Hence, for a single particle at $m_w = 0.67$ and $T = 38.1\,°C$, $l_g \approx 1.5 \times 10^2\,\mu m$, while for a cluster of 1000 particles, $l_g \approx 0.15\,\mu m$.

7.D

7.C. Interaction Strength

The interaction strength can be estimated from the number of free particles following Kraft *et al.* [28]. Analogues to the critical micelle concentration for molecular surfactants, the number of unbound particles, N_1, per volume, V, is given by [28],

$$N_1/V = \frac{1}{\xi^3} \exp\left(\frac{\langle N_b \rangle}{2} \frac{\varepsilon}{k_B T}\right), \tag{7.2}$$

where ξ is the range of the interaction, $\langle N_b \rangle$ is the average number of bonds per particle, ε is the interaction strength, k_B is the Boltzmann constant, and T is the temperature.

We estimate the attraction energy for poly(styrene-*co*-acrylic acid) spheres in near-critical 3MP/D_2O at $m_w = 0.67$ and $-0.5\,°C$ below the phase separation temperature (App. Fig. 7.1a). The interaction range is estimated from previous colloid-interface measurement for polystyrene particles in near-critical water-poor water/lutidine mixture, $\xi \approx 0.02\,\mu m$ [50]. As about half of the particles is in the interior of the clusters, and the other half is at the surface of the clusters (Fig. 7.1i), we estimate for the average number of bonds, $\langle N_b \rangle \approx 10$. Furthermore, after equilibrating for 12 min, no freely moving, unbound particles are found in the $4.7 \times 10^3\,\mu m^2$ area of the microscopy image, $N_1 < 1$. The axial resolution is $2\lambda n_D/NA^2 = 2\,\mu m$ [96, p207], where $\lambda = 5 \times 10^2\,nm$ is the wavelength of light, $n_D = 1$ is the refractive index of air, and NA = 0.70 is the numerical aperture of the objective. Hence, the imaged volume is about $V = 2 \times 10^4\,\mu m^3$. Inserting these values into Eq. 7.2, and solving for the interaction strength gives $\varepsilon \lesssim -4.3 k_B T$.

For the same system at $\Delta T_{ps} = -0.7\,°C$, the number of unbound particles, $N_p = 12$, after equilibrating for 60 minutes (App. Fig. 7.1b). Hence, at $\Delta T_{ps} = -0.7\,°C$, the interaction strength is about $\varepsilon \approx -3.8 k_B T$.

7.D. Surfactant Number

To predict the morphology of self-assembled clusters, we calculate the surfactant parameter (Eq. 7.1) for the snowman-like particles in App. Fig. 7.2. In the electron microscopy images, the polystyrene protrusions can be recognized from their smooth surfaces, while the poly(styrene-*co*-acrylic acid) cores are relatively rough (App. Fig. 7.2). The size of both lobes is detected as described in Subsection 3.2.5. For our particles, the protrusions have a diameter, $d_\mathrm{p} = 823\,\mathrm{nm}$, and correspond to the non-attractive part of a surfactant, resulting in $A_0 = \pi(d_\mathrm{p}/2)^2 = 5.3 \times 10^5\,\mathrm{nm}^2$. The poly(styrene-*co*-acrylic acid) cores are mutually attractive and correspond to the attractive part of a surfactant. The diameter of the core is $d_\mathrm{c} = 771\,\mathrm{nm}$, and the centre-to-centre distance to the protrusion is $r_\mathrm{cc} = 378\,\mathrm{nm}$. The length of the attractive part is DE, the length of the line segment from point D to E in App. Fig. 7.2c. This length can be obtained from Pythagoras's theorem, and the altitude DC of the triangle with corners ABC [82, p66],

$$\begin{aligned} l_\mathrm{att} &= AE + \sqrt{AC^2 - CD^2} && (7.3)\\ &= AE + \sqrt{AC^2 - (2\sqrt{s(s-AB)(s-BC)(s-AC)}/AB)^2} && (7.4)\\ &= d_\mathrm{c}/2 + \sqrt{{d_\mathrm{c}}^2/4 - 4s(s-r_\mathrm{cc})(s-d_\mathrm{p}/2)(s-d_\mathrm{c}/2)/{r_\mathrm{cc}}^2} && (7.5)\\ &= 547\,\mathrm{nm}, && (7.6) \end{aligned}$$

where s is the semiperimeter of the triangle ABC,

$$s = (r_\mathrm{cc} + d_\mathrm{c}/2 + d_\mathrm{p}/2)/2 = 588\,\mathrm{nm}. \quad (7.7)$$

Finally, the hydrophobic volume is given by the volume of the spherical cap with height, $h_\mathrm{cap} = DE = l_\mathrm{att}$, and radius $AC = d_\mathrm{c}/2$ [82, p2780],

$$V_\mathrm{att} = \tfrac{1}{3}\pi l_\mathrm{att}^2(\tfrac{3}{2}d_\mathrm{c} - l_\mathrm{att}) = 1.9 \times 10^8\,\mathrm{nm}^3. \quad (7.8)$$

Inserting these values into Eq. 7.1 gives $N_\mathrm{sp} = 0.65$.

List of Symbols

γ interfacial tension. 82

γ_{cd} interfacial tension between the continuous and the dispersed phase. 117–120, 122, 123, 137, 144, 145

γ_{sc} interfacial tension between a solid and the continuous phase. 117–119

γ_{sd} interfacial tension between a solid and the dispersed phase. 117–119

Δ difference. 29, 35, 135

ε attraction energy. 162

ε_0 vacuum permittivity. 139, 140, 143

ε_{cc} attraction energy between central spheres. 54, 57

ε_{pp} attraction energy between protrusions. 54

ε_r relative permittivity. 139, 140, 142, 143

$\varepsilon_{r,c}$ relative permittivity of the continuous phase. 139–142

$\varepsilon_{r,d}$ relative permittivity of the dispersed phase. 139–142

ζ zeta potential. 76, 100, 103, 104, 109

θ angle. 145

θ_c contact angle. 17, 19, 35–38, 42–44, 117–120, 122–125, 144, 145

κ inverse Debye length. 76, 102, 104, 128, 139–141, 143

λ wavelength. 80, 162

μ mean. 17, 37, 38, 43, 75, 76, 100, 105, 109

μ critical exponent for the interfacial tension. 119, 120, 132

$\tilde{\nu}$ wavenumber. 13, 14

ξ interaction potential range. 54, 55, 61, 162

ρ density. 134

$\Delta\rho_{cd}$ difference in the density between the continuous and the dispersed phase. 137, 138

ρ_m density of the medium. 107, 150, 158, 159, 162

ρ_p density of particles. 107, 150, 158, 159, 162

σ charge density. 139, 140

σ standard deviation. 17, 33, 37, 38, 43, 75, 76, 100, 104, 105, 109

Φ electrostatic potential. 104

Φ_0 electrostatic surface potential. 104

ϕ volume fraction. 88

Ψ wave function. 59, 68, 69
ψ surface potential. 139, 140, 143
ψ_{img} surface potential of an image charge. 140–143
ψ_{int} potential over an interface. 128, 139, 141–144
ψ_{p} surface potential of a particle. 139–143
A area. 137, 140, 156, 158, 163
A_0 initital area. 55, 56, 68
A_{ex} excluded area. 68
$A_{\mathrm{ex,p}}$ excluded area by a protrusion. 55, 56
A_{s} area covered by a satellite sphere. 55, 56
B brightness. 26, 27
$|\nabla B|$ magnitude of the gradient in the brightness. 27
$|\nabla B_{\mathrm{cc,max}}|$ maximum magnitude of the gradient in the brightness on the line between two centres. 34, 35, 48
$|\nabla B_{\mathrm{ROI,max}}|$ maximum magnitude of the gradient in the brightness in the region of interest. 28
$|\nabla B_{\mathrm{ROI,min}}|$ minimum magnitude of the maximum gradient in the brightness in the region of interest. 28, 48
c constant. 30, 68, 69, 143
d diameter. 13
d_0 diameter of a seed particle. 17–21
d_{c} diameter of a core or central sphere. 12, 17–21, 53–56, 61, 68, 85, 86, 107, 108, 161, 163
d_{hd} hydrodynamic diameter. 75, 100, 105–107, 109
d_{m} diameter of a microcapsule. 81, 84, 108
d_{p} diameter of a protrusion. 17, 53, 54, 56, 107, 108, 161, 163
d_{s} diameter of a satellite sphere. 53, 54, 56, 61, 68
e ellipticity of an oblate ellipsoid. 137, 138
e elementary charge. 139, 140, 143
$\hat{g}$ direction of the gravitational field. 77, 79, 85, 87–90, 92, 94, 97–99, 113, 118, 122, 129, 134, 136, 151, 154, 157, 161
g gravitational acceleration. 11, 12, 74, 89, 107, 137, 138
ΔG_{ad} free energy of adsorption. 122–125
$g(r_{ij})$ radial distribution function. 38, 39, 44, 45, 75, 88, 89
H Hough value. 25, 26, 33, 37
h height. 138, 145
h_{c} height of irregularities at the contact line. 144, 145
h_{cap} height of a spherical cap. 56, 68, 163
H_{max} maximum Hough value. 30

H_{min} minimum Hough value. 46
$H_{\mathrm{min,1}}$ initial minimum Hough value. 32, 33, 37, 45, 48
$H_{\mathrm{min,f}}$ final minimum Hough value. 32, 33, 37, 38, 41
I ionic strength. 102–106, 140
i index variable. 24–27, 30, 31, 33, 34, 38, 39, 143
j index variable. 31, 33
k_{B} Boltzmann constant. 39, 44, 45, 54, 57, 61, 82, 88, 89, 91, 107, 123–125, 128, 139, 140, 142–145, 148, 152, 153, 159, 160, 162
l length. 146, 155–158, 161, 163
l_{c} capillary length. 137
l_{g} gravitational length. 89, 107, 162
l_{px} length of a pixel. 39, 41, 42
Δl_{ROI} length of the margin added to each region of interest. 29, 31, 48
m mass. 12, 17, 107, 138, 146
m_{s} mass fraction of solid content. 11, 12, 75
m_{w} mass fraction of water. 115, 117, 119, 121–123, 126, 128, 129, 135, 136, 142, 146, 147, 149–151, 154, 156–159, 161, 162
N_1 number of unbound particles. 162
NA numerical aperture. 80, 162
N_{b} number of bonds. 60
$\langle N_{\mathrm{b}} \rangle$ average number of bonds per particle. 55, 57, 58, 63, 65, 162
n_{D} refractive index. 80, 162
N_{p} number of particles. 17, 84, 107, 108, 162
$N_{\mathrm{p,max}}$ maximum number of particles. 33, 37, 48
N_{s} number of satellite spheres. 53–58, 61, 62, 65, 66
N_{sp} surfactant packing parameter. 156, 158, 163
PdI polydispersity index. 105–107, 109
pH hydrogen ion activity at logarithmic scale. 4, 19, 76, 101, 102, 105–107
pK_{a} acid dissociation constant at logarithmic scale. 101, 106
R radius. 24–33, 40, 76, 138, 162
$\vec{r}$ position. 24–27, 34, 38, 39, 59, 68, 69
r radial coordinate. 145
R_0 initial estimate of the radius. 28, 29, 34, 45, 48
R_{B} Bohr radius. 68, 69
R_{c} radius of a contact circle. 117, 118, 144, 145
$\vec{r}_{\mathrm{c}}$ position of a centre. 24–31, 33, 45
R_{cap} radius of a spherical cap. 56, 68
r_{cc} centre-to-centre distance. 17, 19, 35–38, 42, 43, 55, 107, 108, 163
$r_{\mathrm{cc,0}}$ initial estimate of the centre-to-centre distance. 34, 48

$\Delta r_{\mathrm{cc,max}}$ estimated maximum deviation in the centre-to-centre distance. 34, 48
$\vec{r}_{\mathrm{c,l}}$ position of the centre of a large disk. 34–36
$\vec{r}_{\mathrm{c,s}}$ position of the centre of a small disk. 34–36
R_{d} radius of a droplet. 117, 118, 145
R_{e} equatorial radius of an oblate ellipsoid. 137, 138
R_{Gauss} radius for Gaussian filtering. 31, 48
R_{grad} radius to calculate the gradient. 27, 29, 31, 39, 40, 48
$R_{\mathrm{grad,ROI}}$ radius to calculate the gradient to determine regions of interest. 28, 31, 48
R_{H} Hough radius. 23–30, 32
r_{ij} distance between two points. 26, 38, 39, 44, 45, 54, 79, 88, 89, 108, 140, 144, 145
r_{ij}^{*} most common distance. 81, 108
R_{l} radius of the large lobe of a snowman-like particle. 34–38, 42, 43
$R_{\mathrm{l,0}}$ initial estimate of the radius of the large lobe. 34, 48
$\Delta R_{\mathrm{l,max}}$ estimated maximum difference in the radius of the large lobe. 34, 48
Δr_{mask} width of a mask. 34, 48
ΔR_{max} estimated maximum difference in the radius. 28, 29, 34, 48
$\vec{r}_{\mathrm{n}}$ position of the nucleus. 68, 69
R_{p} polar radius of an oblate ellipsoid. 122, 123, 137–143, 145
R_{res} resolution in the radius. 27, 29, 30, 41
$R_{\mathrm{res,1}}$ initial resolution in the radius. 29, 30, 40, 41, 48
$R_{\mathrm{res,f}}$ final resolution in the radius. 30–33, 37, 40, 41, 45, 48
R_{s} radius of the small lobe of a snowman-like particle. 34–38, 42, 43
r_{s} distance from the surface. 103, 104
$R_{\mathrm{s,0}}$ initial estimate of the radius of the small lobe. 34, 48
r_{slip} distance between the slip plane and the surface. 103, 104
$\Delta R_{\mathrm{s,max}}$ estimated maximum difference in the radius of the small lobe. 34, 48
r_{ss} surface-to-surface distance. 68, 128, 139–144
r_{ss}^{*} surface-to-surface distance with maximum attraction energy. 141–144
r_x position along the x-axis. 16, 29
r_y position along the y-axis. 29
r_z position along the z-axis. 59, 79
S swelling ratio. 12, 17, 18, 149
s semiperimeter. 163
T temperature. 39, 44, 45, 54, 57, 61, 82–84, 88, 89, 91, 107, 113, 116, 118, 119, 122–125, 128, 135, 139, 140, 142–145, 147–150, 152, 153, 159, 160, 162, 182, 189, 201
t time. 88–90, 97, 122, 129, 136, 151, 154, 157, 161
T_{g} glass transition temperature. 82
T_{ps} phase separation temperature. 115–119, 121–123, 128, 149–151, 153

ΔT_{ps} temperature relative to phase separation temperature. 116, 118–120, 122–125, 128–130, 137, 139, 146, 149–154, 156, 157, 161, 162

T^* critical temperature. 115, 118–120, 123, 135

ΔT^* temperature relative to the critical temperature. 118–120, 123–125, 127–130, 135, 137, 143–145

U_{g} gravitational energy. 138

U_{s} surface energy. 137, 138

U_{tot} total energy. 138

V volume. 18, 19, 36, 107, 138, 156, 158, 162, 163

$\vec{v}$ velocity. 88, 92, 97, 99

ΔV_{r} relative volume increase. 17–19

w interaction potential. 88, 89, 128, 141–144

w_{cc} interaction potential between central spheres. 54

w_{cp} interaction potential between central spheres and protrusions. 54

w_{cs} interaction potential between central and satellite spheres. 54

w_{img} interaction potential to an image charge. 140, 141

w_{int} interaction potential to an interfacial charge. 139, 141

w_{pp} interaction potential between protrusions. 54

w_{ps} interaction potential between protrusions and satellite spheres. 54

$w(r_{ij})$ pair potential. 39, 44, 45

w_{ss} interaction potential between satellite spheres. 54

x_{cs} covered surface fraction. 55, 56, 62–66

x_{e} relative equatorial radius of an oblate ellipsoid. 138, 139

$x_{ij,\mathrm{min}}$ minimum relative distance between two particles. 33, 45, 48

x_{p} dimensionless diameter of a protrusion. 53, 56

x_{s} dimensionless diameter of a satellite sphere. 53–58, 60–62, 65, 66, 68

x_{ss} dimensionless surface-to-surface binding distance. 68

$\mathcal{Z}$ electrostatic double layer interaction constant. 139–142

References

[1] Whitesides, G. M. & Grzybowski, B. Self-assembly at all scales. *Science* **295**, 2418–2421 (2002). doi:10.1126/science.1070821.

[2] Crowther, R. A. *et al.* Three-dimensional structure of hepatitis B virus core particles determined by electron cryomicroscopy. *Cell* **77**, 943–950 (1994). doi:10.1016/0092-8674(94)90142-2.

[3] Wynne, S. A., Crowther, R. A. & Leslie, A. G. W. The crystal structure of the human hepatitis B virus capsid. *Mol. Cell* **3**, 771–780 (1999). doi:10.1016/S1097-2765(01)80009-5.

[4] Gunn, K. L. S. & Marshall, J. S. The distribution with size of aggregate snowflakes. *J. Meteorol.* **15**, 452–461 (1958). doi:10.1175/1520-0469(1958)015<0452:TDWSOA>2.0.CO;2.

[5] Ellis, B. & Smith, R. (eds.) *Polymers: A Property Database* (CRC Press, Baco Raton, 2009), 2 edn. https://books.google.com/books?id=S-TKBQAAQBAJ.

[6] Haynes, W. M. (ed.) *CRC Handbook of Chemistry and Physics* (CRC Press, Boca Raton, 2016). http://www.hbcpnetbase.com/.

[7] Evans, D. F. & Wennerström, H. *Colloidal domain* (Wiley-VCH, New York, 1999), 2 edn. https://books.google.com/books?id=XPjvAAAAMAAJ.

[8] Leunissen, M. E. *et al.* Switchable self-protected attractions in DNA-functionalized colloids. *Nat. Mater.* **8**, 590–595 (2009). doi:10.1038/nmat2471.

[9] Wang, Y. *et al.* Patchy particle self-assembly via metal coordination. *J. Am. Chem. Soc.* **135**, 14064–14067 (2013). doi:10.1021/ja4075979.

[10] Bayer, F. M., Hiltrop, K. & Huber, K. Hydrogen-bond-induced heteroassembly in binary colloidal systems. *Langmuir* **26**, 13815–13822 (2010). doi:10.1021/la101831x.

[11] van Ravensteijn, B. G. P., Kamp, M., van Blaaderen, A. & Kegel, W. K. General route toward chemically anisotropic colloids. *Chem. Mater.* **25**, 4348–4353 (2013). doi:10.1021/cm4025606.

[12] Ho, C. C., Keller, A., Odell, J. A. & Ottewill, R. H. Preparation of monodisperse ellipsoidal polystyrene particles. *Colloid Polym. Sci.* **271**, 469–479 (1993). doi:10.1007/BF00657391.

[13] Sheu, H. R., El-Aasser, M. S. & Vanderhoff, J. W. Uniform nonspherical latex particles as model interpenetrating polymer networks. *J. Polym. Sci. A Polym. Chem.* **28**, 653–667 (1990). doi:10.1002/pola.1990.080280315.

[14] Mock, E. B., De Bruyn, H., Hawkett, B. S., Gilbert, R. G. & Zukoski, C. F. Synthesis of anisotropic nanoparticles by seeded emulsion polymerization. *Langmuir* **22**, 4037–4043 (2006). doi:10.1021/la060003a.

[15] Kraft, D. J., Groenewold, J. & Kegel, W. K. Colloidal molecules with well-controlled bond angles. *Soft Matter* **5**, 3823–3826 (2009). doi:10.1039/B910593J.

[16] Manoharan, V. N., Elsesser, M. T. & Pine, D. J. Dense packing and symmetry in small clusters of microspheres. *Science* **301**, 483–487 (2003). doi:10.1126/science.1086189.

[17] Pusey, P. N. & van Megen, W. Phase behaviour of concentrated suspensions of nearly hard colloidal spheres. *Nature* **320**, 340–342 (1986). doi:10.1038/320340a0.

[18] Bawden, F. C., Pirie, N. W., Bernal, J. D. & Fankuchen, I. Liquid crystalline substances from virus-infected plants. *Nature* **138**, 1051–1052 (1936). doi:10.1038/1381051a0.

[19] Onsager, L. The effects of shape on the interaction of colloidal particles. *Annals New York Acad. Sci.* **51**, 627–659 (1949). doi:10.1111/j.1749-6632.1949.tb27296.x.

[20] Vroege, G. J. & Lekkerkerker, H. N. W. Phase transitions in lyotropic colloidal and polymer liquid crystals. *Reports on Prog. Phys.* **55**, 1241–1309 (1992). doi:10.1088/0034-4885/55/8/003.

[21] van der Kooij, F. M., Kassapidou, K. & Lekkerkerker, H. N. W. Liquid crystal phase transitions in suspensions of polydisperse plate-like particles. *Nature* **406**, 868–871 (2000). doi:10.1038/35022535.

[22] Casagrande, C., Fabre, P., Raphaël, E. & Veyssié, M. Janus beads: Realization and behaviour at water/oil interfaces. *Europhys. Lett.* **9**, 251–255 (1989). doi:10.1209/0295-5075/9/3/011.

[23] de Gennes, P.-G. Soft matter (Nobel lecture). *Angew. Chem. Int. Ed. Engl.* **31**, 842–845 (1992). doi:10.1002/anie.199208421.

[24] Zhang, Z. & Glotzer, S. C. Self-assembly of patchy particles. *Nano Lett.* **4**, 1407–1413 (2004). doi:10.1021/nl0493500.

[25] Chen, Q., Yan, J., Zhang, J., Bae, S. C. & Granick, S. Janus and multiblock colloidal particles. *Langmuir* **28**, 13555–13561 (2012). doi:10.1021/la302226w.

[26] Chen, Q., Bae, S. C. & Granick, S. Directed self-assembly of a colloidal kagome lattice. *Nature* **469**, 381–384 (2011). doi:10.1038/nature09713.

[27] Yi, G.-R., Pine, D. J. & Sacanna, S. Recent progress on patchy colloids and their self-assembly. *J. Phys. Condens. Matter* **25**, 193101 (2013). doi:10.1088/0953-8984/25/19/193101.

[28] Kraft, D. J. *et al.* Surface roughness directed self-assembly of patchy particles into colloidal micelles. *Proc. Natl. Acad. Sci.* **109**, 10787–10792 (2012). doi:10.1073/pnas.1116820109.

[29] Wang, Y. *et al.* Colloids with valence and specific directional bonding. *Nature* **491**, 51–55 (2012). doi:10.1038/nature11564.

[30] Wolters, J. R. *et al.* Self-assembly of Mickey Mouse shaped colloids into tube-like structures: experiments and simulations. *Soft Matter* **11**, 1067–1077 (2015). doi:10.1039/C4SM02375G.

[31] Chen, T., Zhang, Z. & Glotzer, S. C. Simulation studies of the self-assembly of cone-shaped particles. *Langmuir* **23**, 6598–6605 (2007). doi:10.1021/la063755d.

[32] Tompa, P. & Fuxreiter, M. Fuzzy complexes: polymorphism and structural disorder in protein–protein interactions. *Trends Biochem. Sci.* **33**, 2–8 (2008). doi:10.1016/j.tibs.2007.10.003.

[33] Raven, P. & Johnson, G. *Biology* (McGraw-Hill, Boston, 2002), 6 edn.

[34] Freund, S. M. V., Johnson, C. M., Jaulent, A. M. & Ferguson, N. Moving towards high-resolution descriptions of the molecular interactions and structural rearrangements of the human hepatitis B core protein. *J. Mol. Biol.* **384**, 1301–1313 (2008). doi:10.1016/j.jmb.2008.10.020.

[35] Larson-Smith, K. & Pozzo, D. C. Scalable synthesis of self-assembling nanoparticle clusters based on controlled steric interactions. *Soft Matter* **7**, 5339–5347 (2011). doi:10.1039/C0SM01497D.

[36] Akcora, P. *et al.* Anisotropic self-assembly of spherical polymer-grafted nanoparticles. *Nat. Mater.* **8**, 354–359 (2009). doi:10.1038/nmat2404.

[37] Nikolic, M. S. *et al.* Micelle and vesicle formation of amphiphilic nanoparticles. *Angew. Chem. Int. Ed.* **48**, 2752–2754 (2009). doi:10.1002/anie.200805158.

[38] Derjaguin, B. & Landau, L. Theory of the stability of strongly charged lyophobic sols and of the adhesion of strongly charged particles in solutions of electrolytes. *Acta physicochimica U.R.S.S.* **14**, 633–662 (1941).

[39] Verwey, E. J. W. & Overbeek, J. T. G. *Theory of the Stability of Lyophobic Colloids* (Elsevier, New York, 1948). https://books.google.com/books?id=-f9sqibNMeEC.

[40] Hong, L., Cacciuto, A., Luijten, E. & Granick, S. Clusters of amphiphilic colloidal spheres. *Langmuir* **24**, 621–625 (2008). doi:10.1021/la7030818.

[41] Ling, X. Y. *et al.* Janus particles with controllable patchiness and their chemical functionalization and supramolecular assembly. *Angew. Chem.* **121**, 7813–7818 (2009). doi:10.1002/ange.200903579.

[42] Mladek, B. M., Fornleitner, J., Martinez-Veracoechea, F. J., Dawid, A. & Frenkel, D. Quantitative prediction of the phase diagram of DNA-functionalized nanosized colloids. *Phys. Rev. Lett.* **108**, 268301 (2012). doi:10.1103/PhysRevLett.108.268301.

[43] Biancaniello, P. L., Kim, A. J. & Crocker, J. C. Colloidal interactions and self-assembly using DNA hybridization. *Phys. Rev. Lett.* **94**, 058302 (2005). doi:10.1103/PhysRevLett.94.058302.

[44] Sacanna, S., Rossi, L. & Pine, D. J. Magnetic click colloidal assembly. *J. Am. Chem. Soc.* **134**, 6112–6115 (2012). doi:10.1021/ja301344n.

[45] Zerrouki, D., Baudry, J., Pine, D., Chaikin, P. & Bibette, J. Chiral colloidal clusters. *Nature* **455**, 380–382 (2008). doi:10.1038/nature07237.

[46] Yan, J., Bae, S. C. & Granick, S. Colloidal superstructures programmed into magnetic Janus particles. *Adv. Mater.* **27**, 874–879 (2015). doi:10.1002/adma.201403857.

[47] Beysens, D. & Narayanan, T. Wetting-induced aggregation of colloids. *J. Stat. Phys.* **95**, 997–1008 (1999). doi:10.1023/A:1004506601807.

[48] Bauer, C., Bieker, T. & Dietrich, S. Wetting-induced effective interaction potential between spherical particles. *Phys. Rev. E* **62**, 5324–5338 (2000). doi:10.1103/PhysRevE.62.5324.

[49] Gambassi, A., Hertlein, C., Helden, L., Dietrich, S. & Bechinger, C. The critical Casimir effect universal fluctuation-induced forces at work. *Europhys. News* **40**, 18–22 (2009). doi:10.1051/epn/2009301.

[50] Hertlein, C., Helden, L., Gambassi, A., Dietrich, S. & Bechinger, C. Direct measurement of critical Casimir forces. *Nature* **451**, 172–175 (2008). doi:10.1038/nature06443.

[51] Nguyen, V. D., Faber, S., Hu, Z., Wegdam, G. H. & Schall, P. Controlling colloidal phase transitions with critical Casimir forces. *Nat. Commun.* **4**, 1584 (2013). doi:10.1038/ncomms2597.

[52] Everett, D. H. *Basic Principles of Colloid Science* (Royal Society of Chemistry, London, 1988). https://books.google.com/books?id=FP3vAAAAMAAJ.

[53] Ramsden, W. Separation of solids in the surface-layers of solutions and suspensions (observations on surface-membranes, bubbles, emulsions, and mechanical coagulation). preliminary account. *Proc. Royal Soc. Lond.* **72**, 156–164 (1903). http://www.jstor.org/stable/116458.

[54] Pickering, S. U. Emulsions. *J. Chem. Soc. Trans.* **91**, 2001–2021 (1907). doi:10.1039/CT9079102001.

[55] Pieranski, P. Two-dimensional interfacial colloidal crystals. *Phys. Rev. Lett.* **45**, 569–572 (1980). doi:10.1103/PhysRevLett.45.569.

[56] Binks, B. P. Particles as surfactants—similarities and differences. *Curr. Opin. Colloid Interface Sci.* **7**, 21–41 (2002). doi:10.1016/S1359-0294(02)00008-0.

[57] Binks, B. P. & Lumsdon, S. O. Pickering emulsions stabilized by monodisperse latex particles: Effects of particle size. *Langmuir* **17**, 4540–4547 (2001). doi:10.1021/la0103822.

[58] Binks, B. P., Murakami, R., Armes, S. P. & Fujii, S. Effects of pH and salt concentration on oil-in-water emulsions stabilized solely by nanocomposite microgel particles. *Langmuir* **22**, 2050–2057 (2006). doi:10.1021/la053017+.

[59] Pichot, C. Surface-functionalized latexes for biotechnological applications. *Curr. Opin. Colloid Interface Sci.* **9**, 213–221 (2004). doi:10.1016/j.cocis.2004.07.001.

[60] Yoon, R.-H., Flinn, D. H. & Rabinovich, Y. I. Hydrophobic interactions between dissimilar surfaces. *J. Colloid Interface Sci.* **185**, 363–370 (1997). doi:10.1006/jcis.1996.4583.

[61] van Ravensteijn, B. G. P. & Kegel, W. K. Colloids with continuously tunable surface charge. *Langmuir* **30**, 10590–10599 (2014). doi:10.1021/la501993c.

[62] Mirkin, C. A., Letsinger, R. L., Mucic, R. C. & Storhoff, J. J. A DNA-based method for rationally assembling nanoparticles into macroscopic materials. *Nature* **382**, 607–609 (1996). doi:10.1038/382607a0.

[63] Sheu, H. R., El-Aasser, M. S. & Vanderhoff, J. W. Phase separation in polystyrene latex interpenetrating polymer networks. *J. Polym. Sci. A Polym. Chem.* **28**, 629–651 (1990). doi:10.1002/pola.1990.080280314.

[64] Kraft, D. J. *et al.* Self-assembly of colloids with liquid protrusions. *J. Am. Chem. Soc.* **131**, 1182–1186 (2009). doi:10.1021/ja8079803.

[65] Wang, P. H. & Pan, C.-Y. Preparation of styrene/acrylic acid copolymer microspheres: polymerization mechanism and carboxyl group distribution. *Colloid Polym. Sci.* **280**, 152–159 (2002). doi:10.1007/s003960100588.

[66] Hu, X., Liu, H., Ge, X., Yang, S. & Ge, X. Preparation of submicron-sized snowman-like polystyrene particles via radiation-induced seeded emulsion polymerization. *Chem. Lett.* **38**, 854–855 (2009). doi:10.1246/cl.2009.854.

[67] Marchand-Brynaert, J., Deldime, M., Dupont, I., Dewez, J.-L. & Schneider, Y.-J. Surface functionalization of poly(ethylene terephthalate) film and membrane by controlled wet chemistry: Chemical characterization of carboxylated surfaces. *J. Colloid Interface Sci.* **173**, 236–244 (1995). doi:10.1006/jcis.1995.1319.

[68] McMurry, J. *Organic Chemistry* (Brooks/Cole, Belmont, 2004), 6 edn.

[69] Nakajima, N. & Ikada, Y. Mechanism of amide formation by carbodiimide for bioconjugation in aqueous media. *Bioconjugate Chem.* **6**, 123–130 (1995). doi:10.1021/bc00031a015.

[70] Montalbetti, C. A. G. N. & Falque, V. Amide bond formation and peptide coupling. *Tetrahedron* **61**, 10827–10852 (2005). doi:10.1016/j.tet.2005.08.031.

[71] Munkholm, C., Parkinson, D. R. & Walt, D. R. Intramolecular fluorescence self-quenching of fluoresceinamine. *J. Am. Chem. Soc.* **112**, 2608–2612 (1990). doi:10.1021/ja00163a021.

[72] Deegan, R. D. *et al.* Capillary flow as the cause of ring stains from dried liquid drops. *Nature* **389**, 827–829 (1997). doi:10.1038/39827.

[73] Hough, P. V. C. Method and means for recognizing complex patterns (1962). http://www.google.com/patents/US3069654.

[74] Duda, R. O. & Hart, P. E. Use of the Hough transformation to detect lines and curves in pictures. *Commun. ACM* **15**, 11–15 (1972). doi:10.1145/361237.361242.

[75] Ballard, D. H. Generalizing the Hough transform to detect arbitrary shapes. *Pattern Recognit.* **13**, 111–122 (1981). doi:10.1016/0031-3203(81)90009-1.

[76] Hart, P. E. How the Hough transform was invented. *IEEE Signal Process. Mag.* **26**, 18–22 (2009). doi:10.1109/MSP.2009.934181.

[77] Parthasarathy, R. Rapid, accurate particle tracking by calculation of radial symmetry centers. *Nat. Meth.* **9**, 724–726 (2012). doi:10.1038/nmeth.2071.

[78] Cheong, F. C. *et al.* Flow visualization and flow cytometry with holographic video microscopy. *Opt. Express* **17**, 13071–13079 (2009). doi:10.1364/OE.17.013071.

[79] Krishnatreya, B. J. & Grier, D. G. Fast feature identification for holographic tracking: the orientation alignment transform. *Opt. Express* **22**, 12773–12778 (2014). doi:10.1364/OE.22.012773.

[80] Mao, X., Zhang, B. & Ye, Z. Automatic detection of colloidal particles based on a shape regularized integrated active contour model. *Optik - Int. J. for Light. Electron Opt.* **125**, 6835–6840 (2014). doi:10.1016/j.ijleo.2014.08.090.

[81] Kaytanli, B. & Valentine, M. T. Evolute-based Hough transform method for characterization of ellipsoids. *J. Microsc.* **249**, 159–164 (2013). doi:10.1111/jmi.12004.

[82] Weisstein, E. W. *CRC Concise Encyclopedia of Mathematics* (CRC Press, Boca Raton, 2003), 2 edn. https://books.google.com/books?id=D_XKBQAAQBAJ.

[83] Williams, D. B. & Carter, C. B. *Transmission Electron Microscopy: A Textbook for Materials Science* (Springer, New York, 1996). https://books.google.com/books?id=SAv3BwAAQBAJ.

[84] Baumgartl, J. & Bechinger, C. On the limits of digital video microscopy. *Europhys. Lett.* **71**, 487–493 (2005). doi:10.1209/epl/i2005-10107-2.

[85] Glotzer, S. C. & Solomon, M. J. Anisotropy of building blocks and their assembly into complex structures. *Nat. Mater.* **6**, 557–562 (2007). doi:10.1038/nmat1949.

[86] Asakura, S. & Oosawa, F. On interaction between two bodies immersed in a solution of macromolecules. *J. Chem. Phys.* **22**, 1255 (1954). doi:10.1063/1.1740347.

[87] Vrij, A. Polymers at interfaces and the interactions in colloidal dispersions. *Pure Appl. Chem.* **48**, 471–483 (1976). doi:10.1351/pac197648040471.

[88] Lekkerkerker, H. N. W. & Tuinier, R. *Colloids and the Depletion Interaction*, vol. 833 of *Lecture Notes in Physics* (Springer, Dordrecht, 2011). doi:10.1007/978-94-007-1223-2_2.

[89] Casselman, B. The difficulties of kissing in three dimensions. *Notices AMS* **51**, 884–885 (2004).

[90] Asai, M., Cacciuto, A. & Kumar, S. K. Quantitative analogy between polymer-grafted nanoparticles and patchy particles. *Soft Matter* **11**, 793–797 (2015). doi:10.1039/C4SM02295E.

[91] Atkins, P. & Friedman, R. *Molecular Quantum Mechanics* (Oxford University Press, Oxford, 2008), 4 edn.

[92] Berg, J. M., Tymoczko, J. L. & Stryer, L. *Biochemistry* (W. H. Freeman and Company, New York, 2002), 5 edn.

[93] Luiken, J. A. & Bolhuis, P. G. Anisotropic aggregation in a simple model of isotropically polymer-coated nanoparticles. *Phys. Rev. E* **88**, 012303 (2013). doi:10.1103/PhysRevE.88.012303.

[94] Geerts, N. & Eiser, E. Flying colloidal carpets. *Soft Matter* **6**, 664–669 (2010). doi:10.1039/B917846E.

[95] Bates, F. S. Polymer-polymer phase behavior. *Science* **251**, 898–905 (1991). doi:10.1126/science.251.4996.898.

[96] Sibarita, J.-B. Deconvolution microscopy. In Rietdorf, J. (ed.) *Microscopy Techniques*, chap. 4 (Springer, Berlin, 2005). doi:10.1007/b102215.

[97] Dinsmore, A. D. *et al.* Colloidosomes: selectively permeable capsules composed of colloidal particles. *Science* **298**, 1006–1009 (2002). doi:10.1126/science.1074868.

[98] Perlmutter, J. D. & Hagan, M. F. Mechanisms of virus assembly. *Annu. Rev. Phys. Chem.* **66**, 217–239 (2015). doi:10.1146/annurev-physchem-040214-121637.

[99] Caspar, D. L. D. & Klug, A. Physical principles in the construction of regular viruses. *Cold Spring Harb. Symp. on Quant. Biol.* **27**, 1–24 (1962). doi:10.1101/SQB.1962.027.001.005.

[100] Bajaj, C. Geometric modeling and quantitative visualization of virus ultrastructure. In Laubichler, M. D. & Müller, G. B. (eds.) *Modeling Biology: Structures, Behavior, Evolution*, chap. 7 (MIT Press, Cambridge, 2007). https://books.google.com/books?id=xC3bEvRU9A0C.

[101] Gröschel, A. H. *et al.* Guided hierarchical co-assembly of soft patchy nanoparticles. *Nature* **503**, 247–251 (2013). doi:10.1038/nature12610.

[102] Crassous, J. J. *et al.* Field-induced assembly of colloidal ellipsoids into well-defined microtubules. *Nat. Commun.* **5**, 5516 (2014). doi:10.1038/ncomms6516.

[103] Ball, D. W. *Physical Chemistry* (Brooks/Cole, Belmont, 2003), 1 edn.

[104] Kirkwood, J. G. & Shumaker, J. B. Forces between protein molecules in solution arising from fluctuations in proton charge and configuration. *Proc. Natl. Acad. Sci.* **38**, 863–871 (1952). doi:10.1073/pnas.38.10.863.

[105] Lund, M. Electrostatic chameleons in biological systems. *J. Am. Chem. Soc.* **132**, 17337–17339 (2010). doi:10.1021/ja106480a.

[106] Rousseau, D. Fat crystals and emulsion stability — a review. *Food Res. Int.* **33**, 3–14 (2000). doi:10.1016/S0963-9969(00)00017-X.

[107] Sacanna, S., Kegel, W. K. & Philipse, A. P. Thermodynamically stable pickering emulsions. *Phys. Rev. Lett.* **98**, 158301 (2007). doi:10.1103/PhysRevLett.98.158301.

[108] Stratford, K., Adhikari, R., Pagonabarraga, I., Desplat, J.-C. & Cates, M. E. Colloidal jamming at interfaces: A route to fluid-bicontinuous gels. *Science* **309**, 2198–2201 (2005). doi:10.1126/science.1116589.

[109] Herzig, E. M., White, K. A., Schofield, A. B., Poon, W. C. K. & Clegg, P. S. Bicontinuous emulsions stabilized solely by colloidal particles. *Nat. Mater.* **6**, 966–971 (2007). doi:10.1038/nmat2055.

[110] Cox, J. D. Phase relationships in the pyridine series. Part II. the miscibility of some pyridine homologues with deuterium oxide. *J. Chem. Soc.* 4606–4608 (1952). doi:10.1039/JR9520004606.

[111] Cox, H. L., Nelson, W. L. & Cretcher, L. H. Reciprocal solubility of the normal propyl ethers of 1,2-propylene glycol and water. Closed solubility curves. II. *J. Am. Chem. Soc.* **49**, 1080–1083 (1927). doi:10.1021/ja01403a032.

[112] Cahn, J. W. Critical point wetting. *J. Chem. Phys.* **66**, 3667–3672 (1977). doi:10.1063/1.434402.

[113] Widom, B. Surface tension and molecular correlations near the critical point. *J. Chem. Phys.* **43**, 3892–3897 (1965). doi:10.1063/1.1696617.

[114] Warren, C. & Webb, W. W. Interfacial tension of near-critical cyclohexane-methanol mixtures. *J. Chem. Phys.* **50**, 3694–3700 (1969). doi:10.1063/1.1671614.

[115] Fisk, S. & Widom, B. Structure and free energy of the interface between fluid phases in equilibrium near the critical point. *J. Chem. Phys.* **50**, 3219–3227 (1969). doi:10.1063/1.1671544.

[116] Heady, R. B. & Cahn, J. W. Experimental test of classical nucleation theory in a liquid-liquid miscibility gap system. *J. Chem. Phys.* **58**, 896–910 (1973). doi:10.1063/1.1679343.

[117] Hoyer, W. & Kaban, I. G. Liquid-liquid interfacial tension in multi-component immiscible al-based alloys. In Herlach, D. M. (ed.) *Phase Transformations in Multicomponent Melts*, chap. 2 (Wiley-VCH, Weinheim, 2008). https://books.google.com/books?id=iQ8vO6rRWIUC.

[118] Wims, A. M., McIntyre, D. & Hynne, F. Coexistence curve for 3-methylpentane-nitroethane near the critical point. *J. Chem. Phys.* **50**, 616–620 (1969). doi:10.1063/1.1671108.

[119] Sengers, J. V. & Sengers, J. M. H. L. Thermodynamic behavior of fluids near the critical point. *Annu. Rev. Phys. Chem.* **37**, 189–222 (1986). doi:10.1146/annurev.pc.37.100186.001201.

[120] Moldover, M. R. & Cahn, J. W. An interface phase transition: Complete to partial wetting. *Science* **207**, 1073–1075 (1980). doi:10.1126/science.207.4435.1073.

[121] Grattoni, C. A., Dawe, R. A., Seah, C. Y. & Gray, J. D. Lower critical solution coexistence curve and physical properties (density, viscosity, surface tension, and interfacial tension) of 2,6-lutidine + water. *J. Chem. Eng. Data* **38**, 516–519 (1993). doi:10.1021/je00012a008.

[122] Binks, B. P. & Horozov, T. S. *Colloidal Particles at Liquid Interfaces* (Cambridge University Press, Cambridge, 2006). https://books.google.com/books?id=7-5fwUxIPv8C.

[123] Vis, M. *et al.* Water-in-water emulsions stabilized by nanoplates. *ACS Macro Lett.* **4**, 965–968 (2015). doi:10.1021/acsmacrolett.5b00480.

[124] Soret, M. C. Sur l'état d'équilibre que prend, au point de vue de sa concentration, une dissolution saline primitivement homogène dont deux parties sont portées a des températures différentes. *Arch. Sci. Phys. Nat.* **2**, 48–61 (1879).

[125] Zheng, F. Thermophoresis of spherical and non-spherical particles: a review of theories and experiments. *Adv. Colloid Interface Sci.* **97**, 255–278 (2002). doi:10.1016/S0001-8686(01)00067-7.

[126] Piazza, R. & Parola, A. Thermophoresis in colloidal suspensions. *J. Phys. Condens. Matter* **20**, 153102 (2008). doi:10.1088/0953-8984/20/15/153102.

[127] Iacopini, S., Rusconi, R. & Piazza, R. The macromolecular tourist: Universal temperature dependence of thermal diffusion in aqueous colloidal suspensions. *Eur. Phys. J. E* **19**, 59–67 (2006). doi:10.1140/epje/e2006-00012-9.

[128] Vigolo, D., Buzzaccaro, S. & Piazza, R. Thermophoresis and thermoelectricity in surfactant solutions. *Langmuir* **26**, 7792–7801 (2010). doi:10.1021/la904588s.

[129] Stamou, D., Duschl, C. & Johannsmann, D. Long-range attraction between colloidal spheres at the air-water interface: The consequence of an irregular meniscus. *Phys. Rev. E* **62**, 5263–5272 (2000). doi:10.1103/PhysRevE.62.5263.

[130] Kralchevsky, P. A. & Denkov, N. D. Capillary forces and structuring in layers of colloid particles. *Curr. Opin. Colloid Interface Sci.* **6**, 383–401 (2001). doi:10.1016/S1359-0294(01)00105-4.

[131] Leunissen, M. E., van Blaaderen, A., Hollingsworth, A. D., Sullivan, M. T. & Chaikin, P. M. Electrostatics at the oil–water interface, stability, and order in emulsions and colloids. *Proc. Natl. Acad. Sci.* **104**, 2585–2590 (2007). doi:10.1073/pnas.0610589104.

[132] Wang, H., Singh, V. & Behrens, S. H. Image charge effects on the formation of pickering emulsions. *J. Phys. Chem. Lett.* **3**, 2986–2990 (2012). doi:10.1021/jz300909z.

[133] Elbers, N. A. *Experiments in which oil, water and colloidal particles meet*. Ph.D. thesis, Utrecht University (2015).

[134] Tsapis, N. *et al.* Onset of buckling in drying droplets of colloidal suspensions. *Phys. Rev. Lett.* **94**, 018302 (2005). doi:10.1103/PhysRevLett.94.018302.

[135] Quilliet, C., Zoldesi, C., Riera, C., Van Blaaderen, A. & Imhof, A. Anisotropic colloids through non-trivial buckling. *Eur. Phys. J. E* **27**, 13–20 (2008). doi:10.1140/epje/i2007-10365-2.

[136] Kim, J.-W. *et al.* Colloidal assembly route for responsive colloidosomes with tunable permeability. *Nano Lett.* **7**, 2876–2880 (2007). doi:10.1021/nl0715948.

[137] Datta, S. S., Shum, H. C. & Weitz, D. A. Controlled buckling and crumpling of nanoparticle-coated droplets. *Langmuir* **26**, 18612–18616 (2010). doi:10.1021/la103874z.

[138] de Gennes, P. G., Brochard-Wyart, F. & Quere, D. *Capillarity and Wetting Phenomena: Drops, Bubbles, Pearls, Waves* (Springer, New York, 2004), 1 edn. https://books.google.com/books?id=MxLQk8vms-kC.

[139] Israelachvili, J. N. *Intermolecular and surface forces* (Academic Press, Amsterdam, 2011), 3 edn. doi:10.1016/B978-0-12-375182-9.10025-9.

[140] Atkins, P. & de Paula, J. *Atkins' Physical Chemistry* (Oxford University Press, Oxford, 2010), 9 edn. https://books.google.nl/books?id=BV6cAQAAQBAJ.

[141] Fisher, M. E. & de Gennes, P.-G. Phénomènes aux parois dans un mélange binaire critique. *C. R. Acad. Sc. Paris* **287**, 207–209 (1978). https://books.google.com/books?id=c7HUCgAAQBAJ.

[142] Beysens, D. & Estève, D. Adsorption phenomena at the surface of silica spheres in a binary liquid mixture. *Phys. Rev. Lett.* **54**, 2123–2126 (1985). doi:10.1103/PhysRevLett.54.2123.

[143] Edison, J. R. *et al.* Critical Casimir forces and colloidal phase transitions in a near-critical solvent: A simple model reveals a rich phase diagram. *Phys. Rev. Lett.* **114**, 038301 (2015). doi:10.1103/PhysRevLett.114.038301.

[144] Nellen, U., Helden, L. & Bechinger, C. Tunability of critical Casimir interactions by boundary conditions. *EPL* **88**, 26001 (2009). doi:10.1209/0295-5075/88/26001.

[145] Yu, C., Zhang, J. & Granick, S. Selective Janus particle assembly at tipping points of thermally-switched wetting. *Angew. Chem. Int. Ed.* **53**, 4364–4367 (2014). doi:10.1002/anie.201310465.

[146] Nguyen, V. D., Dang, M. T., Nguyen, T. A. & Schall, P. Critical Casimir forces for colloidal assembly. *J. Phys. Condens. Matter* **28**, 043001 (2016). doi:10.1088/0953-8984/28/4/043001.

[147] Israelachvili, J. The science and applications of emulsions — an overview. *Colloids Surfaces A: Physicochem. Eng. Aspects* **91**, 1–8 (1994). doi:10.1016/0927-7757(94)02743-9.

[148] Marczak, W. Speed of ultrasound, density, and adiabatic compressibility for 3-methylpyridine + heavy water in the temperature range 293–313 K. *J. Chem. Eng. Data* **41**, 1462–1465 (1996). doi:10.1021/je960185i.

Summary

The main goal of this thesis is to increase our understanding of self-assembly and to study new mechanisms that direct the formation of well-defined materials. Self-assembly is the spontaneous formation of patterns or structures without human intervention. In self-assembly of proteins, the building blocks have a size of about 1 nm and are complex. Consequently, grasping the basic principles that drive the formation of, for example, viruses is challenging. Colloidal particles, on the other hand, have a typical size up to 1000 nm, and can be used as relatively simple model particles. In this thesis, we use such particles to investigate how deformability and near-critical phenomena can direct self-assembly.

In Part I, we synthesize and characterise colloidal model particles. Chapter 2 describes the synthesis of spherical and snowman-like particles with increasing complexity. First, we synthesize spherical particles with a polystyrene-rich interior and a poly(acrylic acid)-rich brush. Next, a polystyrene protrusion is formed on the spheres, and finally, a fluorescent dye is covalently linked to the poly(acrylic acid) brush. The resulting mutually attractive, anisotropic, deformable (MAD) particles consist of a polymer-grafted, functionalized core and a bare polystyrene protrusion (Fig. S.1a).

The geometry of these particles is determined from transmission electron microscopy images as described in Chapter 3. The so-called Hough circle transformation can be used to detect the radii and positions of disks in images. This method is optimised to automatically analyse the geometry of spherical and snowman-like particles (Fig. S.1b), and to detect the positions of particles in optical microscopy images.

In Part II, we study the influence of deformability on self-assembly. Proteins, for example, are deformable as they can undergo conformational changes upon binding with other (macro)molecules. Chapter 4 describes a simple model that treats deformable particles as mutually attractive spheres with non-attractive satellite spheres. Computer simulations show that anisotropic interactions are

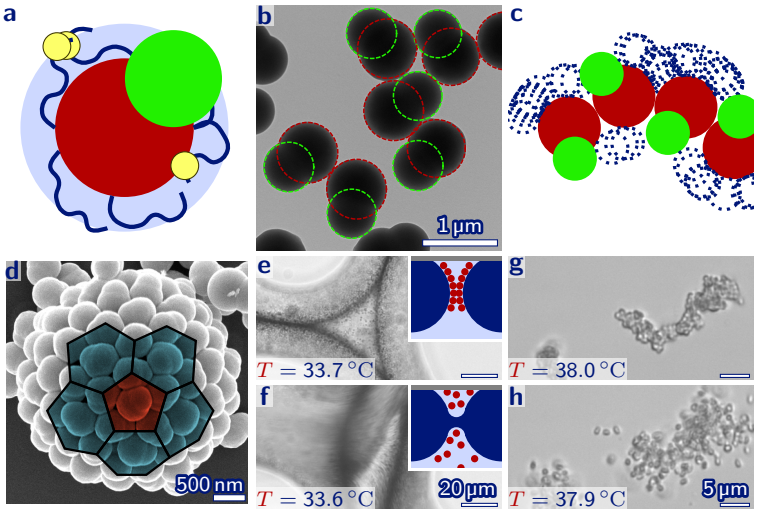

Figure S.1. **Graphical summary.** Mutually attractive, anisotropic, deformable (MAD) particles (**a**) with a polymer-grafted (∿), functionalized (●) core (●) and a rigid protrusion (●) are synthesized. The size and positions of the cores (**b** ◌) and protrusions (**b** ◌) are automatically determined from microscopy images. Computer simulations of MAD particles (**c**) show that redistribution of satellite spheres (◌) stabilizes curved monolayers. In experiments, MAD particles self-assemble into monolayer microcapsules (**d**) with pentagonal (●) and hexagonal (●) faces. In a near-critical mixture, thermoreversible attachment of particles onto interfaces results in temperature-controlled stability of emulsion droplets (**e–f**). Near-critical phenomena also induce thermoreversible self-assembly into micelle-like structures (**g–h**). The QR code links to a movie of a height series through a microcapsule (phd.chrisevers.com/5qr2b.mp4).

induced as the satellite spheres redistribute upon binding. We refer to this process as colloidal bond hybridization, analogous to the redistribution of electrons that induces anisotropic bonds in quantum chemistry. The fraction of the surface of the particles that is covered by satellite spheres dictates the number of bonds each particle makes, i.e. the valency. Furthermore, mutual attraction and deformability are shown to stabilize planar monolayers, while adding a protrusion induces a shift to curved monolayers (Fig. S.1c).

Next, we experimentally study self-assembly of deformable particles (Chapter 5). Mutually attractive, isotropic, deformable (MID) particles self-assemble into planar monolayers. The hydrophilic polymer brush of MID particles is thought to rearrange upon binding, resulting in anisotropic interactions for chemically and geometrically isotropic particles. Mutually attractive, anisotropic, deformable (MAD) particles (Fig. S.1a), on the other hand, form monolayer microcapsules (Fig. S.1d). Similar as in the computer simulations (Fig. S.1c), the addition of a protrusion induces curvature. Consequently, the MAD particles self-assemble into dramatically more complex structures than similar isotropic or non-deformable particles. Finally, we propose that microcapsules are formed at high concentrations with cavities as intermediates.

In Part III, we investigate the influence of near-critical phenomena on colloidal interactions. We study partially miscible liquids with a lower critical point. These liquids are miscible at room temperature. Above the lower phase separation temperature, however, two coexisting phases are formed. Near the critical point, the compositions and interfacial properties of these phases strongly depend on the temperature. In Chapter 6, we observe that polystyrene spheres thermoreversibly attach onto the surface of phase-separated, near-critical droplets. We discuss two explanations for these observations. First, we estimate the contact angle and the interfacial tension as a function of the temperature, resulting in an adsorption energy of zero just above the critical temperature, and a steep increase in the adsorption energy at higher temperatures. Alternatively, we discuss contactless attachment of particles onto the interface. Next, thermoreversible attachment is applied to prepare and destabilize emulsions by simply changing the temperature (Fig. S.1e–f). Furthermore, we demonstrate that heating followed by cooling can also induce the formation of colloidal microcapsules.

In Chapter 7, we study particles in mixtures just below the lower critical point. At these conditions, near-critical-solvent-mediated interactions or critical Casimir forces are induced. Attraction between spherical particles with a hydrophilic poly(acrylic acid)-rich brush is induced at a mass fraction of water just below the critical composition. Furthermore, the attraction strength can be externally tuned with temperature to be several times stronger than the thermal energy, and thermoreversible aggregation is observed. Particles without a brush, on the other hand, are only slightly attractive. Next, we study non-functionalized, anisotropic, deformable (NAD) particles, that consist of a core with a hydrophilic brush and a polystyrene protrusion. These particles have interactions that are externally

tunable as well as anisotropic. Consequently, they thermoreversibly self-assemble into structures that resemble micelles of molecular surfactants (Fig. S.1g–h). Finally, the morphology of the structures is related to the geometry of the particles using theory for molecular surfactants.

The results in this thesis show that deformability and near-critical phenomena can take colloidal self-assembly a significant step further. Deformability allows relatively simple building blocks to self-assemble into complex structures. This enabled the first colloidal realisation of self-assembly into microcapsules without a template. Systematically varying the mutual attraction strength, anisotropy and deformability of particles is expected to result in additional novel materials. Furthermore, while details are different, the MAD characteristics can also be recognized in proteins, suggesting that these properties could be important in the self-assembly of virus microcapsules as well. Near-critical phenomena, on the other hand, allow for externally tunable, directional interactions. These properties could facilitate self-assembly into structures that are up till now kinetically inaccessible. Finally, creating and destabilizing emulsions by simply changing the temperature could make the preparation of industrial and food products more straightforward.

Samenvatting voor een breed publiek

Zelfassemblage

Orde ontstaat vaak spontaan uit wanorde. Zo organiseren de sterren in sterrenstelsels zich vaak in spiralen die draaien rondom een centraal punt. Maar ook koeien ordenen zich spontaan: ze komen spontaan samen om in kuddes te grazen (Fig. S.2a–b). Zelfs minuscule watermoleculen ordenen zich spontaan wanneer ze ijskristallen vormen beneden het vriespunt. In deze drie processen vormen bestaande bouwstenen (sterren, koeien en watermoleculen) spontaan geordende structuren (sterrenstelsels, kuddes en ijskristallen) zonder dat de mens er aan te pas komt. Dat noemen we zelfassemblage of zelforganisatie.

Zelfassemblage komt ook voor bij virussen. Virussen dringen de cellen van mensen, dieren of andere organismen binnen. Daar kapen ze het controle-centrum van de cel, zodat de cel bouwstenen voor nog meer virussen gaat produceren. Deze bouwstenen vormen vervolgens spontaan nieuwe virussen. Als je de losse bouwstenen in water met een beetje zout gooit, vormen ze vaak uit zichzelf holle, bolvormige capsules met een specifieke grootte (Fig. S.2c–d). Deze capsules vormen een beschermende mantel rondom het DNA of RNA van het virus. Zo kan het genetisch materiaal dat je ziek maakt, van de ene cel naar de andere cel en van de ene mens naar de andere mens reizen. Onder andere het griepvirus, het humaan immunodeficiëntievirus (HIV), het zikavirus en het hepatitis B-virus verspreiden zich volgens dit principe. Meer begrip van de zelfassemblage van deze virussen kan helpen bij de bestrijding van virusziektes.

Sterrenstelsel, kuddes, ijskristallen en virussen worden dus vanzelf gevormd uit hun bouwstenen. Bijna alle niet-natuurlijke producten worden echter nog met de hand of met machines in elkaar gezet. Helaas vormen de losse onderdelen uit een IKEA-pakket niet spontaan een garderobekast, maar moet deze met de hand worden opgebouwd (Fig. S.2e–f). Voor de productie van bijvoorbeeld zonnepanelen en processoren in computers en telefoons zijn dure machines nodig om deze precieze materialen in elkaar te zetten. Opgooitentjes komen al meer in de buurt van

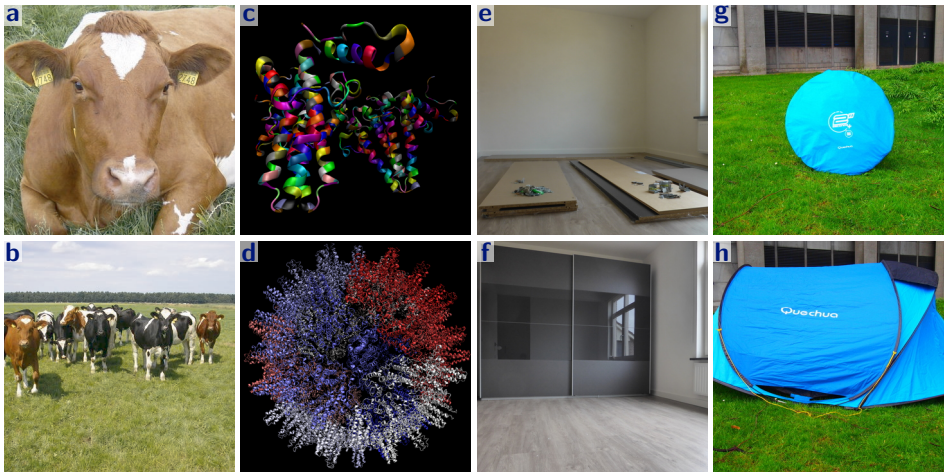

Figuur S.2. Assemblage en zelfassemblage. Bij zelfassemblage vormen bouwstenen spontaan geordende structuren. Zo vormen koeien uit zichzelf kuddes (**a–b**) en vormen virusbouwstenen spontaan holle bollen (**c–d**, protein data bank 1QGT). Schroeven en planken vormen niet spontaan een kast (**e–f**), maar een opgooitentje klapt vanzelf uit (**g–h**). De QR-code verwijst naar een filmpje van bouwstenen die zelfassembleren in een virusachtige structuur (phd.chrisevers.com/sqr2.mp4).

zelfassemblage. Als je een opgevouwen opgooitent loslaat zet deze zich vanzelf op (Fig. S.2g–h). De QR-code bij Fig. S.2 verwijst naar een filmpje van bouwstenen met magneetjes aan de zijkanten die zich spontaan in elkaar zetten tot een virusachtige structuur. Meer begrip van zelfassemblage kan helpen om een opgooivariant van zonnepanelen en processoren te ontwikkelen. Losse bouwstenen zouden zichzelf dan spontaan in elkaar kunnen zetten tot een zonnepaneel of een processor.

Om virussen te bestrijden en zelfassemblerende zonnepanelen te maken, moeten we de scheikunde en natuurkunde die voor zelfassemblage zorgen beter begrijpen. Bestuderen hoe virussen zichzelf in elkaar zetten is helaas erg ingewikkeld. De bouwstenen van een virus zijn nogal complex, waardoor het lastig is te onderscheiden welke onderdelen belangrijk zijn en welke niet. Bovendien zijn de bouwstenen zo klein dat ze niet direct kunnen worden bekeken met een microscoop. Daarom zijn modelbouwstenen nodig die simpeler en groter zijn.

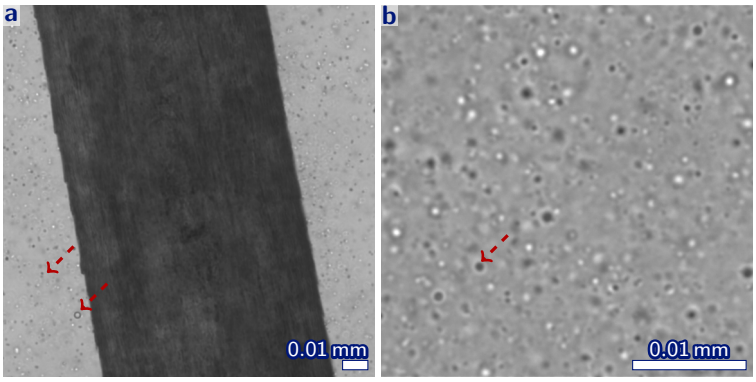

Figuur S.3. **Colloïden.** **a**) Microscopiefoto van een gedeelte van een haar van de auteur van dit proefschrift (donkere vlak), colloïden (lichte en donkere puntjes (⇢) en colloïden die zijn gezelfassembleerd in een bolvormige capsule (→). **b**) Microscopiefoto van Campina halfvolle melk met daarin colloïdale vetdruppeltjes (⇢). De QR-code linkt naar een filmpje van **b** (phd.chrisevers.com/sqr3.mp4).

Colloïden

In dit proefschrift gebruiken we colloïden als modelbouwstenen voor zelfassemblage. Colloïden zijn deeltjes met een grootte tussen de 0.000001 millimeter en 0.001 millimeter. De colloïden in ons onderzoek zijn ongeveer 0.001 millimeter oftewel 1 micrometer groot, en daarmee ongeveer honderd keer kleiner dan de dikte van een haar (Fig. S.3a) en een miljoen keer kleiner dan wijzelf. Daarmee zijn deze modelbouwstenen ongeveer net zoveel kleiner dan een mens, als dat een mens kleiner is dan de maan. Colloïden zijn dus superklein.

Maar om zelfassemblage te begrijpen hadden we toch juist bouwstenen nodig die relatief groot waren? Dat zijn colloïden ook. Hoewel ze een miljoen keer kleiner zijn dan wijzelf, zijn ze ruim honderd keer groter dan de bouwstenen van virussen, en tienduizend keer groter dan watermoleculen. In tegenstelling tot virusbouwstenen en watermoleculen kunnen we colloïden daardoor zien met een lichtmicroscoop. Hierdoor kunnen we direct bestuderen hoe colloïden zichzelf ordenen.

Doordat colloïden tegelijkertijd erg klein zijn, bewegen ze uit zichzelf. Dat doen alle superkleine deeltjes. Doordat bijvoorbeeld moleculen in de lucht spontaan bewegen, verspreiden geurtjes zich bijvoorbeeld door een klaslokaal. Ook

watermoleculen zijn voortdurend in beweging. Als je bijvoorbeeld een scheut aanmaaklimonade toevoegt aan een ogenschijnlijk stilstaand glas met water, zie je dat de kleur zich langzaam over het hele glas verspreidt. Een laatste voorbeeld van spontane beweging in het dagelijks leven is vet in melk. Vet lost niet op in water, maar om zuigelingen toch van vet te voorzien zitten er minuscule bolletjes vet in melk (Fig. S.3b). Deze bolletjes zijn ongeveer een micrometer groot en dus colloïden. Ze zijn veel groter dan moleculen, zodat we ze kunnen zien met een lichtmicroscoop. Tegelijkertijd zijn ze nog klein genoeg om spontaan te bewegen. De QR-code bij figuur Fig. S.3 verwijst naar een filmpje van uit zichzelf bewegende vetdruppeltjes in halfvolle melk. De richting en de snelheid van de vetdruppeltjes zijn willekeurig. Hun beweging wordt dan ook een dronkemanswandeling genoemd. De dronkemanswandeling wordt alleen veroorzaakt doordat de vetdruppeltjes erg klein zijn, ze leven dus niet!

Doordat colloïden uit zichzelf bewegen en zichtbaar zijn met de microscoop zijn ze ideale modelsystemen voor zelfassemblage. De dronkemanswandeling zorgt ervoor dat de colloïden geregeld met andere colloïden botsen. Als colloïden elkaar aantrekken kan zo'n botsing voor de vorming van een binding zorgen. Twee colloïden die elkaar 'leuk' vinden vormen dan een paar en laten elkaar niet meer los. Op die manier kunnen steeds grotere structuren ontstaan. In tegenstelling tot de bouwstenen in Fig. S.2QR hoeven colloïden dus niet geschud te worden om ze te laten zelfassembleren. Omdat de colloïden groot genoeg zijn om te zien met de lichtmicroscoop kunnen we deze zelfgeassembleerde structuren vervolgens direct bestuderen.

De vorm van de structuren die gevormd worden hangt af van de eigenschappen van de bouwstenen. Door bijvoorbeeld de vorm van de bouwstenen of de aantrekkingskracht tussen de bouwstenen te veranderen, worden andere structuren gemaakt. De vetdruppeltjes in melk zijn rond, maar in het lab kunnen we colloïden met allerlei verschillende vormen maken. In dit proefschrift bestuderen we bijvoorbeeld sneeuwpopachtige colloïden (Fig. S.4a). Zoals een sneeuwpop uit meerdere sneeuwballen bestaat, betaan onze colloïden uit een grote bol en een kleine bol. In Hoofdstuk 2 wordt beschreven hoe sneeuwpopcolloïden gemaakt worden. We beginnen met kleine ronde plastic bolletjes van ongeveer een halve micrometer (0.0005 millimeter) groot. Deze ronde bollen lijken op sponzen, ze kunnen zich volzuigen met een vloeistof. De minuscule sponsjes kunnen leeggeknepen worden door ze te verhitten. De vloeistof wordt dan uit de bol gedrukt en er ontstaat een

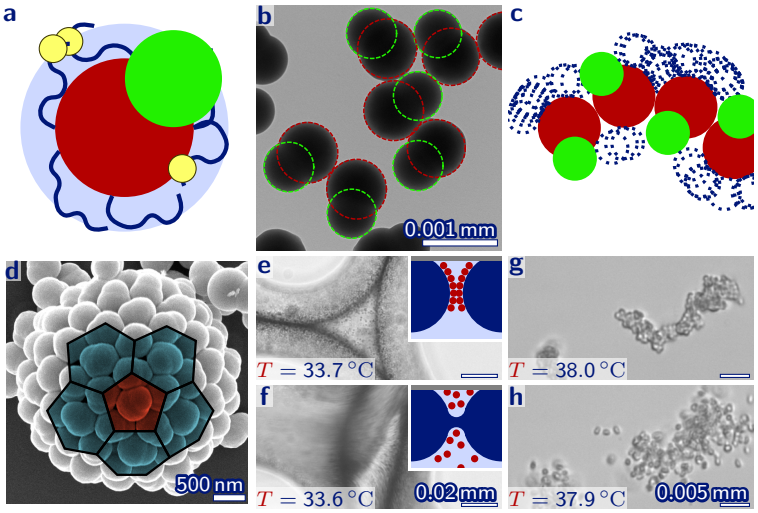

Figuur S.4. Grafische samenvatting. We hebben sneeuwpopcolloïden (**a**) met een kale bol (●) en een harige (∿) bol (●) met daaraan elkaar aantrekkende moleculen (●) gemaakt. Deze colloïden hebben we bekeken met een microscoop (**b**) en de grootte en de positie van de harige bollen (◌) en de kale bollen (◌) zijn automatisch bepaald. De haren kunnen bewegen en zorgen ervoor dat de colloïden vervormbaar zijn. Computersimulaties laten zien dat hierdoor gekromde structuren worden gevormd (**c**). De vervormbare sneeuwpopcolloïden vormen spontaan bolvormige capsules (**d**) met vijfvlakken (●) en zesvlakken (●). Colloïden kunnen aan het oppervlak van druppels hechten en zo voorkomen dat druppels fuseren (**e**). Nabij het kritisch punt kan een kleine temperatuursverandering er voor zorgen dat colloïden het oppervlak loslaten en druppels fuseren (**f**). Nabij-kritische fenomenen kunnen ook voor aantrekking tussen sneeuwpopcolloïden zorgen (**g**). De aantrekkingskracht wordt veel minder sterk wanneer de temperatuur een klein beetje daalt (**h**). De QR-code verwijst naar een filmpje van dwarsdoorsnedes door een bolvormige capsule (phd.chrisevers.com/5qr2b.mp4).

druppel op het oppervlak van de bol. Deze druppel kunnen we vervolgens omzetten in een vaste stof en het resultaat is een sneeuwpopachtige deeltje (Fig. S.4a).

De aantrekkingskracht kan bijvoorbeeld veranderd worden door verschillende moleculen aan het oppervlak van de colloïden te hangen. Als deze moleculen elkaar aantrekken, trekken de bouwstenen elkaar ook aan en kunnen bindingen worden

gemaakt. Stoten de moleculen aan het oppervlak elkaar af, dan worden juist minder bindingen gemaakt. Door verschillende moleculen aan verschillende kanten van een bouwsteen te hangen, kunnen steeds gecompliceerdere structuren worden gemaakt (Fig. 1.1). In Hoofdstuk 2 hangen we bijvoorbeeld elkaar aantrekkende moleculen aan een kant van de sneeuwpopcolloïden (Fig. S.4a).

We kunnen de sneeuwpopcolloïden dus bekijken met de microscoop. Om de colloïden goed te beschrijven moeten we de grootte en de positie van beide bollen bepalen. Dit kan met de hand, maar dat is erg veel werk. In Hoofdstuk 3 beschrijven we een methode om de computer automatisch de beide kanten van een sneeuwpopdeeltje te laten herkennen in microscopiefoto's (Fig. S.4b).

Vervormbaarheid

Virusbouwstenen kunnen van vorm veranderen als ze zichzelf in elkaar zetten tot een virus. Ze lijken dus een beetje op Barbapapa, die zijn gedaante ook kan veranderen. In Hoofdstuk 4 bestuderen we de invloed van vervormbaarheid van de bouwstenen op zelfassemblage. We maken een simpel computermodel van colloïden die elkaar aantrekken en vervormbaar zijn. Doordat de colloïden elkaar aantrekken, vormen ze bindingen en dus grotere structuren. De vervormbaarheid zorgt ervoor dat colloïden van gedaante veranderen als ze een binding aangaan. Hierdoor vormen relatief simpele bouwstenen complexere structuren dan onvervormbare colloïden. Ten slotte bestuderen we sneeuwpopcolloïden. Deze colloïden zijn behalve elkaar aantrekkend en vervormbaar ook een beetje asymmetrisch doordat ze uit twee bollen bestaan. In computersimulaties vormen deze colloïden gekromde structuren (Fig. S.4c).

In Hoofdstuk 5 bestuderen we zelfassemblage van vervormbare colloïden in het lab. We gebruiken hiervoor de sneeuwpopachtige bouwstenen die we in Hoofdstuk 2 hebben gemaakt. Deze bouwstenen zijn vervormbaar omdat ze haren aan het oppervlak hebben (Fig. S.4a). Zoals je de haren op je hoofd naar een kant kunt kammen of juist rechtop kunt zetten door er gel in te smeren, kunnen de haren op de colloïden ook plat liggen of zich juist uitstrekken. De haren op de bouwstenen zijn zo lang, dat de vorm van de bouwstenen verandert als de haren bijvoorbeeld plat liggen of naar een kant uitsteken. Bovendien bestaan de haren uit verschillende delen die elkaar aantrekken of juist afstoten. Wanneer twee bouwstenen dicht bij elkaar komen passen ze hun kapsel aan zodat de aantrekkende delen dicht bij elkaar zijn en de afstotende delen juist ver van elkaar zijn. Het resultaat is dat de bouwstenen uit zichzelf holle, bolvormige capsules vormen (Fig. S.4d). Net als een

voetbal hebben de capsules vijfvlakken en zesvlakken op het oppervlak. De capsules van onze bouwstenen lijken ook op de capsules rondom virussen (Fig. S.2d).

Nabij-kritische fenomenen

Sommige vloeistoffen mengen met elkaar, terwijl andere vloeistoffen onmengbaar zijn. Water en alcohol vormen bijvoorbeeld een heldere, homogene oplossing. Water en olijfolie zijn echter onmengbaar en olijfolie blijft drijven bovenop water. Een tussenweg bestaat ook, dat zijn combinaties van vloeistoffen die bij bepaalde verhoudingen en temperaturen mengen, maar bij andere verhoudingen en temperaturen onmengbaar zijn. Een voorbeeld is water en 3-methylpyridine (3MP). Bij kamertemperatuur zijn water en 3MP mengbaar in alle verhoudingen. Boven de zogenaamde lagere kritische temperatuur zijn er echter verhoudingen waarbij water en 3MP ontmengen. Er ontstaan dan druppels met een bepaalde verhouding 3MP/water in 3MP/water met een andere verhouding. De verhouding 3MP/water waarbij druppels worden gevormd op de kritische temperatuur is de kritische verhouding. Als de temperatuur dicht bij de kritische temperatuur is, en de 3MP/water verhouding dicht bij de kritische verhouding, treden nabij-kritische fenomenen op. De invloed van deze fenomenen op zelfassemblage bestuderen we in Hoofdstuk 6 en Hoofdstuk 7.

Colloïden worden niet alleen gebruikt als modelsysteem, ze komen ook voor in verf op de muur en slagroom op de taart. Ook in mist, bloed, e-readers, melk, crèmes en mayonaise zitten deeltjes met een typische grootte tussen de 0.000001 millimeter en 0.001 millimeter. De laatste drie voorbeelden zijn emulsies. Dat zijn vloeistoffen waarin minuscule druppeltjes zitten die worden gestabiliseerd door een emulgator. Mayonaise wordt bijvoorbeeld gemaakt door een eidooier, mosterd en citroensap te mengen en al roerende druppelsgewijs olie toe te voegen. Hierbij hechten moleculen uit de eidooier aan het oppervlak van oliedruppeltjes. Op die manier voorkomen ze dat de oliedruppeltjes samenvloeien tot een olielaag bovenop de saus. De moleculen in de eidooier zijn dus een emulgator en stabiliseren de mayonaise. Colloïden kunnen zelf ook als emulgator worden gebruikt. Ze hechten dan aan het oppervlak van bijvoorbeeld oliedruppeltjes. Doordat het oppervlak van de druppels vol met colloïden zit, kunnen ze niet meer samenvloeien en blijft de emulsie stabiel.

In Hoofdstuk 6 bestuderen we de invloed van nabij-kritische fenomenen op door colloïden gestabiliseerde emulsies. We voegen colloïden toe aan vloeistoffen die bij kamertemperatuur mengen, maar boven de kritische temperatuur ontmengen.

Boven de kritische temperatuur ontstaan dus kleine druppeltjes. Als we de temperatuur nog verder verhogen, hechten de colloïden aan het oppervlak van die druppeltjes. Hierdoor kunnen de druppels niet meer samenvloeien en hebben we een emulsie gemaakt (Fig. S.4e). Door simpelweg de temperatuur te verhogen is een vloeistof met colloïden dus verandert in een stabiele emulsie. Deze manier van emulsiebereiding is een stuk makkelijker dan druppelsgewijs toevoegen onder roeren zoals bij mayonaise in de keuken. Dicht bij het kritische punt veranderen de eigenschappen van de vloeistoffen sterk met de temperatuur. Ver boven de kritische temperatuur hechten de colloïden aan het oppervlak van de druppels, terwijl ze een paar graden lager het oppervlak loslaten. Hierdoor kunnen we de stabiliteit van de emulsie controleren met de temperatuur. Bij relatief hoge temperaturen is het oppervlak van de druppels bedekt met colloïden en is de emulsie stabiel. Daalt de temperatuur, dan laten de colloïden los en vloeien de druppels samen (Fig. S.4f). Door de temperatuur te veranderen kunnen we dus zowel emulsies creëren als destabiliseren.

In Hoofdstuk 7 zorgen nabij-kritische fenomenen voor aantrekking tussen colloïden. We zetten de thermostaat een paar graden lager dan hierboven, zodat de temperatuur net beneden de kritische temperatuur is. Bij deze temperatuur zijn de twee vloeistoffen dus nog net mengbaar. Afhankelijk van hun oppervlak en de verhouding van de vloeistoffen, trekken de colloïden elkaar dan aan of stoten ze elkaar af. Over de oorzaak van de aantrekking tussen colloïden discussiëren wetenschappers nog, maar deze is voor ons onderzoek van ondergeschikt belang. Wij gebruiken de aantrekking om colloïden te laten zelfassembleren. We bestuderen zowel harige colloïden als vergelijkbare haarloze colloïden. Als er relatief weinig water in de mengsels zit, trekken de harige colloïden elkaar aan, terwijl de haarloze colloïden elkaar niet aantrekken. De aantrekkingskracht tussen de harige colloïden verandert sterk met de temperatuur. Door de temperatuur met een fractie van een graad te laten stijgen zien we een overgang van vrijwel geen aantrekkingskracht naar een redelijk sterke aantrekking tussen de colloïden. Ook bestuderen we sneeuwpopcolloïden die bestaan uit een harige bol en een haarloze bol. Deze colloïden zelfassembleren in structuren waarbij de harige bollen aan de binnenkant lijken te zitten, terwijl de haarloze bollen aan de buitenkant lijken te zitten (Fig. S.4g). Deze structuren zijn vergelijkbaar met de structuren die zeepmoleculen maken in water. Net als de sneeuwpopcolloïden bestaan zeepmoleculen uit twee verschillende delen, die we bij zeep de kop en de staart noemen. De koppen stoten elkaar af, terwijl de staarten elkaar aantrekken. In tegenstelling tot zeepmoleculen kunnen

we de sterkte van de aantrekkingskracht tussen de sneeuwpopcolloïden gemakkelijk veranderen met de temperatuur. Door de temperatuur met een fractie van een graad te veranderen, vallen de gezelfassembleerde structuren bijvoorbeeld weer uit elkaar (Fig. S.4h).

Wat leren we hiervan?

Het doel van dit proefschrift is ons begrip van zelfassemblage te vergroten en nieuwe mechanisme te bestuderen om goed gedefinieerde materialen te vormen. De resultaten laten zien dat vervormbaarheid en nabij-kritische fenomenen zelfassemblage een significante stap verder kunnen helpen. Vervormbaarheid zorgt ervoor dat simpele colloïden kunnen zelfassembleren in complexe structuren. Hierdoor kunnen we voor het eerst bouwstenen maken die zelfassembleren in holle, bolvormige capsules. Door de eigenschappen van de bouwstenen systematisch te veranderen verwachten we dat nog meer nieuwe materialen gevormd kunnen worden. Verder zijn zowel de colloïden als virusbouwstenen elkaar aantrekkend, vervormbaar en net niet helemaal rond. Virusbouwstenen zijn echter een stuk ingewikkelder en hebben nog veel meer eigenschappen (vergelijk Fig. S.2c en Fig. S.4a). De drie eigenschappen die onze colloïden delen met virusbouwstenen zouden ook belangrijk in de zelfassemblage van virussen kunnen zijn.

Nabij-kritische fenomenen, aan de andere kant, kunnen voor meer controle over de aantrekking tussen colloïden zorgen. In de toekomst zou dit gebruikt kunnen worden voor zelfassemblage van structuren die nu nog te ingewikkeld zijn om spontaan te vormen. Tot slot hebben we een manier laten zien om emulsies te bereiden en te destabiliseren door simpelweg de temperatuur te veranderen. Deze methode zou de productie van industriële, farmaceutische en voedingsproducten gemakkelijker kunnen maken.

Dankwoord / Acknowledgements

Jarenlang deeltjes maken, bestuderen en beschrijven is niet mogelijk zonder de hulp van anderen. Daarom wil ik graag onderstaande mensen, en al die anderen die de afgelopen jaren mijn wetenschappelijke of persoonlijke leven hebben veraangenaamd hartelijk danken.

Allereerst, Willem, wil ik jou bedanken. Boven alles hebben je nieuwsgierigheid en enthousiasme een grote bijdrage geleverd aan dit proefschrift. Ik leerde je kennen toen ik als eerstejaarsstudent een kort project deed bij een van je toenmalige promovendi. Het staat me nog steeds levendig bij hoe enthousiast je reageerde toen je een kijkje kwam nemen bij de microscoop. Je colleges en oratie hebben mijn liefde voor de fysische chemie verder aangewakkerd en toen ik op zoek ging naar een promotieplek heb ik je uiteraard weer benaderd. Ik ben ontzettend blij dat ik uiteindelijk heb gekozen bij jou te promoveren. Hoewel je het al snel drukker kreeg als departementshoofd, maakte je altijd tijd om over verrassende microscopieplaatjes, nieuwe stappen en mogelijke verklaring van gedachten te wisselen. Ook zorgde je voor een goede sfeer in de breinstormsessies waaruit veel ideeën uiteindelijk in dit proefschrift terecht zijn gekomen. Daarnaast wil ik je danken voor de vrijheid die je gaf mijn eigen ideeën te volgen, en je scherpe inzicht dat mij soms van gedachten deed veranderen. Je aanstekelijke lach en de gezelligheid tijdens de whisky- en potluckavonden bij jou en Marianne thuis hebben zeker bijgedragen aan de open sfeer in onze groep.

The members of the Van 't Hoff Laboratory provide the perfect habitat for a scientist. I'd like to thank my office mates Joost (thanks for a great time in Les Diablerets), Jos, Julius, and Pepijn for the productive environment in N708 and their advice on scientific, mathematical or didactic matters. Jan's unstoppable flow of fresh ideas resulted in many hypotheses that ended up in this thesis. Bonny, Dominique, Emile, Kanvaly, Marina, and Stephan are thanked for their support with technical or administrative issues. Carla, Chris, Ernst and Hans provided excellent support with the electron and optical microscopes. I'd like to thank my über Sonja

and ünter Bas for the team work in the Borrelcommissariaat. All other (former) colleagues at FCC, Dzina, Laura, Anke, Ping, Samia, Ben, Andrei, Henk, Albert, prof. Vrij, Hans, Remco, Gert-Jan, Lia, Mikal, Mark, Rocío, Nina, Yong, Jasper, Frans, Bob, Rob, Susanne, Roel, Fuqiang, Burak, Faranaaz, Jan, Janne-Mieke, Jaakko, Antara, Esther, Ivan, Álvaro, Regina and all students contributed to a great time in the lab, at the coffee table, at conferences and on the dance floor. I also like to thank the other members of the Dutch soft matter community for their indispensable scientific and recreational input.

I also had the pleasure to collaborate with scientists from other labs. The computer simulations by Jurriaan and Peter made publication of our work on deformable particles possible in Nature. Anh, Triet and Peter introduced me to near-critical mixtures and the combination of their solvent and my particles resulted in the chapter on thermoreversible self-assembly. David, Mark, Henrique, David, Bhaskar, Kazem and Andy are thanked for their insight in image analysis, optical trapping and holographic microscopy and an excellent time at New York University.

Ik heb de afgelopen jaren het voorrecht gehad enkele studenten te begeleiden die enkele weken tot ruim een jaar onderzoek bij mij hebben gedaan. Niet al hun resultaten zijn in dit proefschrift terecht gekomen, maar ze waren wel belangrijk om te besluiten welke zijwegen we verder zouden verkennen. Frans bestuurde als derdejaarsstudent of we de sneeuwpopdeeltjes ook zelfvoortstuwend konden maken. De bachelorthesis van Joris zorgde voor meer inzicht in de vervormbaarheid van colloïden. Tweedejaarsstudenten Laura, Maaike, Maarten en Thomas en derdejaarsstudent Sven verkenden hoe polyelektrolyten voor aantrekking tussen colloïden kunnen zorgen. Micah zorgde als masterstudent voor vrijwel alle experimentele resultaten in het hoofdstuk over emulsies. Heel erg bedankt voor jullie bijdrage!

Graag wil ik mijn vrienden bedanken voor de broodnodige afleiding, maar ook voor hun interesse in mijn plastic virussen. Andy, Ceriel, Nick, Paul en Pascal, judoën doen we bijna allemaal niet meer, maar dat maken we meer dan goed in de kroeg, tijdens roadtrips en met carnaval. Annelore, Jeroen, Marco, Miesje, Lennart en Silvan, ook al zien we elkaar minder dan op de middelbare school, het is altijd ontzettend vertrouwd weer bij elkaar te zijn. Daan, Paul, Robin en Sabine, bedankt voor de gezellige bestuursetentjes en -weekenden. Anıl, Björn, Johan, Kalle, Mikael, Marie, Martin, Nigar och mina andra svenska kompisar, tack för alla underbara vistelser i Sverige. Axel, Ben, Dwayne, Esther, Fleur, Giel, Ivo, Jesper, Jetske, Karen, Lyle, Max en al die andere leden van GroenLinks en DWARS, of ik jullie nu tijdens vergaderingen, op straat of in de kroeg tegenkom, altijd is het even gezellig en

ga ik weer vol nieuwe energie naar huis. Joost, Marco, Robbert en al die andere stapmaatjes, bedankt voor alle gezelligheid op en naast de dansvloer. Mathijs, bedankt voor je wijze raad en voor het doorlezen van mijn proefschrift. Tim, bedankt voor de mooie tijd samen en dat je er ook nu nog altijd voor me bent. Emma, bij jou kan ik altijd terecht, of het nu om Proton, promoveren, liefde of GroenLinks gaat. Ik ben blij dat je mijn paranimf wilt zijn!

Ook mijn familie wil ik bedanken. Oma, ooms, tantes, neven, nichtjes en Sharonna, bedankt voor jullie interesse en steun. Jos, met jou is geen enkel ogenblik saai, ik hoop dat we nog veel avonturen mogen beleven. Gijs, je hebt een uitstekend luisterend oor en waar ter wereld ik ook zit, bedankt dat je me me altijd op komt zoeken. Ik ben blij dat je onze boerderij voortzet en dat je mijn paranimf wilt zijn!

Ten slotte wil ik mijn ouders bedanken. Pa en ma, jullie hebben mijn brede interesse van kinds af aan gestimuleerd en mijn onderzoekende geest altijd aangemoedigd. Jullie wijsheid heeft me gemaakt tot wie ik nu ben. Ik bewonder jullie enorme kracht en doorzettingsvermogen. Bedankt voor jullie liefde, steun en vertrouwen.

List of Publications

This thesis is based on the following publications:

- Evers, C. H. J., Luiken, J. A., Bolhuis, P. G. & Kegel, W. K. Self-assembly of microcapsules via colloidal bond hybridization and anisotropy. Nature *accepted*. doi:10.1038/nature17956. (Hoofdstuk 2, 4 and 5)
- Evers, C. H. J., Grier, D. G. & Kegel, W. K. Automated image analysis using Hough circle transformations. *In preparation* (Hoofdstuk 3)
- Evers, C. H. J., Van der Vaart, M. J. M. & Kegel, W. K. Pickering-like emulsions by thermoreversible attachment of colloids onto near-critical interfaces. *In preparation* (Hoofdstuk 6)
- Evers, C. H. J., Nguyen, T. A., Kegel, W. K. & Schall, P. Thermoreversible self-assembly into micelle-like structures in near-critical mixtures. *In preparation* (Hoofdstuk 7)

Other publications by the author:

- Evers, C. H. J., Andersson, T., Lund, M. & Skepö, M. Adsorption of unstructured protein β-casein to hydrophobic and charged surfaces. Langmuir **28**, 11843–9 (2012). doi:10.1021/la300892p.

Curriculum Vitae

Chris H.J. Evers

April 2, 1987
Vierlingsbeek

chris.evers@gmail.com
+31 (0)6 4839 5994
chrisevers.com

2011-2016 PhD Physical and Colloid Chemistry (Utrecht University)

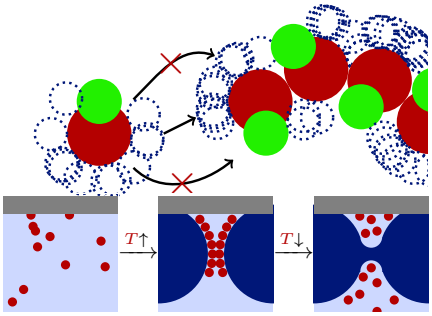

- Colloidal self-assembly driven by deformability & near-critical phenomena supervised by Willem Kegel (this thesis).
- Model systems for spontaneous formation of ordered structures: synthesis, microscopy studies and modelling of functional polymer nanoparticles.
- Supervision of student projects, practical courses, tutorials and group discussions.
- Presentations at (inter)national conferences.
- Evers *et al.* Nature (accepted)

2009-2011 MSc Nanochemistry (Lund University)

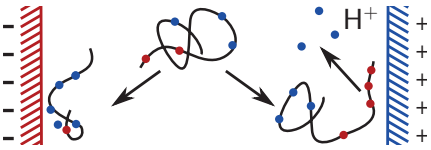

- Computer simulations of attachment of milk proteins to packaging materials supervised by Thorbjörn Andersson (Tetra Pak), Mikael Lund and Marie Skepö (Lund University)
- Evers *et al.* Langmuir (2012)

2005-2008 BSc Chemistry, cum laude (Utrecht University)

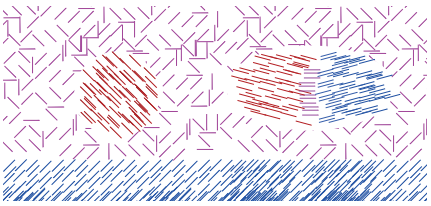

- Synthesis of rod- and platelet-shaped colloids and microscopy of liquid crystals supervised by Lia Verhoeff and Henk Lekkerkerker.
- Chairman of the Utrecht Association for Chemistry Students "Proton" (2008-2009).
- Supervision of practical courses and of tutorials in quantum chemistry.